Ph.D. Thesis
in
Physics

UNIVERISTY OF CATANIA
INFN – LABORATORI NAZIONALI DEL SUD

A MOBILE XRF SCANNER FOR A REAL-TIME ELEMENTAL IMAGING OF PAINTED ARTWORKS

Claudia Caliri

Supervisor: Dr. Francesco Paolo Romano

Tutor: Prof. Dr. Agatino Musumarra

January 2017

Contents

Abbreviations

XRF	X-ray Fluorescence
SR	Synchrotron Radiation
MA-XRF	Macro-XRF
MSI	Multispectral Imaging
XRR	X-ray Radiography
NAAR	Neutron Activation Auto-Radiography
FWHM	Full-Width-at-Half-Maximum
FP	Fundamental Parameters
SDD	Silicon Drift Detectors
DXP	Digital X-ray Processor
RTOS	Real Time Operative System
CU	Control Unit
ICR/OCR	Input/Output Count Rate
FoM	Figure of Merit
Y	Chemical sensitivity
LOD	Limits of Detection
cps	counts per second
μ-XRF	micro-XRF
TLIST	Time List
ROI	Region of Interest
RGB	Red-Green-Blue

Index of figures

7

Index of tables

Introduction

Paintings, come down to us and nowadays collocated in galleries and museums, are a valuable part of the cultural heritage of mankind. Their artistic, aesthetic and historical relevance categorizes them as objects of inestimable value. The pictorial art has seen over the time the evolution of several techniques that differ mainly in pigments and supports.

Art historians and conservators are constantly concerned with the questions of where, when and by whom a painting was made. In many cases, stylistic considerations combined with aesthetic evaluations and archive studies are not able to provide comprehensive answers. Further, styles were sometimes imitated and attribution can be difficult to be determined.

A painting consists of several layers subsequently applied for giving the desired optical effect: the shine of colors, the suggestion of shadows or the convincing illusion of an object's texture, are realized by deliberately including multiple layers. In many historical paintings, pictorial layers have been applied for purposely hiding previous drawings due to a changing of the intent of the artist. The understanding of the chemical nature of pigments and the study of the creative process through the visualization of hidden figures "*overpaintings*" and retouches "*pentimenti*" create a direct link with the historic period of the artwork and they are helpful for its authentication.

The preciousness of the paintings requires the assessment of their integrity and the continuous attention of their state of conservation. Discoloring and degradation processes of paints must be cured or prevented before they become visible. Thus, the knowledge of the original materials is of crucial importance for the programming a restoration treatment or for the choice of environmental conditions of conservation, in manner to preserve their original structure as much possible.

In this context, historical paintings have been object of intensive studies for several decades. A large range of spectroscopic and spectrometric methods have been developed and combined for the understanding compositional aspects as well as to know stratigraphy. Scientific investigations need to preserve the original structure of the painting, limiting to the minimum the sampling. In order to fulfil this mandatory requirement, the development of non-destructive techniques (mainly based on portable instrumentation), allowed to not expose artworks to environmental stress or damage risks and it increased considerably the number of investigated objects, contributing to expand their knowledge and conservation procedures.

Nowadays, macro X-ray fluorescence (MA-XRF) is a well-established technique for the non-invasive and element-specific imaging of painted surfaces. It allows the determination of the spatial distribution of chemical elements over large areas, thus enabling to infer the presence of pigments or mixtures thereof across the entire surface of a work of art.

Its multispectral capabilities allow gaining information on pigments below the visible surface and to put in evidence the existence of hidden details. The technique is performed by scanning the painting with an X-ray beam of few hundreds of microns and the fluorescence radiation, properly detected, is used to build-up point-by-point the chemical mapping with high spatial resolution.

Recently, a novel mobile MA-XRF scanner has been developed allowing the (near) real-time elemental imaging of large dimension painted artworks.
To date, performances of this device in terms of lateral resolution, scanning speed and dimensions of the scanning area, makes it as one of the most (or even the most) efficient portable MA-XRF systems available in the scientific community for studying paintings.
The development of the MA-XRF scanner and its application to the study of painted artworks represents the focus of this PhD project carried out at the LANDIS laboratory of LNS-INFN and IBAM-CNR in Catania (Italy).

The instrument is based on microfocus X-ray tube coupled to a polycapillary optic for transmission and focusing of primary radiation on the sample. The fluorescence induced on the sample is detected by a large area SDD detector operating in time-list event-mode. The scanner is fully controlled by a custom developed control unit programmed for the real-time control of all sensors and for a real-time data analysis. It allows the analysis of large surfaces up to $110 \times 70 \ cm^2$. MA-XRF elemental mapping is performed with a sub-millimetric lateral resolution by placing the painting out-of-focus of the optic. However, images with a lateral resolution of 38 μm can be achieved for analysis of pictorial details with a simple adjustment of sample in the optic focus position. MA-XRF scanner operates acquisitions in continuous mode with a maximum scanning speed of 100 mm sec^{-1}, covering the full area in 4.2 hours.

MA-XRF scanner works with an in-house programmed software allowing a real-time least square fitting of pixel spectra. Up to 5000 fit per second are operated in a live mode.
Elemental maps are available for interpretation at the end of scanning.

The analytical capabilities of the scanner have been verified in a number of case-studies in collaboration with Museums and for which the MA-XRF scanner has been used in-situ. In the present PhD work we discuss MA-XRF technique applied for studying three different typologies of artworks.

As a first example, it is presented the MA-XRF investigation of "Paston Treasure", a precious painting allocated at the Norwich Castle Museum (UK) and considered one among the most important painting in the history of British Arts. The research activity was carried out in collaboration with the Fitzwilliam Museum (UK, Cambridge), the Yale Centre for British Art (USA) and the Norwich Castel Museum (Norwich). MA-XRF analysis has provided knowledge of original painting materials of the artist and information concerning the creative process. Elemental images have revealed a hidden figure of a woman in the center of the composition and details emerged by X-rays analysis as her gown and hair ornaments have been helpful for inferring her identity, still now object to various interpretations.

As a second example, it is discussed the use of MA-XRF at the Museo Egizio in Torino (Italy) for analysis of the funerary objects in the tomb of Kha and Merit (1428-1351 BC). This is one of very few known examples of Egyptian tombs never depredated before its discovery and never subject to the scientific analysis. The elemental maps of painted wooden coffers has revealed a complex palette of pigments and presence of hidden "*pentimenti*" identified in the painted scenes. Some parts of the written text in the body of the coffers that has become unreadable over the time was unveiled as well.

Finally, a collaboration with the Fitzwilliam Museum, has seen MA-XRF analysis of illuminated manuscripts, created in Italy during 14th century. MA-XRF analysis has allowed to study the palette employed by illuminators, contextualizing their historic attribution. Further, macroscopic X-ray imaging allows to make readable the inscriptions in Latin present on the back side of the fragment, until then never decoded.

This work is arranged in four main Chapters:

The first Chapter discusses capabilities and potentialities of several imaging techniques that have given a great contribution in the field of art and conservation, with major emphasis to MA-XRF methodology.

The second Chapter is dedicated to fundamental aspects of the X-ray fluorescence and components to be used in X-ray spectrometry.

The third Chapter discusses the development of the MA-XRF scanner trough the detailed description of components, sensors and control system. The presentation of spectrometric figures of merit, acquisition-scanning mode and scanning speeds performances is also included in the third session of this work. In addition, the third Chapter explains the architecture and the functionalities of the in-house programmed software for the real-time elaboration of the images.

Finally, in the fourth Chapter the value of the technique is illustrated through the presentation of three analytical cases. Analytical results are presented and discussed.

Chapter 1

The paintings

Since antiquity up to the modern times paintings reflect the evolution of human creativity in application of natural and synthetic pigment materials on different pictorial supports.

Paintings are complex materials with a multi-layered structure. In a very general description they can be schematized as in the sketch of Figure 1 [1].

The first layer is the *support* that can be of different nature. Since the intensive production of painting from middle ages up to the modern time, easel paintings making use of canvas or wood panels as pictorial supports are the most significant. However, other materials like metals, paper, parchments, marbles, etc., have been used since antiquity.

In the case of canvases, they were mounted on a frame and covered with an organic gelatinous glue for ensuring its protection and a sufficient adhesion of successive layers.

The layer over the canvas is the *ground*. It is an intermediate layer between the support and the painting. A common materials used as a ground was whited gypsum or chalk (CaCO3), forming a smooth surface ready for the paint application. A white ground was employed for its capability of creating artistic effects on the full paintings (for instance giving more brightness to the colours). The ground composition was subject to changes over the time and even coloured ground have be used. Typically, they were obtained with a layer of lead-white (2PbCO3·Pb(OH)2), gypsum (CaSO4·2H2O), and a mixture of earth pigments.

The ground is usually used by the artists to draw initial sketch of their work by using charcoal, chalk, metal points, inks, etc.
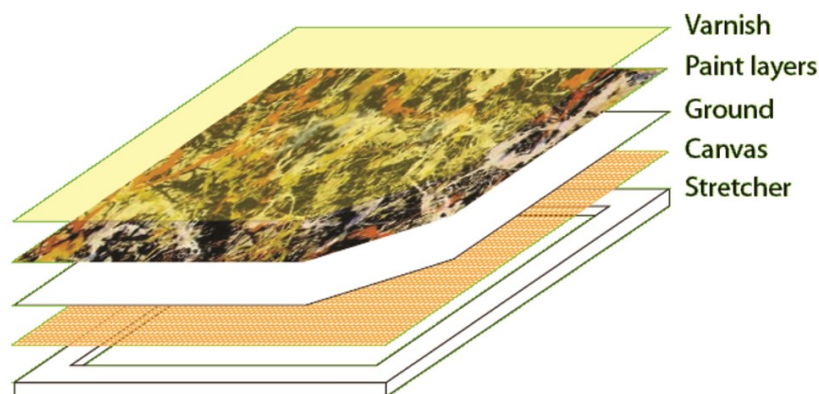
Figure 1: structure of a painting [1].

The layer over the ground is the *artistic paint*, obtained by a mixture of fine powders responsible for the color: the *pigments*. A binder is used to keeps the particles of these powders together. Among binders for oil paintings there are walnut, linseed, and poppy seed oils, among binders for tempera, egg yolk, egg white, casein and Arabic gum are mostly employed. Sometimes, paint may also contain a diluent to make the paint spread more uniformly and (or) to change its transparency to the desired degree.

The *varnish layer* is transparent and optional. It may just bring addition protection to the outer layers of the painting or enhance the visual perception of the paint layers underneath. Varnish is often made of natural or synthetic resin.

Pigments represent an extended topic including nature of raw materials, manufacturing technologies, painting techniques [2]. They are both *organic* (e.g., madder lake, indigo) and *inorganic* (e.g. smalt, vermilion). Mostly, they can be found in *nature* as minerals, while others are prepared *artificially*. They can be found in the artworks as pure pigments or as mixture at a typical concentration level of several mass percent and thickness form a few up to tens of microns. Table 1summarizes some of the most commons pigments used in paintings including the period of use from antiquity since modern time.

Blue pigments	Chemical name	Formula	Source/Date	Used until
Azurite (Blue verditer)	Basic copper (II) carbonate	$2\,\textbf{Cu}CO_3 \cdot \textbf{Cu}(OH)_2$	mineral (Egyptians) /artificial (1600)	1700
Cerulean Blue	Cobalt (II) stannate	$\textbf{Co}O \cdot n\,\textbf{Sn}O_2$	artificial 1821	in use
Cobalt Blue	Cobalt (II)-doped alumina glass	$\textbf{Co}O \cdot Al_2O_3$	artificial 1775	In use
Egyptian Blue	Calcium copper (II) silicate	$\textbf{CaCu}Si_4O_{10}$	mineral third millenium BC	Romans
Lazurite (from Lapis Lazuli) Utramarine	sulfur-containing sodium aluminum silicate	$Na_{8\text{-}10}Al_6Si_6O_{24}S_{2\text{-}4}$	mineral 1100 artificial 1828	in use
Manganese Blue	Barium manganate (VII) sulfate	$\textbf{BaMn}O_4\text{-}\textbf{BaSO}_4$	artificial 1907	in use
Phthalocyanine Blue (Winsor Blue)	Copper (II) phtalocyanine	$C_{32}H_{16}N_8\textbf{Cu}$	artificial 1936	in use
Prussian Blue	Iron (III) hexacyanoferrate (III)	$\textbf{Fe}[\textbf{Fe}^{3+}\textbf{Fe}^{2+}(CN)_6]_3$	artificial 1704	in use
Smalt	Cobalt(III)silicate	$SiO_2+ \textbf{K}_2O + Al_2O_3 + \textbf{Co}O$	artificial 1400	1700
Verdigris	Basic copper (II)	$\textbf{Cu}(OH)_2 \cdot (CH_3COO)_2 \cdot 5\,H_2O$	Cu corrosion products (acetates)/Greeks	1800
Red	Chemical name	Formula	Source/Date	Used until
Cadmium red	Cadmium sulfide (CdS) + cadmium selenide (CdSe) in varying proportion	$\textbf{Cd}S + \textbf{CdSe}$	artificial 1919	in use
Chrome red	Basic lead(II)-chromate	$\textbf{PbCr}O_4 \cdot \textbf{Pb}(OH)_2$	artificial 1809	1900
Realgar	Arsenic sulfide	As_4S_4	mineral and artificial / Antiquity (Egyptians)	1800
Red lead (minimum)	Lead(II,IV)-oxide	Pb_3O_4	mineral and artificial / Antiquity (Greeks), artificial (Romans)	1800
Red ochre	Anhydrous iron(III)-oxide	Fe_2O_3	natural earth and artificial / prehistoric	in use
Vermillion (cinnabar)	Mercuric sulfide	HgS	mineral antiquity (Greeks)/ artificial / 1700 (vermilion)	1800
Ochre	Iron oxide and hydroxide	$\textbf{Fe}$ oxide and hydroxide	mineral antiquity	in use
White	Chemical name	Formula	Source/Date	Used until
Titanium white	Titanium dioxide	$\textbf{Ti}O_2$	artificial 1921	in use
Barytes	Barium sulfate	$\textbf{BaSO}_4$	mineral / artificial (1800)	in use
Chalk (whitening)	Calcium carbonate	$\textbf{CaCO}_3$	mineral antiquity	In use
Lead white	Lead (II) carbonate (basic)	$2\,\textbf{Pb}CO_3 \cdot \textbf{Pb}(OH)_2$	artficial antiquity (Greeks)	in use

Lithopone	Zinc sulfide and barium sulfate	**Zn**S**BaSO4**	1874	
Zinc white	Zinc oxide	**Zn**O	artificial 1834	in use
Black	**Chemical name**	**Formula**	**Source/Date**	**Used until**
Bone/Ivory Black	Calcium phosphate + calcium carbonate +carbon	$Ca_3(PO_4)_2$+C+ $CaCO_3$/$Ca_3(PO_4)_2$ +C+ $MgSO_4$/	animal prehistory	in use
Green	**Chemical name**	**Formula**	**Source/Date**	**Used until**
Cobalt green	Cobalt(II)-oxide-zinc(II)-oxide	$CoO \cdot ZnO$	artificial 1780	in use
Emerald green	Copper(II)-acetoarsenite	$Cu(CH_3COO)_2 \cdot 3 Cu(AsO_2)_2$	artificial 1814	1900
Green earth	complex aluminosilicate minerals	$K[(Al,Fe^{III}),(Fe^{II},Mg)] (AlSi_3,Si_4)O_{10}(OH)_2$	Mineral antiquity (Greeks)	in use
Malachite (Green Verditer)	Basic copper(II) carbonate	$2\ CuCO_3.Cu(OH)_2$	mineral and artificial / antiquity (Egyptians)	1500
Verdigris	Basic Copper acetate	$Cu(OH)_2 \cdot (CH_3COO)_2 \cdot 5\ H_2O$	artificial antiquity (Greeks)	1800
Viridian (Chrome oxide)	Chromium(III)-oxide dihydrate	$Cr_2O_3 \cdot 2\ H_2O$	artificial 1838	in use
Yellow	**Chemical name**	**Formula**	**Source/Date**	**Used until**
Cadmium yellow	Cadmium sulfide	CdS	artificial 1820	in use
Chrome yellow	Lead(II)-chromate	$PbCrO_4$	artificial /1816	in use
Cobalt yellow	Potassium cobaltinitrite	$K_3[Co(NO_2)_6] \cdot H_2O$	artificial /1852	in use
Lead tin yellow	Lead stannate (Type I) lead tin oxide silicate (Type II)	Pb_2SnO_4 (Type I) $Pb(Sn,Si)O_3$ (Type II)	artificial /1200	1700
Ochre	Iron oxide and hydroxide	Fe oxide and hydroxide	mineral/ antiquity	in use
Lemon yellow	Barium chromate or strontium chromate or mixture of lead chromate + lead sulphate	$BaCrO_4$	artificial 1830	in use
Orpiment	Arsenic sulfide	As_2S_3	mineral and artificial / Antiquity (Egyptians)	1800
Naples yellow (Lead antimonate)	Lead(II)-antimonate	$Pb(SbO_3)_2$ or $Pb(SbO_4)_2$	artificial 1500	in use
Strontium chromite	Strontium chromate	$SrCrO_4$	artificial 1900	in use
Zinc yellow	Complex zinc potassium chromate	$K_2O \cdot 4\ ZnCrO_4 \cdot 3 H_2O.$	artificial 1850	in use
Brown	**Chemical name**	**Formula**	**Source/Date**	**Used until**
Umber	Iron(III)-oxide, partly hydrated +	$Fe_2O_3 (\cdot H_2O)$ + $MnO_2 \cdot (n\ H_2O)$+ Al_2O_3	nature earth prehistoric	in use

	manganese oxide + aluminium oxide			
Van Dyke brown	Iron(III)-oxide, partly hydrated + manganese oxide partly hydrated + humic acids	Fe_2O_3 ($\cdot\ H_2O$) + $MnO_2 \cdot (n\ H_2O)$ + humic acids	nature earth 1600	in use

Table 1: Inorganic pigments.

1.1. Scientific investigation of paintings

1.1.1 XRF technique in Art and Archeology

In the study of art objects and other historical materials, the ability to employ non-destructive analytical methods and techniques which can be operated in situ is often mandatory. The artworks can be of different nature (e.g. paintings, metals, glass, wood, stone, ceramic, etc.). They can be decorated with pigment materials, and they may be well preserved or in a serious state of deterioration. In any cases their sampling for analysis is severely limited, or in many cases forbidden [3].

Studies involving scientific methods [4 - 6] are aimed to the identification and knowledge of different aspects concerning an art object. In many cases, the chemical composition is the primary type of information to be investigated. In addition, analytical results can provide novel insights on provenance, historical context, manufacturing technology and geographical spread of investigated cultural objects [7-12].

In this work our attention is focused on painting study, for which chemical analysis is aimed to the comprehension of the nature of pigments to the painting techniques and to the materials identification that distinguish a particular artistic movement.

Next to these *cultural–historical* motivations, scientific methods may also be applied to evaluate the *state of conservation* of artworks. In this way, the information obtained may be used to identify the most appropriate conservation policy and restoration [13-16].

Similarly, objects that have been subjected to restoration treatments (recently or in the past) may be investigated to discriminate original materials from new ones or to evaluate the efficacy of past treatments.

Finally, scientific methods are also suitable to gain information concerning the *authentication* of artworks [17-18]. In the case of paintings, the occurrence of modern pigments in a historic painting is often used to address question of authenticity. In such a case, conservators usually verify whether there is discrepancy between the assumed date of the painting and the date of introduction of the anomalous pigments.

Mostly, the scientific techniques applied to an art object need to be [19-20]:

    i.   *Non-destructive.* The analysis doesn't have to cause any (visible) damage to the sample. Sampling, if allowed, should be limited to very small amounts;

ii. *Fast.* The analysis should be fast because the time conferred for investigation of artworks is subjected to restrictions. In addition, a fast analysis allows to investigate a large numbers of objects allowing systematic and comparative studies.

iii. *Versatile.* The use of a single instrument should allow the analysis of many materials and objects of various shapes and dimensions;

iv. *Sensitive.* Analytical techniques should present the highest chemical sensitivity in order to allow the investigation of major, minor and trace elements.

v. *Multi-elemental.* – A single measurement should allow to detect most of the elements composing a sample simultaneously.

Conventional X-ray Fluorescence (XRF) satisfies many of above mentioned requirements. Nowadays, XRF is a widely employed analytical method in scientific examination of artworks [21-24]. XRF is based on the irradiation of samples with a primary X-ray beam inducing atomic species to emit characteristic X-ray fluorescence. Identification of these X-ray lines in the spectrum provides information on the chemical elements composing the sample [25-29]. Moreover, a quantification of spectra is possible. Quantitative analysis is based on a calibration with reference materials of similar composition to the one under investigation or, more appropriately, it is based on absorption calculations taking into account the expected matrix composition through an opportune calibration procedure based on the well-established fundamental parameters [30- 36]. In the second Chapter of this work the important aspects of X-ray fluorescence methods, schematized in Figure 2, will be extensively discussed.
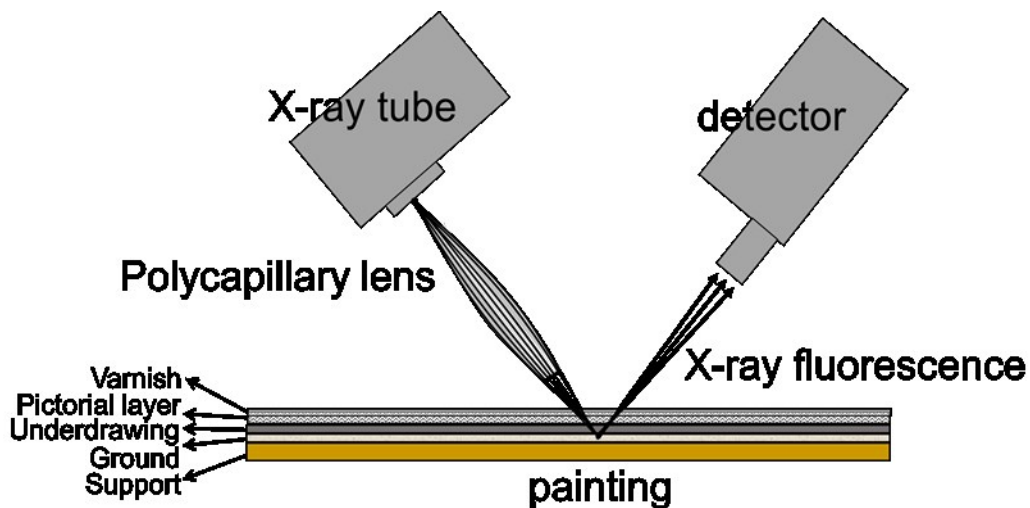
Figure 2: schematic of X-ray fluorescence technique.

X-ray spectrometry started to be extensively used in the Cultural Heritage field with the development of portable XRF instruments (PXRF). The portability of the XRF technique has allowed to increase noticeably the number and typologies of objects to be studied [37-

46]. Since spectrometers have been moved directly to museums or archaeological sites, immovable or otherwise inaccessible objects, have been easily reached for analysis [47-48, 3].

In the case of paintings, conventional XRF technique is operated locally and, in many cases, information obtained by the analysis can give misleading information.

1.2. XRF imaging techniques

A considerable impulse to further development of the XRF technique is arose from scholars, conservators, art historians of knowing more about the creative process and the artist's modus operandi together to the need to assess and predict the current and future conservation state of artworks.

The first motivation is essentially of art-historical nature and seeks to (better) reconstruct the history of an artwork, whereas second motivation is more strongly linked to potential conservation treatment of an artwork.

In particular, the main motivations to perform XRF analyses on valuable paintings can be synthetize in three interest aspects:

1) to study the original materials used by artist and establish a link between the painting and artist to whom it is attributed or (in the case of autograph works) to obtain novel insights into the evolution of his painting technique and materials. In several analytical cases, this purpose involves the combination and the comparison between data obtained from several paintings by the same artist, or to resort to combined measurements with other methods;

2) to visualize sub-surface layers that can be interested by overpainted hidden drawings, or the so-called *pentimenti*. The penetration capability of X-rays allows to go in deep besides the first pictorial layer (several tens to hundreds of micrometres), so elements present below the surface contribute to the elemental distribution images, revealing what that is not visible to naked eye. Overpainted drawings help to reconstruct the history of the painting;

3) to document the state of conservation of paintings and learn more about the material changes due to past conservation treatments or to the environmental conditions.

Over the time, in order to meet the above demands the possibility of going beyond the local investigation has been investigated and many efforts have been aimed towards the development of XRF imaging techniques [49].

XRF imaging is aimed to study an art objects in its full dimensions without leaving any parts not examined. It should provide readable results in the form of images that can be easily interpreted by archaeologists, conservators, art scientists and scholars.

In the 1990s, the first spectrometers coupled to a scanning device were developed for mapping the pigments distribution of decorated surfaces of artworks [50].

In scanning XRF as in conventional XRF, the sample is locally irradiated by a focused or collimated X-ray beam and the emitted fluorescence is recorded by an energy-dispersive X-ray detector. The sample is moved by using motorized stages; measurements are repeated sequentially pixel-by-pixel and the investigation is extended to the whole painted surface [51].

Scanning XRF imaging is a variant of XRF technique and its ability lies in the spatial visualization of the distribution of detected elements, providing additional concerning pigment signature, painting techniques, conservation state. Moreover, as discussed in the present work, the multispectral capability of XRF imaging technique allows to look beyond the painting surface putting in evidence hidden paintings or details not visible by the eyes.

A further elaboration of the XRF imaging technique was possible thanks to the increasing availability of X-ray microbeams in Synchrotrons [52-57]. This allowed to develop advanced imaging technique for investigating samples at a microscopic scale obtaining elemental images with a lateral resolution in the micrometre scale of length. Its application allowed to map very small pictorial details of art objects [58-60]. Measurements based on synchrotron X-ray beams present several advantages as the high intensity and the monochromaticity of primary radiation. High brightness allows visualizing heavy elements of a paint with dwell times in the ms range with a better contrast and a higher lateral resolution. Furthermore, the tunable energy offers the possibility of inducing selective excitation of specific elements. The rapid diffusion of polycapillary lens and microfocus tubes, has allowed to develop the technique to portable instruments [38].

Later on, many efforts have been done in order to transfer the established Synchrotron Radiation- (SR)-μ-XRF imaging to the study of larger size objects (up to several square metres), starting the development of the macroscopic XRF imaging (MA-XRF). Macro XRF imaging uses a slightly broadened beam of about few hundred micron to illuminate the large paintig surfaces [61].

In general, the separation link between the established μ-XRF and the novel MA-XRF imaging, consists in resolving power of the mapping. An arbitrary border between both variants is usually taken at the 100 μm level.

Although the outstanding performances of SR based techniques, only small and medium sized artworks have been examined. In addition, the necessity of transporting artworks at synchrotron laboratory has limited further developments.

The new developments of microfocus X-ray tube with high performances and the increasingly diffusion of focusing polycapillary optics pushed the development of novel self-built and commercial mobile scanning XRF systems. Portable XRF scanners allowed the application of the study art objects, avoiding their mobility solving implications related to risks of theft, damage, non-optimal climatic conditions and additional costs [62, 63].

The first example of portable instrument for MA-XRF analysis of historical paintings was commercially available in 2001, it allowed to analyse a small area up to 5×5 cm^2 [64]. Later, system developed by Hocquet et al. [65] introduced the possibility to scan a larger area but a still too slow scanning velocity (5 days for an area of 30×30 cm^2 with 1 mm step size and 5 sec dwell time). A remarkable contribute in the MA-XRF portable systems

development has been given from Alfeld et al., making effectively possible the examination of large sample areas [66, 61, 55]. In [62] Alfeld et al. describe the design and optimization of different versions of mobile instruments and their comparison in term of spectroscopic capabilities. These devices were based on powered X-ray tubes, multi-detectors, and polycapillary lens instead collimators (pinholes) [63].

Although tube-based scanning systems are probably still not able to reach the capabilities of a synchrotron radiation-based scanner, its mobility, allowing in-situ investigations, compensates the more long acquisition times. Nevertheless, efforts for increasing the capabilities of portable MA-XRF instruments represent nowadays an open research field, so that their development can limit the SR-scanners to more demanding study-cases in terms of resolution or sensitivity.

In view of information provided by MA-XRF analysis particularly relevant in art-historical field and in art-conservation research, efforts have been undertaken for extending the applicability of the method to other types of two-dimensional art objects. Thus, MA-XRF analyses has seen recent innovative applications with promising results directed to study of painted artworks with support from canvas, as illuminated manuscripts [67], stained-glass panels [68], enamelled artworks [69] and painted woods.

1.3. Other imaging techniques

Over the past decades, a large range of sophisticated imaging techniques, each with its own sphere of application, strengths and weaknesses, have been fine-tuned, and used as complementary methods to chemical analysis of a painting or a cultural good in general [70, 1]. To use scientific analyses as a tool for art research, comprehensive understanding needs of a full range of available analytical methods allied with a solid knowledge of art history. Imaging techniques such as Multispectral imaging (MSI), X-ray radiography (XRR), Neutron activation auto-radiography (NAAR) are largely used as complementary methods to understanding the artist's use of materials and for providing information on features as alterations or the physical structure of a painting. Each technique has a differentiated penetration-depth, as showed in Figure 3 their combination contributes to reconstruct the layers sequence and to detect underdrawings, changes "*pentimenti*", or previous compositions hidden over time.

Further, imaging techniques are often combined with Raman and Fourier transform infrared (FTIR) spectroscopy for molecular and structural information about organic and inorganic pigments making it possible the detection of varnishes, blinders, complex mixtures [71-75]. This section explores the contribution of imaging techniques aimed to the study and to the conservation of the cultural heritage.
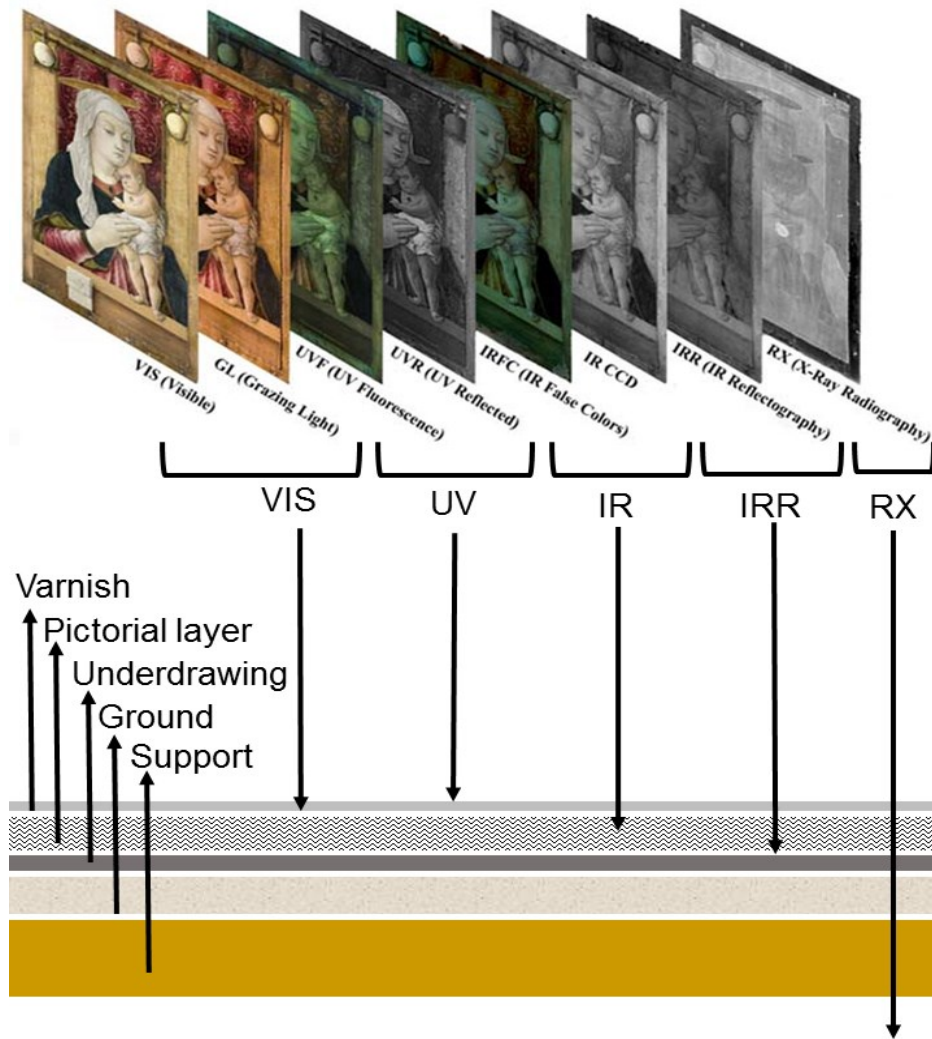
Figure 3: imaging techniques energy ranges and corresponding penetration depth into painting structure.

1.3.1 Multispectral Imaging (MSI)

Multispectral [76-78] imaging (MSI) consists of many pictures of the same scene acquired at a different wavelength. Generally, four electro-magnetic spectrum bands are employed: ultraviolet (UV, 360–400 nm), visible (VIS, 400–780 nm), infrared (IR, 780–1100 nm) and Infrared Reflectography (IRR 1000–1700 nm). The images can be acquired in reflection mode (R), fluorescence (F) or false color (FC) and they can also be performed in transmission, where the light which passes through the painting is recorded. Multispectral methods do not fulfil the analytical capabilities offered from the spectroscopic methods; however, their use has the advantage of being a rapid and relatively low-cost solution for the examination of large areas [79]. In order to identify pigments with an acceptable degree of certainty, at least one other material specific technique must be used to complement multispectral imaging diagnostics. The principle is based on the fluorescence of some pigments or other materials such as varnishes that are sensitive to emit light after having been illuminated with UV, visible or infrared radiation, in particular:

1) Visible light (VIS) imaging with the usual colour photograph serving as the reference for the other images. Visible Transmitted (VISTR) technique allows a better separation of paint layers and can make later alterations more visible.

2) Ultraviolet Fluorescence (UVF) is indicated as a surface technique, based on the illumination of the painting by ultraviolet radiation and the recording of the resulting emitted fluorescence [80]. Organic compounds can easily be detected as the presence of natural resin varnishes. In addition, UV based technique is sensitive to the identification of retouching applied on top of an aged varnish, that appear darker than the original materials. Ultraviolet Reflected (UVR) technique is useful for spotting different pigments that look alike in the visible range and for visualizing faded inks and prints. A more powerful variation of the UVR method is UV false colour (UVFC) combining UVR images to the visible image. In Figure 4, the simple UVF measurement setup is showed, it consists of a UV lamp and of a digital camera equipped with a cut UV filter. The experimental set up for the UVR is identical to the UVF except that you substitute a VIS cut filter for a UV cut filter. The result will be a monochromatic image of the UV reflected from the painting.
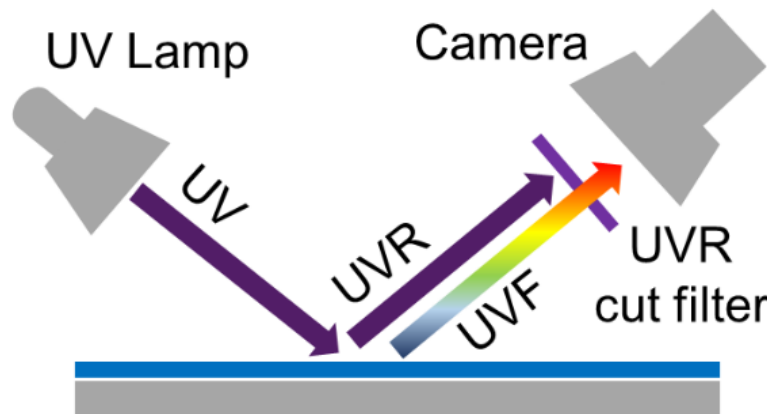
Figure 4: setup for Ultraviolet reflection (UVR) and fluorescence (UVF) analysis.

3) Infrared reflectography (IRR) technique is based on the illumination of the painting with infrareds or only visible light (Infrared Fluorescence- IRF) and by recording the reflected infrared radiation, as sketched in Figure 5. IR radiation penetrates the surface layers of the painting and the underdrawing becomes visible, due to the transparency of some pigments, as such as lead white and titanium white [81]. IRR analysis has provided important information for authentication in paintings based on black carbon sketches drawn on a white gesso ground (calcium sulfate). Due to the IR radiation absorption by black carbon and reflection back from the ground, black carbon underdrawing become visible. In Section 1.3.1 a detailed description of the capabilities of IRR method follows. In some other cases, a better visual representation of underdrawings and alterations is given by performing Infrared

technique in transmission mode (IRTR) (see Figure 5). Further, IR based technique can be combined to a visible picture and infrared picture in the Infrared False Colour imaging (IRFC), it allows to distinguish different pigments that appear the same to the naked eye and retouches. The technique is very suitable for some pigments such as cadmium yellow that emits fluorescence in the infrared region.
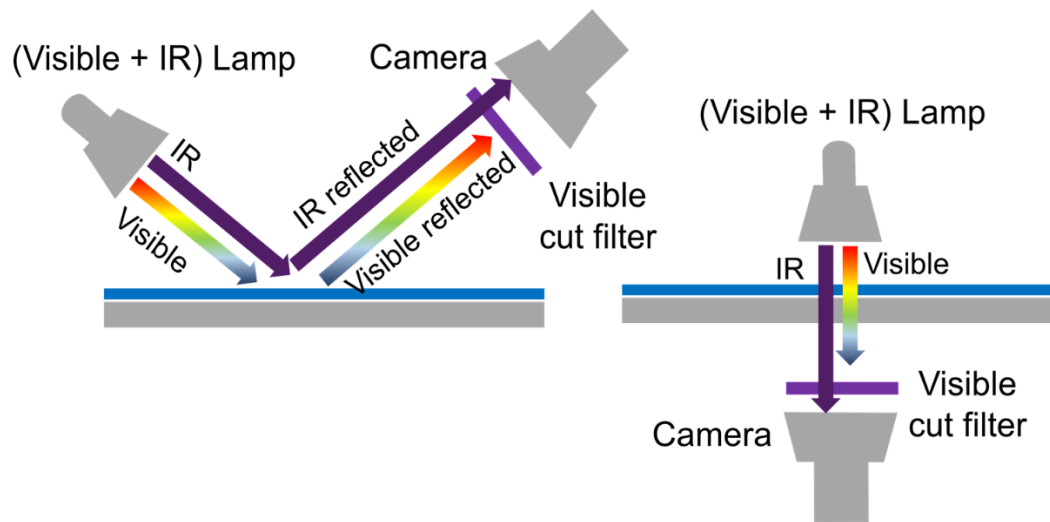
Figure 5: (left) Setup for Infrared (IRR) reflected (IRR) and fluorescence (IRF) analysis; (right) Infrared transmitted setup (IRT).

4) Recently, Terahertz (THz) electro-magnetic spectral band has been explored for art objects studies. It is complementary to the other techniques and it lies between the infrared and microwave regions, about 0.1–10 THz; however, the 0.5–13 THz frequency range is preferred for paintings investigation [82-84]. THz technology is relatively less diffused than other parts of the electro-magnetic spectrum, because the devices are relatively bulky and have not yet been optimized for use on-site in museums and in field sites [85-87]. THz radiation can penetrate non-metallic optically opaque materials and it reaches all painting layers up to the support, revealing structural problems or paint's flacking. Further, radiation induces molecular bending and stretching by exciting collective motions, so the technique results sensitive to humidity content, important for the conservation of paintings.

1.3.2 Infra Red Reflectography (IRR)

Infra-Red Reflectography (IRR) is, like X-ray radiography, a traditional well-established technique for the in-situ investigation of historical paintings [88]. Similarly, the technique allows the revelation of pictorial layers hidden by superimposed ones, due to the artist's changes or to subsequent restorations, as well as the visualization of the under-drawing, executed by the artist on the preparation before laying the colors [89-91].

IRR was first employed by J.R.J. van Asperen de Boer in the 1960's [92, 81] and nowadays, is performed routinely in many museums worldwide.

In particular, for the investigation of sub-surface layers of historical paintings, Near Infra Red (NIR) using the electromagnetic spectrum from 0.7 to 1.1 μm and Short-Wave Infrared (SWIR) referred to the band of 1.1–2.5 μm are highly suitable for visualizing carbon-based underdrawings (charcoal, graphite, soot ink and black chalk), especially used in 15th-16th century dated back paintings [93]. Sometimes, there is no common agreement on distinguishing NIR and SWIR. In different publications one can find various wavelengths for these ranges, or even no distinction for the SWIR band. IRR technique is based on the light exposure of a paint surface that partly reflects it from the top surface and partly penetrates it. Light propagating inside the paint layer is scattered by the pigment particles and the binder, which eventually returns part of the intensity back to the observer.

The under-drawing visibility essentially depends on the contrast between the radiation reflected by the preparation and that one absorbed by the drawing itself. For dark pigments (e.g., ivory black or carbon black) the factor of absorption is predominant, while for the bright white pigments as white gesso (calcium sulfate) the scattering is the only factor. In particular, sketches made by black carbon appear dark and can easily be observed because of the high absorption from carbon based pigments [94].

Also, the contrast depends on the layer (or multilayer) transparency – i.e. the grain size and concentration of the pigment, the medium used, the layer thickness – and on the existence of an enough reflecting ground. For example, the contrast is maximized when the former is traced out with carbonaceous pencils or inks on a gypsum ground. On the contrary, the drawing may not be visible when it is realized with iron-gallic inks, which are nearly transparent to IR radiation. Thus, the main IRR limitation is due to impossibility to visualize underdrawings, which were not realized with a carbon-based material, white (calcium carbonate) and red chalk (haematite) and metal points.

IRR measurement is performed in reflection geometry and full-field mode, and the technique has the advantage that the radiation employed is conveniently available by using conventional incandescent lamps and electronic flash tubes and does not constitute no health hazards. At first, IR radiation reflected by the painting impressed photographic films, but their limited sensitivity in the 0.7-0.9 μm spectral range produced poor quality images. Indeed, radiation in this range passes through some pigments, in particular reds and whites, while greens and blues resulted nearly opaque.

The later development of Vidicon tubes sensitive up to 1.9 μm [95, 92] allowed to visualize underlying features of the paintings in a more effective way compared to IR films. Vidicon tubes limitation is that they have scarce light sensitivity, so that measurements request an intense illumination, which can induce a detrimental warming of the painting surface. Moreover images are characterized by a very low contrast due to the limited number (some tens) of grey levels, and are affected by

geometrical distortion, due to the camera lens and to the device intrinsic characteristics. In order to have a high spatial resolution the measured area must be very small (10×10 ^{cm2} to have a resolution of 4×4 pixel/mm^2).

The reproduction of a large panel thus requires the collection of several images (more than 100 for an area of 1 m^2) that are successively combined in a mosaic. Since the single images are brighter in the centre and darker on the borders as consequence of the non-uniform sensitivity of the detector's area, the resulting reflectogram generally appears tiled, in many cases even after equalization. Over the time, Vidicons were replaced by solid state array cameras, as CCD or CMOS cameras, with sensitivity from 0.7 to 1.1 µm [96]. Although Low-cost CCD detectors have a higher intensity resolution, less geometrical distortion and the image has a much better uniformity than in Vidicon case, they do not improve the quality of the acquired images in a significant way, indeed, their sensitivity is limited up to 1.1 µm so that the acquired images have the same low informative content. However, expensive CCD devices may strongly improve the underlying features.

Among the first materials employed for solid state arrays there was PtSi (sensitive to 1.0-5.0 µm) [97, 98] that required liquid nitrogen cooling and the spectral range acquired was adjusted by IR filters, selecting the best spectral band suited for the underdrawings visualization. Today the most common material is InGaAs [99, 100]. These detectors are sensitive to radiation between 0.9 and 1.7 µm, no require liquid nitrogen cooling and are featured a higher quantum efficiency compared to vidicon tubes and PtSi solid state arrays. In order to record higher wavelengths also solid state detectors made of HgCdTe and InSb are available, these devices are considerably more expensive and require cooling in order to obtain acceptable signal-to-noise ratios.

However, solid state detectors commonly available have a size of considerably less than 1 Mpixel, so that the assembling of sub-areas cannot be avoided. In complementary way to the full field IRR mode, in 1990 Bertani describes an IRR scanning system achieving a spatial resolution of 200 µm in the spectral region between 1.1 and 1.5 µm [101]. In addition, recently, a multiband approach based on acquisitions in narrow-bands [102], introduces some advantages over the conventional IRR performed in wideband modality (i.e., in the large near-infrared band).

Multiband IRR opens the way to new applications for the study of artists' materials, allowing acquisition of information about some pigments and their mapping across the painting. Daffara et al. [103, 104] describe an advanced IRR scanning device which records 14 bands in the NIR and SWIR from 0.7 to 2.3 µm and allows for multispectral imaging, achieving a spatial resolution of 500 µm. Scanning systems require measurement times in the range of hours to scan 1 square meter at maximum resolution. Finally, measurements in transmission geometry of canvas paintings [105-107], exploiting their slight transparency to IR radiation, have been described several decades ago but until recent periods its application was hindered by the low sensitivity of IR detectors, which necessitated long exposure times. However,

transmission IR images are less surface sensitive than reflectograms, so that the underdrawings weakly visible in the IRR, can be observed in the transmission image.

1.3.3 X-Rays Radiography (XRR)

Among the imaging techniques that may reveal the inner structure of a painted artifacts in non-destructive way XRR (X-Rays Radiography) is a well-established technique, performed from the end of the 19th century soon after discovery of the X-rays [108].
Conventional X-ray radiography is mainly done in transmission mode with no energy discrimination. Typically, an X-ray tube is placed on one side of the painting and the transmitted X-rays are detected using an X-ray film, phosphor imaging film or pixel detector, as is showed in Figure 6.
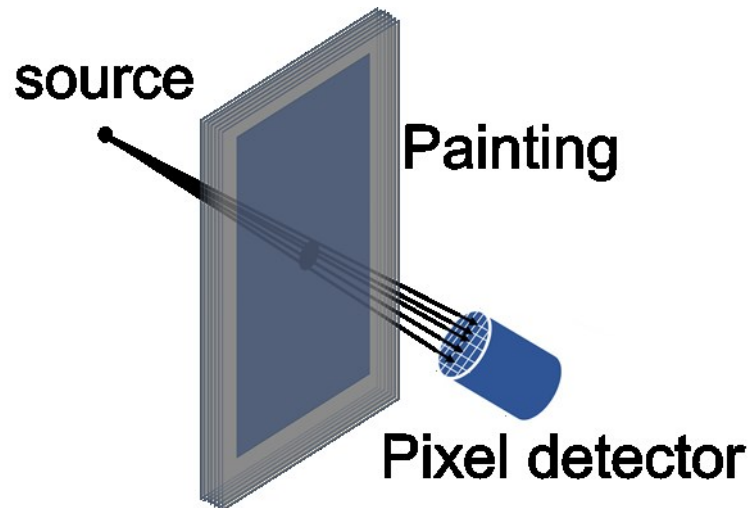
Figure 6: X-ray radiography setup.

The development of X-radiography gave conservators and art historians access to information related to the entire three-dimensional structure of an art object. Paintings are multi-layered objects structured with a support (wooden panel, canvas on a frame, copper plate, etc.), a ground (layer of gypsum, chalk or lead white), and the pictorial layer [109].
Radiography is used to visualize the distribution of these layers through the primary beam absorption that follows the *Beer-Lambert* law [110, 66, 52, 61]. However, the most interesting information comes from the paint layers, allowing different artists' hands to be distinguished in different stages of a painting, the discovery of previous compositions beneath the surface of the painting and, in a few cases, the detection of fakes. Each layer is characterized by its attenuation coefficient, that depends by density and thickness, and the absorbance image is directly proportional to the attenuation coefficients. The use of analogue films for the detection allow the main advantage of a higher lateral resolution in the range of 2 μm related to the grain size in X-ray films, but these have been gradually replaced by pixelated detectors. Although, the lateral resolution obtained with commercial digital

detectors is several tens of μm due to the pixel size, their higher sensitivity requires shorter exposures and it results in a lower dose of radiation absorbed by the investigated object. In addition, digital radiography requires no time consuming processing of films and directly provides digital data for advanced image processing. Conventionally XRR technique is operated in full-field mode, but also XRR scan is possible using small beam instead a broad X-ray beam.

Although, the technique is suitable to investigate large numbers of painted surface, because a single radiography can be taken in a time of minutes it has a number of important limitations. In contrast to MA-XRF technique, XRR is not able to discriminate the chemical nature of the elements, because the X-ray absorbance observed is an integration over all the absorbance of the specific elements. Contributions to the radiographic contrast map from (small quantities of) weakly absorbing elements (with low atomic number or without metals in their formulae) may frequently be obscured by those of heavier elements that are present in higher concentrations. Thus, the absorption contrast in XRR images is mostly caused by the heavy metal paint components limiting the readability of hidden compositions. In general, the pigments that are most likely to block X-rays are those made of lead as lead white (lead Z=82), chrome yellow (lead chromate), Naples yellow (lead antimonate) and minium (lead oxide). The pigments with weaker absorption power are zinc white (zinc Z=30), cadmium yellow (cadmium Z=48) and emerald green (arsenic Z=33). Also, very weak absorbers include lime white (calcium Z=20), umber (manganese Z=Mn, iron Z=26), cobalt blue (cobalt Z=27), red/yellow ochre (iron Z=26), Prussian blue (iron Z=26) and the worst absorbers are the organic pigments based on carbon (Z=6): carbon black and carmine lake.

For the same reason the contributions of support and ground layers can make the radiographs difficult to read, so that different approaches to reduce their influence have been developed. In several cases, acquisition of X-radiographs of the same area using different operating conditions for the X-ray source and varying the exposure time can be a useful method for providing different features of the structure to be highlighted in the resultant images. Many of the techniques developed to make X-radiographs more readable have made use of moving X-ray sources or paintings [111].

This approach consists in developing a simple form of tomography, named *strato-radiography* or *strati-radiography* [112, 113].Methods have also been developed to minimise the tonal differences between the different regions in an X-ray plate during the printing process. Radiographs produced by this method are often named *logetronic radiographs*. The technique relies on exposing different parts of the X-ray plate to different amounts of light during printing, either by using masks, or by using a cathode ray tube, whose output at a given point in its raster scan can be varied. Another method of minimising the tonal differences created by structures such as cradles is to expose the X-ray plate with the interstices between cradle members filled with a material that has a similar X-ray absorbency to the surrounding wood [114].

Moreover, the influence of the support can be nearly removed by performing electron emission based on the positioning the film directly on the paint layers [115, 114]. Both are exposed to the X-rays, which pass through the film before reaching the painting. The X-ray tube is operated at a high voltage (several hundred kV) with a suitable filter absorbing the

lower energetic part of the tube spectrum. The photoelectrons emitted by the surface layers of the painting darken the film, while the high energy X-rays pass through it without interaction. Given the strong absorbance of electrons in paint layers the images obtained are dominated by surface paint layers with covered layers making only minor contribution.

On the other hand XRR allows for a study of the support of paintings [116, 117], in contrast to the MA-XRF that does not result in information deeper than a few tens of micrometres from the sample surface due to the self-absorption effect. In this way, paintings made on canvas from the same loom can so be identified [118, 119].

In the conventional XRR, the detector has basically no energy discrimination only some influence can be exercised on the absorption process by varying the voltage of the X-ray tube. However an alternative is to perform Energy resolved radiography (ED-XRR) that generates pixelated images because energy dispersive detectors are employed to collect the images. Thus, ED-XRR may be developed by using a monochromatic X-ray beam (SR radiation) in combination with a detector without energy discrimination [120, 121].

The dichromography or K-edge imaging is a radiographic method that employs monochromatic X-rays of different energies that allows to obtain elemental distribution image by subtracting images acquired with energies above and below the absorption edge of an element. Also, ED-XRR may be performed by employing polychromatic beam in combination with an energy dispersive X-ray detector [122]. In several research groups Zemlicka et al. [123], Scharf and al. [124, 125], F.P.Romano et al. [126] , Color X-ray Cameras, conventional CCD detectors and Timepix detectors supported by proper processing procedure of the experimental data are employed for creating images in given energy intervals which enable identification and separation of elements.

1.3.4 Neutron Activation Auto-Radiography (NAAR)

The purposes of the neutron activation method are almost the same as those of X-rays analyses. Namely, the main end is to reveal details of composition hidden by the top layers of the painting under investigation. In the same way of X-rays, neutrons penetrate through material and become absorbed differently by different elements [127-129].

Neutron Activation Auto-Radiography (NAAR) technique was developed by Sayre and Lechtman [130, 131] and it is based on the transient radioactivity induced in the sample by exposing it to the low-energy thermal or cold neutrons for a period adequate to generate the desired level of internal radioactivity.

The flux of incident neutrons, when absorbed by certain atomic nuclei in the irradiated material, transforms the nuclei into radioactive isotopes, In this way, the sample is activated and placed in contact with a photographic medium, photographic film or image plates, which becomes darkened by the radioactive decay, as sketched in Figure 7. This resulting radiation may include alpha particles, beta particles and gamma radiation [132].

The presence of different activated radioisotope with different half-lives allows to acquire the different elemental distributions by changing the photographic medium in appropriate time windows. Similar to the X-ray fluorescence spectroscopy, the study of gamma radiation energies allows for distinguishing the elemental composition of the pigments because of direct correlation between the energies of the gamma-ray photons and the atomic number.

The image produced on a photographic film by β-particles emitted by the activated painting provides an image of pigment distribution. The darkening of the photographic medium indicates the greater abundance of an element.

Painting

Neutrons radiation

Radiation sensitive film

Development of film
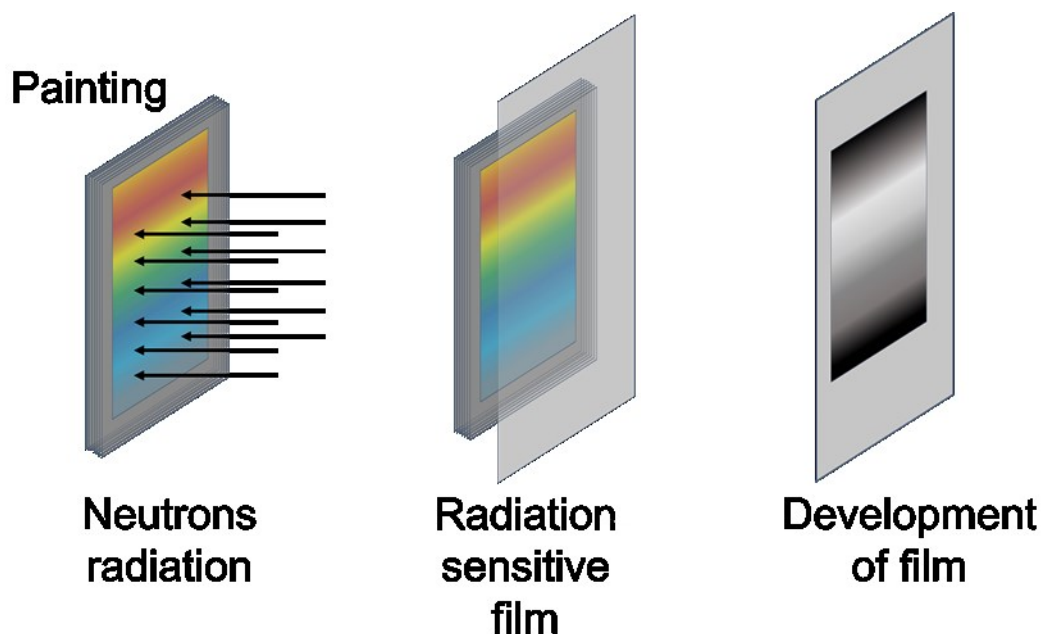
Figure 7: NAAR experimental setup.

The contrast obtained is dependent on the exposure time of the photographic medium, which cannot be extended indefinitely to avoid overlap with slower decaying isotopes and overexposure in areas of high concentration. The lateral resolution of NAAR images is dependent on the grain size and thickness of the film employed and the distance between film and paint surface. Finally, the energy of the emitted β-radiation influences the lateral resolution, as it determines the absorption in the photographic medium.

Unlike X-rays, neutrons are better absorbed by light elements, which allows for the detection of *phosphorus-* (present in bone/ivory black-carbon), *carbon-* (carbon-based black pigments containing a mixture of $Ca_3(PO_4)_2$, $CaCO_3$ and C), also *hydrogen-* and *nitrogen-*containing substances surrounded by heavy elements.

NAAR represents a very suitable tool for the visualization of elements such as manganese (present mainly in oxidized form in the earth pigment umber), copper (present in copper-based greens and blues) and mercury (present in vermilion) due to their susceptibility to activation. Differently, lead (present mainly in lead white) and iron (present in a broad range of pigments, among them earth pigments and Prussian blue) are not transformed into radioactive equivalents and cannot be imaged by this method. Neutron activation is also applied for detection of trace elements in artistic materials, which helps in determining pigment origin [133].Among the main drawbacks of NAAR analysis, there is that of requiring the transport of the painting to the place where the research reactor is installed. Furthermore, after activation the painting needs to stay for several weeks at the reactor facility to acquire the autoradiographs and, from a safety point of view let, needs that the

transient radioactivity decreases below the legal limits. Consequently, due to the considerable financial and logistical effort of transporting the painting and prolonged absence from the exposition to the public, the number of paintings studied by NAAR is subjected to restrictions.

Chapter 2

X-ray Fluorescence spectroscopy

X-ray Fluorescence Spectroscopy (XRF) is an analytical method based on the atoms excitation by means a primary X-rays source and their consequently de-excitation accomplished by the characteristic X-rays emission. An energy-dispersive detector records the X-rays emitted from the material and the collected characteristic spectral lines reveal the chemical nature of the sample without destructive analysis.

2.1 Basic Interaction between photons and atoms

2.1.1 Mass attenuation and linear attenuation coefficient

X-rays are electromagnetic radiation with a wavelength ranged between 0.01 and 10 nm, corresponding to an energy range between 0.1 and 100 keV [134, 135]. A peculiar property of X-rays is their penetrating character. This aspect is correlated to their energy: high energy photons penetrate the materials more deeply that low energy X-rays. Otherwise, this property can be treated in terms of X-rays attenuation in the matter [136-139]. A material (or an absorber) with thickness x and density ρ reduces the incoming photon count N_0 to:

$$N(x) = N_0\, exp(-\mu\rho x) = N_0\, exp(-\mu_{lin}x) \qquad\qquad 1$$

where μ (cm^2/g) is the mass attenuation coefficient and μ_{lin} (1/cm) $= \mu\rho$ is the linear mass attenuation coefficient.

The mass attenuation coefficient can be expressed as $\mu = \left({^{N_A}}/{_A} \right) \mu_{Atom}$ with N_A the Avogadro constant* and A the atomic mass. The fraction of incoming photons (dN) absorbed in the material is just:

$$dN = \mu \rho x \qquad\qquad 2$$

Real materials, such as chemical compounds, alloys, or (homogenized) mixtures consist of several elements. If the mass fractions (concentrations) C_j of the components are known for each j-element ($\sum_j C_j = 1$), then the mass attenuation coefficient of the composed material corresponds to the weighted sum of the individual mass attenuation coefficients, μ_j, with weight fractions as weight factors:

$$\mu = \sum_j C_j \mu_j \qquad\qquad 3$$

Only some of the incoming photons are absorbed in the material from the j-element; this fraction is given by the concentration of the element multiplied by the ratio between the mass absorption coefficient of j-element and that of the material $C_j \left(\frac{\mu_j}{\mu} \right)$. Therefore, the absorption by the j-element in the volume under consideration is given from the equation 3 by [140, 141, 134]:

$$\left[C_j \left(\frac{\mu_j}{\mu} \right) \right] (\mu \rho dx) = C_j \, \mu_j \rho dx \qquad\qquad 4$$

The incoming photons number available to produce fluorescence is found by multiplying the equation 4 times the equation 2:

$$dN = N_0 (C_j \, \mu_j \rho \, dx) \, exp(-\mu \rho x) \qquad\qquad 5$$

The mass attenuation coefficient takes in account the processes that occur in the interaction of a photon with matter in the X-rays energetic domain. In particular, for the X-rays energy range used in this work μ is expressed as:

$$\mu = \tau + \mu_{coh} + \mu_{incoh} \qquad\qquad 6$$

---

*N_A=6.0221367×10^{+23} mol^{-1}

where τ is the photoelectric absorption coefficient, μ_{coh} and μ_{incoh} the coherent and incoherent mass scattering coefficient [142, 143, 134].

2.1.2 Atomic cross-section

The theoretical value of μ is defined with the total cross section per atom, σ_{atom}, that is related to μ according:

$$\mu = \frac{N_A}{uA} \sigma_{atom} = \frac{N_A}{uA}(\sigma_{pe} + \sigma_{coh} + \sigma_{incoh}) \qquad 7$$

In this equation, N_A is Avogadro's number, u is the atomic mass unit (1/12 of the mass of an atom of nuclide ^{12}C), A is the relative atomic mass of the target element [144, 145, 134]. Total cross section σ_{tot} can be written as the sum over contributions from the principal photon interactions. In Table 2 are reported the elementary interactions between X-ray photons and atoms and their relative dependence from the atomic number (Z). Furthermore, Figure 8 shows the values of cross-section and the mass absorption coefficient as function of photon energies for a lead pure target. Photoelectric absorption and scattering processes will be discussed in detail in the following Section 2.1.3.
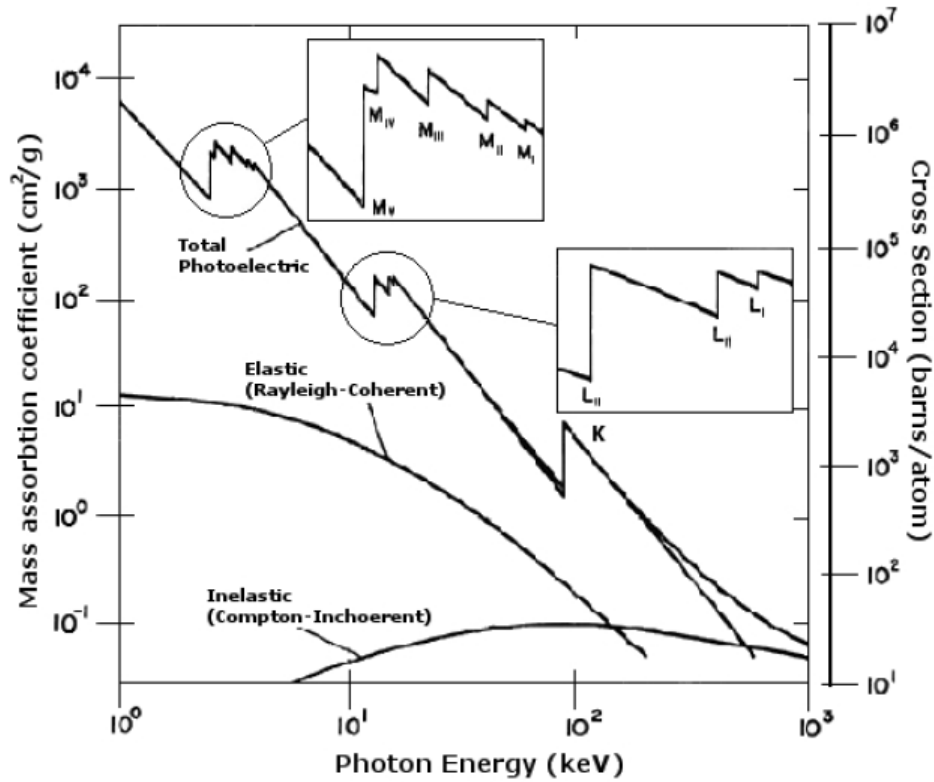
Figure 8: cross section and mass absorption coefficient for incident photons between 1 keV and 100 keV on a lead (Pb) target [146, 147].

Type of interaction	Absorption	Scattering	
Interaction with:		Elastic (Coherent)	Inelastic (Incoherent)
Atomic electrons	**Photoelectric effect** $\sigma_{pe} \begin{cases} \sim Z^4 (L.E.) \\ \sim Z^5 (H.E.) \end{cases}$	Rayleigh scattering $\sigma_R \sim Z^2$ $(L.E.)$	**Compton scattering** $\sigma_C \sim Z$

Table 2: Classication of elementary photon interactions [148].

2.1.3 Photo-absorption process

The term "*interaction*" is often not clearly distinguished from that of "*absorption*". The interaction includes all events in which a photon can participate, while with the term absorption a transfer of energy from a photon to an atom is described. In the photons interaction with matter, the Photo-effect and Compton effect (incoherent scattering) transfer energy, contrary to the coherent scattering. Absorbed energy generates not only the creation of fluorescent radiation (by photo-absorption), but also it changes the chemical nature of absorbing atoms. Usually the concept of attenuation coefficient, discussed above, is related to unspecified interactions (photo-absorption, Compton- and coherent scattering in the analytical range of X-rays), while absorption coefficient is referred specifically to photo-absorption [149, 134].

2.1.4 Excitation and de-excitation of an atom

Photo-absorption process consists in the absorption of an incoming photon from an inner electron of an atom. The photon energy is transferred to the core electron and consequentially its ejection is observed. The atom is left in its exited state from the ejected electron and electrons from outer shells fill the generated hole (or vacancy) producing a fluorescence photon or inducing Auger and Coster-Kroning transition. This is a cascade process and it continues until all allowed transitions are exhausted. Finally, a free electron fills the remaining vacancy in an outer shell. The kinetic energy carried by the ejected (photo-) electron is given by the following equation [134]:

$$E_{kin} = h\nu - E_{binding} \qquad\qquad 8$$

where $E_{binding}$ is the binding energy of the electron, h is the Planck constant[†] and ν is the frequency of incoming photon. From equation 8 it can be seen that for ejecting a bound electron from an atom, the energy of incoming photon must be higher than the binding energy of electron (i.e., photon energies just above an absorption edge are most effectively

---

[†]h=6.6260755x10^{-34} J·s =4.1356692x10^{-15} eV· s

absorbed by that shell) and that the photon energy is absorbed completely. Fluorescence photon has an energy corresponding to the energy difference of the involved shells in the atomic transition. The transitions are governed by quantum-mechanical selection rules. Within the regime of X-rays, fluorescence radiation is observed only from those transitions with reasonable intensity (probability) where:

$$\Delta j = -1, +1, 0 \; and \; \Delta l = -1, +1 \qquad\qquad 9$$

(l and j are the quantum numbers with the usual meaning). For example, if the K-shell is ionized, the most probable electron transition into the K-hole is K ← L3. Also possible, however with lower probability, are K ← L2, and K ← M3, etc. The vacancy in L3 after a K ← L3 transition can be filled by L3 ← M5 or L3 ← M4 and so forth.
Additionally, the K ← L1 and L1 ← M1 are forbidden transitions. Any of these transitions allows the emission of a photon or an Auger electron, this kind of emission will be discussed later.

The probability that a K-shell electron will be ejected rather than an L- or M-shell electron, is give by the "absorption jump ratio" (J_K) [137]:

$$J_K = (r_K - 1)/r_K \qquad\qquad 10$$

Where r_K is the K-shell absorption jump defined as the ratio of the mass absorption coefficients at the K absorption edge. These jump ratios have been measured and some of them are shown in Table 3

Element	Atomic Number	J_K
Ti	22	0.888
V	23	0.885
Cr	24	0.882
Mn	25	0.880
Fe	26	0.877
Co	27	0.874
Ni	28	0.872
Cu	29	0.869
Zn	30	0.867
Mo	42	0.842

Table 3: Some K-shell absorption jump ratios [137].

The detection of fluorescence photons is based on their attribution to the specific atoms that compose the sample. A mathematical relationship exists between the energy of the characteristic X-radiation and the atomic number of the emitting atom, which is called Moseley's law [150, 134]

$$E_K = a(Z - b)^2 \qquad\qquad 11$$

where Z is the atomic number of the atom, E_K is the energy of the K-shell, and a and b are constants. The detected fluorescence lines appear broadened in the X-ray spectrum due to detection efficiency. In the Section 2.6.1 spectrum artifacts will be illustrated in detail.

In X-ray spectroscopy, the emitted fluorescence lines are differentiated by a specific nomenclature based on two different notations: IUPAC and Siegbahn [151, 152].
The IUPAC notation (i.e. K-L3) is referred to the atomic shells involved in the fluorescence emission phenomenon, while the Siegbahn (i.e. Kα1) was developed historically and according the intensity. Table 4 reports the two notations; if the atomic de-excitation occurs from M4 shell to L3 shell, the transition will be identified as M4-L3 in the IUPAC notation and L$_\alpha$2 in the Siegbahn notation. In this thesis work the second notation will be used.

	L1	L2	L3	M1	M2	M3	M4	M5	N1	N2	N3	N4	N5	
L3				Ll			Lα2	Lα1	Lβ6			Lβ2	Lβ2	
L2				Lν			Lβ1					Lγ1		
L1					Lβ4	Lβ3				Lγ2	Lγ3			
K		Kα2	Kα1		Kβ3	Kβ1	Kβ5	Kβ5		Kβ2	Kβ2	Kβ4	Kβ4	

Table 4: Nomenclature of X-ray lines. IUPAC (i.e. K-L3) and Siegbahn (i.e. Kα1) notation *[151, 152]*.

The probability that Kα1 radiation will be emitted rather than that of another K line is called transition probability g $_{Kα1}$ and is given by:

$$g_{K\alpha1} = [I(K\alpha1)/I(K\alpha2)] / \{[I(K\alpha1)/I(K\alpha2)] + 1\} \qquad\qquad 12$$

Some values for the Kα1/Kα2 intensity ratio are given in Table 5 [137]

Element	Atomic Number	Kα1/Kα2
Ti	22	7.52
Cr	24	7.52
Fe	26	7.46
Ni	28	7.41
Zn	30	7.41
Mo	42	5.18

Table 5: Some measured relative intensities [137].

2.1.5 Auger emission and Coster-Kroning transition

The relaxation of an excited state by an electron transition is not necessarily associated with the emission of a photon. In a complex quantum-mechanical process, the fluorescence X-ray photon either can leave the sample unperturbed, or can interact with a higher-shell electron of the atom. When a fluorescence X-ray photon ejects another electron of the same atom it originated from, the ejected electron is called an Auger electron [153, 134]. This is a radiationless relaxation. All the energy of the fluorescence photon is transferred to the Auger electron, which leaves the atom with a kinetic energy of:

$$E_{kin} = E_{ExitedState} - E_{GroundState} - E_{binding} \qquad\qquad 13$$

In the Auger emission, three electrons are involved: the first is the photoelectron, which is emitted when the photon is absorbed. In the subsequent relaxation process, an outer electron fills the vacancy and appears to release the energy $E_{ExitedState} - E_{GroundState}$ transferring it to a third electron, which is bound to the atom by $E_{binding}$. However, quantum-theoretical models treat the relaxation and emission of the Auger-electron as a single process. Auger electron emission and fluorescence photon emission are competing processes. The probability that it occurs the first process or the other one is given by:

$$1 = p_{Auger} + \omega \qquad\qquad 14$$

Where ω is the fluorescence photon yield [154, 155, 137] . Both the probabilities are function of atomic number (Z) and the (sub-)shells. In particular, the fluorescence yield for the K-shell vacancies is given by:

$$\omega_K = \frac{\sum_{i=1}^{n} n_K}{N_K} \qquad\qquad 15$$

where n_K is the number of the electrons de-excited from the different L-, M-, N-, etc. shells to the K-shell per unit time, while N_K is the number of K-shell vacancies created per unit time. Fluorescence yield can be defined in a similar way for the other shells as well, and the L-shell (and higher shells) yield is much lower than ω_K. Fluorescence yields have been determined both experimentally and theoretically, some K fluorescence yields are shown in Table 6 [137]:

Element	Atomic Number	ω_K
Ti	22	0.219
V	23	0.250
Cr	24	0.282
Mn	25	0.314
Fe	26	0.347
Co	27	0.381
Ni	28	0.414
Cu	29	0.445
Zn	30	0.479
Mo	42	0.765

Table 6: Some K fluorescence yields [137].

The Auger-probability dominates significantly over the emission of fluorescent radiation at light elements. For example, $\omega_K \approx 1.4 \times 10^{-3}$ for Carbon and $\omega_K \approx 7 \times 10^{-4}$ for Beryllium. The poor photon count rates resulting from such low fluorescent yields are among the main reasons for the difficulties arising in light element analysis by XRF.

Another radiationless transition possible is the Coster-Kröning transition [153, 134]. It is an inner-shell transition, that takes place within the L- and M-, and higher sub-shells. For instance, an electron from an L3-shell fills an electron hole on the L2-shell after L2-ionization or KL2 relaxation. It differs from the Auger-effect only by its confinement to a set of subshells. The (small) excessive energy is transferred to an outer shell electron or the environment of the atom. The fact that Coster–Kronig transitions effectively move vacancies into outer subshells has a considerable effect on the intensities of the corresponding emission lines, which are proportional to the number of vacancies. In Figure 9 a schematic overview of all photoelectric interactions is shown [134]:
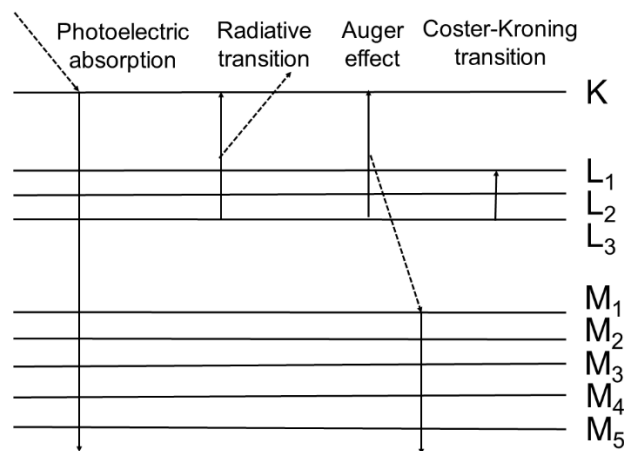
Figure 9: photoelectron interactions diagram.

The sum of fluorescence yield, ω, Auger yield, p_{Auger}, and Coster-Kronig yield, p_{CK}, modify the previous equation 14 in the following [156, 153, 157]:

$$1 = p_{Auger} + p_{CK} + \omega \qquad\qquad 16$$

In Figure 10 is shown the fluorescence, Auger electron yields and Coster-Kronig yield as a function of atomic number for K-, L1-, L2- or L3- shell vacancies. It can be seen from plot in the upper right plot, for the K-shell vacancies, that Auger transitions are more probable for lighter elements; while X-ray yield becomes dominant at higher atomic numbers.
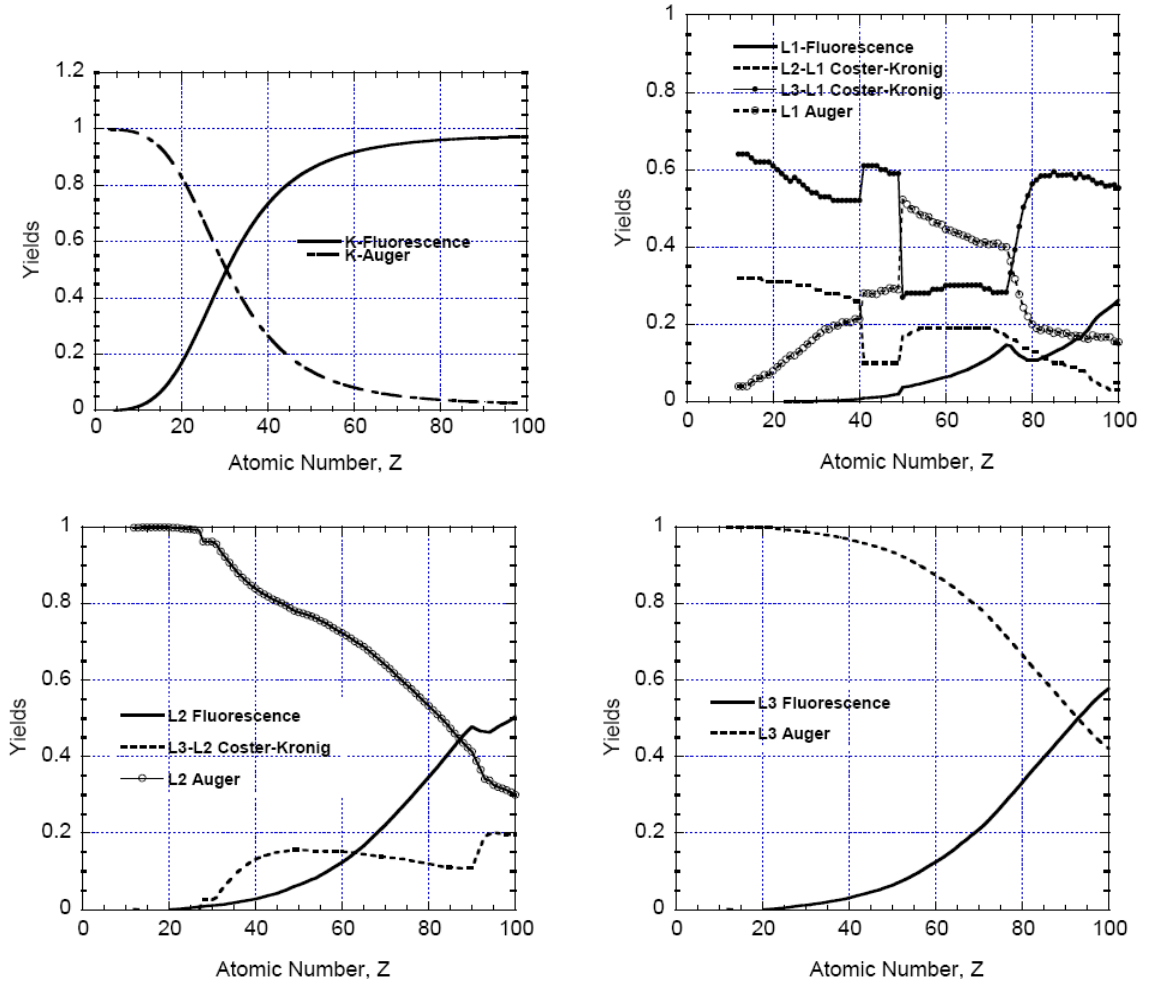
Figure 10: florescence yields, Auger electrons and Coster-Kronig after the K-, L1-, L2- or L3-photoelectric effect [158].

In conclusion, the contribution to the number of the primary fluorescence photons dN (x) of j-element is given by the product of the above factors in equations 4, 9, 11, and 14. After integration,the result is:

$$N_i = \left\{ \frac{\left[\left(N_0 \, C_j \mu_j J_K \, g_{Ka} \omega_K \right) \left(\frac{\Omega}{4\pi} \right) \right]}{\left(\mu + \, \mu_{E_i} \right)} \right\} \left\{ 1 - exp\left[-\rho h \left(\mu + \, \mu_{E_i} \right) \right] \right\}$$

17

In the equation 17, $\left(\frac{\Omega}{4\pi} \right)$ is the fluorescence photons fraction that enters the detector, h is the sample thickness, and $\exp\left(-\mu_{E_i} \rho x \right)$ is the fraction of the fluorescent radiation (E_i) transmitted through the path length x to the detector.

2.1.6 Scattering processes

Other two kinds of interactions occur between photons and atoms:

i. *Incoherent* (inelastic) or *Compton* scattering; where the change of propagation direction of photon is accompanied with an increasing of wavelength and change of phase.

ii. *coherent* (elastic) or *Rayleigh* scattering; that is not affected by phase and energy change.

Figure 11 shows Compton and Rayleigh cross section plotted as functions of atomic number and photon energy. The probability for Compton scattering increases with increasing photon energy and decreases with the atomic number. Rayleigh scattering decreases with increasing energy and increases with atomic number.
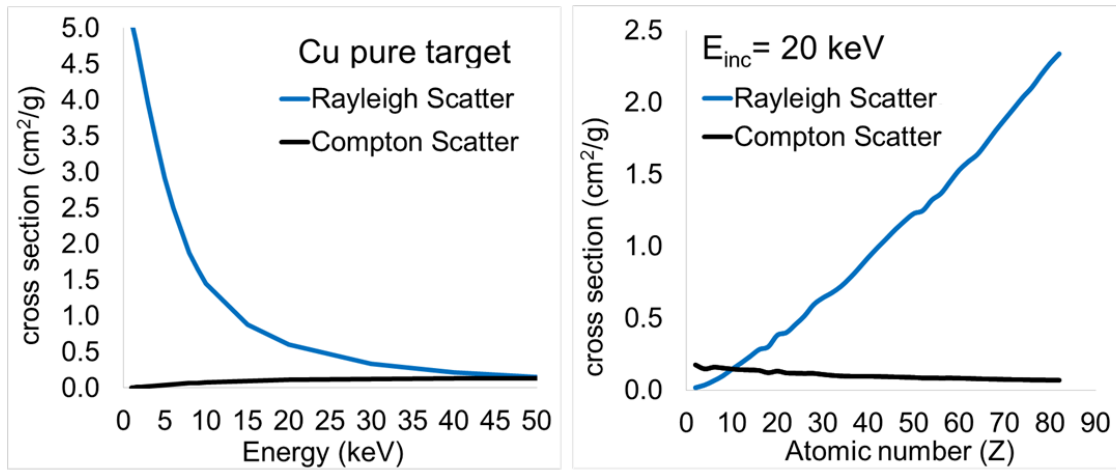
Figure 11: cross section for Compton and Rayleigh scattering as function of energy of incident photons and atomic number of the atomic target [159].

2.1.7 Compton scattering

Compton scattering consists in a photon, that in its collision with an electron, loses some of its energy, it is deflected from its original direction of travel, as is drawn in Figure 12.

The theory that well describe the Compton scattering is that of Klein and Nishina, where in first approximation, the electron is assumed to be initially free and at rest. This scenario configures electrons in the outer shells of atoms and high incident photons. The weak binding of the electrons to the atom may be neglected, because the momentum transferred to the electron greatly exceeds the momentum of the electron in the bound state.
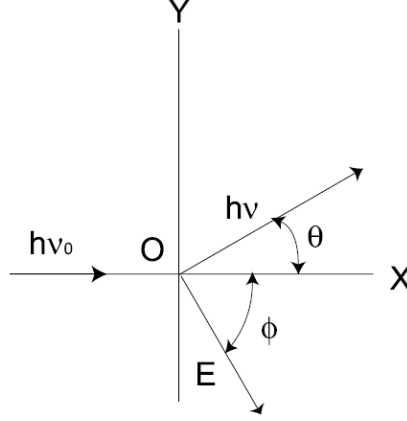
Figure 12: Compton scattering in the assumption of free electron at rest [148].

The relation between photon deflection and energy loss for Compton scattering is determined from the conservation of momentum and energy between the photon and the recoiling electron. This relation can be expressed as:

$$hv = \frac{hv_0}{1 + \left(\frac{hv_0}{m_e c^2}\right)(1 - cos\theta)} \qquad 18$$

$$\Delta E = hv_0 - hv = m_e c^2 \ \frac{2(hv_0)^2 cos^2\Phi}{(hv_0 + m_e c^2)^2 - (hv_0)^2 cos^2\Phi} \qquad 19$$

$$tan\Phi = \frac{1}{1 + \left(\frac{hv_0}{m_e c^2}\right)} cot\frac{\theta}{2} \qquad 20$$

where hv_0 is the energy of incident photon, hv is the energy of scattered photon, E is the energy of recoil electron, m_e is the rest mass of an electron, and c is the speed of light. The intensity of the scattered radiation is inversely proportional to the mass attenuation coefficient μ_s of the specimen:

$$I_s(\lambda_s) \sim \frac{1}{\mu_s(\lambda_s)} \qquad 21$$

In this work, and in general in the X-ray spectroscopy based on unpolarized beam, the Klein and Nishina angular distribution function per steradian of solid angle (cm^2 sr^{-1} electron^{-1}) is given by [148, 160]:

$$\frac{d\sigma_c^{KN}}{d\Omega}(\theta) = r_0^2 \frac{1+cos^2\theta}{2} \frac{1}{[1+h\nu(1-cos\theta)]^2} \times$$

$$\times\left\{1 + \frac{[1+h\nu(1-cos\theta)]^2}{(1+cos^2\theta)\,[1+h\nu(1-cos\theta)]}\right\} = \frac{1}{2}r_0^2\left(\frac{k}{k_0}\right)^2\left(\frac{k}{k_0} + \frac{k_0}{k_0} - sin^2\theta\right) \qquad 22$$

where $k_0 = \frac{h\nu_0}{m_e c^2}$ $k = \frac{h\nu}{m_e c^2}$ \hfill 23

where r_0 is the classical electron radius. The integration of the equation 22 over all angles gives the total Klein and Nishina cross section (cm^2 electron^{-1}):

$$\sigma_c^{KN} = 2\pi r_0^2 \left\{\frac{1+k}{k^2}\left[\frac{2(1+k)}{1+2k} - \frac{\ln(1+2k)}{k}\right] + \frac{\ln(1+2k)}{2k} - \frac{1+3k}{(1+2k)^2}\right\} \qquad 24$$

2.1.8 Electron binding and Doppler correction

The energy range of X-rays involved in this work is between 1 and 40 keV. In this energy range and in particular for low-Z material, the assumption that the atomic electrons are free and at rest is not a good approximation. Binding correction treated by Waller-Hatree theory takes in account not only of the K-shell, but all of the atomic electrons. Electron binding correction is formalized as a multiplicative function called incoherent scattering $S(q,Z)$ to the differential Klein and Nishina formula (equation 22) [161]:

$$\frac{d\sigma_c^{BD}}{d\Omega}(\theta) = S(q,Z)\frac{d\sigma_c^{KN}}{d\Omega}(\theta) \qquad 25$$

Figure 13 shows the ratios of σ_c^{BD} C to σ_c^{KN} for photon energies of 1, 10, and 100 keV
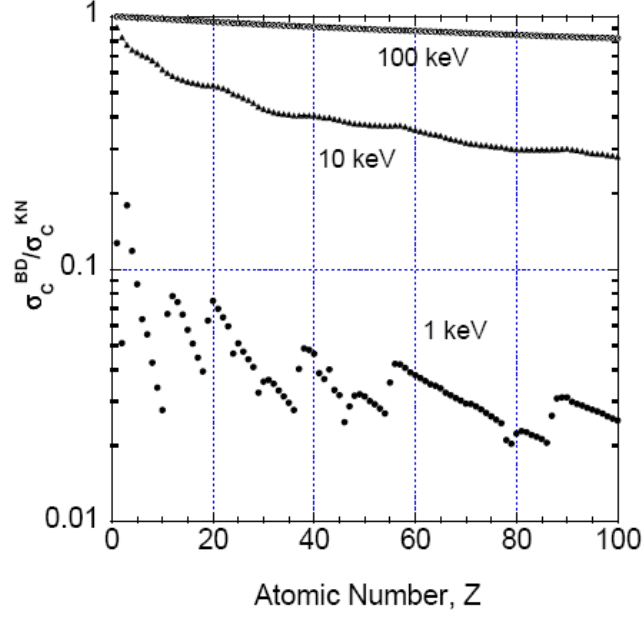
Figure 13: ratio of the bound-electron Compton scattering cross section σ_c^{BD} and that for free electrons evaluated from the Klein-Nishina formula σ_c^{KN} [162].

In the energy region where the binding correction is necessary, the motion of the atomic electrons around the atomic nucleus generates a Doppler broadening, resulting in a corresponding broadening of the Compton "modified line" for a given deflection angle of the outgoing scattered photon. Additionally, in the XRF technique, the angle θ is not a discrete, but a scattering over a small series of angles is measured. The broadening of the Compton peak is given by [163, 164, 148]:

$$4\beta\lambda\sin\left(\frac{\theta}{2}\right) \qquad\qquad 26$$

where $\beta = \frac{v}{c}$ for electrons moving in random directions with the velocity v.

2.1.9 Rayleigh Scattering

Rayleigh scattering is a process where photons are scattered by bound atomic electrons and in which the atom is neither ionized nor excited. The scattering from different parts of the atomic charge distribution is thus "coherent," i.e., there are interference effects. This process occurs mostly at low energies and for high-Z material, in the same region where electron binding effects interference the Compton-scattering cross section. Through the "atomic form factor", $F(q,Z)$, from the Thomas-Fermi and Hartree theory of model of the atom, it is possible to consider the charge distribution of the all atomic electrons at once [148]. The form factor squared represents the probability that the Z electrons of an atom take up the recoil momentum, q, without absorbing any energy. In this process q is well-represented by the following equation, since it is assumed that $k_0 - k = 0$:

$$q = 2k \, sin\left(\frac{\theta}{2}\right) \hspace{3cm} 27$$

The differential Rayleigh scattering cross section (cm^2 sr^{-1} atom^{-1}) for unpolarized photons is:

$$\frac{d\sigma_R}{d\Omega}(\theta) = \frac{r_0^2}{2}(1 + cos^2\theta)[F(q,Z)]^2 \hspace{2cm} 28$$

During XRF measurements is advantageous to minimize the Compton and Rayleigh scattering intensities, as this will reduce the risk of overloading the detector with X-ray photons that hold no element specific information. This can be done, according to above equations, by placing the detector under an angle of 90-degree respect to the source.

2.2 Direct and Indirect Excitation

2.2.1 Fluorescent radiation excited by polychromatic sources on a bulk material

Direct or primary excitation is defined as the primary fluorescent radiation emitted from atoms of a sample when they are exited by primary photons from an external source [165]. This can be an X-ray tube, a radioactive source, a synchrotron radiation [166], and charged particles. In this work the main sources employed will be the X-ray tubes, that produce polychromatic radiation. The fluorescent radiation excited by a polychromatic source on a bulk material‡ is given from the sum of photons excited by all primary photons of energies within $E_{edge,i}$ and E_{max}. In particular E_{max} is the maximum photon energy in the spectrum ($E_{max} = eU$ for X-ray tubes with operating voltage U) and $E_{edge,i}$ is the absorption edge energy of the analyte line of the element i [134].

The primary fluorescent radiation excited by a polychromatic source can be expressed as following:

$$N_{i,observed} = G_i \, C_i \int_{E_{edge,i}}^{E_{max}} \frac{\tau_i \, N_0(E) dE}{\mu^*} \hspace{2cm} 29$$

with $N_0(E)$ the spectral distribution function, μ^* is the total effective mass absorption coefficient for the specimen, C_i is the concentration (weight fraction) of analyte i and G_i is the number of i -photons (analyte line) emitted after absorption of a primary (tube) photon in element i. In the particular case in which the polychromatic radiation is generated by an X-ray tube the integral over E is practically solved by approximating it by a sum:

---

‡ Bulk material is defined as a material in which thickness $T \rightarrow \infty$ and mass per area $\hat{m} \rightarrow \infty$

$$N_{i,observed} \approx G_i \, C_i \sum_{E_{edge,i}}^{E_{max}} \frac{\tau_i \, N_0(E) \Delta E}{\mu^*} \qquad 30$$

It is important specify that in the spectral distribution function $N_0(E)$ contains the continuous radiation as well as characteristic tube lines [134].

2.2.2 Fluorescent radiation excited by polychromatic sources on a thin film

In cases of excitation of very thin layers, can be applied the approximation $1 - \exp(-\mu^* \widehat{m}) \approx \mu^* \widehat{m}$ with $\widehat{m}$ its mass per area, and correspondingly $1 - \exp(-\mu^* \rho T) \approx \mu^* \rho T$ with T the thickness (of thin layers). The previous equation 30 becomes [134]:

$$N_{i,observed} \approx G_i \, C_i \sum_{E_{edge,i}}^{E_{max}} \tau_{i,E} \, \rho T N_0(E) \Delta E \qquad 31$$

2.2.3 Indirect Excitation

The indirect excitation is defined as a variety of excitation mechanisms that can occur within a sample: fluorescent photons, scattered photons, or particles (photo-electrons, Auger-electrons), these are generated by interaction of primary photons with atoms of the specimen. As mentioned above when the primary fluorescent radiation has sufficient energy to excite fluorescent radiation of other atoms in the specimen, the interaction is called secondary excitation and the emitted photons are secondary fluorescent photons. In the same way secondary fluorescent photons can excite tertiary fluorescent photons. Higher levels interactions are possible but negligible. Mathematical models for secondary and tertiary excitation are taken in account in available software based on Fundamental Parameters theory (FP) developed for XRF Data Analysis. In this paragraph a detailed mathematical treatment concerning secondary and tertiary fluorescence radiation will be omitted [134].

2.3 Refraction and reflection of X-rays

The macroscopic interactions of X-rays and matter can be described by the refraction index with a real part smaller than 1 [134]:

$$n = 1 - \delta + i\beta = 1 - \frac{r}{2\pi} N\lambda^2 + i\beta \qquad 32$$

where N is the number of electrons per cubic meter, r is the classical electron radius, λ is the radiation wavelength and β defines the absorption of radiation in the medium: $\beta = \lambda\mu/2\pi$ with μ linear absorption coefficient. Low reflection and refraction abilities of matter in the X-ray range (100 eV < E < 250 keV) is due to the small deviation of the refractive index from the value 1. On the other hand, the fact that the real part of a refraction index is smaller than 1 means that the optical density of any substance in the X-ray range is smaller than that of vacuum and the phenomenon of total external reflection can take place at grazing angles of incidence. Equation 32 can be written in the following way, where refraction index dependence on the X-ray energy is highlighted [134]:

$$n = 1 - \delta + i\beta = 1 - \sigma_1 E^{-2} + i\sigma_2 E^{-1} \qquad\qquad 33$$

Where σ_1 and σ_2 are constants.
The application of the Snell's law at the system, schematized in Figure 14, is:

$$\frac{\sin(\Phi_r)}{\sin(\Phi_i)} = \frac{1}{1-\delta} \qquad\qquad 34$$
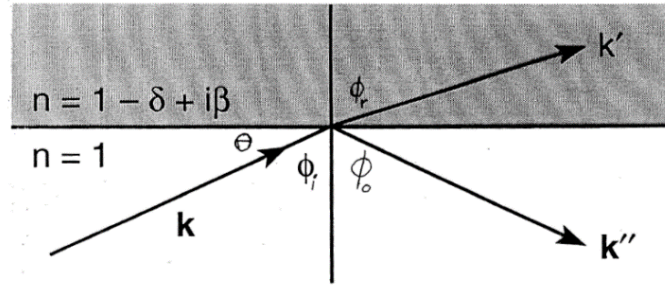
Figure 14: X-ray refraction scheme.

The total reflection occurs when $\Phi_r = 90°$ and the equation 34 becomes:

$$\sin(\Phi_i) = \cos(\theta_{critical}) \approx 1 - \frac{\theta_{critical}^2}{2} = 1 - \delta \qquad\qquad 35$$

$\theta_{critical}$ can be expressed as following:

$$\theta_{critical} \approx (2\delta)^{\frac{1}{2}} \approx 1.6\sqrt{\rho\lambda} \approx 20\frac{\sqrt{\rho}}{E} \qquad\qquad 36$$

In the equation 36 the relation $E = hc/\lambda$ has been used.
Equation 36 expresses the dependence of the critical angle for the total reflection from the density of reflecting material and from the incident energy of X-rays, this relation is plotted

in Figure 15 for a glass as reflecting material and in the energy range of X-rays used in this work [134]:
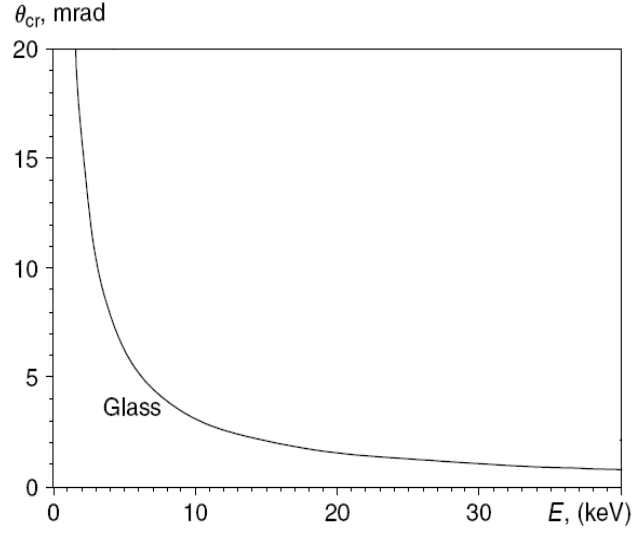
Figure 15: critical angle of total external reflection on glass as function of the energy of photons [134].

The critical angle for borosilicate glass is approximately:

$$\theta_{critical} \approx \frac{30 \; keV}{E} \; mrad \qquad\qquad 37$$

The reflection coefficient for an X-ray beam at an angle θ is given by the Fresnel formula:

$$R(\theta) = \frac{(\theta - \theta_1)^2 + \theta_2{}^2}{(\theta - \theta_1)^2 + \theta_2{}^2} \qquad\qquad 38$$

where

$$\theta_1 = 2^{-1/2}\big[((\theta^2 - \alpha)^2 + \beta^2)^{1/2} + \theta^2 - \alpha\big]^{1/2}$$
$$\theta_2 = 2^{-1/2}\big[((\theta^2 - \alpha)^2 + \beta^2)^{1/2} - \theta^2 + \alpha\big]^{1/2}$$

being $\alpha^{1/2} = \theta_{cr}$, while the imaginary part of the refraction index β describes absorption of radiation in substance $\beta = \lambda\mu/2\pi$ [134].

In Figure 16 is shown the reflection coefficient $R(\theta)$ as function of angle θ at different energies of the incident photons on a smooth glass surface. Reflection coefficient increases when θ approaches to $\theta_{critical}$, and it decreases rapidly to zero at $\theta > \theta_{critical}$. Besides, the phenomenon of reflection is more efficiently with increasing the energy of X-rays [134].
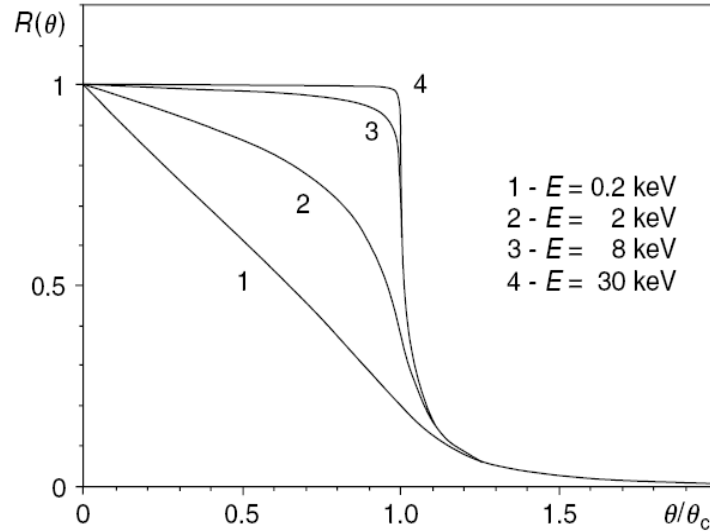
Figure 16: reflection coefficient as function of angle on a glass surface [134].

X-ray that is subjected to a single reflection grazing incidence angle changes its propagation direction, and this very small change does not exceed $2\theta_{critical}$. If the reflection is repeated N times, a beam can be reflected to a relatively large angle of the order of $2N\theta_{critical}$. Multiple reflection at grazing angle incidence represents the main idea on which is based the technology of polycapillary optics in a manner analogous to the way fiber optics guide light. The potential for guiding X rays down single-capillary tubes by total reflection was noted in the 1950s [167, 168] and measured in the 1960s [169] and 70s [170-173]. In the 1990 the technology of optics was developed and start to be commercialized approximately ten years later [134]. The features of the X-ray optics will be described in detail in the following Section 2.4.

2.4 Polycapillary Optics

Polycapillary optics are widely used for all types of X-ray analyses aimed to enhance the performance of the XRF technique [174, 175]. In several cases, high intensities of the primary beam are needed for the detection of low concentration elements. Further, the use of optics allows to perform local analysis at high spatial resolution (e.g., below 100 µm) [176, 177]. Before their diffusion, high intensity beams were achieved by using powerful X-ray tubes with a rotating anode and their collimation was based on the use of pinholes [178-183]. However, pinholes exploit only small part of the primary beam intensity. X-ray focusing optics capture radiation emitted from a source within of a relatively large solid angle and concentrate it on a small spot [184]. The difficulty in the X-ray transmission is connected with their small reflectivity of all substances at large angles of incidence and their strong absorption in matter. X-ray optics guide and shape radiation. They are of different typology: monocapillaries, cylindrical, ellipsoidal or paraboloidal capillaries or polycapillaries, consisting of a monolithic system of a large number of hollow capillary channels, as shown in Figure 17 [185]. Usually, they are categorized trough the number of

internal reflections. A polycapillary is a multiple-bounce capillary consisting of a monolithic system of many bent hollow capillary channels. Their technology is based on the total external reflection of photons from the internal smooth surfaces. For incidence angles lower than critical angle the reflection coefficient reaches values near to 100 percent and the X-radiation is guided with low losses through the optics. The critical angle depends mainly of the reflecting material and the X-ray photon energy. The basic material for X-ray capillaries is glass. The low roughness of reflective glass surfaces leads to a low portion of diffuse scattered X-rays, so an efficient transport of X-radiation through glass capillaries is realized.
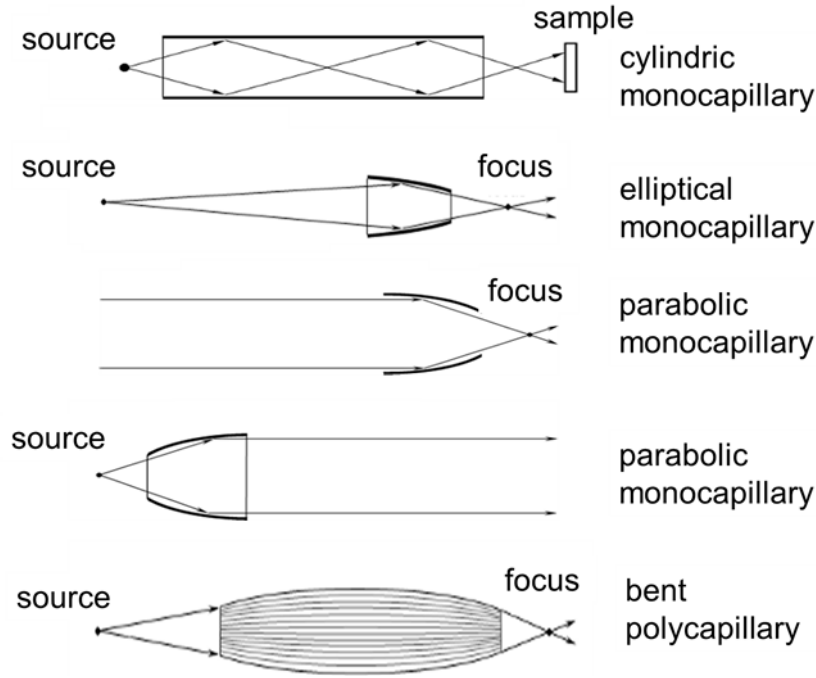
Figure 17: lens for X-rays [186].

2.4.1 Multiple reflections of photons

A material able to do total external reflection for X-rays must guarantee that the incidence angle remains smaller than the critical angle and at the same time that multiple subsequent reflections are maintained. Polycapillary optics, composed of thousands hollow glass channels (monocapyllaries) bundled together guarantee that the second and all subsequent reflections occur automatically at incidence angles smaller than the critical angle ($\theta_{critical}$). The working principle of a polycapillary lens is schematized in Figure 18 [187, 134]:
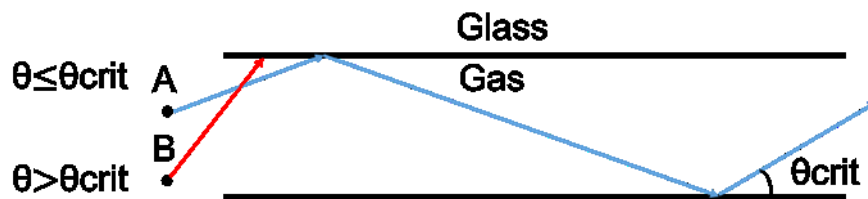
Figure 18: working principle of a polycapillary

2.4.2 Intensity gain

The main benefits of polycapillary optics is to reduce the inverse-square dependence of X-ray intensity with the distance between source and sample. This aspect is formalized in the *intensity gain*. It is defined from the comparison with a pinhole collimator instead of a capillary and can be estimated in the following formula, neglecting the intensity losses at reflections [134]:

$$gain \approx \left(\frac{2\theta_{critical}F_2}{d}\right)^2 \sim N^2_{reflections} \qquad 39$$

The intensity gain expressed by equation 39 is given by the ratio between the angular aperture of capillary $2\theta_{critical}$ over the angular aperture of the pinhole d/F_2, where d is the pinhole (and capillary) diameter and F_2 is the source-sample distance. Also, the gain is proportional to the number of the reflections occurred inside the capillary. Therefore, the gain is dependent on distance between lens and focus.

2.4.3 Spot beam size

The value of the spot beam shaped by a polycapillary can be estimated according to the following formula [134]:

$$s_2 \approx d + (2\theta_{critical}F_2) \qquad 40$$

with F_2 is the capillary-sample distance, including in this way the divergence of the beam from the capillary end. The relative contribution of the second term becomes dominant for small capillary diameters (below 10 um ca) so that small capillary-sample distance is needed. The beam intensity gained with a polycapillary, in comparison with the micrometer collimator (pinhole) , is achieved at the expense of a certain increase of the beam divergence up to $\sim 2\theta_{critical}$.

2.4.4 Bent polycapillary

Polycapillary optics can operate in *focusing* and *collimating* modes by gently bending the capillaries to an appropriate curvature. They can be catalogued in [134]:

    i.   *full lens* collects radiation from a spot source and focuses it,
    ii.   *half-lens* focuses parallel radiation as well as collects radiation from a spot source and parallelizes it.

In Figure 19 the both typologies are sketched.
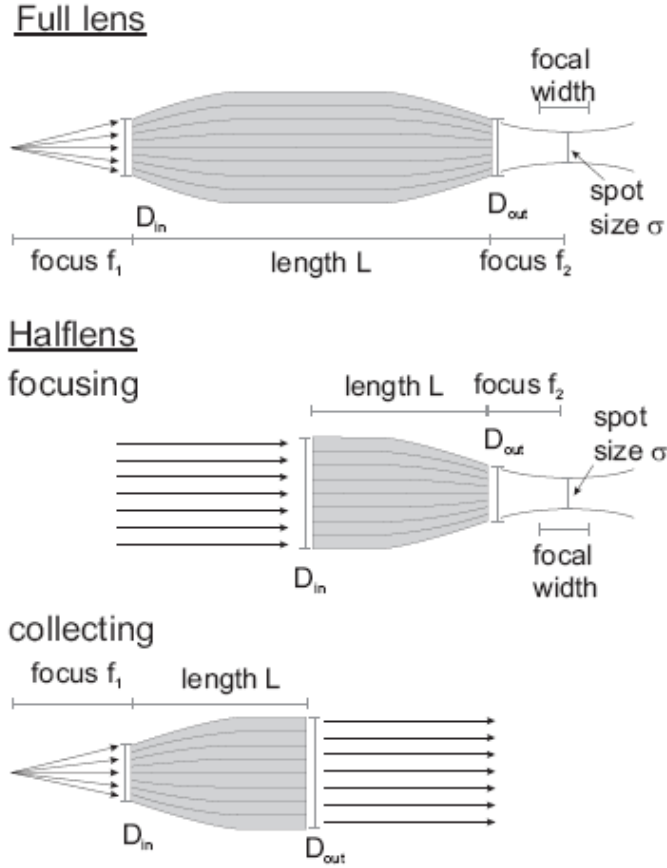
Figure 19: full lens and half-lens [186].

Differently from straight capillaries, with the bent polycapillary the condition of the total external reflection is not automatically fulfilled for all incoming rays at the first reflection. From geometrical considerations, the rays of a quasi-parallel beam entering a capillary fall onto its inner wall at incidence angles smaller than the critical angle $\theta_{critical}$ only if the following condition is fulfilled [134]:

$$\gamma \equiv \frac{r\vartheta_{critical}^2}{2d} \geq 1 \qquad\qquad 41$$

where r is the radius of curvature and d is the capillary diameter. Consequently, at $\gamma < 1$ the radiation is not totally captured by a bent capillary and its cross-section is partly filled with radiation, as is shown in Figure 20:
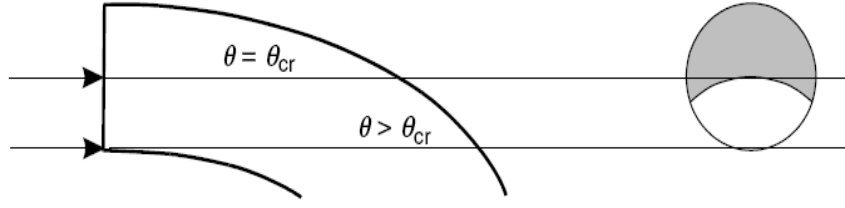
Figure 20: capture zone for a bent polycapillary [134].

Remember the energy dependence of $\vartheta^2_{critical} \sim E^{-2}$, γ parameter decreases fast with the increase of the radiation energy. Consequently, the transmission (i.e. the ratio of the number of photons passing along the channels to the number incident on the front face of the optic) through a bent capillary becomes neglectable in the high-energy region. In order to compensate this effect, it is possible to use capillary with smaller channel diameter, typically between 2 and 50µm. In reference [187] MacDonald, C. A. et al. measured the transmission at the focal distance as a function of photon energy, the result is showed in Figure 21.
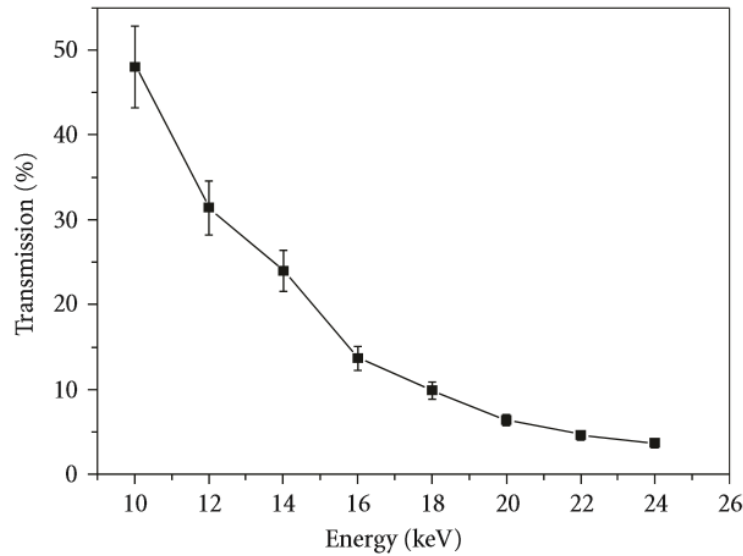
Figure 21: transmission versus energy for a focusing optic [187].

2.4.5 Multiple reflections on a bent surface

The value of reflection coefficient $R(\theta)$, introduced in the equation 38 in Section 2.3, can be approximated by the following expression for reflections to a large angle ϕ ($\phi \gg \theta_{critical}$) as a consequence of multiple reflections $N \sim \phi/2\vartheta$:

$$R_\phi \approx exp\{-\phi\beta\delta^{-3/2}\} \qquad\qquad 42$$

with $\delta \propto E^{-2}$ and $\beta \propto E^{-1}\mu(E)$ (see equation 32) the reflection coefficient can be rewritten as following:

$$R_\phi \propto exp\{- \phi E^2 \mu(E)\} \qquad\qquad 43$$

R_ϕ does not depend on the incident angle and on the number of reflections, it contains only the material constants and the angle of reflection. The reflection coefficient, expressed as in formula 42, describes the intensity losses when an X-ray beam is reflected to a large angles. In the region of relatively small energies reflectivity R_ϕ depends strongly on the mirror material and on the photon energy due to the presence of absorption lines. The best reflectors are light elements, because their K-lines of absorption lie at still smaller energies, this explains the choice of glass for their manufacturing. Above K-lines of absorption, the reflectivity of all substances increases monotonically reaching its maximum and then begins to decrease. Therefore, every substance has its natural energy range where the reflectivity is maximal. The position of the reflectivity maximum moves towards higher energies with increasing Z, whereby its peak value decreases. In the energy range where the mass attenuation coefficient $\mu(E)$ is dominated by the photoelectric absorption, i.e. between absorption edges, the reflectivity decreases. For higher energies, the E^2-term dominates and the reflectivity decreases [134].

2.4.6 Coupling polycapillary optics to an X-ray tube

In the development of an experimental setup, the choice of optical components depends strictly to the concrete application field, in terms of energy range, source size, source-sample distance, desired beam spot, etc. The geometrical features of a polycapillary are illustrated in Figure 22:
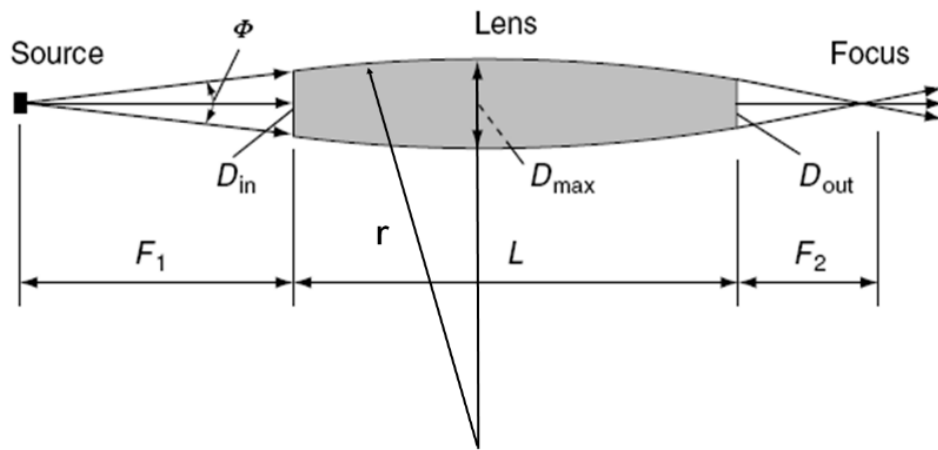
Figure 22: geometric parameters of a focusing polycapillary [134].

F_1 is source-optics distance, i.e., the entrance focal distance, L the length of the lens, F_2 the optics–sample distance, i.e., the exit focal distance, r the radius of curvature of the single channel and Φ is the capture angle.

The radius of curvature R is related to the length of the lens L and to the capture angle Φ by following expression:

$$r \approx \frac{L}{\Phi}$$

<div align="right">44</div>

where, from geometrical consideration Φ can be expressed as following:

$$\Phi = 2 \, atan \left(\frac{D_{in}/2}{F_1} \right)$$

<div align="right">45</div>

The optimum size of the source s_1 and the expected size of the focal spot s_2 are estimated according to equation 40 in section 2.4.3, and both depend on the photon energy.

For an optimum coupling lens-source, F_1 should be chosen in such way that the parameter s_1 corresponds to the anode spot size of the X-ray tube, in this way the efficiency of the optic will be optimized. In the focal position, the maximum source size captured by the optic can be approximated as following:

$$s_1 \sim \theta_c F_1$$

<div align="right">46</div>

As shown in Figure 23, the output beam shaped by a focusing polycapillary has a global divergence α and a local divergence β [187]. In the optic where the channels are parallel the global divergence is zero (α = 0). The local divergence β can be measured experimentally and typically is ~1.3 θ_c, less than the maximum divergence $2\theta_c$.
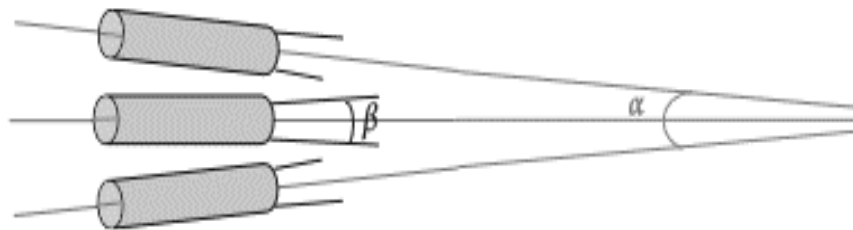
Figure 23: focusing optic divergence [187].

Differently from pinhole collimation, the local divergence of the beam does not depend on the source size, although, as it may be seen in the previous equation 46 , large sources may not be efficiently captured by the optic.

Among the polycapillary optics indicated for XRF analysis we distinguish between *microlens* and *minilens*. Both lenses are asymmetric, the entrance focal distance is three times larger than the exit one, so the obtained focal beam size is smaller than the source size. Their main difference consists properly in the length and focal distances and consequently in different spot size. The more compact *microlenses,* have focal distance less than 10 μm

for a beam size below 20 μm. Diversely, *minilenses* provides beam size between 20 and 100 μm. Minilens can be coupled to the source of dimension between 30-1000 μm while in the case of microlens between 30-50 μm. In the course of this work, our XRF spectrometer is based on a microfocus tube (50 μm beam spot) coupled to a minilens for a beam focalization between 44-26 μm in the energy range of 3-30 keV. The features of the used spectrometer will be described in Section 3.1 in the third Chapter. In conclusion, it is good to remind that the drawback of polycapillary use remains the energy dependent transmission, operating as a low pass filter to the primary radiation, especially in the region above 20 keV [188-190, 134].

2.5 Sources

XRF technique is based on the detection of the characteristic fluorescence lines. The fluorescence emission can be induced on a sample through different kinds of sources.

In particular, X-rays sources are based on two different principles: the spontaneous radioactive decay of isotopes and the interaction of accelerated electrons with matter (X-ray tubes) or with magnetic fields (accelerators or storage rings).

The use of natural sources shows several advantages, they are: compact, low cost, continuously radiating at high constancy, independent on surrounding conditions and do not need any power supply. The great limitation is their radiation hazard potential, leading to very stringent safety conditions. For this reason the natural sources are unsuitable to be employed in portable instruments [191-194, 134].

X radiation can be generated by any charged particle undergoing centripetal acceleration. Mostly known, is the synchrotron radiation (SR) emitted by electrons or positrons in storage rings that circulate at constant relativistic energies (typically ranging from a few hundreds of MeV to several GeV) or similar circular high-energy particle accelerator facilities. SR is a highly polarized and intense radiation emitted in very short pulses of a few *ps* to *ns* duration. The radiation is concentrated in a cone tangent to the curved trajectory of the charged particle initiating it, allowing access to several tens of experiments simultaneously, on the dedicated beamlines [195-199, 134]. X-ray synchrotron radiation presents some main advantages: high intensity beam of several order of magnitude higher than that reached with X-ray tubes, the monochromaticity of the beam that in some cases can simplify data evaluation, and the advantage to use highly parallel beam, so that it is easier focus and collimate respect to the beam emitted from an X-ray tube.

X-ray tubes generate polychromatic radiation with limited intensity; however, the main advantage consists in their portability. In this work, XRF analyses have been based on the employment of X-ray tubes as primary radiation. In this section features and the operating principles of X-ray tubes will be introduced.

2.5.1 X-ray tubes

A constant characteristic radiation over a long time is needed for XRF analysis. X-ray tubes are based on electrons emission from a cathode and accelerated towards an anode in an electric field created by a positive potential of the anode relative to the cathode.

Anode and cathode are mounted in a vacuum chamber. The common materials used for manufacturing tube chamber are glass, metal and ceramic [134]. Figure 24 shows the main components of an X-ray tube.
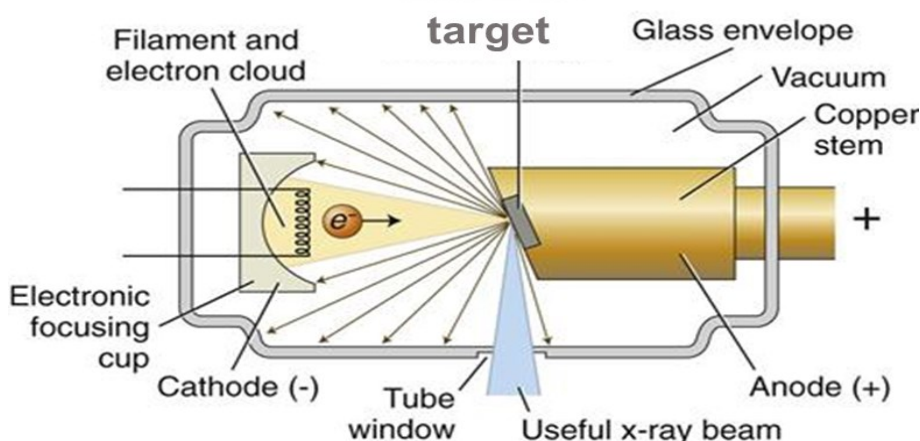
Figure 24: scheme of an X-ray tube [200].

The interaction of electrons with the anode target generates elastic and inelastic processes (see Section 2.1). In particular, elastic scattering dominates, not being connected with energy losses, and only a relatively small part of incident electrons takes part in inelastic scattering decelerating continuously in a strong Coulomb field of nuclei and gradually losing their initial energy. The gradual energy loss of electrons occurred through *Bremsstrahlung* radiation and it generates a continuous spectrum in the X-ray tube radiation. Inelastic collision between electrons and target can see the removal of atomic electron from its orbit with consequently ionization of the atom. The filling of the vacancies created thought outer orbital electrons gives rise to the characteristic lines in the X-ray emission spectrum.

Figure 25 shows simulated spectra based on Ebel equation [201] for a Rhodium anode tube at different anode voltages *U* (8° take-off angle, 100 μm Berillium window).
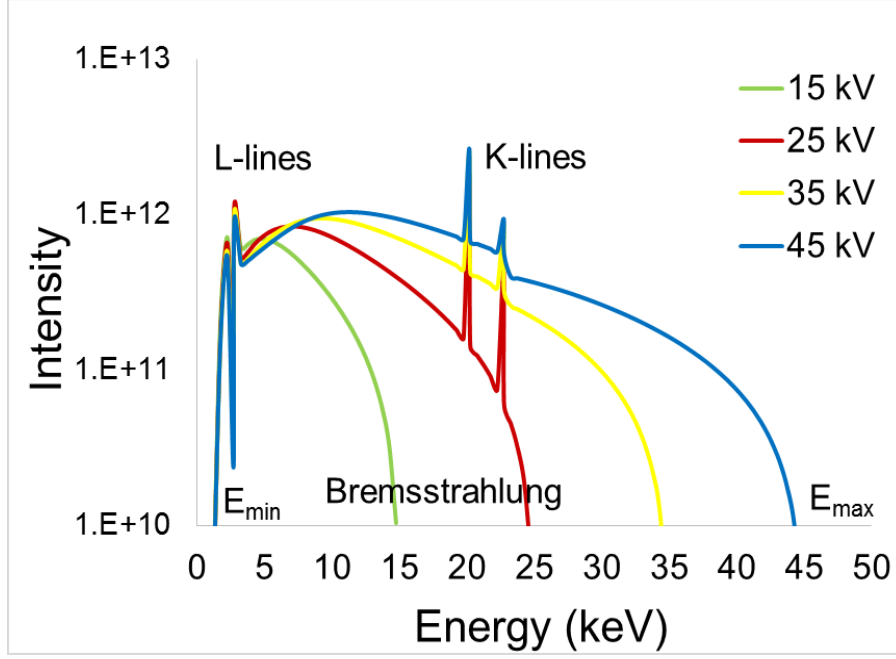
Figure 25: simulated spectra for a Rh-anode X-ray tube at different voltages using Axil analysis software [202].

A characteristic X-ray tube spectrum is a superposition of a continuous part and characteristic lines (fluorescence X-lines of the anode material). The sharp termination of the continuous spectrum at the short wavelength side corresponding with the maximum kinetic energy of the electron $E_{kin} = eU$.

$$\lambda_t[nm] = \frac{c}{v_t} = \frac{hc}{E_{kin}} = \frac{1.24}{U[kV]} \qquad\qquad 47$$

The shape, the intensity and the maximum energy of a continuous spectrum depend on the value of the high voltage, so as the discrete lines presence. If the high voltage (i.e. electrons energy) overcomes the excitation threshold corresponding to the absorption edge of the anode material, discrete lines will be present in the spectrum, and their intensity increases with the accelerating voltage. The falloff of the spectral distribution at low energies is usually due to X-ray absorption in the tube exit window. Experimentally, the voltage of X-ray tube is operated at ca 1.5-2 times the energy of the absorption edge of the element of interest.
 The total irradiated X-ray power can be estimated according to the following expression [134, 203, 204]:

$$P[kW] = CZIU^2 \qquad\qquad 48$$

where Z is the atomic number of the anode material, I is the anode current (A) ; U is the high voltage (kV); C is a constant equal approximately to 10^{-6} (kV^{-1}). It means that the efficiency coefficient η can be approximated as in the following formula [134]:

$$\eta \equiv P/IU \approx 10^{-6} ZU \ [kV]. \qquad\qquad 49$$

The value of the efficiency is usually ranged between 0.1–1%, for this reason a high thermal energy dissipation occurs in anodes of the X-ray tubes.

Anode material is usually a metal (chromium, copper, molybdenum, tungsten, etc.). The X-rays emission from the anode is isotropic; the exit window is usually made from a thin beryllium film and the anode angle is the angle between the target surface and the normal to the window.

Three typologies of X-ray tubes commercially available can be distinguished according their power [134]:

   i.   Low-power X-ray tubes (<1kW);
   ii.   High-power X-ray tubes (1–5 kW);
  iii.   High power X-ray tubes with rotating anode (>5kW).

A low-powered microfocus tube (30 W) has been used in this work. The typical power of a microfocus tube (in Watt) is given as following [134]:

$$P[W] \approx D[\mu m], \qquad\qquad 50$$

where *D* is the diameter of the anode focal spot in microns.

As discussed in the previous Section 2.4.6, the diffusion of microfocus tubes have grown significantly with the technological developments of optics. Their combined use provides high intensity beams focused in a small spot, without wasting most of the source's brilliance, that otherwise may be obtained only with high-power tubes. Furthermore, microfocus tubes do not require water cooling and can be powered by conventional power outlets, simplifying the in-situ usage of the instruments they are incorporated in.

2.6 Detectors

The detection of fluorescence is based on the conversion of the energy released by a photon in the detector material into an electrical signal. The preferred detectors in X-ray spectroscopy are the semiconductor detectors [205-207]. Their main advantages are due to high detection efficiency and high energy resolution. This aspect is related to the fact that, the mean energy needed to create one primary elementary charge is of few electronvolts (3.62 eV for Silicon), ten times lower than others X-rays detectors (scintillators and gas-detectors). In this way, the energy/charge conversion factors, i.e. the number of charge carriers generated for a given energy is higher for semiconductors than for other detectors, leading to a much smaller statistical broadening of the fluorescence peaks.

2.6.1 Detection Efficiency

X-rays release their energy in the detector crystal through the interaction mechanisms of the X-radiation with the matter: photoelectric effect, Compton Scattering and Rayleigh scattering, of which processes the energy and atomic number dependence is showed in table Table 1, Section 2.1.2. Detection efficiency expresses capabilities of a detector. It is defined as the fraction of the total number of photons emitted by the source, which interacts in the detector volume and that are absorbed completely. It is formalized by the product of the following terms [205-207]:

$$\eta = \eta_{geom} \cdot \eta_i \cdot \eta_{photo} \qquad\qquad 51$$

where:

i.   *geometrical efficiency* $(\boldsymbol{\eta_{geom}})$, the fraction of the photons emitted by the source which enter the detector volume. It takes in account the active area of the detector and the distance with respect to the source.

ii.   *intrinsic efficiency* $(\boldsymbol{\eta_i})$, the fraction of photons entering the detector, which interact in the detector material.

iii.   *photo-peak efficiency* $(\boldsymbol{\eta_{photo}})$, the fraction of the photons interacting in the detector, which deposit their full energy in the material.

The photo-peak efficiency can be limited by (1) *escape processes*. These consist in the not-reabsorbing in the detector material of the X- ray photon generated by the interaction of the fluorescence photon with the detector crystal. The energy of the photon that leaves the detector without be absorbed is:

$$E_{escape} = h\nu - E_{atom} \qquad\qquad 52$$

where E_{atom} is the fluorescence energy of the detector crystal atoms. For silicon-based detectors E_{atom} corresponds to the Si-Kα fluorescence energy of 1.74 keV. In the case of X-ray photons absorbed close to the detector surface where usually the low-energy photons detection occurs, the escape process becomes a not-negligible effect.

Others processes, occurred during the detection, can give rise an *artifacts* presence visible in the XRF spectrum. Among these, there are the (2) *pileup peaks*, generated if two photons reach the detector in a time, that cannot be discriminate from detector electronics. The result is a sum peak of the two photon energies. Figure 26 shows the Fe spectrum measured by using a Silicon detector where, in addition to the Fe-Kα and Fe-Kβ characteristic lines is present a pileup peak at 12.8 keV (Kα pileup) and an escape peak at 4.66 keV.
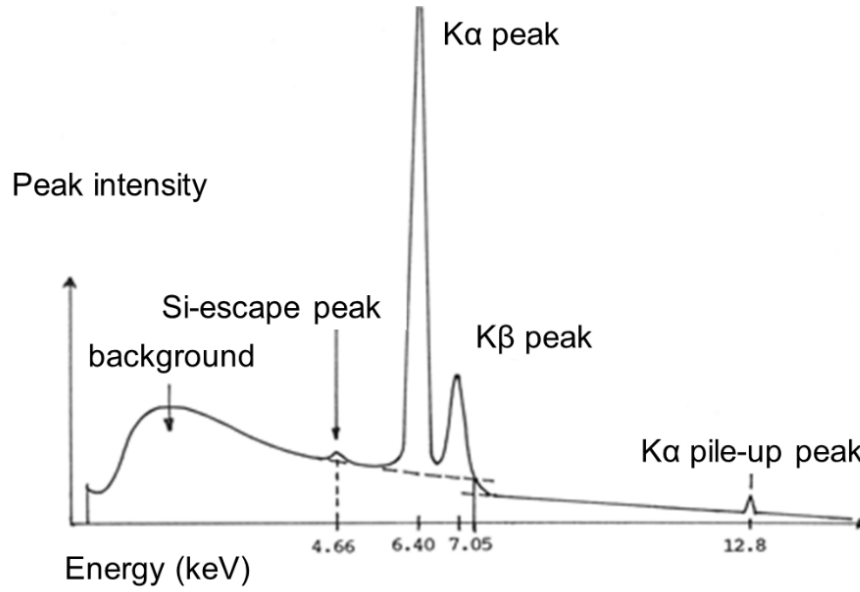
Figure 26: Fe spectrum acquired by Silicon Drift Detector.

Another distortion may be introduced if a photon interacts in the detector close to the front contact. Because, the charge cloud created can be only partially absorbed in the detector material. The (3) *incomplete charge collection* (ICC) typically generates a tail on the low energy side of the peak. All detectors suffer from incomplete charge collection to some extent. Low energy X-rays have a very shallow penetration depth and charge collection is usually poor near the front contact [208]. The peak at low energy will therefore be broader and it will have a mean energy lower than expected.

Finally, the (4) *shelf effect*, also, has to be considered if the first interaction occurs in the front contact side. In this case, the high energy photo- or Auger-electrons can leave the detector, reducing the detected photon energy.

2.6.2 Energy Resolution

In spectroscopy, an important requirement of a detection system is the capability of the system to distinguish photons closely separated in energy. The energy resolution is commonly expressed as full-width-at-half-maximum (FWHM) of the measured distribution. Alternatively, it can be expressed as percentage R, defined as the ratio between the FWHM and the centroid value of the distribution:

$$R = \frac{\Delta E_{FWHM}}{E_0} \qquad\qquad 53$$

The measured distribution can be described by a Gaussian function, whose expression is given by [205-207]:

$$G(E) = \frac{N_0}{\sigma\sqrt{2\pi}} \exp\left(\frac{(E - E_c)^2}{2\sigma^2}\right)$$

<div align="right">54</div>

with σ the standard deviation, N_0 the peak area, and E_c the peak centroid. For a Gaussian distribution the FWHM results related to the σ as $FWHM = 2.35\,\sigma$.

Several noise sources limit the energy resolution of detector and contribute to the broadening of the peaks. In particular, for semiconductors, the ΔE_{FWHM} (or standard deviation σ) includes:

i.   *statistical noise* related to the conversion process of the photon energy into charge carriers.

ii. *electronic noise* of the detector–amplifier system.

iii. *collection noise* related to the partial collection of the signal charge.

$$\Delta E^2{}_{FWHM} = \Delta E^2{}_{statistical} + \Delta E^2{}_{el.noise} + \Delta E^2{}_{collection}$$

<div align="right">55</div>

For semiconductors, statistical noise is expressed through the *Fano factor (F)*:

$$\Delta E_{statistical} = 2.35\sqrt{(FE\varepsilon)}$$

<div align="right">56</div>

where E is the photon energy and ε is the average energy needed for the pair electron-vacancy production. The Fano factor is 0.11 for silicon crystal detectors.

2.6.3 Silicon Drift Detector

In this work Silicon Drift Detectors (SDD) have been used for collection fluorescence radiation. In recent years, their use has been grown compared to the more conventional planar detectors (Si(Li) and Si-pin detectors). They offer higher performance in term of lower electronic noise at very short peaking times. This provides a better energy resolution at moderate count rates and much better energy resolution at high-count rates. In addition, SDD detectors are liquid nitrogen-free making their portability easier than a conventional detector. The main components of a SDD detector are [209]:

1) *Sensor*, converts the photon energy into an electric charge of proportional size. SDD devices use a field gradient applied with ring electrodes on its back surface to drift the charge to the anode.

2) *Field effect transistor (FET)*, connected directly to the sensor, represents the first stage of the amplification process. It measures the charge liberated and converts it to a voltage output.

3) *Peltier (thermoelectric) cooling system*, allows to operate at few tens of degrees below zero.

4) *Window,* maintains vacuum within the detector. Usually, Beryllium windows are used, because more robust than polymer-based thin windows. It makes possible the detection of elements with $Z > 11$ (from Na) due to the absorption of low energy photons

The working principle of a SDD detector is schematized in Figure 27. It consists of a three-stage process: (1) the photon energy conversion into a charge by the ionization of atoms in the semiconductor crystal, (2) the charge conversion into a voltage signal by the FET preamplifier, (3) the voltage signal is taken as input into the digital signal processor (DSP).
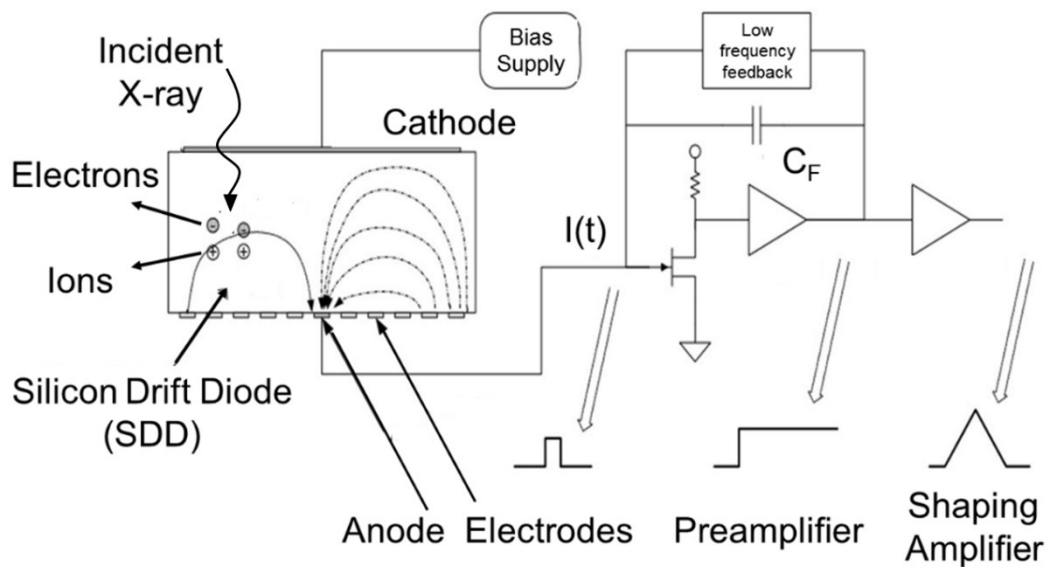
Figure 27: scheme of the working principle of a SDD detector [209].

Differently from conventional detectors with planar structure and uniform electric field between anode and catode. The SDD technology is based on a cylindrically symmetric structure with a radial electric field, as is showed in Figure 28. The anode is a small circle and the drift electrodes are annular. The small area of the anode translates in a very small capacitance. The active volume can be enlarged by adding more electrodes keeping the same anode area. This technology allows to reduce the voltage noise proportional to the anode capacitance and provides a better energy resolution especially at high-count rates.
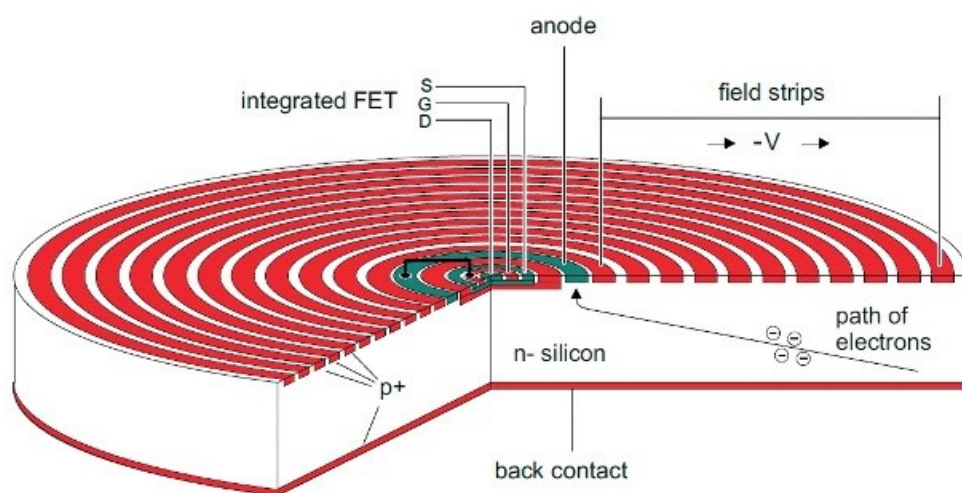
Figure 28: scheme of a SSD sensor [210].

Chapter 3

Mobile scanning MA-XRF

The development of the mobile scanning MA-XRF system of the present research work have included several optimization in terms of: a) chemical sensitivity and scanning speed for acquiring elemental images of atomic species in the samples at low concentrations and with dwell time the millisecond range; b) portability for moving the instrument at museums and galleries; c) capability to analyze large areas even with a selectable lateral resolution; d) possibility to perform a real-time imaging during scanning with a least square fitting procedures applied on the fly on the data; e) the full control of the instrument through an intuitive software.

The MA-XRF scanner of the present work is composed by the following main components: (1) the measurement head equipped with a microfocus X-ray tube focused with a polycapillary and a SDD detector operated in time-list-mode, (2) a custom designed three axis-system with a long travel range and (3) a custom-developed Control Unit (CU) for the real-time control of the instrument.

In this Chapter, a full description of experimental set-up is presented including the figures of merit of the devices in terms of chemical sensitivity, limit of detection and spatial resolution. Moreover, scanning modes, speed performance and control software will be discussed.

3.1. The measurement head

Spectroscopic head of the scanning system is illustrated in Figure 29. It is composed of a microfocus X-ray tube (1) equipped with a polycapillary lens (2), a Silicon Drift Detector (SDD) (3) coupled to a Digital X-ray Processor (DXP) module (4), a long-range microscope (5) and a precision laser sensor (6).
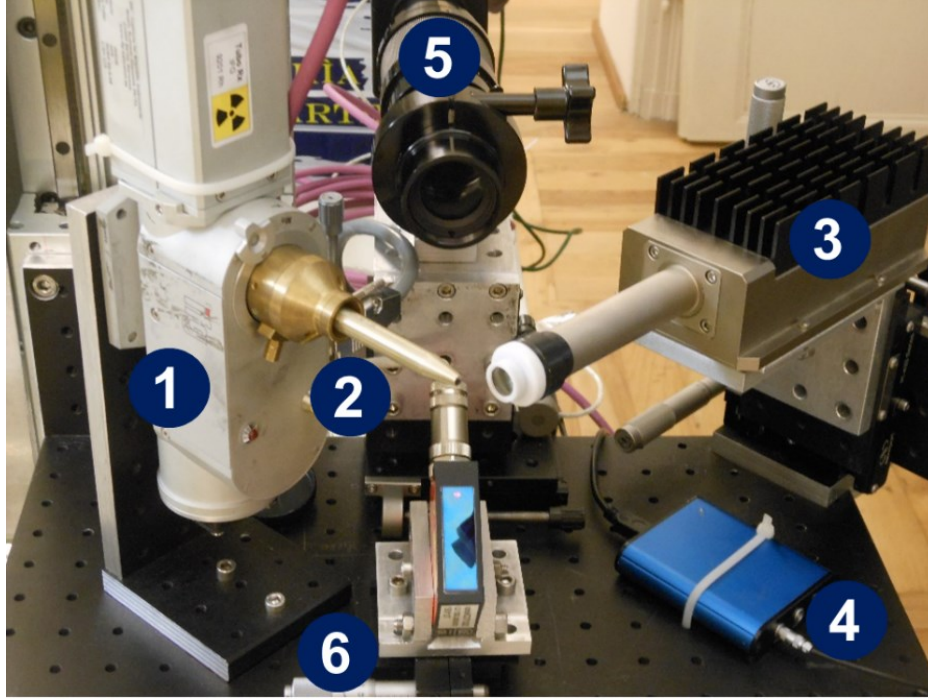
Figure 29: measurement head equipped on MA-XRF scanner.

3.1.1 X-ray Source and detection system

The fluorescence emission of the sample is induced by a 30 W Rh-target microfocus X-ray tube (by IFG) with a beam size of 50×50 μm^2. The tube is equipped with a 100 μm Be window and it can operate up to 50 kV of voltage and 0.6 mA of current.

In order to transport primary radiation and maintaining it focalized on a small spot the X-ray tube is equipped with a customized polycapillary mini-lens (by IFG).

Table 7 reports the beam size as a function of the energy at the focus distance of the lens (i.e., 10.3 mm); also gain values are given in the range 5-15 keV.

E (keV)	3-5	5-7.5	7.5-10	10-15	15-20	20-25	25-30
Focus size	44	44	43	37	28	26	26
Gain	4470	8955	9753	9242	7139	3267	724

Table 7: beam size and gain of polycapillary lens.

The fluorescence signal that comes out from the sample is collected by a SDD detector (by KETEK) with a large active area of 50 mm^2 and thickness of 450 μm. Detector is optically shielded by a 12.5 μm Be window and cooled by a Peltier system allowing to work at high ambient temperatures (up to 30°) with a noise not influencing its energy resolution.

The intrinsic detection efficiency is higher than 90% in the range 2.4-11.5 keV range. The energy resolution has been measured at 5.9 keV by using a ^{55}Fe radioactive source and it is plotted in Figure 30 at different values of the peaking time of the Digital X-ray Processor (DXP) installed in the scanner. DXP will be described in the following Sections. As

expected, better resolution is achieved for slow detector peaking times. The drawback is a higher dead time because more data processing time per event is spent.
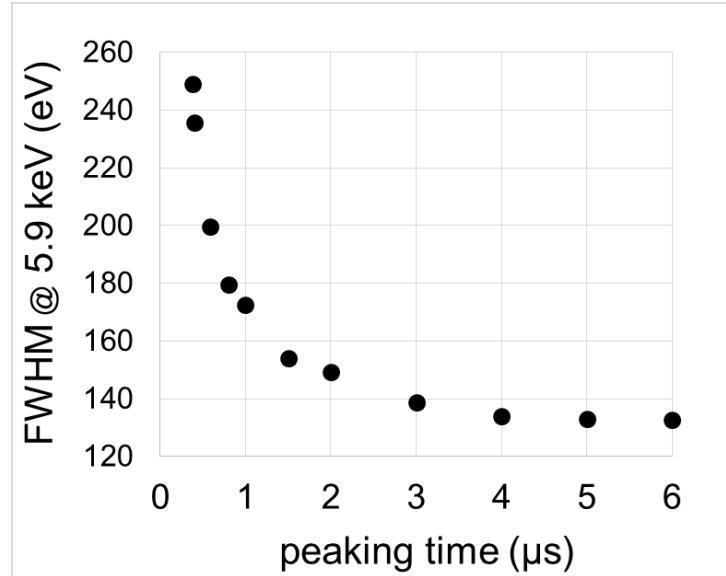
Figure 30: energy resolution measured at 5.9 keV for different peaking times of the Digital X-ray Processor (DXP).

In order to optimize the performance of the detector during measurements, the energy resolution (FWHM) versus the output count rate (OCR) has been investigated by limiting the dead time to a reasonable value of the 30%. Results are shown in Figure 31 for different peaking times and flat top values of the DXP. The characterization is direct to individuate the best working conditions, in other terms the best compromise between throughput and peak resolution.

Measurements have been performed by using a Fe pure target placed on the focal point of the source. The fluorescence signal has been induced on the sample by setting different X-ray tube voltages and currents. In particular, measurements have been repeated at 35 kV, 38 kV and 40 kV and current has been increased progressively keeping the dead time less that the 30%. Each spectrum has been acquired for 50 sec live time.
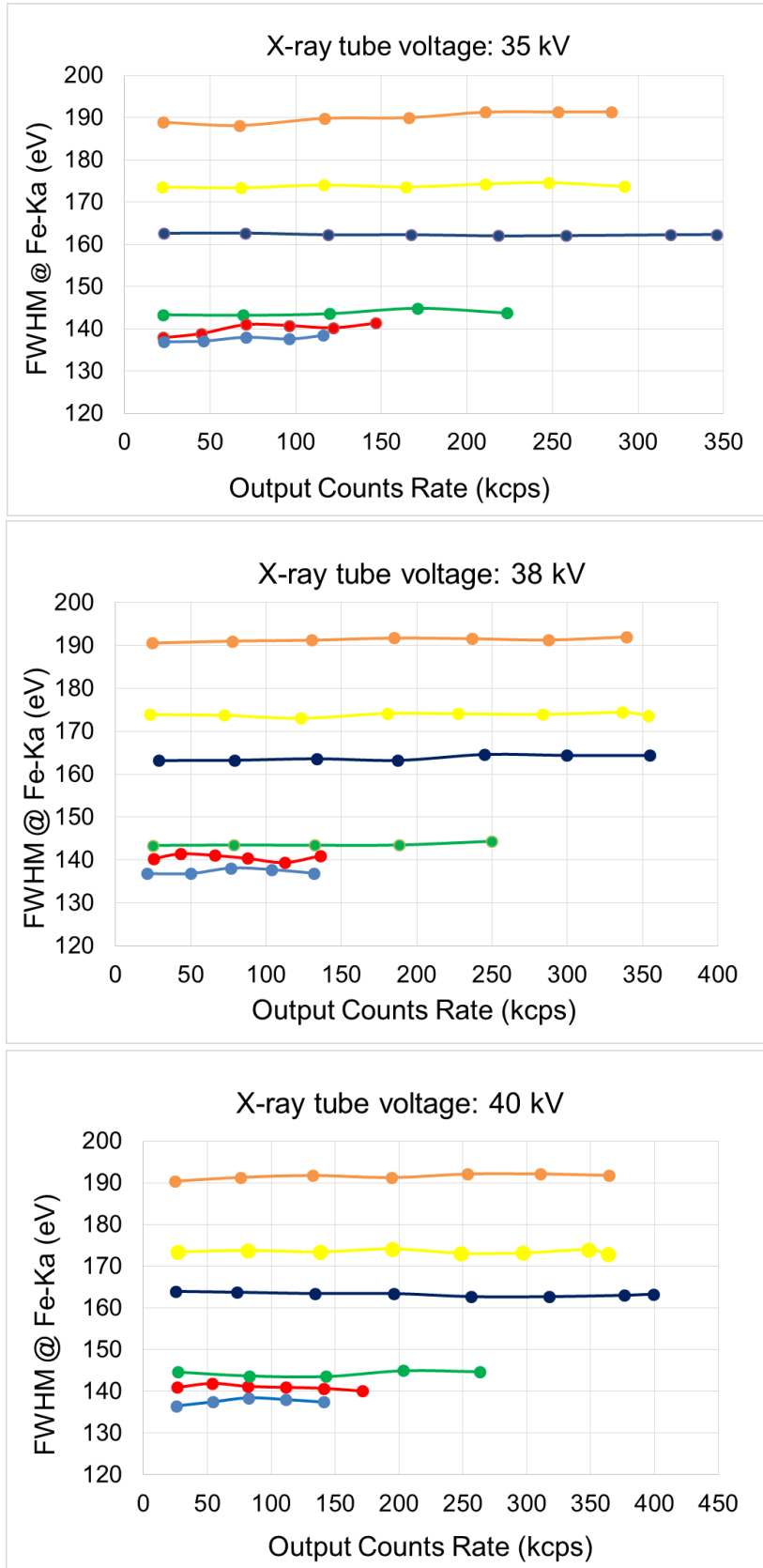
Figure 31: energy resolution versus Ouput Count Rate (OCR).

The SDD detector has been equipped with a new compact Digital X-ray Processor (DXP) module (68 × 48 mm) that allows high incoming fluorescence count rate minimizing dead time. As we will see, this aspect is crucial in order to obtain elemental mapping at high contrast even when the scanner operates fast scans.

The DXP has been customized for our MA-XRF scanner by the Belgium Brightspec. Main technical characteristics are reported in the Table 8:

Device	14-bit flash ADC running at 50MHz
	100MHz processor in high-performance FPGA
	200 MHz 32-bit CPU
Data acquisition	spectral memory size up-to 16 384 (16K) channels
	acquisition modes: PHA, MCS, LIST and TLIST event time resolution (LIST and TLIST): 40 nsec
Data settings	trapezoidal filter
	rise time: 0.1-20 µsec in steps of 0.2 µsec
	flat top: 0.1-8.0 µsec in steps of 0.1 µsec
	threshold: 1 to 255
	Digital Base Line Restorer (BLR)
	Pile-Up Rejector (PUR)

Table 8: DXP technical specifications.

In particular, the module supports the acquisition functionality in Time LIST mode (or event mode) with an event time resolution of 40 ns. It differs from a conventional DXP analyzer that measures the spectrum of incident events. Our DXP module acquires continuously the stream of data giving at the outputs a list of points in (time, energy) coordinates. In this way the stream of data can be processed by selecting different time intervals allowing during the continuous scanning described in Section 3.8 to change the pixel size even during acquisition based on user needs.

Customized libraries in Linux 64 (RTOS) and real-time Labview have been specifically developed by the producer in order to be included in the Control Unit of the scanner describe in Section 3.3.

Based on DXP technical characteristics and results in Figure 30 and in Figure 31 we usually operate the MA-XRF acquisition with default values of peaking time at 1.5 µsec. This leads to a resolution of the SDD of about 155 eV at 5.9 keV.

3.1.2 Irradiation and detection geometry

X-ray tube and detector are positioned according the conventional 90 degree geometry, source and detector are oriented at 45° respect to the normal to the sample surface, as sketched in Figure 32:
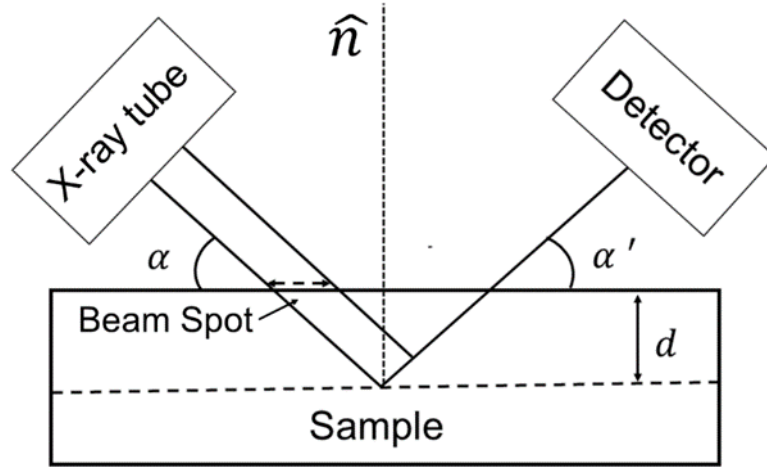
Figure 32: spectrometer geometry.

The geometric configuration at 90° minimizes the Compton background, but the inclination of the source produces a broadening of the beam in the amount of $1/sin\,\theta$ on the sample surface along the horizontal direction. Also, geometry influences the penetration depth of X-rays in the sample. Similarly, the X-rays fluorescence induced at inner layers of the sample are absorbed form outer layers (and also air path and Be window) before reaching the detector. These considerations are expressed in the equation 57, where the absorption $A(E)$ in any homogeneous layer between the spectrometer and the sample with the mass attenuation coefficient μ, thickness d and density ρ is defined as:

$$A(E) = \exp(-\chi(E, E'))\rho d \qquad\qquad 57$$

where

$$\chi(E, E') = \mu(E)\frac{1}{sin\,\alpha} + \mu(E')\frac{1}{sin\,\alpha'} \qquad\qquad 58$$

Equation 58 indicates as a lower inclination angle (α) than 45° degree corresponds a larger broadening of the beam spot on the sample making worse the lateral spatial resolution, but at the same time the absorption in the upper layers is minimized. Diversely, it can be observed that to minimize the beam spot, source (α) and detector (α') should approach to 90° degrees.

As better explained in Section 1.2 in the first Chapter, MA-XRF technique usually do not allow to fix the measurement distance. However, as reference we consider as preset distance the one where the sample is in the focus of the optic (about 10 mm). At this distance the sample-SDD distance is also 10 mm. Figure 33 shows the fluorescence transmission in function of energy for "in focus" experimental geometry.
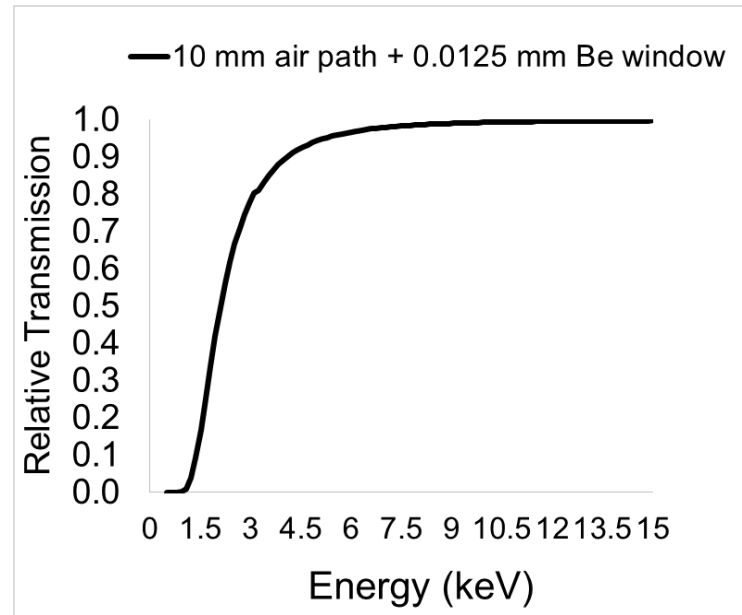
Figure 33: fluorescence radiation transmitted before to be detected.

3.1.3 Microscope system

The spectrometric head of the MA-XRF scanner has been equipped with a long distance microscope (by Infinity). It is placed along the normal direction to the sample surface. The microscope presents a reduced depth of field of 19 μm and it is used for positioning the sample at the focal distance of the optic (where beam-spot is minimal).
Table 9 reports the resolution specification of microscope.

Working Distance (WD) (mm)	60
Magnification (MAG)	4.47
Numerical Aperture (NA)	0.17
Resolution (lpmm)	500
Resolution (μm)	2
Depth of Field (DOF) (mm)	0.019

Table 9: Optical resolution data of microscope.

In addition, it is used for acquiring optical images with a high resolution (down to 2.8 μm) of small area in specimen. This allows in many cases useful comparison of elemental distribution XRF images of small painted details with a direct optical microscope image.
Thus, the optical focusing of the microscope assigns the distance at which the MA-XRF device can be used as a high resolution micro-XRF scanner. Analytical results obtained by

performed micro-XRF imaging will be illustrated and discussed in APPENDIX-A. It will be shown in Figure 45 (Section 3.5) that beam-size at this distance is 38 µm on the Mo-Kα lines. Figure 34 shows the optical microscope image of the beam reflected on a fluorescent screen placed at the focus distance of the polycapillary lens. Differently, MA-XRF analysis is performed with a wider beam (i.e., some hundreds of microns), positioning the sample out of focus. Beam dimensions versus distance will be in Figure 45 (Section 3.5).

Figure 34: microscope image of the beam spot transmitted by a polycapillary lens at the focus distance.

Due to this aspect two different analytical techniques (i.e., µ-XRF and MA-XRF) can be applied on artworks with the same instrument allowing investigation of painting materials at different scale of length. As discussed in Section 1.1 (first Chapter), MA-XRF is suited to have global information on pigment signature, hidden paintings and attribution/authenticity, while µ-XRF allows to study at microscopic level the chemical correlations among elements giving new insights on painting techniques and conservation state.

The beam dimension at the measuring distance is also related the lateral resolution of the elemental maps. As demonstrated in the next Sections, others parameters which influence the lateral resolution of the final elemental maps are beam size, step-size used during the scan and counting statistics that determines the contrast by means the ratio signal to background.

3.1.4 Laser sensor for a dynamic determination and correction of distances

In several analytical cases, elemental maps may be interested by a not uniform lateral resolution. This effect, is caused by a not perfectly flat sample. In order to provide for this limitation, the MA-XRF scanner has been equipped with a laser sensor (by Micro-Epsilon)

based on a triangulation technology for a real-time measurement of the polycapillary-sample distance.

Firstly, the use of laser sensor is related to the safety of artworks during the scanning. The laser performs a continuous monitoring of artworks distance from the spectrometer with a 750 Hz frequency and a resolution down to 4 μm. Laser spot size on the sample is about 200 μm. A *safe distance* is selected by user as initial parameter before starting the scanning, the continuous information exchanged between the laser and Control Unit (describe in Section 3.3) allows the immediate interruption of the movement if this limit is reached and exceeded Optionally, the laser sensor is used to dynamically correct the distance of the sample under investigation from the measurement head along the Z direction. The laser system communicates to the Control Unit (CU) the distance and if necessary the CU acts on the motorized Z axis bringing again the sample to the initial distance. In this way the distance sample-source is guaranteed be quite constant during the scanning. *Correction spee*d of the Z axis has to be chosen comparable with the speed at which the scan is performed. Diversely, distortion effects could be introduced in elemental maps.

3.2.   The XYZ high precision travel system

The spectrometric head is moved during scanning by means of a custom-designed three-axis system that cover a total area of $110 \times 70 \times 20$ cm^3 (XYZ) At the present this is the largest area covered by a MA-XRF scanner.

The XYZ axes present a precision of 52 μm/300 mm and a bidirectional reproducibility of ± 10 μm. The position of the measurement head is based on a wire sensor, designed *ad-hoc*. The wire sensors allow to retain the reference position in the XYZ coordinates even after that the system has been switched on/off without requiring any calibration procedure.

Main advantage introduced by a large scanning area device is the possibility to analyze the whole artworks in a single acquisition, without any separation of the surface in sub-parts, thus avoiding the need of a off-line mosaic reconstruction of the elemental images. This aspect leads the main advantage to minimize the introduction of graphic imperfections in the assembling procedure.

The motion of axes is entirely controlled by the Control Unit (CU). The XY scanning is performed in a continuous movement of the X axis with a maximum speed of the scanner 100 mm/sec. The Y step is selected by the user initially. The scanner is so designed for making ultra-fast scans covering the total area in 4.2 hour with a lateral resolution of 500 μm.

The Z-axis enables the sample movement with high accuracy along the beam focal direction. Thus, allowing the sample positioning in order to have the desired beam size as described by the data in Figure 45 (Section 3.5).

In addition, as described in Section 3.1.4, the Z axis is used for the on-line monitoring of the object position by means the laser sensor, allows to maintain fixed the object distance from the spectrometer even in the presence of curvatures.

The travel system of the scanner is shown in Figure 35 the MA-XRF during the in-situ analysis of the Flemish painting "*Paston Treasure"* at the Norwich Castel Museum in Norwich (UK).
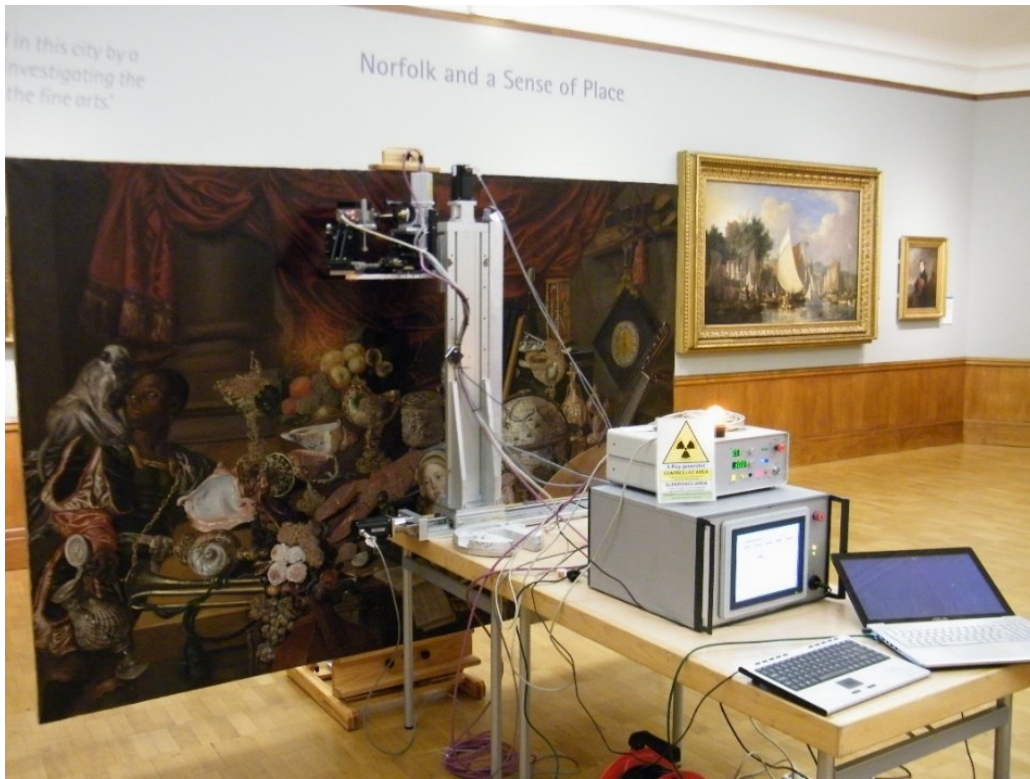
Figure 35: MA-XRF scanner for the analysis of "Paston Treasure" at Norwich Museum (UK).

3.3. Control Unit

The MA-XRF scanner is fully controlled by a custom developed and programmed Control Unit (CU) that is used for synchronizing the travel of the measuring head in the XYZ dimensions with the X-ray data acquisition. The CU guarantees this high precision synchronization via embedded drivers and libraries of all sensors installed in the device; moreover it allows to monitor the instrument operation in a real-time mode. The CU hardware component has been designed employing a cRIO controller (by National Instruments) based on a deterministic Linux real-time operating system (RTOS) and controlled via LabVIEW real-time software, [211]. In detail, the cRIO platform is equipped with a real-time microprocessor for communication, signal processing and data logging via embedded LabVIEW real-time applications and a user-programmable FPGA component (Field-Programmable Gate Array) with direct access to the I/O modules for implementing high-speed control and custom timing, triggering, and synchronization directly in hardware. The cRIO architecture is shown in Figure 36:
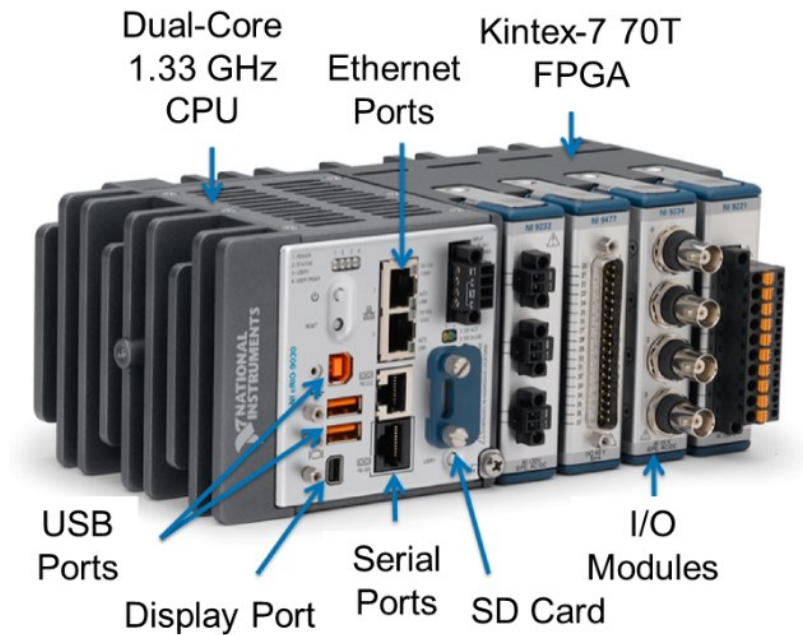
Figure 36: cRio architecture scheme.

The CU has been interfaced with a customized user-friendly software programmed in a real-time LabVIEW for controlling all sensors of the instrument and for monitoring its executions in real-time. The software graphical structure is composed of four sub-windows, and each allows the operating parameters selection of the single scanner components.

3.3.1 Detector window

The "detector" panel (see Figure 37) allows to select the operating conditions of detector (gain, threshold, rise time, flat top, live or real-time, etc.), to visualize XRF spectrum, dead time, Input and Output Count rate (ICR/OCR). XRF spectra can be saved in *.spe* format (i.e., IAEA ASCII file format) from the same window. Its use is particularly suitable for single spectrum acquisitions, that often are combined with the elemental mapping, or for the identification of the scanning acquisition parameters, as the choice of the time acquisition in basis on the recorded counts on several single spots of the sample.
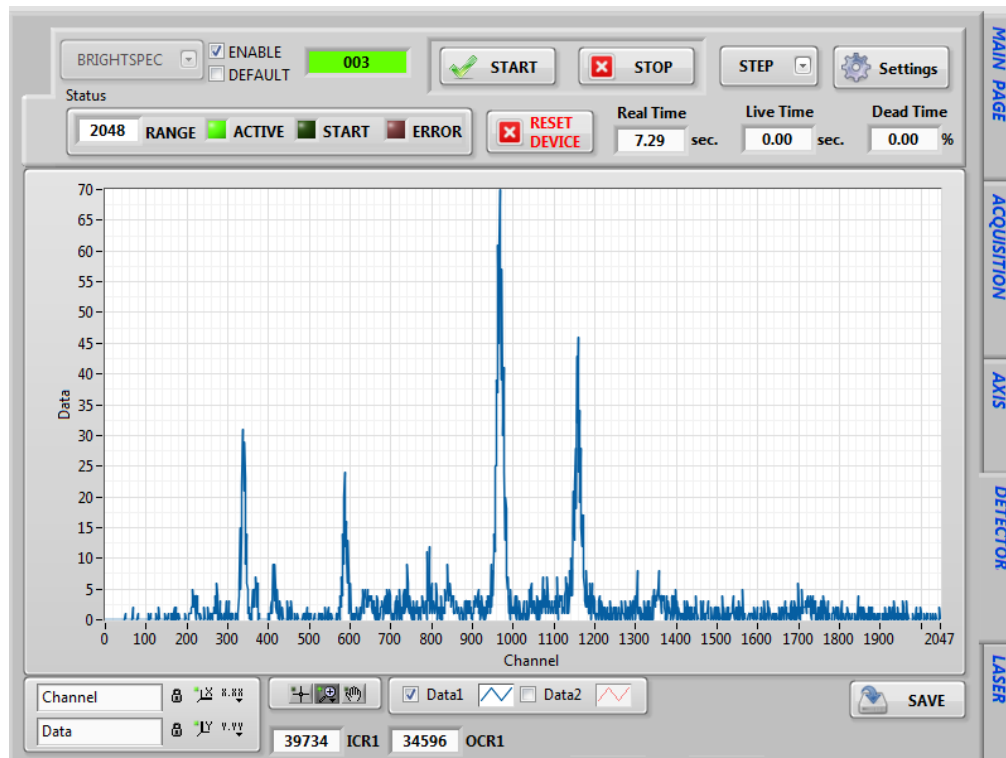
Figure 37: *detector* sub-window of the graphic interface

3.3.2 Laser window

The "laser" panel (see Figure 38) allows the operating parameters selection of the laser device for the focal position monitoring of the sample during the scan. The distance object-sample is continuously displayed on the same panel. The laser system can operate in two different mode: *Autorange* and *Safe distance*.

The *Autorange* operating mode requires the use of the auxiliary motorized axis (Z axis) for displacing the sample along the focal plane, and the selection of the following operating settings:

i. *Focus distance,* i.e. the spectrometer-sample distance to be maintained constant during the scan;

ii. *Dead band,* i.e. the tolerance distance within which the correction is not operated, in manner to avoid not-significant corrections as that occurred in presence of small protrusions of decorative layers in the painting. Usually a dead band of 0.5 mm is selected for measurements;

iii. *Velocity,* i.e. the correction speed chosen based on scanning speed;

iv. *Warning Stop distance,* that, if overcame generates the interruption of the movement of the axes via Control Unit in order to preserve artworks from any damage.

The *Safe distance* operating mode is usually executed for MA-XRF measurements; in this second configuration the (i) Focus distance works as Safety distance (Warning

Stop distance), while the parameters: Dead band and Velocity are disabled because system is using Z axis for dynamical correctional the position.
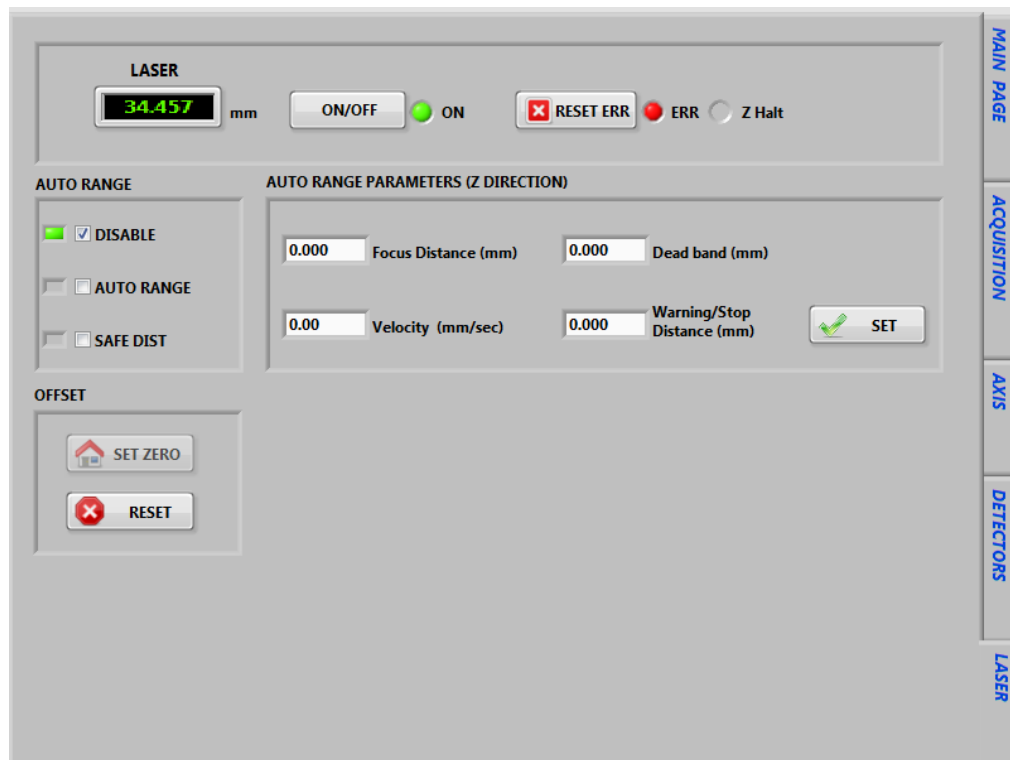
Figure 38: *laser* sub-window of the graphical interface.

3.3.3 Axis window

The "Axis" panel (see Figure 39) allows to control the axes movement, via absolute and relative displacement (up-down and right-left) to the desired position at several speeds up to 100 mm /sec and with 1 μm accuracy. The absolute position of the axes is continuously displayed on the same panel during acquisition.
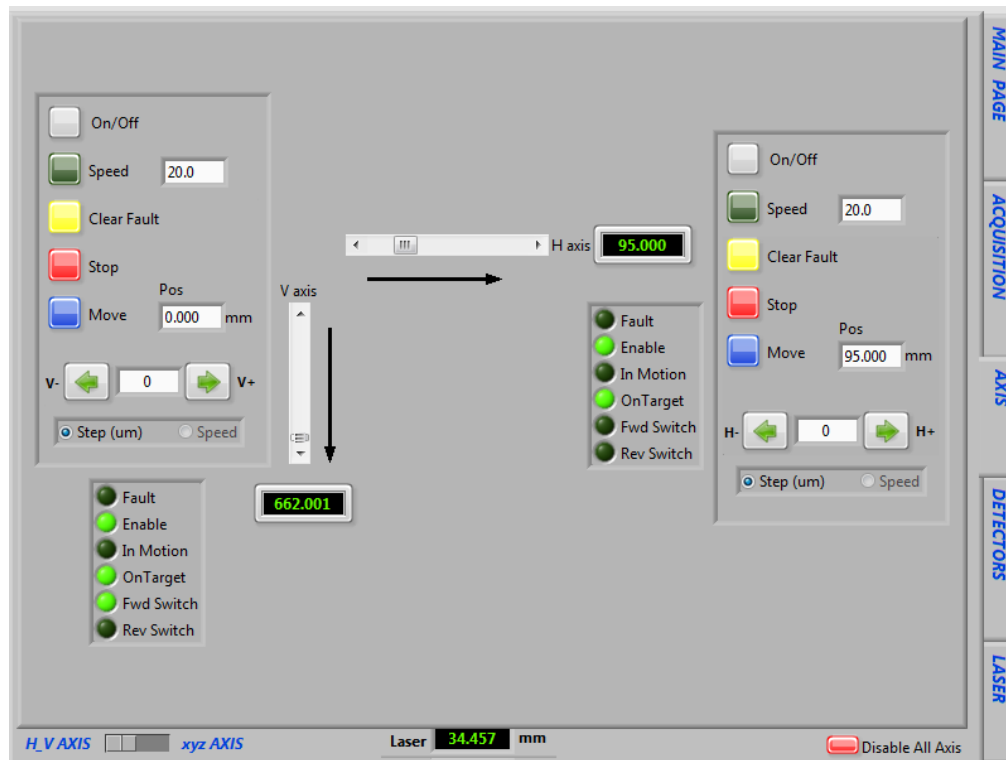
Figure 39: *axis* sub-window of the graphical interface.

3.3.4 Acquisition window

The scanning mode (continuous or step mode) and scanning parameters (scanning speed, step size, number of pixels) can be selected via "Acquisition" panel (see Figure 40) and soon after the start of acquisition, the parameters selection is saved a summary file created in the same folder containing raw data. During the scan, from the Acquisition window all scan parameters can be monitored, in particular the scan status by progressing a percentage bar, the absolute position of the axes, the spectrum and collected events and the spectrometer-sample distance.

The acquisition can be momentarily arrested via pause command and recovered from the end position, without setting the scanning parameters again. In addition, MA-XRF acquisitions done on two (or more) adjacent areas can be acquired in a single dataset, by selecting before to acquire the new area, the same directory where previous data have been saved, thus new data will be named in progressive succession. In this way, the two datasets will be worth concatenated in a single acquisition and they can be analysed as a unique map without resorting to the mosaic assembling.
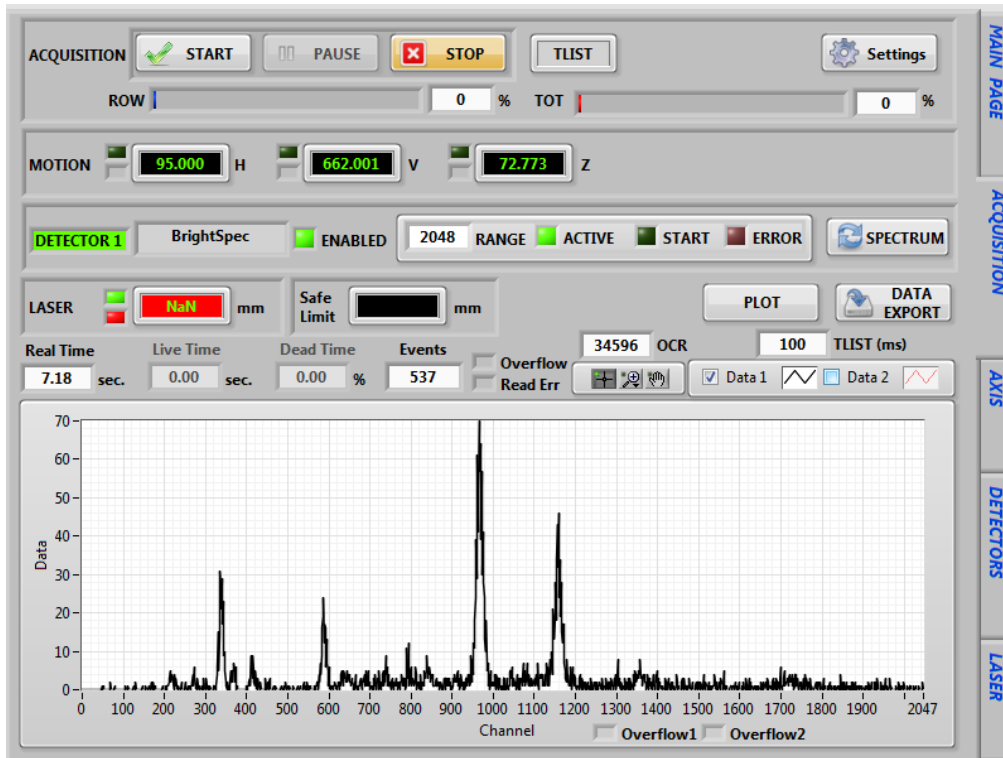
Figure 40: *acquisition* sub-window of the graphical interface.

3.4. Figures of merit

The MA-XRF system has been characterized by determining the Limit of detection (LOD) and chemical sensitivity (Y). This figure of merit (FoM) has been experimentally determined by using the 611 Standard Reference Material (SRM) by the National Institute of Standards and Technology (NIST). The reference sample is a 1 mm thick glass matrix (with nominal composition of 72% SiO_2, 14% Na_2O, 12% CaO and 2% Al_2O_3) containing 24 elements with a nominal concentration (mass fraction) in the range of 100 mg/kg (100 ppm) to 500 mg/kg (500 ppm). The standard contains also additional elements for which concentration values are not assigned [212].

It should be noted that FoM is not evaluated in absolute way but it is relative to the matrix of the reference standard. In addition, effects of self-absorption in the material is not taken in account. An absolute determination of chemical sensitivity and detection limits is in general more complicated and it would require an accurate definition of the all self-absorption effects and the knowledge of penetration depth of primary beam.

Measurements on the SRM 611 have been perform for 100 s real-time with the X-ray source operated at 50 kV and 0.6 mA. The standard has been positioned in the focus of the lens at about 10 mm. Acquisition were performed with peaking time and flat top at 1.5 μs and 0.2 μs respectively, taken as default parameter for the scanner.

Chemical sensitivity (Y) and Limits of detection (LOD) have been measured by means the following equations 59 and 60:

$$Y = \frac{N_{signal}}{c_i \cdot t} \qquad\qquad 59$$

$$LOD = 3 \times \frac{\sqrt{N_{back}}}{N_{signal}} \times c_i \cdot t \qquad\qquad 60$$

where N_{signal} is the net intensity peak of the i-element and N_{back} is the intensity of the background below the peak considered, c_i is the mass fraction of element i in the standard and t the acquisition time of the measurement. Figure 41 shows the measured K-lines sensitivity expressed in in counts per second (cps).

Chemical sensitivity results more than 100 cps for elements ranged between K (Z=19) and Mn (Z= 25). It increases for heavier elements, at values larger than 1000 cps.

The scanner is less sensitive to elements heavier than Rh, as Cd (Z = 48), Sn (Z = 50) and Sb (Z = 51). The sensitivity for these elements is about 100 cps\mg\g. This is due to the use of the polycapillary for focusing the beam, which has a lower transmission for the high energy components of the primary radiation. However, heavy elements (Z > 51) can also be detected by their L-lines.

Similar considerations can be done by observing the limit of detection plotted in Figure 42.

Limit of detection for elements ranged between K (Z=19) and Mn (Z= 25) is slightly higher than 100 ppm and it decreases below 100 ppm for the elements ranged between Fe (Z=26) and Sr (Z=38).
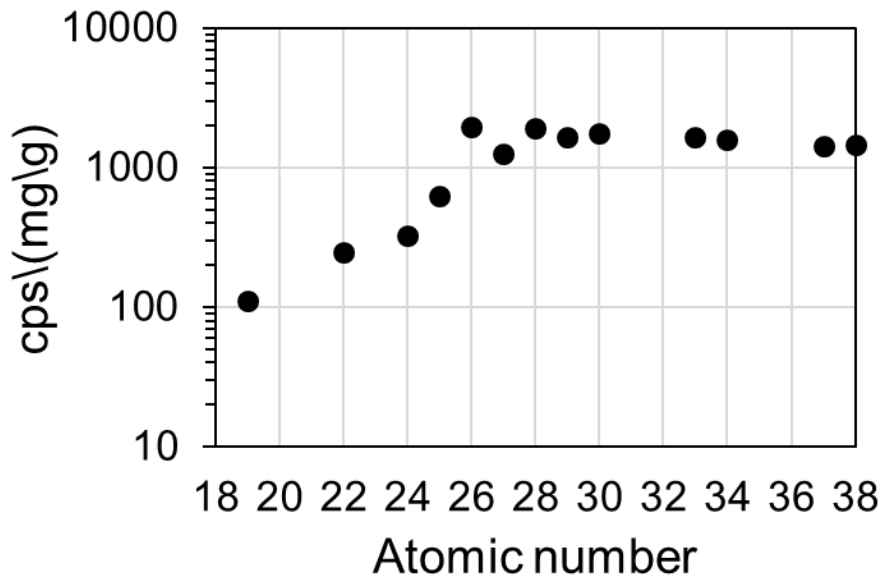
Figure 41: K-lines sensitivity for elements from K (Z = 19) to Sr (Z = 38).
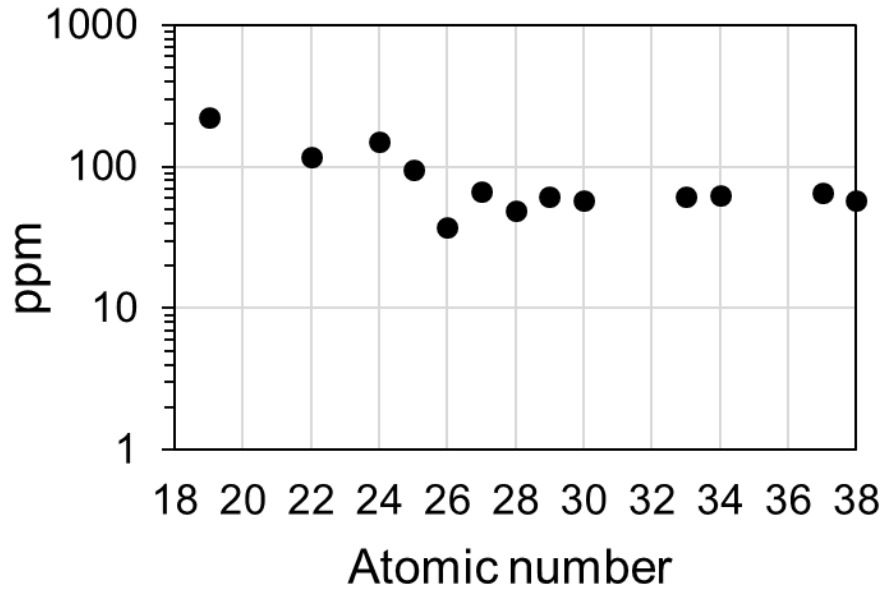
Figure 42: K-lines limit of detection for the elements from K (Z = 19) to Sr (Z = 38).

3.5. Beam-size measurement

The beam size has been determined experimentally as a function of the optic-sample distance. As described in previous sections, the XRF scanner has been developed in order to be used both for a microscopic XRF (µ-XRF) imaging investigation - which need a beam size of less than 50 µm - and for a macroscopic XRF (MA-XRF) scanning that is better performed with a beam in the submillimetre range (i.e., in the range 300-500 µm). This condition is easily obtained by taking advantage of the optic divergence by positioning the sample out of the focus.

Beam size σ corresponds to the diameter of the focal spot, where the intensity distribution reaches a 1/e value of its maximum. The spot size, in the hypothesis of a Gaussian distribution, can be converted to the full width half maximum with the following relation:

$$FWHM = 2\sqrt{2\ln(2)}\ \sigma = 2.3548\,\sigma \qquad\qquad 61$$

Full-Width-Half-Maximum (FWHM) has been calculated with knife-edge method [213] by using a Molybdenum foil with thickness of 25 µm placed on a Fe pure target. Figure 43 shows the optical microscope image of the sharp edge.
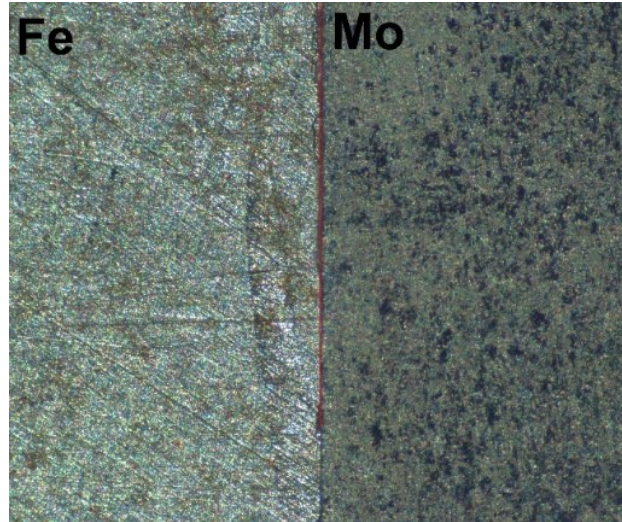
Figure 43: Fe-Mo knife edge at the microscope.

Knife-edge measurements consisted of a horizontal scanning (along the X-direction) of the Fe-Mo surface with a 5µm step size for a total of 1600 points (spectra), with a 0.5 sec dwell time and X-ray tube operated at 35 kV and 0.5 mA.

A fitting procedure has been applied to the spectra for obtaining net counts for Mo-Kα and Fe-Kα fluorescence peaks. The net counts, plotted as a function of longitudinal position, are distributed on a step function (or sigmoidal curve) and the Gaussian beam diameter has been calculated by means the first order derivative of the sigmoidal function. Figure 44 shows Mo-Kα counts in function of the longitudinal step acquired in the minimum beam size position, in red the sigmoidal fit curve and in blue the Gaussian function found by means first derivative calculation.
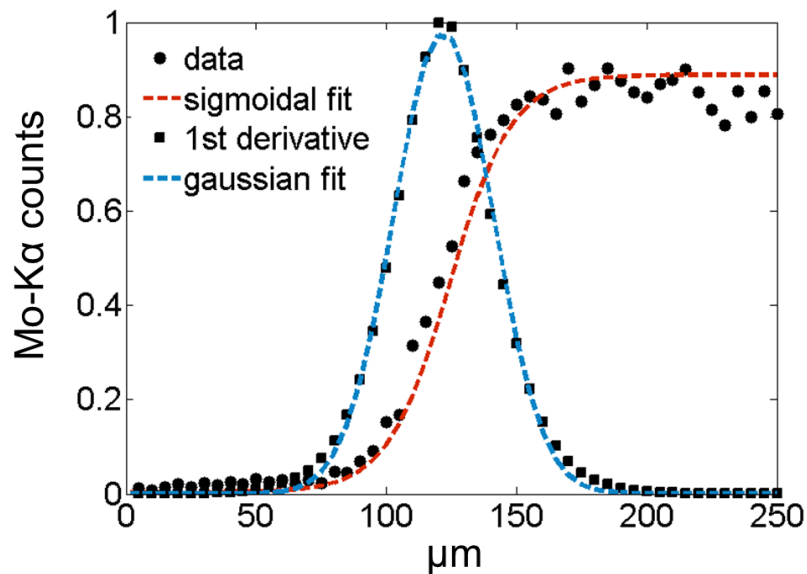
Figure 44: Mo-Kα counts versus horizontal position (x-direction).

Horizontal linear scansions have been repeated by moving sample along the Z direction with a step of 100 μm. Minimum value of beam size is of 38 μm for Mo- Kα-line energy and 73 μm for Fe-Kα-line energy, when sample is placed at about 10 mm from the lens. Furthermore, the distance interval where to perform MA-XRF analysis ranges from 12 mm to 13.5 mm (corresponding to 300 -500 μm beam size) from the lens exit. Plots in Figure 45 reports beam size values obtained as function of lens end distance.
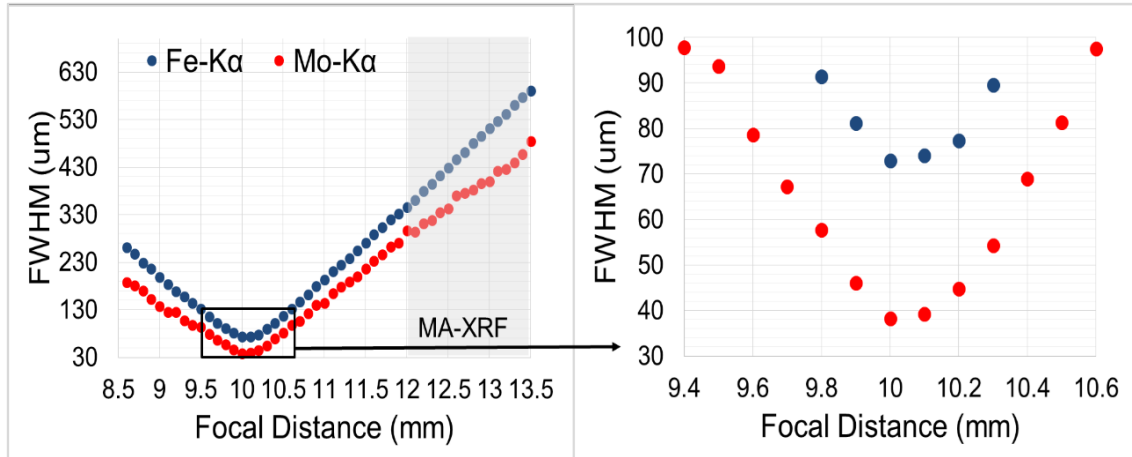
Figure 45: beam sizes along z- direction determined for Fe-Kα-line and Mo-Kα-line energy.

3.6. Lateral resolution

The lateral resolution represents a physical quantity likewise important for imaging technique and it is determined not only from the beam size but also from the step size and the accumulated intensity per pixel. In order to improve the spatial resolution the step size can be reduced to a quarter or to a fifth of the beam size [214].

However this is recommended only if an increasing intensity per pixel is guaranteed, differently this measuring procedure can be not convenient due to the significant time consuming for the acquisition and for a very large number of the spectra to be analysed.

The lateral resolution for the scanning MA-XRF has been experimentally determined using a resolution test target named USAF-1951 (by Newport) made of a glass substrate covered by a chrome coating. [215].

USAF-1951 test target is a pattern composed by reference lines with well-defined spacing. The lines groups are repeated with dimensions from big to small in the range from 1 mm to 4 μm. The lateral resolution has been calculated by a step-by step mapping of the central area of the target where higher resolution power are needed for resolving the pattern. The map has been performed on an area of 500 × 500 pixels at 10 μm step, with a pixel dwell time of 0.3 sec and X-ray tube operated at 36 kV and 0.35 mA.

Cr-Kα map, in Figure 46, shows that the resolving power of instrument allows to distinguish lines up to the element number 3 of group 6, thus defining a lateral resolution of about 35 μm obtained by applying the following equation [216]:

85

$$\frac{\text{Space width}}{\text{Line}} \text{ (mm)} = \frac{1}{2LP} = \frac{1}{28,5} = 0.035 \text{ mm} = 35 \text{ um} \qquad 62$$

where Line Pairs per millimetre is 14.25 for the element number 3 of the group 6.
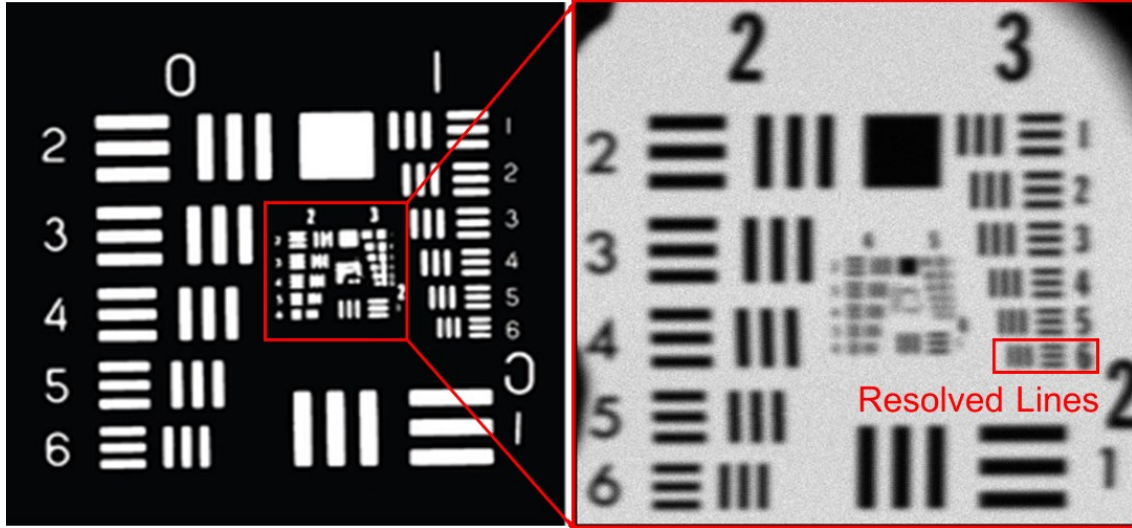
Figure 46: Cr- Kα map of the USAF1951 resolution test target.

3.7. MA-XRF system scanning speed performances

In several scanners developed over the time, the scanning speed was not as much limited by the statistics of the data acquired, but by synchronization of motorized stages and detector. In the scanning system described in this work a scanning speed up to 100 mm/sec can be reached by coupling of a 100 MHz DXP processor for events collection and a cRIO system based on Linux real-time operating system.

In this section the comparison between maps acquired at different scanning speeds, are showed; for testing the instrument performances has been used a modern oil painting of 47×38 cm^2 dimensions. The total time employed for mapping was of 10 hours, 4 hours, 2 hours and 1 hours for the different scanning speeds, respectively of 10 mm/sec, 25 mm/sec, 50 mm/sec and 100 mm/sec; the scans were performed in continuous acquisition mode, with the X-ray tube operated at 35 kV voltage and 0.4 mA current.

Figure 48 shows Ti-K and Se-K distribution images at different scanning speed; the two elements are present with different concentration in the painted layer. The comparison between the sum spectra calculated on the entire scan and showed in Figure 47, highlights their relative abundance in term of counts. Titanium white is a high-concentration element uniformly distributed in the painted surface, contrarily selenium is concentrated in some small areas and used in correlation with cadmium in form of cadmium orange pigment used for colouring orange/red tones [217].
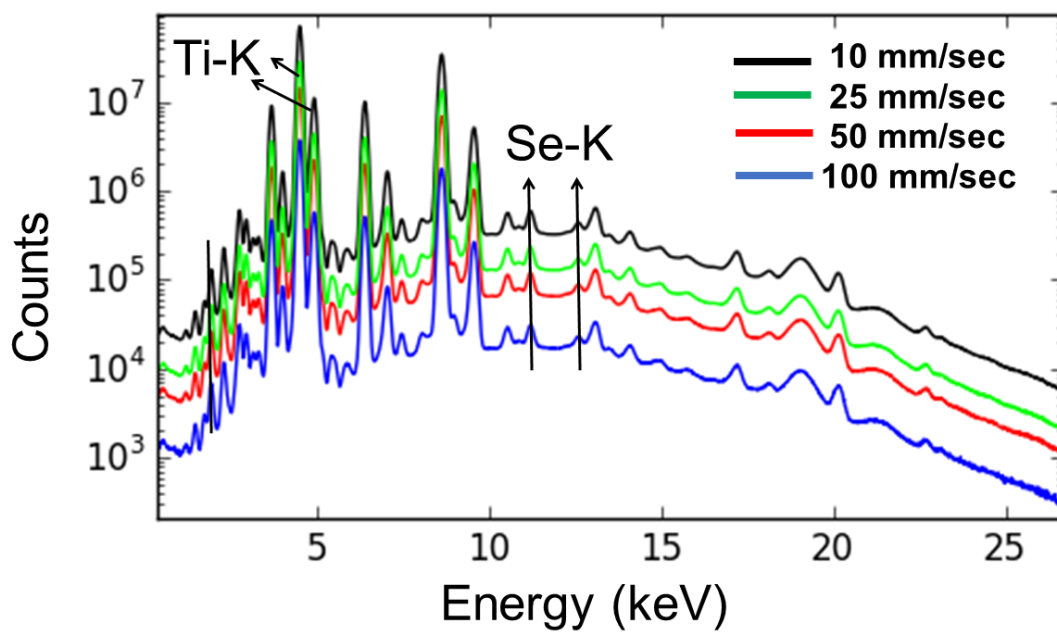
Figure 47: sum spectra comparison.
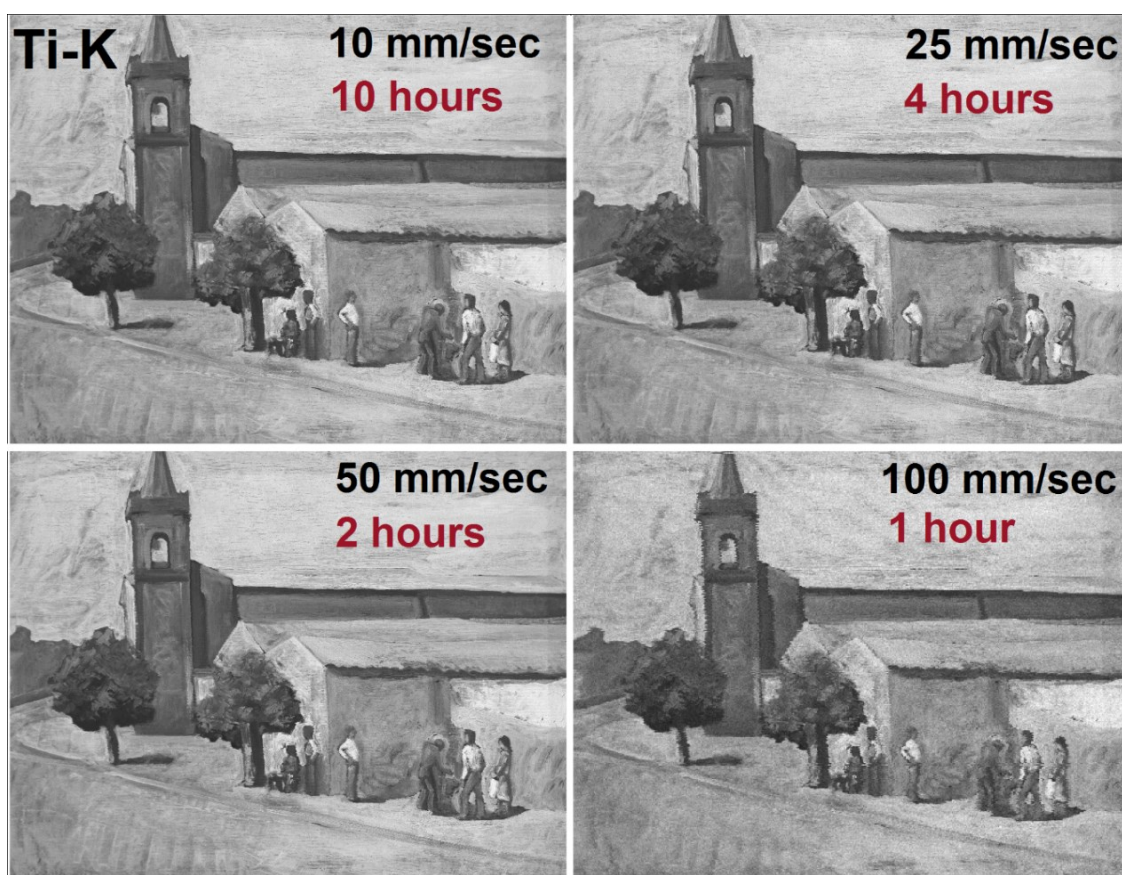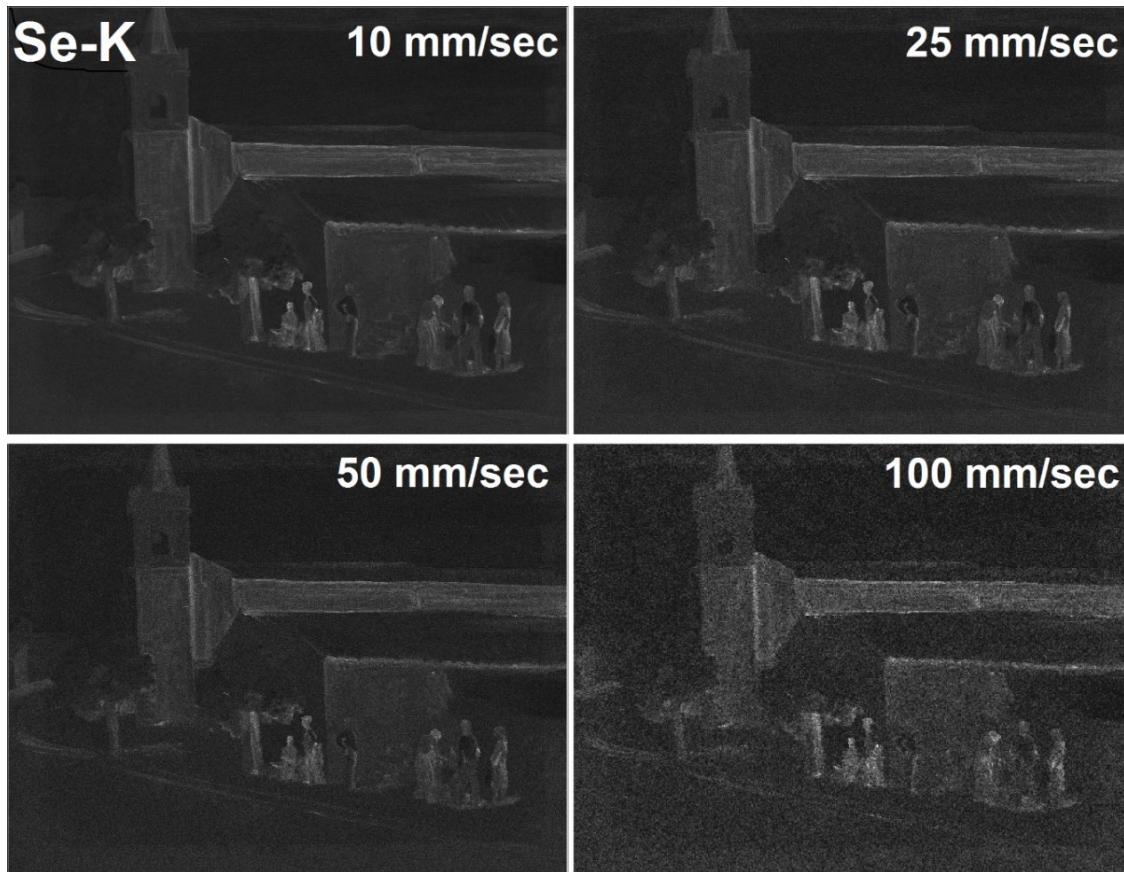
Figure 48: Ti-K and Se-K images acquired at different scanning speeds

3.8. Step mode and continuous mapping

The scanner operates two different scanning modes: *step* and *continuous* or *time-list* mode. A conventional step-by-step measurement is based on acquisition of a set of pixel-spectra with a selected dwell time for pixel. The pixel-spectrum acquisition is repeated on sample surface covering a pixels matrix (n × m) equally spaced of a precise step. The total acquisition time is given by: dwell time on each pixel, shifting time between two consecutive pixels, and dead time of each pixel-spectrum, all multiplied for the pixels number.

A step mode acquisition provides elemental images with an *a-priori* fixed lateral resolution. Indeed, the pixel size defined by beam size, the map graininess regulated by step size and the map contrast (i.e. pixel intensity) defined by dwell time, are chosen before to start the scan and their selection set the imaging resolution.

Usually, the step size selection is subordinated to the beam size. If the scan is performed with a selected beam size larger than the pixel size, this acquisition occurs in *oversampling* mode, differently is named *undersampling*. The oversampling acquisition mode leads to a more blurred image, while the undersampling gives more sharp images. However, commonly the oversampling is preferred for reasons due to time restriction or when the

surface of the sample is very large. In this case the blurring effects become neglectable. Acquisition with a larger number of pixels, as in the case of undersampling, requires not only an increase of acquisition time, but also an additional time for data processing.

In the conventional step-by-step acquisition, the DXP collects the incident events distribution forming a histogram (spectrum) containing the number of events that occur within each data channel (or energy range). Differently, in continuous or time-list-mode (TLIST), DXP records events including not only the pulse height information (energy), but as well the event arrival time with a time resolution of 40 ns.

Although the time list mode requires more computational power to process data in comparison to conventional step mode, it has several advantages such as higher temporal resolution and higher flexibility of data manipulation. Data acquired in TLIST mode can be packed with any time interval during or post the scanning. The selected time interval for the modelling of spectra define automatically pixel size, being scanning speed constant.

The selection of a longer time interval corresponds to increase the pixels size, useful for increasing counts statistic of the single pixel, or vice versa the pixel size can be reduced for a better quality of maps. In this manner, in a continuous scanning the unique fixed parameter is the scanning speed that determines the lateral resolution only in terms of contrast (or counts statistic).

The time-list mode allows to perform real-time scanning where the total time strictly coincides with the scanning rapidity of acquisition of the single lines.

The continuous stream of data is transferred to the Control Unit (CU) with a preset time interval (usually 100 ms), however in case of data overflow occurring at the higher count rates, the CU automatically stops the scanning and dynamically adjusts the data transfer time in order to eliminate the acquisition error. Scanning is automatically restarted at the beginning of the row where the data overflow occurred so to avoid any loss of data.

Figure 50 shows the comparison between imaging performed in step-by-step mode and in time-list at different speeds using a copper target (200 µm thickness) having six circular apertures of 50 µm diameter and each other equally spaced of 100 µm centre to centre (by Comar Optics). Measurements have performed covering an area of 600×600 µm^2 with a fixed pixel size of 10 µm also for time-list acquisitions. X-ray tube was operated at 30 kV and 0.1 mA. The other scanning parameters and acquisition times are following listed:

a) Step mode, step size 10 µm, dwell time 500 ms, 0.76 h total acquisition time;
b) TLIST mode, speed 0.01 mm/sec (10 µm/sec), 1 h total acquisition time;
c) TLIST mode, speed 0.02 mm/sec (20 µm/sec), 0.5 h total acquisition time;
d) TLIST mode, speed 0.04 mm/sec (40 µm/sec), 0.23 h total acquisition time.

The comparison between the Cu-K images shows how the transition from the step mode acquisition to a continuous acquisition does not imply the loss of information in terms of lateral resolution; however, it offers the advantage to make the mapping in a shorter time. In terms of contrast, or intensity for pixels, a lower scanning speed allows to obtain a better signal/background ratio, as it can be seen in Figure 51, where the sum spectra comparison is shown.
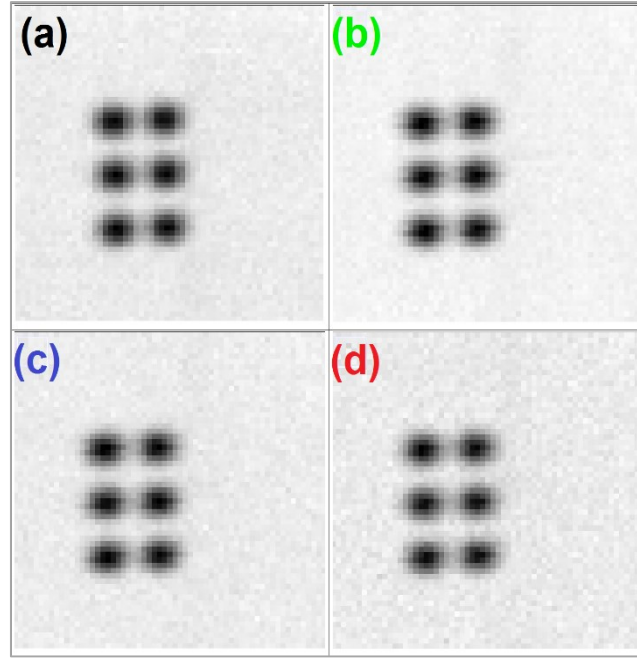
Figure 49: Cu-K maps of a copper target performed in step mode (a) and continuous mode at different scanning speed: 10 µm/sec (b), 20 µm/sec (c) and 40 µm/sec (d).

A direct comparison between measurement performed in step mode (a) and map obtained in continuous mode (c) can be made because both present a comparable count statistics (see spectra drawn in blue and black in Figure 51). However, the two acquisitions differ in the total time with a reduction factor of 1.5 for the continuous scanning respect to the step scanning.
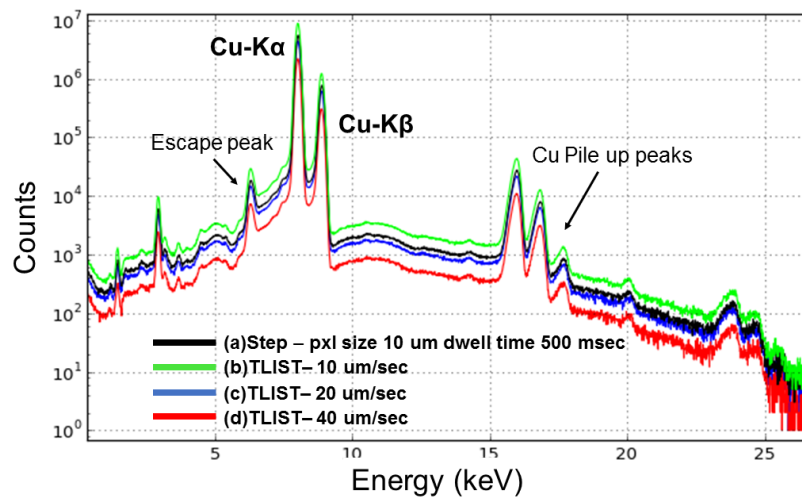
Figure 50: cumulative spectra comparison

3.9. Spectra analysis

MA-XRF measurement allows simultaneous mapping of chemical elements in a same scan. The creation of each map takes place through the separation of the fluorescence lines from the other components of the pixel spectra.

Usually, spectra fitting procedure is applied off-line, as a home task, to be performed at the end of in-situ campaigns. This is due to the huge processing resources, usually necessary for a simultaneous real-time control of scanner sensors, the data transfer and the application of a suitable fitting procedure.

Real-time analysis allows to have elemental images available when the acquisition ends, this implicates a significant gain in terms of time, allowing an immediate preliminary interpretation of data to be discussed with conservators and art historians for establishing the appropriate measurement strategy to be adopted. Real-time analysis gives the possibility of monitoring the right progress of the scan, particularly suitable when in-situ measurements are performed and the possibility to repeat analysis is often limited.

In recent scanning systems the real-time analysis (if present) is based on the selection of region of interest (ROI) of the spectra.

The MA-XRF scanner of the present research work performs the X-ray fluorescence lines separation through a fitting procedure developed for PyMCA and integrated on the system [218]. The fitting procedure applied to spectrum is based on the non-linear least-squares method discussed in next section and description of the functionalities of the in-house developed analysis software will follow after.

3.9.1 Spectrum evaluation

XRF spectra consist of overlapping fluorescence lines of the elements present in the sample and of the spectral background due to the scattering of the primary radiation and the incomplete charge collection in the detector, as it shown in Figure 51. Thus, if the escape and sum peaks (see section 2.6.1, Chapter 2) are neglected and the spectral background is assumed to be of constant shape, a spectrum S can be described by a function y_i in channel i as in equation 63:

$$y_i = c_0 B_i + \sum_{k=1}^{k} c_k\, x_{i,k}(a_{0,}, a_1,\ a_2, \dots a_m) \qquad 63$$

where B is the spectral background, k the peak profiles and x represent appropriately grouped transitions in the excited atom. Their shape is dependent on the non-linear variables a that contains the energy calibration and resolution of the detector and other characteristics of the spectrometer. The peak intensity is expressed in the linear factor c. In elemental distribution images the colour intensity of a pixel is directly correlated to this factor.
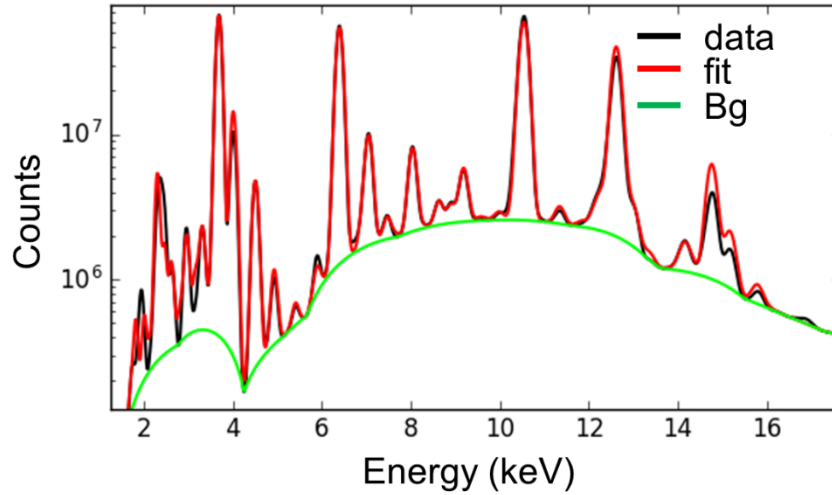
Figure 51: XRF spectrum fast fitting performed using PyMca software

In order to discriminate the overlapping fluorescence peaks and to derive the area of each peak, the individual components are modelled using mathematical functions, based to the knowledge of the fundamental parameters theory [219, 220, 221, 222, 221, 137].

Fitting a mathematical function to n experimental data (x_i, y_i) consists in determining the optimum set of m parameters $(a = a_0, a_1, a_2, ... a_m)$ such that the computed values with function $f(x_i, a)$ will be a close as possible to the experimental values y_i .The different parameters of the fitting function are obtained by the *non-linear least-squares method* (NL-LS) the same approach is followed for processing XRF spectra [223] [224].

Generally, if Φ is the function to minimize:

$$\Phi = \sum_{i=0}^{n} \left(\frac{f(x_i; a) - y_i}{\sigma_i} \right)^2 \qquad\qquad 64$$

Where σ_i is the standard deviation of experimental value y_i. The parameters values are obtained by minimization of Φ, i.e. by cancelling out the values of its partial derivatives:

$$\frac{\partial \Phi}{\partial a_j} = 0 \qquad\qquad 65$$

In the fast linear fitting procedure used in the MA-XRF this minimization is performed by using the *Marquardt-Levenberg* algorithm [225, 226]. This is based on two different approaches as fitting progresses: far from the minimum, the gradient method is first used, then, when near the minimum, it is replaced by the *Hessian* method [227].

In both cases, solving the equation system requires computation of the first derivative for each of m parameters. Uncertainties (variances) associated to each parameter are calculated during the fitting procedures, as well as covariances of the different parameters.

A complete description of the algorithms and the theoretical databases on which is built the fitting procedure can found in references [218-222, 224].

3.9.2 Peak shape model

The response function of most solid-state detectors is predominantly Gaussian, thus common kinds of spectra, gamma, alpha or X-rays are modelled on Gaussian function:

$$G(x) = \frac{A}{\sigma\sqrt{2\pi}} \cdot exp\left[-\frac{(x - x_0)^2}{2\sigma^2}\right]$$
66

A Gaussian peak is characterized by three parameters: the position x_0, amplitude A, and standard deviation σ. It is preferable to describe the peak in terms of its area rather than its height because the area is directly related to the number of X-ray photons detected, while the height depends on the spectrometer resolution. The peak area, in equation 66 is a linear parameter; the width and position are non-linear parameters. This implies non-linear least-squares procedure, described above, in order to find optimum values for the latter two parameters [224].

Instead of a Gaussian function, in certain instances it may be necessary to resort to more complicated models such as *Voigt or Hypermet functions*. In particular, this latter is used in the XRF spectra analysis of this work.

The *Hypermet fitting function* was first introduced by Philips and Marlow [223] and it consists in the sum of a Gaussian (see equation 66), a low-energy tail and a discontinuity centred on the peak position:

$$f_{\text{Hypermet}}(x) = G(x) + T(x) + S(x) = TG(x) + S(x)$$
67

The Gaussian tail $T(x)$ in equation 67 is modelled by an exponential function truncated at the peak position, convolved with a Gaussian representing the instrumental broadening. This shape can be used to take into account events due to incomplete charge collection in the detector [224].

$$T(x) = \int_{-\infty}^{x_0} A \cdot T(\tau \cdot x^{'}) \cdot exp\left[-\frac{\left(x^{'} - x_0\right)^2}{2\sigma^2}\right] dx^{'}$$
68

$T(x)$ function includes two more parameters to the Gaussian function $G(x)$: tail relative amplitude T and exponential slope τ.

The discontinuity $S(x)$ results from the convolution of a step function, with a constant value for $x \leq x_0$ and zero value for $x > x_0$, by the Gaussian instrumental broadening [224].

$$S(x) = \int_{-\infty}^{x_0} A \cdot S \cdot exp\left[-\frac{\left(x^{''} - x_0\right)^2}{2\sigma^2}\right] dx^{'}$$

The function $S(x)$ is entirely characterized by six parameters, the first five are the same as those of the Tailed Gaussian $TG(x)$ and the last one is S the step function relative amplitude.

3.9.3 Continuum/Background evaluation

The spectral background B can be modeled in two possible ways: estimation or fitting [228]. In the first, the estimated background is subtracted from the experimental data prior to the least-squares fitting of the fluorescence peaks. In the fitting mode the continuum is described by an analytical function which enters into the least squares fitting algorithm.
In both models, the background is evaluated through an iterative procedure in which the content of each channel i is compared against the average of the content of its neighbours, at a distance of w channels. If the content is above the average, it is replaced by the average, so that after several iterations, the peaks are eroded away (see equation 70).

$$y_i = \min\left[y_i, \frac{y_{i-w} + y_{i+w}}{2}\right]$$

70

For the XRF spectra analysis object of this work, due to the a large data sets collected in a MA-XRF scan, a faster processing of data, Statistical Non-linear Iterative Peak procedure (SNIP) is used in the fitting Background procedure [229, 230, 202]. SNIP allows to take i as a fraction of the peaks full-width-half-maximum (FWHM) at the beginning of the iterative process, reducing the unity at the end of it. Diversely, in the most simple case, named STRIP procedure, w is set to 1. STRIP procedure needs of several thousand iterations while less than 50 are necessary with SNIP procedure.

3.10. In-house programmed software

The in-house programmed analysis software on the CU runs during scan and allow a (near) real-time data transferring. This analysis software is supplied with an additional user-friendly interface structured in five control windows (sub-widgets), for images processing. Figure 53 shows the analysis software in execution during scanning for forming elemental images.
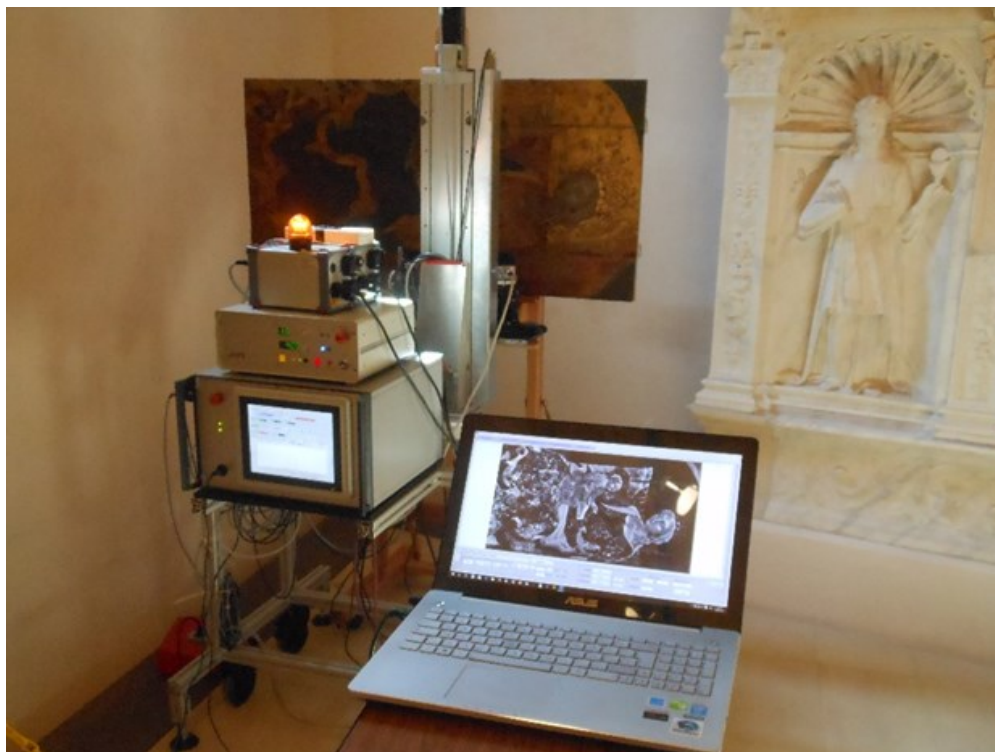
Figure 52: analysis software in running on a laptop connected to Control Unit.

A control panel allows to enable a new analysis: X-ray data, that are accumulating during acquisition, are read and analysed line-by-line. The software converts the raw-data format into EDF format (European synchrotron radiation facility Data Format) and a suitable fitting model is applied to the spectra, allowing the simultaneous creation of images. Fitting model, applied to data is configured using PyMca software [218] and it contains the selection of mathematical functions for peaks and background shapes, the experimental conditions (excitation type, detector specifications, measurement geometry), the energy calibration and the fluorescence peaks composing spectrum. Fitting procedure separates so the several spectrum components and gives as result the net area of each fluorescence peak.

In this way, the net counts image (of float image) is created line-by-line repeating the procedure, until the completion of the entire map, its running can be visualized in the same panel, as shown in Figure 54.

The analysis running speed is more than 5000 spectra/sec as maximum processing speed. Finally, as before mentioned, the pixel size of images can be changed during analysis using

the same control panel, if images are not satisfactory in terms of lateral resolution or counts statistic.
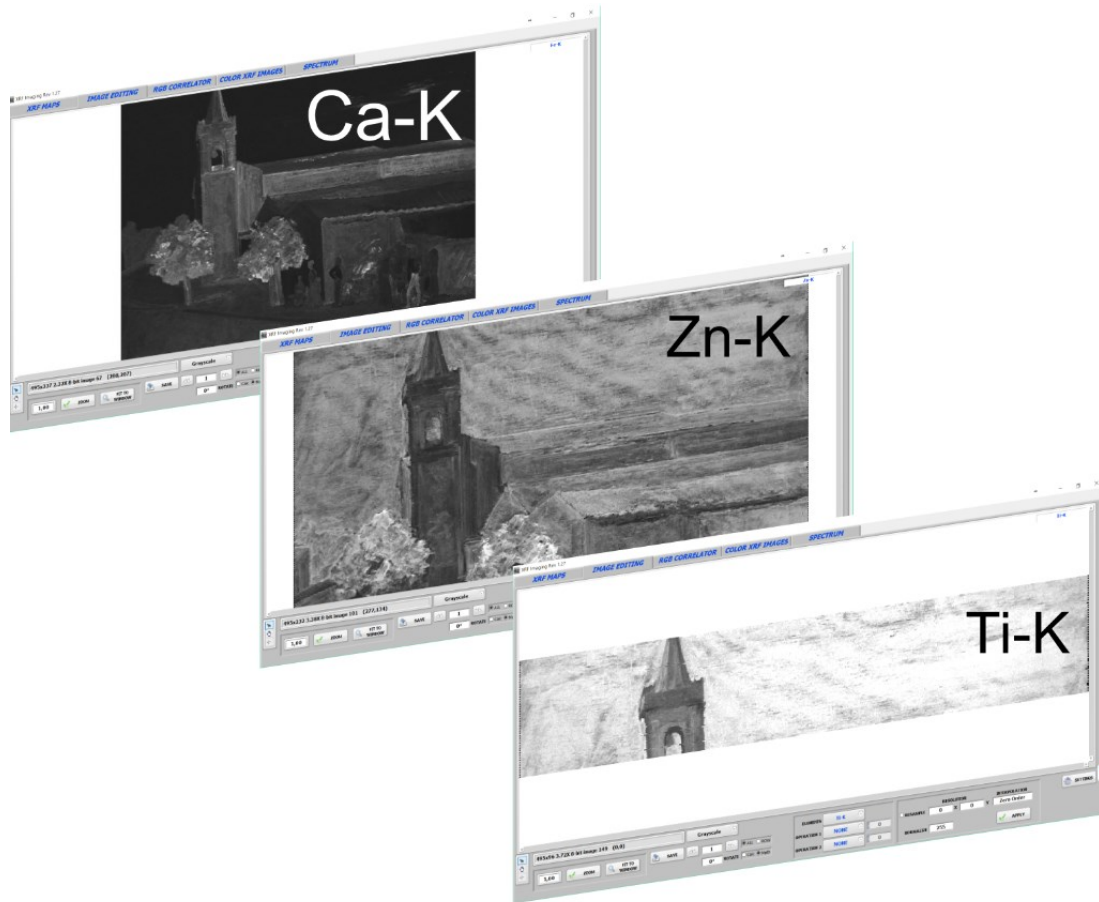
Figure 53:(near) real-time maps creation using in-house programmed analysis software.

Analysis software is also supplied with a second panel "image editing"*,* for the images elaboration. This control panel allows the image graphical processing during or at the end of imaging procedure. Intensity (or float) maps are converted in 0-255 range grayscale images, having the possibility to change graphical settings as colormap, contrast and brightness, resizing, etc.. In addition, arithmetic and logical operations can be applied to the images for subtracting noise or contaminations and also eventual systematic shift correction can be done, as is shown in Figure 55. However, shift pixel effect occurs especially when a fast acquisition is performed as result of a systematic errors between axes sensors and acquisition system [231].
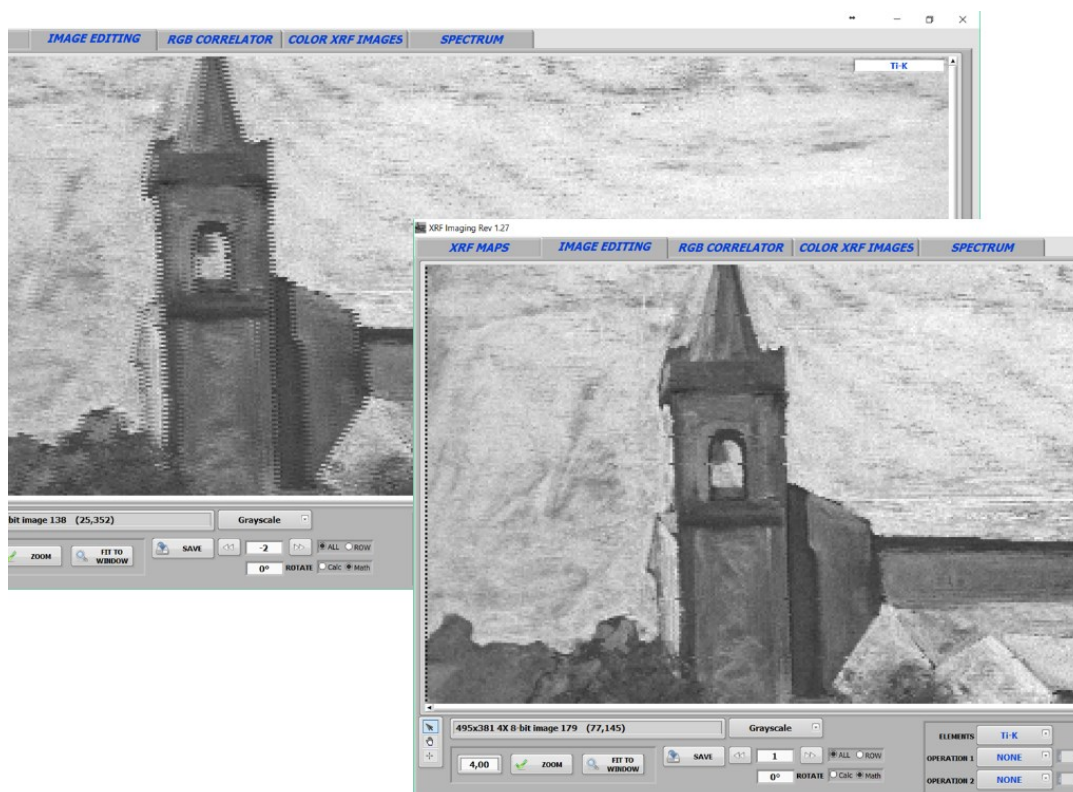
Figure 54: shift correction of images in live mode.

The correlation of several maps in a Red-Green-Blue (RGB) composite images highlights the presence of two or more chemical elements in the same area, as shown in Figure 56. In several cases, RGB maps correlation is a useful analysis tool for facilitating identification of pigments or canvas preparation. The analysis software allows to combine up to three maps in a single RGB image from the "RGB correlator" panel and up to nine maps using "Color XRF Image" panel.
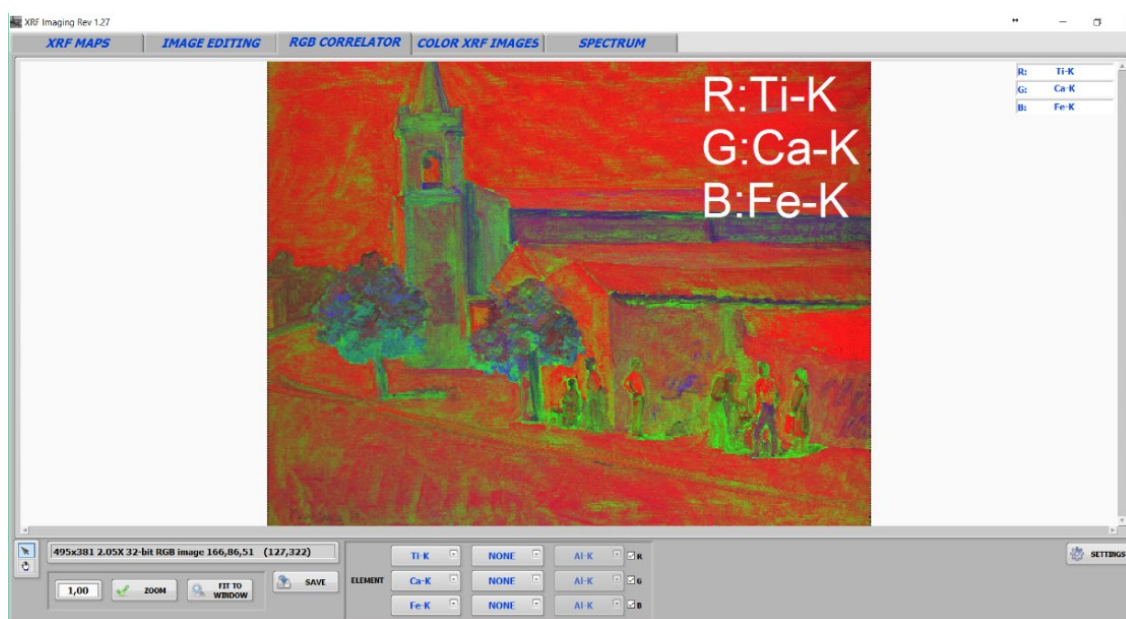
Figure 55: RGB composite image.

The last software panel: "spectrum", visualizes the sum spectrum in live mode. It is obtained as sum of pixel-spectra recorded on the entire scanning surface. In combination to the sum spectrum, in order to identify better the low concentration elements, spectrum of maxima is calculated as showed in Figure 57. In particular, spectrum of maxima is obtained by setting the value of each channel to the maximum value of this channel in the whole scan data. In this way, also elements distributed on few pixels emerge and can be clearly distinguished, generally they are not well visible in the sum spectrum, because covered from higher concentration elements.
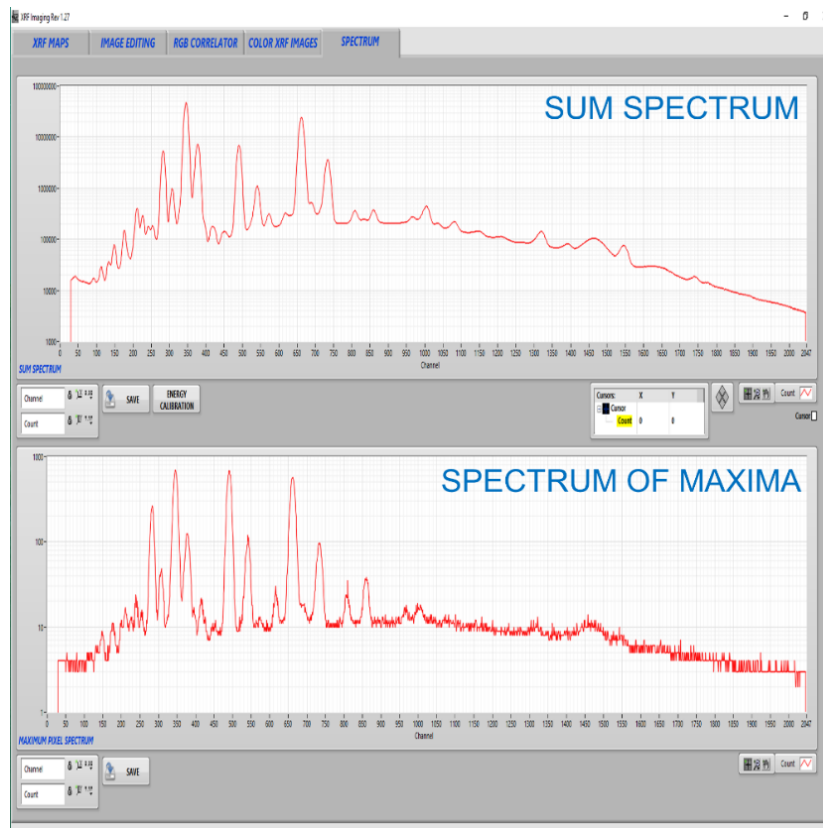
Figure 56: sum spectrum and spectrum of maxima calculated in live mode.

Analysis software allows to save spectra and images, including graphical changes and shift correction, in several graphical file format. For RGB images, the software automatically correlates the maps with all other. Finally, an *image.edf* file is created at the end of analysis, where all images are included, so maps are available for a further post-processing without the needs of a new fitting procedure of spectra.

Chapter 4

MA-XRF cases-study

The analytical capabilities of the scanner have been verified in a number of case-studies in collaboration with Museums and for which the device has been used in situ. This Chapter discusses MA-XRF technique applied for studying three different typologies of artworks: (1) the "Paston Treasure", a mid-1670s oil on canvas painting, allocated at the Norwich Castle Museum (UK); (2) a painted wooden coffers belonging to the funerary collection of the tomb of Kha and Merit (1549-1292 BC) at the Museo Egizio in Torino (Italy); (3) an illuminated manuscripts of Italian provenance, manufactured in the 14th century, belonging to the collection of the Fitzwilliam Museums (Cambridge). Experimental measurements and analytical results will be presented and discussed.

4.1. The Paston Treasure: origin and art history

The Paston Treasure is one of the most important artwork in the history of British Art. The painting in Figure 57 is an oil on canvas of 165 x 246.5 cm^2 dimensions; it belongs to the collection of Norwich Castle Museum and Art Gallery in Norwich (UK).

Figure 57: Paton Treasure, oil on canvas, 165 cm x 246.5 cm, Norwich Castle Museum.

The painting was commissioned by Sir Robert Paston in the mid-1670s and depicts objects from the family's collection. It is likely that the painting was made by a Dutch artist visiting Oxnead Hall, the Paston family home in Norfolk, because the painting fits into the tradition of Dutch and Flemish still life painting. The painted objects belong to the collection gathered by Robert and his father, Sir William Paston, during the long journeys through Europe, Cairo and Jerusalem. This collection consisted of over 200 objects and included many sculptures, gems, gold and silver artworks, enamels and natural history specimens. The collection was sold shortly after that the painting was finished due to the Paston failing and many of these objects were dispersed in museums around the world and private collections. Apart from its visual beauty and thematic complexity, its importance lies in the interest of the objects portrayed, reflecting both exotic nature and the skills of man of that period.

The painting contains many symbolic details with the intent to transmit the Paston family's learning and wealth and at the same time of revealing the meaning of the fragility of life.

The richness is represented through the gold objects and silverware; further, intricately made vessels were high fashion items. The young girl wears silk dress trimmed with gold raid and jewels. The young unknown man, is the earliest portrait of an African in Norfolk by almost 200 years. He is a slave and wears an exotic version of classical Roman dress. His silk tunic, pearls, emeralds, rubies and garnets, underlines the wealth of their 'owners'. Chinese porcelain and exotic pets, as well the ostrich eggs and shells emphasize the international connections of Pastons and their opening to the influence of the modern science emerging in that period.

However, the "death" is the central theme of the picture. The young girl in the central part of composition is Mary Paston, Robert and Rebecca Paston's younger daughter, prematurely died in 1676 of smallpox. She is holding roses, frail emblems of human life, and a songbook, on which the words are, scarcely legible, are referenced to death. The clock and the hourglass

are positioned close her figure together with the extinguished candle. The lute has a broken string, and the instruments lie unplayed, these symbolize the silence and the death. Probably, the painting was started and the Mary Paston death while it was being painted altered its artistic intent.

4.2. In situ non invasive MA-XRF investigation

The research activity for the investigation of the Paston Treasure was carried out in collaboration with the Fitzwilliam Museum (Cambridge, UK), the Yale Centre for British Art (USA) and the Norwich Castel Museum an Art Gallery (Norwich, UK). MA-XRF measurements were performed in situ and they employed five days in total.

In order to cover the entire 246 x 165 cm^2 surface of the painting, the full area has been analyzed in six sub macro areas. Continuous scans were performed along the X direction at a scanning speed of 50 mm/sec and with a fixed step-size of 500 µm along the Y direction. These parameters correspond to a dwell time per pixel of 10 ms. The bottom part of the painting was investigated at 100 mm/sec along X. The pixel size of the mapping for the bottom part was 500 µm (dwell time per pixel 5 ms).

The time for covering each top sub-part (100 x 67 cm^2) was about 7.5 hours; the analysis of the bottom part at 100 mm/sec was 4 times shorter. Figure 58 shows the mosaic of all sub-areas in a RGB composite image (R: Hg-L - G: Cu-K- B: Co-K) distinguishing between the upper and central part analyzed at 50 mm/sec scanning speed and the bottom part of painting investigated at 100 mm/sec:
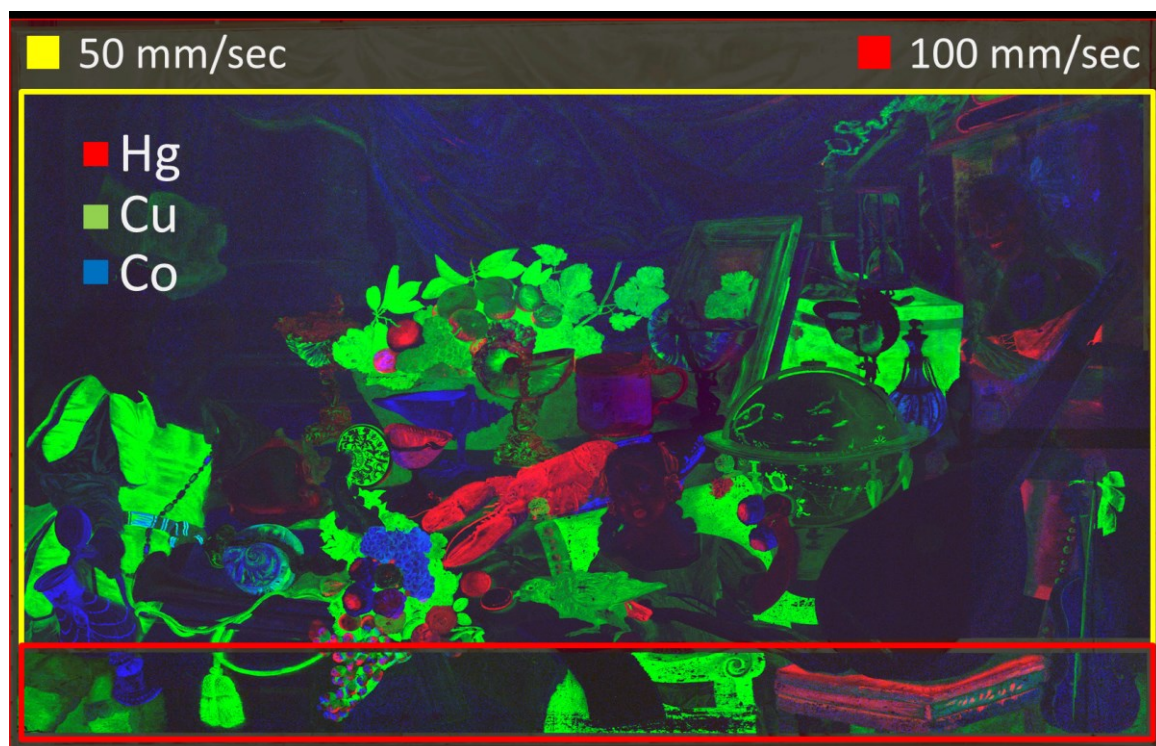
Figure 58: RGB composite image of the entire surface of painting subdivided in five sub-areas during the measurements.

The painting was positioned at a distance of about 1.5 cm from the spectrometer head, corresponding to a beam size of 500 μm. The high resolution images were elaborated in real-time by using the in-house programmed software described in Section 3.10, Chapter 3.

 The dynamic correction of the sample distance was not operated due the small curvature of the canvas. However, the laser system has been used during scan for controlling the preconfigured safe distance (0.8 cm) of the painting from the instrument. X-ray tube was operated at 35 kV and 0.35 mA. The detection system parameters were selected at 1.5 μs peaking time and 0.2 μs flat top, corresponding to an energy resolution of 160 eV. In Figure 59 is showed the MA-XRF scanner in execution.

Figure 59: MA-XRF measurement on the Paston Treasure.

Cumulative spectrum and the spectrum of maximum pixel, Figure 60 and Figure 61, show the main elements of the pigments palette of the artist, predominantly calcium (Ca), tin (Sn), iron (Fe), copper (Ca), lead (Pb), mercury (Hg) and arsenic (As) and cobalt (Co). The elemental distribution images obtained during the scanning of the painting are discussed in detail in the next paragraph.
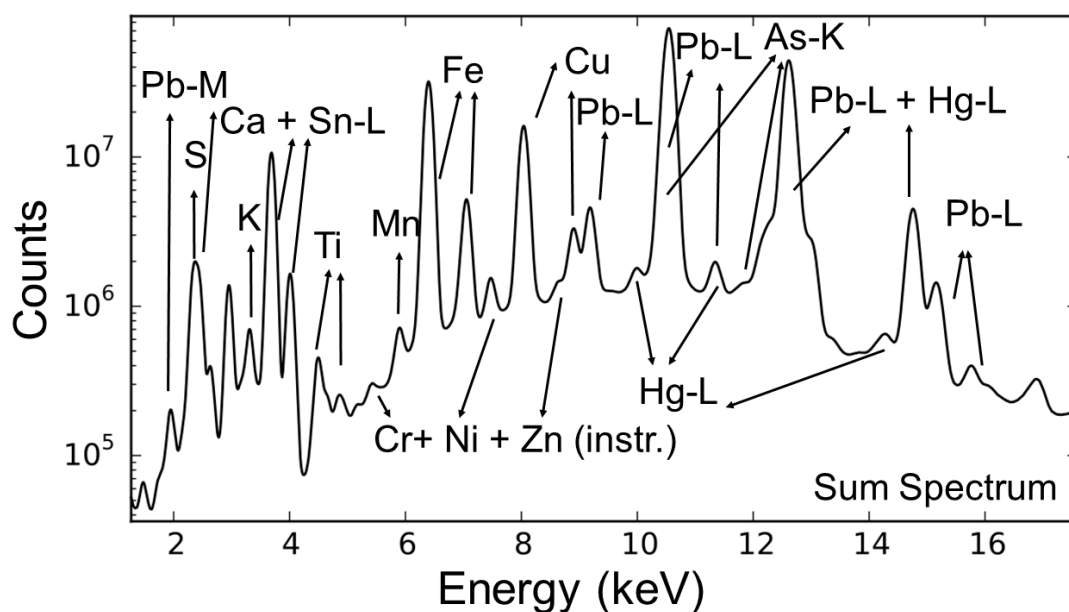
Figure 60: sum spectrum measured on the entire painted surface.
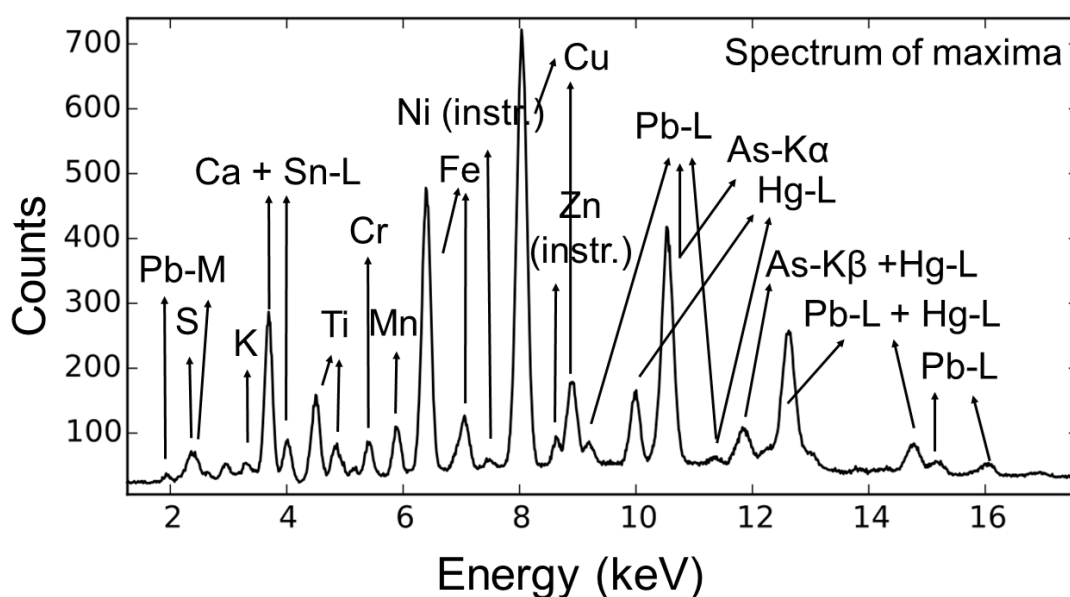
Figure 61: spectrum of maxima measured on the entire painted surface

4.2.1 Elemental distribution images

The elemental images highlight the chromatic complexity of the painting and the accurate research of the artist in the use of the pigments and in their mixture. The objects have been depicted with richness of particulars for reproducing their ornamental features and to confer as much possible their realistic aspect to the observer. The pigments have been combined for giving the light and shadow effects, the colour brilliance and a three-dimensional vision of the objects by means a meticulous creative process. Further, some colour shades that appear close optically reveal a different chemical nature underlining the artistic choices of

103

the painter in the creative development of the artwork. The main elemental images that characterized the artist palette are following reported.

4.2.2 Canvas preparation and white pigments

The uniform distribution of lead (Pb-L), showed in Figure 62, suggests that lead white $(2PbCO_3 \cdot Pb(OH)_2)$ was used as canvas ground [232-234].

In addition to this, the artist used a Pb-based pigments to paint as for example the monkey on the servant's shoulder (1), the big shell on his left (2), the skin tones of Mary Paston (Robert Paston's younger daughter) (3), the music book (4), the globe (5), and the inner part of the wall clock (6).

In these white painted areas, the major abundance of lead is not well contrasted in the map due to the presence of the same pigment used as ground and being the information of the MA-XRF scanning integrated long pictorial layers.

A similar analytical result was obtained for calcium providing as in the case of lead a white coloration. This aspect is more clearly visible in the composite image (Red: Pb-L - Blue: Ca-K) in Figure 63 , where the distribution in blue includes both the uniform ground layer as well as the white painted areas, as for example the numbered figures 1-6. The areas in magenta (Red + Blue = Ca-K + Pb-L) characterize the distribution of the calcium-based pigments applied on the ground of the canvas. Finally, the calcium-based pigments, commonly in the form of calcium oxide (CaO), calcium carbonate ($CaCO_3$) or gypsum ($CaSO_4 \, 2H_2O$), have been employed predominantly by the artist as whitening for creating the evident effect of light and shadows present in the composition, [235]. Figure 64 shows the grayscale Ca-K map.
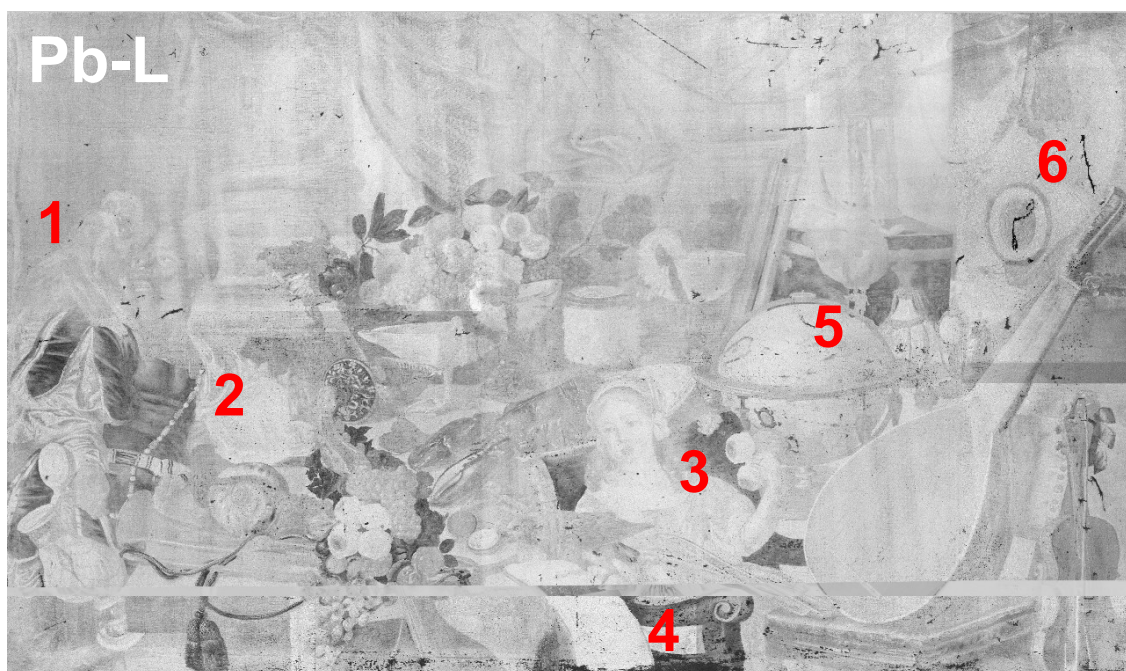
Figure 62: Pb-L image and some painting details where lead white was used (1-6).

Figure 63: Blue: Pb-L - Red: Ca-K composite image.

Figure 64: Ca-K distribution image.

4.2.3 Red pigments

The red pigments are characterized by the presence of mercury, identified in the use of cinnabar (HgS) (used from ancient time) or most probably in its artificial variety, the vermilion, produced in the 8th century and used until 19th century.

In the painting, the red vermilion was used both in the pure form, as for example for painting the food (oranges, lobster, grapes) (1) and also it was added to the lead white for conferring the rose-coloured shades as for the skin tones of the young girl (2). In addition, it was used with iron-based pigments for the warmest reddish-brown tones as for the chair on the right of painting (3) [236]. Figure 65 shows the Hg-L map and its correlation with lead white (Red: Hg-L, Blue: Pb-L) and iron (Red: Hg-L, Blue: Fe-K) in the composite images related to the area 2 and 3 of the painting.

However, some regions interested by the vermillion presence appear faded, deprived of its intense red natural colour. This is due to a greying effect corresponding to a degradation process. Despite, the vermillion is largely a permanent pigment, in the presence of hydrogen sulphides and sun light it reacts chemically and it converts into mercury chloride products. They form a thin superficial grey\black patina and sometimes physical degradation may take place as result of breakdown of the binding medium [237-240].
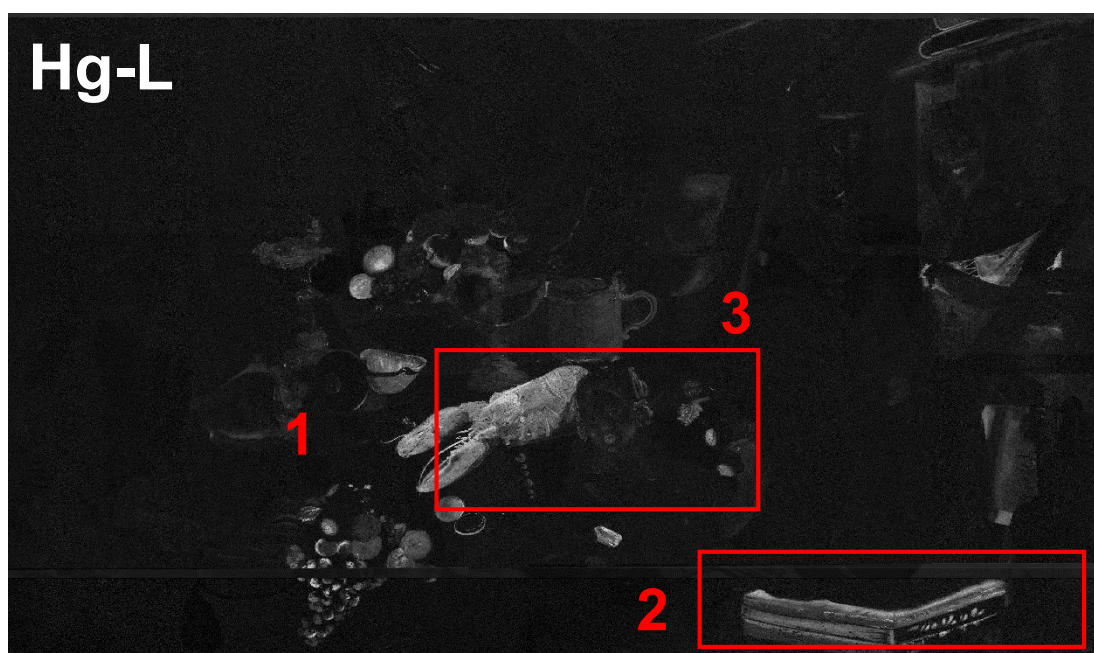
Figure 65: Hg-L image and composite images: (2) Red: Hg-L - Blue: Pb-L, (3) Red: Hg-L - Blue: Fe-K.

4.2.4 Green and Blue pigments

Copper distribution, showed in Figure 66 (Cu-K), characterizes the blue and green pigments, which can be either natural as malachite ($Cu_2CO_3OH_2$), used until 16th century, and azurite ($Cu_3(CO_3)_2(OH)_2$), used until 18th century, or their synthetic equivalents green or blue verditer [241]. Beyond that, copper can be present in the green pigment verdigris, consisting of copper corrosion products, mainly acetates, used until 19th century [242], and copper resinate ($Cu(C_{19}H_{29}COO)_2$), used from 15th century until 17th century [243]. However, a distinction between the different copper-based pigments by XRF alone is not possible, but addition information can be obtained by means of molecular spectroscopy. Copper based pigments were used to paint several figures as for example the foliage of fruits (1), the servant's Roman-style dress on the left part of painting (2), the chair where the girl is seated, the parrot (3), the trumpet rope (4), the trunk on which are placed the hourglass and the candle (5) and some other details. All copper-based pigments are subject to oxidation processes by sunlight or by atmospheric conditions. They change in black or brownish by exposure to hydrogen sulfide present in polluted air [244, 245]. In the case of azurite, it can change from blue into green caused by an increased oxidation or into black due to the copper content oxidation [246]. Originally, the artist painted the image of foliage reflected in the mirror on the background of the composition (1), it appears visible, only, in the copper distribution image (see detailed Figure 66- 4), caused by oxidation that made it completely black.

Figure 66: Cu-K image and some painting details where copper was used (1-4).

4.2.5 Brown pigments and ochres

Brown colours and the warm red and yellow tones are based on natural earth pigments containing iron minerals (hydroxide and oxide), as showed in Figure 67 [247, 248].
Red ochres were used to paint the curtain on the background (1), the borders of the dress of the servant, the chair where the lute is placed. Darker tones tending to brown are used for the servant's skin tone (2) and for the violin on the right (3), also for drawing the musical instrument, partially visible in the center of the composition. Yellow ochres with orange tonality have been used for painting the large table where the objects are collected, the hair of the girl, the wall clock (4) and the hourglass. In addition, iron-based pigments were used for creating the effects of light and shadows.
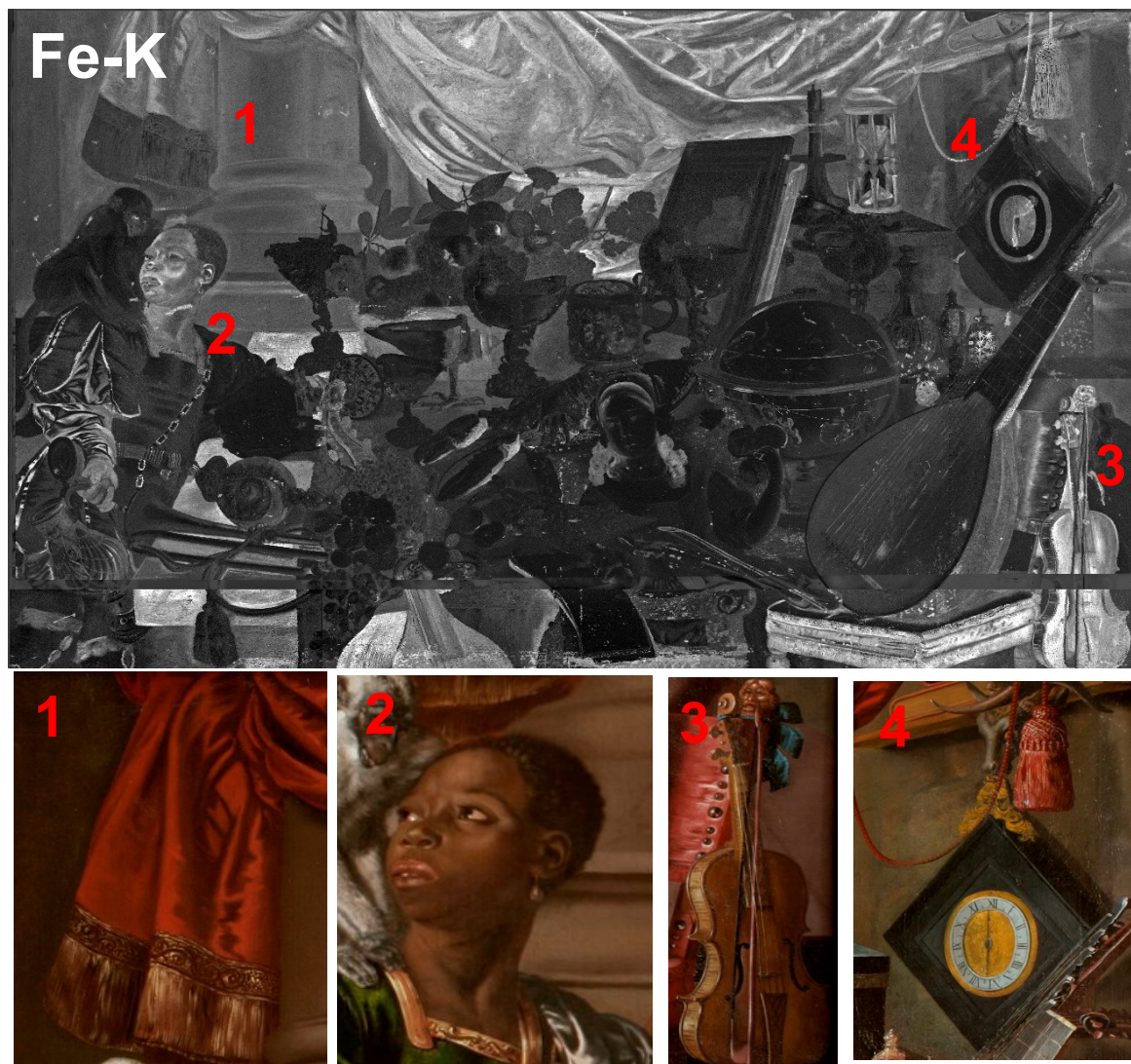
Figure 67: Fe-K distribution image and some painting details where iron was used (1-4).

4.2.6 Yellow pigments

The lead-tin pigment (Pb2SnO4) (commonly employed from 15th to 17th centuries) characterizes the brilliant yellow tones tending to golden [249]. The distribution of the yellow pigment on the painted surface is identified only through the Sn-L elemental image, showed in Figure 68, because its correlation with lead, homogeneously present under the pictorial layers, does not provide any significant information to identification of the pigment. Lead-tin is largely distributed in the painting, it was used by the artist for drawing several details as the fruits (1), the silver-gilt objects (2), the curtain fringes (3), the lute (4), the globe support (5), and the trumpet (6).

Figure 68: Sn-L distribution image and some painting details where tin was used (1-6).

4.2.7 Golden details

In the painting, arsenic sulpfhide in form of orpiment (As2S3) (known from the antiquity and used until the 19th century) confers the optic gilding effect to the precious objects of the collection. Orpiment pigment characterizes the painting of smallest details, as it can be seen in the drawing of the shells mounted on precious handles and in silverware , in detailed Figure 69. Its use highlights the meticulous painting process and reveals the care of the artist in the reproducibility of particulars [250, 251].

Figure 69: As-K image and some painting details where arsenic sulphide was used (1-7).

4.2.8 Smalt

MA-XRF analyses highlighted the presence of cobalt used for painting small grey-blue areas, as it showed in Co-K map in Figure 70. Among all known cobalt-based pigments compatible with the historical period of the painting, its usage is associated to the smalt presence, it consists of a finely blue potassium glass containing small amounts of cobalt oxide and used between 15th and 18th century [252-255]. In Europe, the use of smalt as pigment was widespread certainly as early as the late 16th century. The pigment was popular because of its low cost and its manufacture became a specialty of the Dutch and Flemish

artists in the 17th century. The distribution of smalt in the painting emerges in yellow areas (Red: K-K + Green: Co-K) of Figure 71, given by the combination of cobalt (in green) and potassium (in red) maps. It was used for painting small details of the amphora that the servant holds (1) and his belt (2), for decorating shells (3,4) , the grapes (5) and the Chinese porcelain where the lobster is placed (6).

Figure 70: Co-K image and some painting details where smalt was used (1-6).
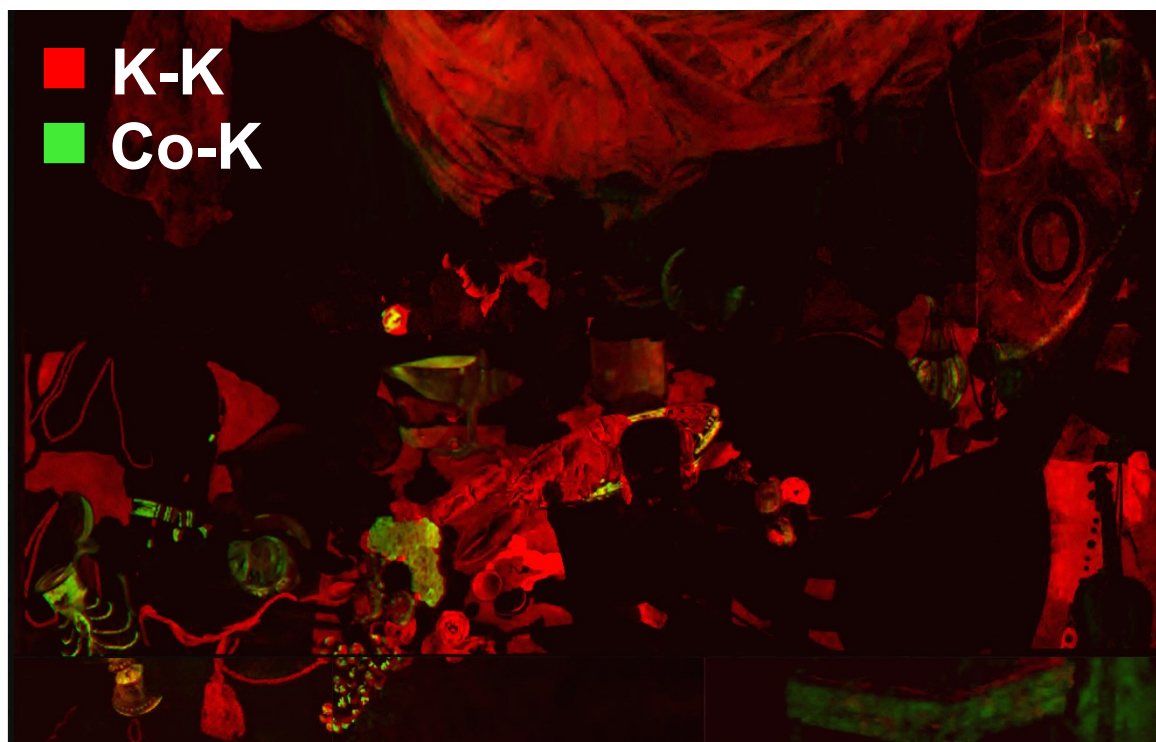
Figure 71: Red: Co-K and Green: K-K composite image identifies the presence of smalt in the yellow areas.

4.2.9 Lake pigments

In addition, the presence of potassium has been revealed in other areas of the painting not correlated to the cobalt distribution, as it can be observed in Figure 71. In European easel paintings from the 12th century or earlier until the end of the 18th century, it is known that, apart from the dyestuff, by far the most common ingredient was potash alum or potassium aluminium sulphate (KAl(SO4)2·12H2O). It is a metallic salt used as a reagent to form a substrate for the dyestuff. It is inert, colourless, chemically neutral and insoluble in the liquid medium. Alum is also indicated as lake pigment[§], used in oil painting to produce effects of richness and depth over the opaque pictorial layers. In addition, by changing pH of the alum-based solution, a weak difference in the hue of pigments can be obtained.

4.2.10   The mysterious overpainted figure

A previous analysis based on X-ray radiography (XRR) highlighted the presence of an overpainted figure on the top-right part of the painting. The figure, placed under the pictorial layer between the clock and the hourglass, is painted half-length and it seems to look in towards the centre of the composition. Figure 72 shows the detail of the hidden figure unveiled by means XRR and MA-XRF analysis.

[§] Lake pigments: any of various pigments prepared from animal, vegetable, or coal-tar colouring matters by chemical or other union with metallic compounds.

Probably the original drawing was left incomplete and later covered due to an emphasis change of the artist or under a precise choice made by the Paston family. Art conservators and specialists speculate various theories concerning her attribution: probably she was the Robert Paston's elder daughter, who scandalized her family by eloping with an unsuitable man or was the Paston's wife, Rebecca. Further, its position collocated outside of the composition has been considered unusual from experts.

MA-XRF analysis provided information about the original colors of the hidden figure by the determination of pigments nature, not accessible by XRR imaging. In addition, MA-XRF technique allowed unveiling several particulars of dress and combing, useful for attributing of the identity of the woman. In particular, MA-XRF elemental images make visible the figure through the correlation of vermillion red pigment (Hg-L) used for drawing the skin tones, copper green or blue pigments (Cu-K) for the drape dress and blue smalt containing cobalt (Co-K) for the floral ornament of hair, as showed in the RGB composite image in Figure 72.

Figure 72: hidden woman unveiled by previous XRR and MA-XRF analysis.

4.3. The Tomb of Kha and Merit (1428-1351 BC)

The tomb of Kha and Merit, dated back to the 18th Dynasty (1549-1292 BC), was found in 1906 during excavations in the north of Deir el Medina. It belongs to a wealthy married couple: Kha, the architect-in-chief of the pharaoh Amenhotep III [256], and his wife Merit [257-259]. Contrary to that of Nefertari, the tomb is one of very few known examples of Egyptian tombs never depredated before its discovery. Therefore, it was found intact and full of all the rich grave goods, which, according to the Egyptian cult, accompany the deceased in the afterlife.

Funeral collection include, besides the sarcophagi of Kha and Merit, daily objects such as tunics, robes, furniture, bath items for the personal care, beauty objects, jewelry, food remnants and several instruments that Kha used for his job. Also, in the tomb was found a papyrus containing formulas of the Book of the Dead. The entire collection is exposed in the Egyptian Museum in Turin and it has never been subjected to scientific analyses.

Egyptian paintings and writings are fascinating and complex materials to be investigated. Very often, the use of color is associated to symbolic meanings, especially when painted objects concern religious or mortuary use. From the technological point of view, various pigments and painting techniques were developed over a long period for decorating different supports (wood, papyri, stones, cloth, etc.) [260, 259].

In the course of the research activity, MA-XRF technique has been applied to the study of four painted wooden coffers (S.8212, S.8213, S.8613, S.8440), they are showed in Figure 73. The artworks belong to the funeral collection of Kha and Merit and they were used as toilette objects for containing both ointments and creams for the personal care and linen underwear. The coffers are of different shapes with flat lid or gabled and decorated along the sides with floral motifs, geometric designs or with scenes of daily life. Among the analyzed wooden coffers, only one is decorated with geometric motifs, while the remaining three describe offer's scenes devoted to the architect and his wife depicted in front of a sumptuous table.

MA-XRF imaging allowed to reveal the pigments palette and provided important information concerning the painting technique. Further, MA-XRF maps have allowed the identification of changes introduced during the creation of the work and the visualization of original written texts, not more readable due to degradation processes occurred over the time.

Figure 73: the painted wooden coffers analysed by MA-XRF at the Egyptian Museum (Turin, IT) (Kha and Merit tomb, New Kingdom, 18th Dynasty).

4.4. MA-XRF analysis on Egyptian wooden coffers

MA-XRF analysis on painted wooden coffers were carried out in situ in the context of a collaboration with the Egyptian Museum in Turin (Italy). The lateral surfaces of wooden coffers (35×45 cm^2) have been analyzed in a single scan of a duration of 3 hours. Continuous scans were performed along the X direction at a scanning speed of 17 mm/sec and a fixed step-size of 500 µm was selected along the Y direction. These parameters correspond to a dwell time per pixel of 30 ms. Different scanning parameters have been used for the investigation of artwork S.8440. Its painted surface has been analyzed in less than 1 hour, at a horizontal scanning speed of 50 mm/sec (X direction), corresponding to 10 ms of dwell time per pixel and a fixed step-size of 500 µm in the Y direction. MA-XRF scans were performed with a beam size of 500 µm by positioning the painted surfaces at 1.5 cm from the spectrometer and the elemental maps have been created in real-time by using the in-house programmed software (see Section 3.10, Chapter 3). During acquisition, the laser system was operated for controlling the preconfigured safe distance sample-spectrometer (0.8 cm) and the measurements were performed at 36 kV X-ray tube voltage and 400 µA current. The mapping was obtained with an energy resolution of 160 eV based on the selected

117

detection parameters (1.5 µs peaking time and 0.2 µs flat top). Figure 74 shows the XRF scanner during the acquisition.

Figure 74: MA-XRF scanner in execution installed at the Egyptian Museum.

4.4.1 Elemental distribution images

This section presents the elemental images obtained by the MA-XRF analysis operated on the coffer S.8613 (see Figure 75). The original pigments characterizing the artist's palette and the creative process are discussed. In addition, a different use of materials and differences in the painting technique emerged from the comparative studies with the other artworks (S.8212, S.8213, S.8440) that were analyzed in the same measurements campaign. The painted scene of the wooden coffer (Figure 75) depicts Kha and Merit seated in the act of receiving an offer in front of a round table on which triangular breads, vegetables and fruits are placed. The chair with lion's paws of the deceased is placed on a pedestal decorated with vertical bands. Kha and Merit wear a long transparent tunic; Kha keeps, with his hand a lotus flower, while Merit an object no longer identifiable. Under the chair are painted a mirror and an ointment vase. On the opposite side of the scene, there is a pair of bidders: a young woman, dressed in a long white dress, and a young man wearing a white kilt. The two young figures could be the sons of Kha and Merit, or they may be a sister and her husband. The woman raises a jar libation to purify the offers, the man holding a lotus flower as symbol of rebirth. At the top of the scene are painted seven columns of hieroglyphics inked in black and separated by vertical red stripes.

Figure 75: painted surface on wooden coffer (S.8613-New Kingdom, 18th Dynasty) analysed by MA-XRF technique at the Egyptian Museum (Turin, IT).

The chemical elements composing the pigment materials in the painting are evidenced in the sum spectrum and in the spectrum of maxima in Figure 76and Figure 77. In particular, sulphur (S), calcium (Ca), iron (Fe), copper (Cu) and arsenic (As) are present with major abundance, and also traces of manganese (Mn) and strontium (Sr) have been detected, while other minor elements as silicon, potassium and titanium come from the raw materials used for manufacturing pigments and from wooden support itself [261].

These elements are the basis of the pigment palette used by artists in Egypt at the time of the 18th Dynasty (New Kingdom, c.1549–1292 BC) as summarized in Table 10 [262].
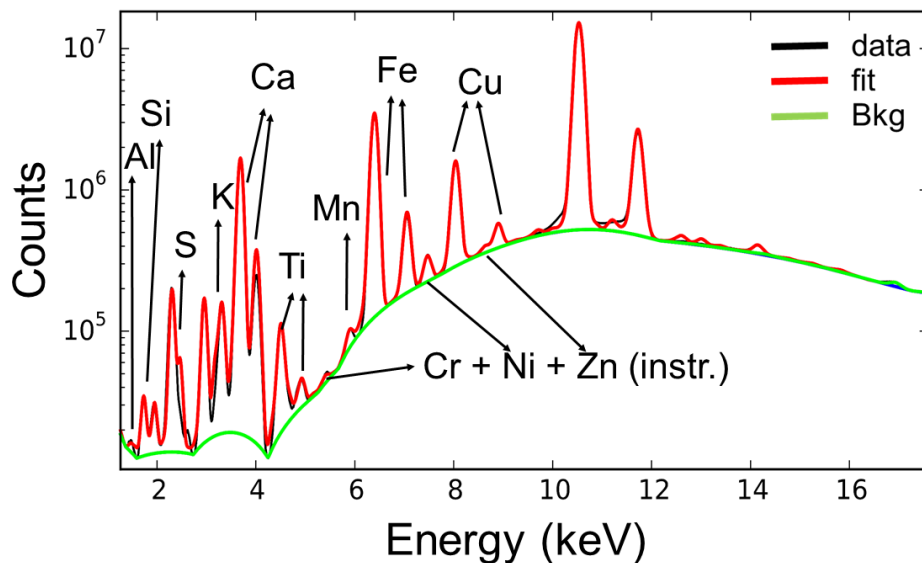
Figure 76: sum spectrum of the entire painted surface.
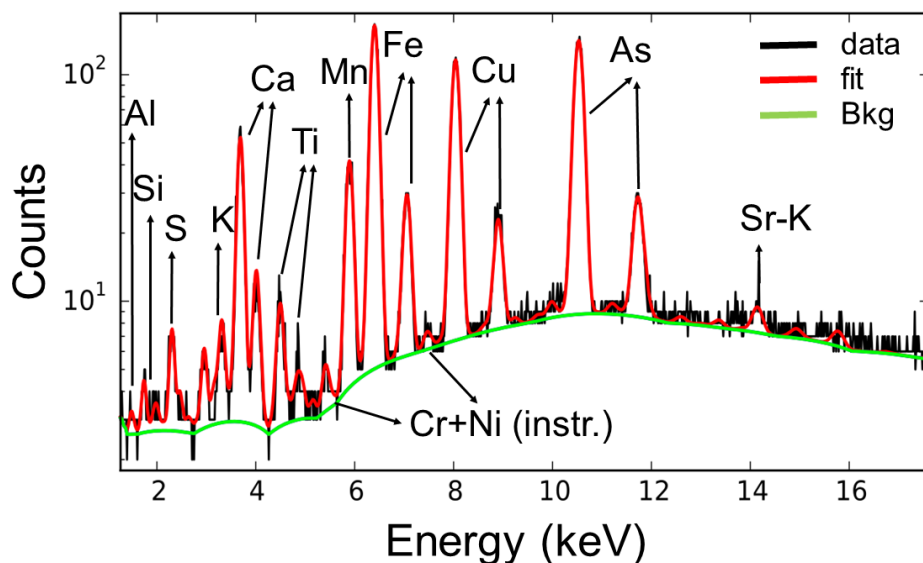
Figure 77: spectrum of maxima of the entire painted surface.

Colour	Pigments	Chemical formula	Egyptian period (from/until)
Blue	Lapis lazuli	(Na,**Ca**)4(Al,SiO$_4$)3(SO$_4$,S,Cl)	doubtful identification in the 18th Dynasty (1549-1292 BC)
	Egyptian blue	**CaCu**Si$_4$O$_{10}$	from the 5th Dynasty (c. 2750–2625 BC) until the Roman period
	Azurite	2**Cu**CO$_3$-Cu(OH)$_2$	from the 4th Dynasty (c. 2613 to 2494 BC) until the 18th Dynasty (1549-1292 BC)- needs confirmation
Green	Egyptian green	in some cases, is a greenish shade of Egyptian blue, but more often it is a mixture of Egyptian blue (**CaCu**Si$_4$O$_{10}$) with yellow ochers (**Fe**O(OH))	from the 6th Dynasty (c. 2345 – 2181 BC) until the 20th Dynasty (1189−1077 BC)
	Malachite	**Cu**CO$_3$-**Cu**(OH)$_2$ (use rare)	From the Predynastic Period (4400 BC) until the Roman Period
Red	Red Ochres	**Fe**$_2$O$_3$ (hematite)	from the Predynastic period until the Roman period
	Madder	C$_{14}$H$_8$O$_4$, C$_{14}$H$_8$O$_5$	the 18th Dynasty (1549-1292 BC) to the Roman period
Yellow	Yellow ochres	**Fe**O(OH)	from the Predynastic period until the Roman period
	Orpiment	**As**$_2$**S**$_3$	from the 4th Dynasty (c. 2613 to 2494 BC) until the 12th century (Medieval)
	Realgar	**AsS** or **As**$_4$**S**$_4$	from the 5th Dynasty (2498–2345 BC) until the Late period (343 BC)
	Jarosite and natrojarosite	**KFe**$_3$(SO$_4$)$_2$(OH)$_6$	from the 3rd Dynasty (c. 2686 – 2613 BC) until the Roman period
White	Chalk	**Ca**CO$_3$	from the 3rd Dynasty (c. 2686 – 2613 BC) until the 12th century (Medieval)
	Gypsum	**Ca**SO$_4$-2H$_2$O (very common)	from the 3rd Dynasty (c. 2686 – 2613 BC) until the 12th century (Medieval)

	Huntite	$Mg_3Ca(CO_3)_4$ (less common)	4th Dynasty (c. 2613 to 2494 BC) and 6th Dynasty (c. 2345 – 2181 BC), also from the 11th (2025 – 1991 BC) until the Ptolemaic Period (305–30 BC)
	Anhydrite	$CaSO_4$ (less common)	from the 5th Dynasty (2494 – 2345 BC) until the Roman Period
Black	Carbon black	C	from Predynastic Period (3500 BC) until the Roman Period
	Pyrolusite	MnO_2 (use rare)	from the 1th Dynasty (3100 – 2890 BC) until the 18th Dynasty (1549-1292 BC)
Binder	Beeswax	myricyl palmitate $C_{15}H_{31}COOC_{30}H_{61}$	from Predynastic Period (3000 BC) until the Roman Period
	Egg		from the 18th Dynasty (1549–1292 BC) until Roman period
	Glue		from Predynastic Period (3000 BC) until the Roman Period
	Gums		from the 11th Dynasty (2025 – 1991 BC) until Roman period
Varnish	Bitumen	hydrocarbon	from the 18th Dynasty (1549–1292 BC) until not know

Table 10: Main inorganic Egyptian pigments used in the 18th Dynasty (New Kingdom).

4.4.2 Ground layer and white pigments

Natural calcium carbonate pigments (or calcite, CaCO3) [263], calcium sulfates, as gypsum (CaSO4.2H2O), and anhydrite (CaSO4) obtained by heating gypsum to 200°C, were extensively known from Egyptians as white pigments [264, 265]. They were combined with gum Arabic or animal glue as binder. Further a fourth white pigment, unknown to modern science until 1953, was discovered to be present in the Egyptian palette: the huntite. It is a mineral magnesium calcium carbonate (Mg3Ca(CO3)4) that was found in papyri and wooden coffins [266- 268], statues, sculptures and other wooden objects [269, 270].

Huntite was preferred for its bright white colour that reflects light from the paint giving it more colour saturation and brightening. It was also used as a pigment underlayer covered with red and yellow ochres. The use of huntite became predominant in the New Kingdom (18th - 20th Dynasty, 1549- 1077 BC) [271] and in the same period, sulfates and carbonates white pigments have been declined.

Due to the low emission energy at 1.25 keV Mg cannot be detected with MA-XRF set-up used during the measurements,

However, the discrimination between white pigments by the only calcium detection is not possible and additional information is needed in order to assess the nature of the white ground.

In the painting, the calcium-based pigments were most likely used in a pure form as white pigments in the painted scene or in the preparatory layer (ground), as it emerges in the Ca-K map in Figure 78. In particular, the calcium-based pigments characterize the drawings of the white robes and kilts of the characters of the scene (1), the contours of the chairs of Kha and Merit, the skin tones of the standing female figure (2) and some food (3) in the

composition. Calcium is also present in the Egyptian blue pigments as it will be showed in the next paragraph 4.4.3.
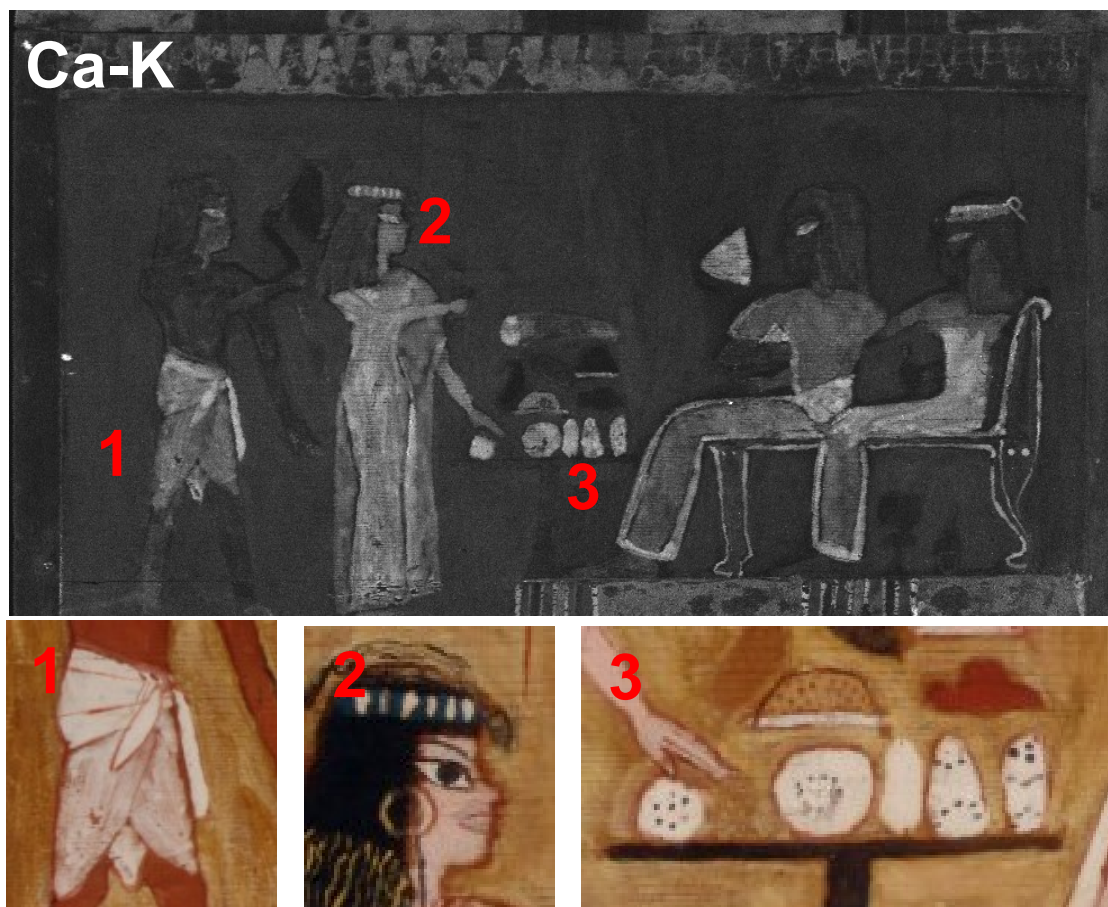
Figure 78: Ca-K distribution image.

The analysis of XRF spectra (see Figure 76 and Figure 77) reveals the presence of strontium usually associated to calcium as impurity. However, previous scientific works evidenced the use of celestite (4SrSO4) (sulphate) or strontianite (4SrCO3) (carbonate) as pigment materials in ancient Egypt [272, 273]. In this case strontium is associated with calcium in the ground layers and whites, as it is observable from the correlated distribution plot in Figure 79.

Figure 79: Red: Ca-K and Gree: Sr-K composite image.

MA-XRF analyses carried out on other wooden coffers (S.8212, S.8213, S.8440) have revealed the presence of calcium-based pigments used as ground of the painting. The Ca-K distribution resulting from the analysis of S.8212, S.8213, and S.8440 coffers are showed in Figure 80. In the same way, the analogous strontium distribution has been identified in combination with the calcium distribution.
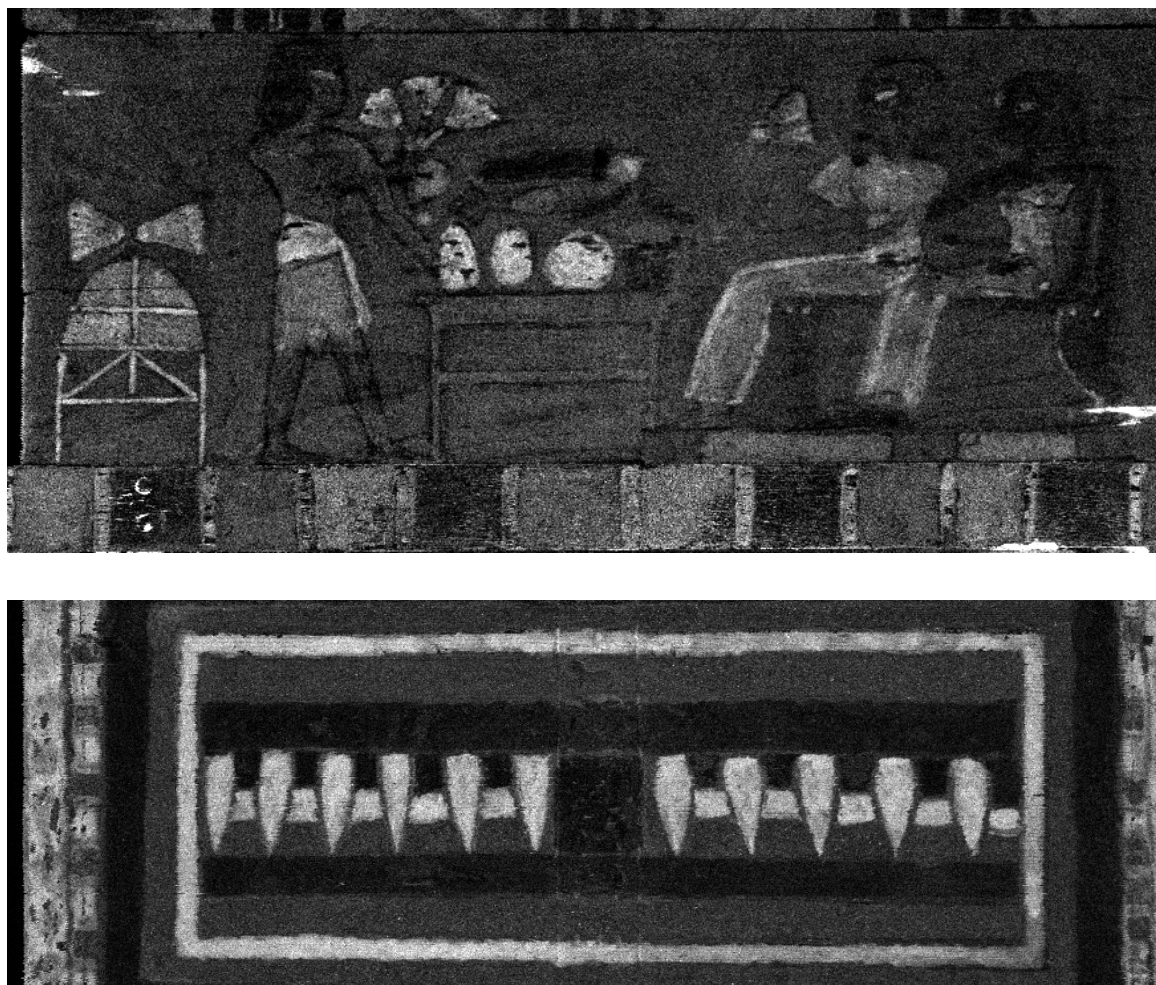
Figure 80: Ca-K images obtained from the MA-XRF analysis on the artworks S.8212, S.8213, and S.8440 (from top to bottom).

4.4.3 Blue pigments

Copper distribution in the coffer (Figure 81, top), characterizes the intense blue coloration. It appears in the geometric decorative motif on the upper part of the coffer (1) and in the pedestal on which Kha and Merit are depicted, in the hair of the characters and the hair ornament of the female figures (2); also it is present in the lighter blue tone used for painting the food and the lotus flower kept from Kha (3).

The presence of copper may be attributed to the use of Egyptian blue ($CaCuSi_4O_{10}$ or Cuprorivaite) [274-280, 260] or Azurite ($2 CuCO_3 \cdot Cu(OH)_2$) [260]. Both pigments were employed since the $4^{th}/5^{th}$ Dynasty (c. 2639 to 2504 BC) in Ancient Egypt. However, the presence of calcium in combination with copper suggests that Egyptian blue is present in the painting [281]. Although, the natural mineral Azurite is among the first blue pigments used in the history, soon thereafter Egyptians manufactured Egyptian blue. It is considered the first synthetic pigment, largely used for 3000 years for decorating wood, papyri, stone, cartonnage, stucco, plaster, and metallic objects.

In Figure 81 (bottom), the magenta areas of the composite image between Ca-K (red) and Cu-K (blue) identifies the Egyptian blue distribution on the painting.

Figure 81: (top) Cu-K image and some painting details where copper-based pigments were used, (bottom) the Red: Ca-K –Blue: Cu-K composite image identifies the Egyptian blue presence.

In addition, copper has been detected in different areas of the painted surface. The comparison between the XRF spectra taken in three different white and yellow painted areas (20×60 pixels) of the painting (area 1-3 in Figure 82) shows a small content of copper. Probably, it indicates that Egyptian blue was used in combination with other pigments: orpiment in the yellow area and gypsum in the white area for giving the final desired chromatic effect. Further, the higher presence of silicon in the blue area (area 3) is also associated to the Egyptian Blu as evidenced in the chemical formula of the cuprorivaite formula above mentioned.
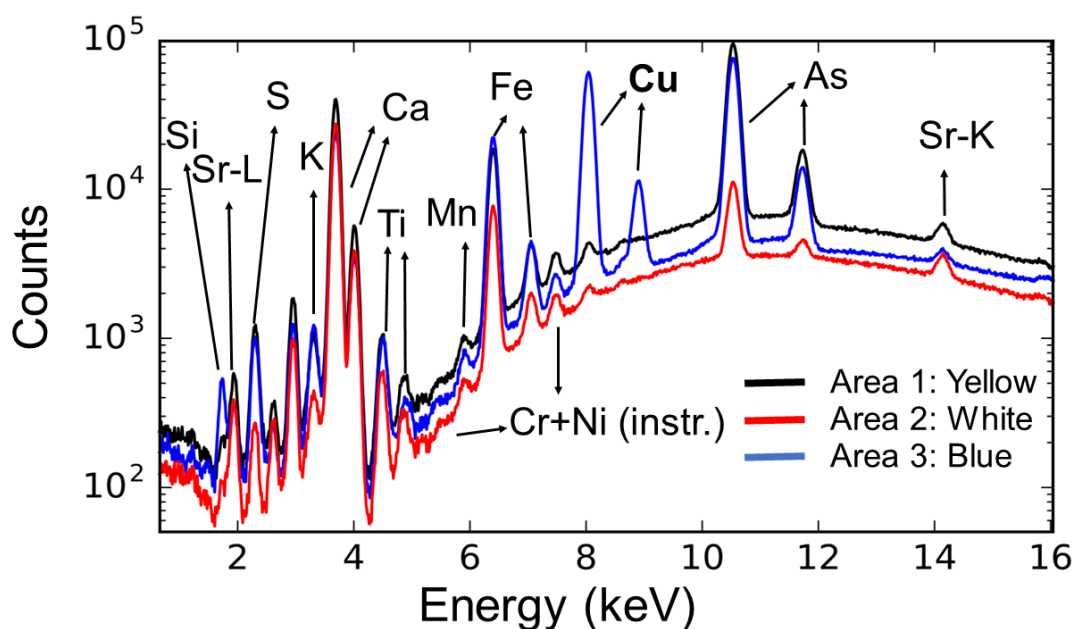
Figure 82: comparison between XRF cumulative spectra taken in three different areas of the painting (area 1-3).

Several studies report that Egyptian blue was also used for the greenish tones in a mixture with yellow ochre. However, identification of green Egyptian pigments is a quite complex task. Several green pigments, based on the presence of copper, have been used since the 4th Dynasty. As an example, MA-XRF analysis has revealed the presence of copper in a green decorations of S.8440 coffer. The nature of this pigment is not possible by using the alone elemental analysis. The un-correlation between calcium and copper in Figure 83 demonstrates only that this green pigment is not a mixture of a yellow pigment with Egyptian Blue.

Figure 83: Ca-K (red) - Cu-K (blue) composite image (artwork S.8440)

4.4.4 Reddish-brown pigments

The reddish coloration is characterized by the presence of iron oxides or ochres [282, 264]. Their use is dated back from the 4th Dynasty (c. 2613 to 2494 BC) and it extends through to the Late period (664-332 BC). Red ochres are by far the most commonly reported red pigment in ancient Egypt, they generally contain a varying amount of iron oxide in several mineral forms as goethite (FeO(OH)), limonite (FeO(OH)-nH2O) or haematite (Fe2O3). However, the red colour is conferred by the dominant presence of hematite.

In the painting, iron-based red pigments are present in the geometric decoration on the top part (1) and in the pedestal where Kha and Merit are drawn, they appear in the thin brown strokes for decorating the pattern on the lateral frame and in the red stripes that separate the hieroglyphics (1). Further, the artist used red ochres for drawing the profiles of the figures in the composition and other pictorial details like some foods on the table (2).

The brown tones are associated to the use of umbers or burnt ochre (iron oxides) [264]. However, studies carried out over the time have identified the browns obtained as red ochre painted over black [282] or as a varnish over a deep yellow ochre [276]. Other studies report the use of brown on one early 18th Dynasty (1549-1292 BC) papyrus as a mixture of hematite (Fe2O3) with orpiment (As2S3) and carbon black [276], while on a 19th Dynasty (1292–1189 BC) papyrus was found as mixture of realgar (AsS or As4S4) and hematite [283]. In particular, browns characterize the reddish-brown skin tones of the male figures (3). However, iron-based pigments have been blended with orpiment (see paragraph 4.4.5-yellow pigments paragraph) with different compositions for giving the different shades of color from yellow to reddish brown through dark yellow.
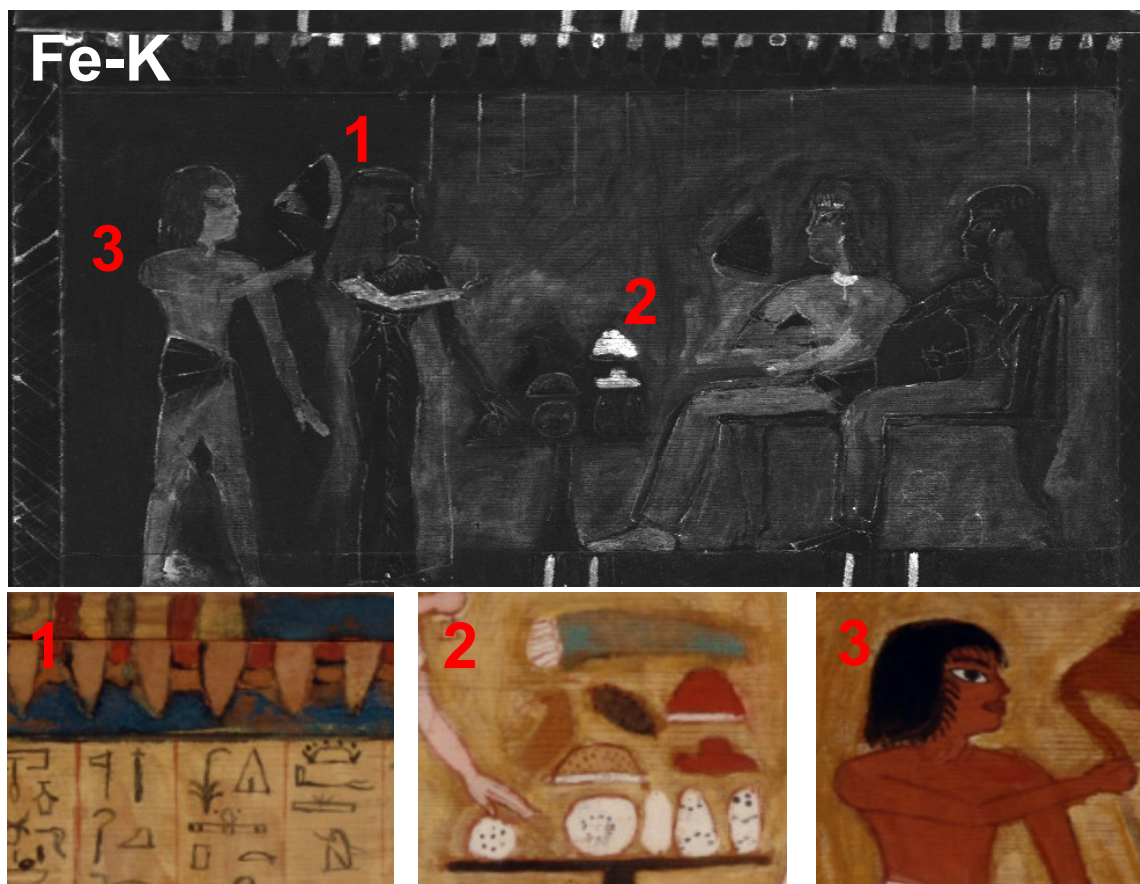
Figure 84: Fe-K distribution image and some painting details where ochres were used.

Table 11 reports the As-K/Fe-K net counts ratio calculated in the different areas of the painting (see correlated figure) where different chromatic shades were obtained by mixing different quantities of arsenic and iron-based pigments. In Figure 85 are showed the normalized cumulative spectra recorded on the area 1 (reddish-brown pigments) and area 3 (dark yellow pigments), in order to appreciate the different intensity peaks correlated to concentration of arsenic and iron respectively.
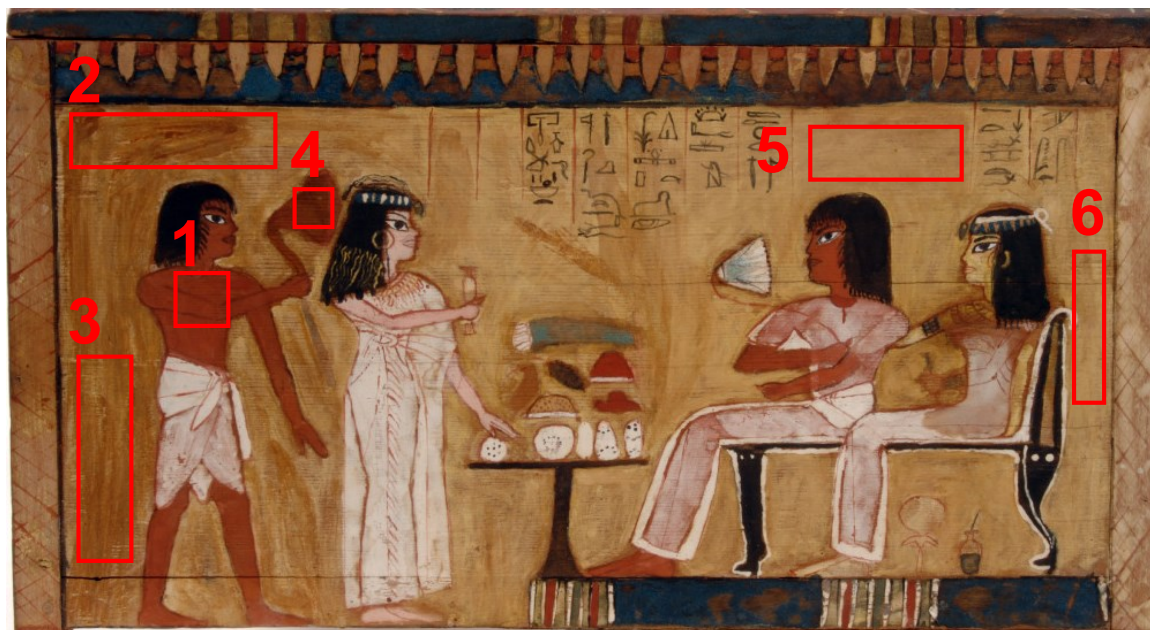
Sub-area/pixel size	Coulor	Fe-K (counts)	As-K (counts)	As-K/Fe-K
Area 1-50×50 pxls	Reddish-Brown	6.3E+05	6.3E+05	1
Area 2-160×40 pxls	Dark Yellow	2.8E+05	5.7E+06	20.3
Area 3-160×40 pxls	Dark Yellow	5.5E+05	1.1E+07	20.5
Area 4-30×30 pxls	Reddish-Brown	4.9E+04	1.1E+05	2.2
Area 5-150×40 pxls	Yellow	1.1E+06	1.9E+07	18.1
Area 6-30×130 pxls	Yellow	1.8E+05	2.3E+07	14

Table 11: As-Fe K-lines ratio calculated in different sub-areas (1-3) of the painting.
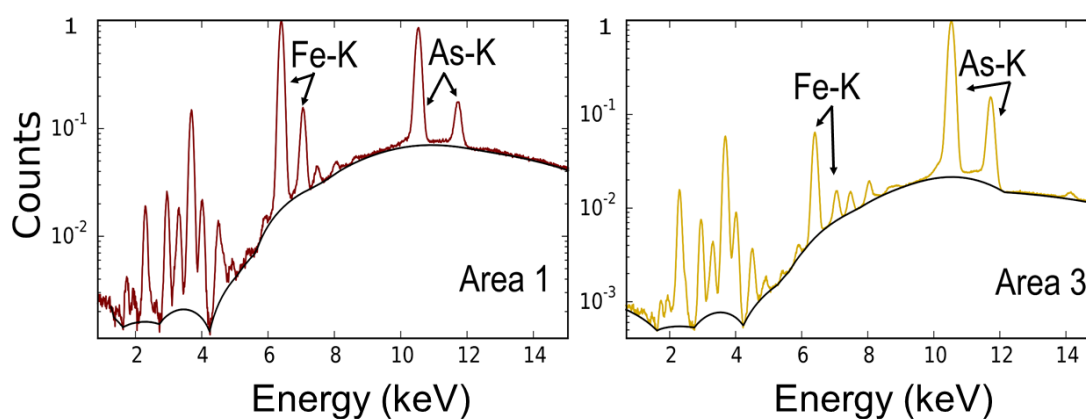
Figure 85: area 1 (right) and area 3 (left) normalized cumulative spectra.

The same technique that sees the mixture of ochres and orpiment for creating the yellow-reddish-brown tones was also found in other analyzed wooden artworks. The cumulative spectra, showed in Figure 86, related to the area 1 and 2 of artwork S.8212 identify, anew,

the combination of two pigments. Finally their mixture is also used in white and blue areas, as it can be seen in the spectra of Figure 82, specifically for giving a chromatic effect.
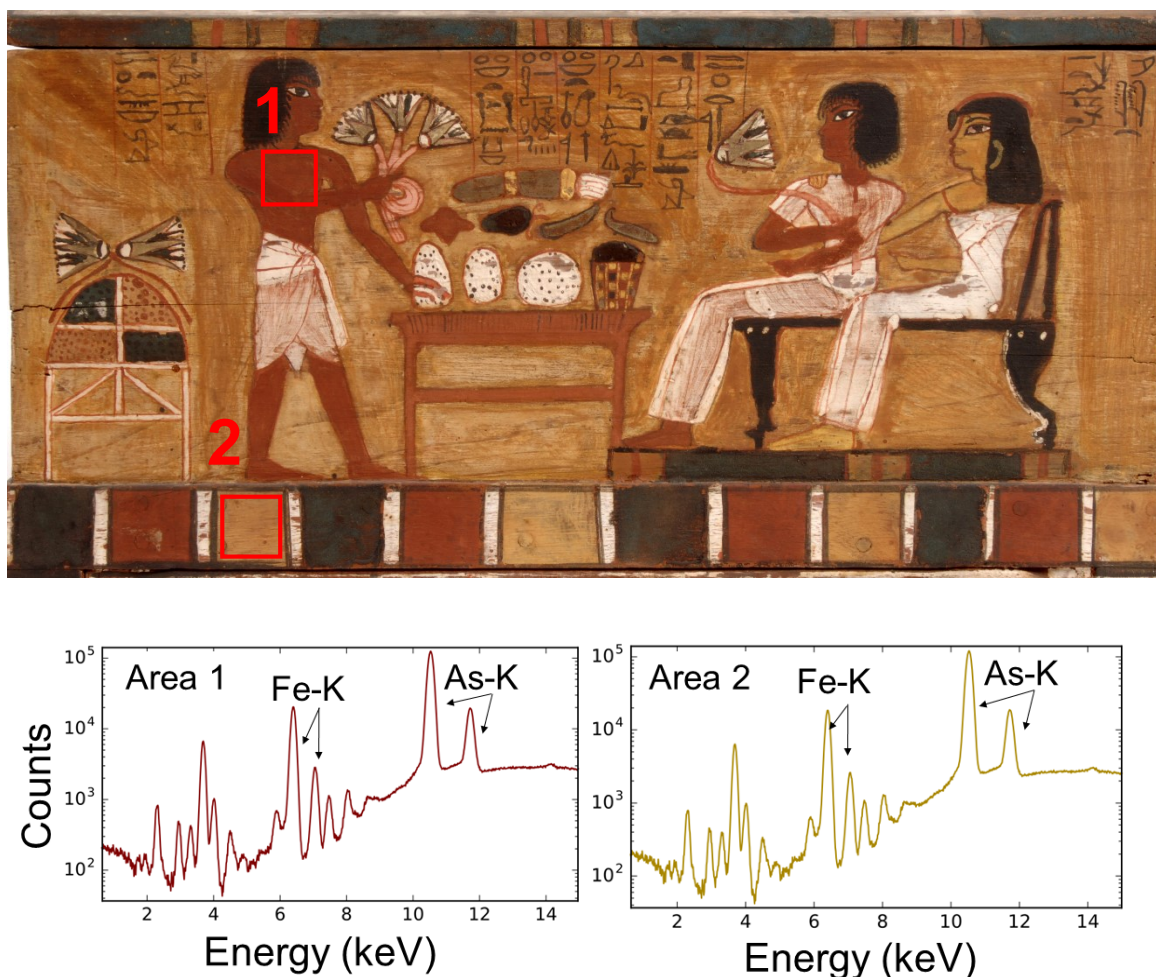
Figure 86: cumulative spectra in two different areas (1-2) of the artwork S.8213.

4.4.5 Yellow pigments

The correlated distribution of arsenic (As-K) and sulfur (S-K) (Figure 87), has to attribute to the presence of orpiment (4As2S3) used as yellow pigment. Orpiment, named also King's yellow, was employed starting from the 4th Dynasty (c. 2613 to 2494 BC) in Egypt and mostly identified as a sole pigment in coffins dated from the New Kingdom (18th – 20th Dynasty) to the end of the third intermediate period (21st – 25th Dynasty) [284-286]. However, it is possible to associate the yellow coloration to realgar (As4S4), a bright orange-red mineral composed of arsenic di-sulfide, often found with orpiment.
Realgar has never been observed as Egyptian pigment before the New Kingdom, however its presence could be associated to pararealgar (AsS), a light induced alteration product of realgar [249, 287-290].

In the painting, orpiment or generically arsenic sulfides combined to ochres has been identified in background of the scene, in the dark yellow/brown skin tones of the male characters, in the geometric decoration on the top and in the Merit's face tones.

Figure 87: Red: As-K – Green: S-K composite image.

4.4.6 Black pigments

In the painting several details are painted in black as the hair of the characters, the hieroglyphics in the upper part, the chair of Kha and Merit, the table (see Figure 75). However, the organic nature of the pigments does not allow their identification by XRF. Commonly, carbon black pigments including various pigments as lampblack, charcoal black and bone black, were extensively used in ancient Egypt. They are derived from a partial carbonizing of natural gas, fats, tar, oils, wood, animal's bones, resins and other organic materials [291-293, 285, 264]. Further, a rare use of pyrolusite, (MnO2) was identified starting from the 12th Dynasty (1991 − 1802 BC) [294, 264, 291].

In the coffer in exam, the artist used the manganese black only in correspondence to very small areas: the lower symbol of the first visible column of hieroglyphs and two short strokes in the body profile of the standing male figure, as it can be seen in the detailed Figure 88.

.

Figure 88: Mn-K image.

However, the alternation of manganese black and black pigments of organic nature has been also found in MA-XRF maps obtained by investigating the other decorated coffers.

In the painted surface of the S.8212 artwork, the manganese distribution image (Figure 89-green) shows how the manganese-based black has been widely used for painting the hieroglyphic inscriptions, the profiles of figures, and also small decorative details of the food emerge in the map. This result reveals interesting aspects concerning the creative process operated by the artist and it suggests new questions to be investigated. For example, it is not clear if the alternation of the two blacks can be attributed to the more practical motivation correlated to the availability of material or to a specific intent of the painter, perhaps attributable to a pure aesthetic needs and subordinated to the chromatic difference that the two different pigments exhibit. In Figure 89 are also combined the calcium (red) and copper (blue) maps.

Manganese as black pigment was also found in a second coffer (S.8213), on which, in addition to the drawings of outlines of the figures, it has been employed for the lateral

decorations that reproduce the grain of the wood. The choice of this type of drawings that meet the nature of the pictorial support material expresses the particular aesthetic taste of the artist. The composite image Red: Fe-K- Green: Mn-K- Blue: Cu-K is showed in Figure 90. Finally, the MA-XRF analysis on the coffer S.8440 did not reveal the presence of manganese black. All black decorations are of organic nature. However, it was possible to unveil the vertical inscription of hieroglyphics at the centre of the painting, as will be shown in the next section.
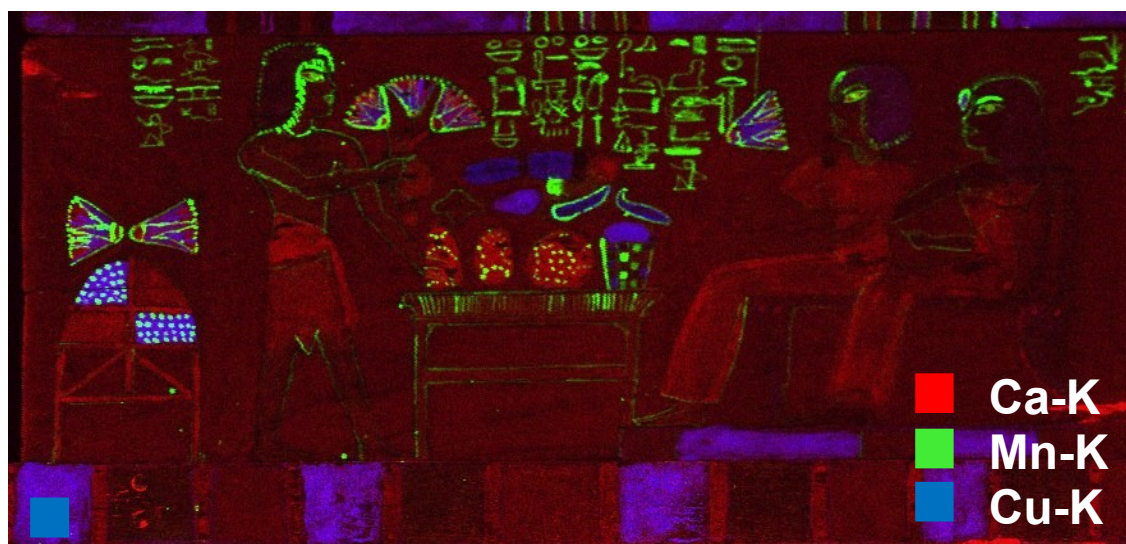
Figure 89: Red: Ca-K – Green: Mn-K – Blue: Cu-K composite image (artwork S.8212).
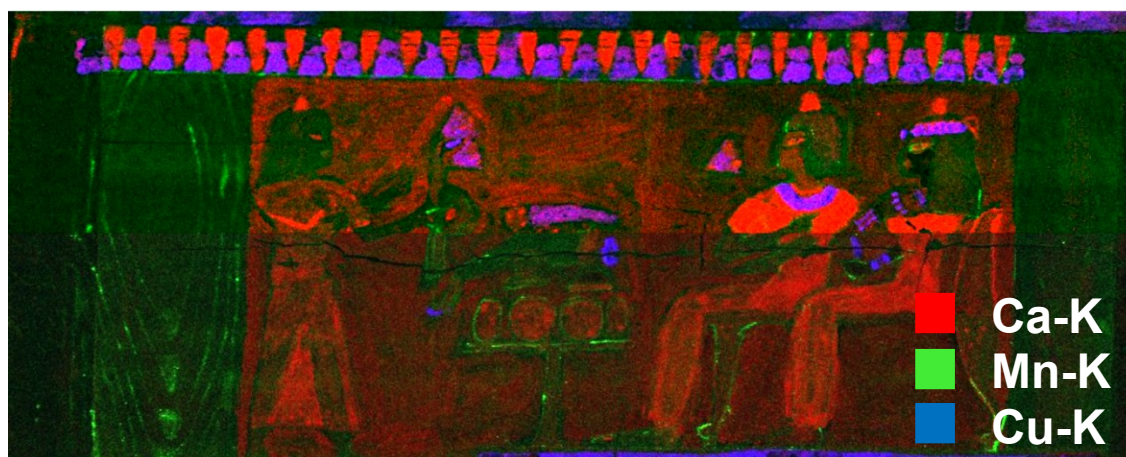
Figure 90: Red: Ca-K – Green: Mn-K – Blue: Cu-K composite image (artwork S.8213).

4.4.7 "Pentimenti" of the original painting and hidden inscriptions

MA-XRF technique has allowed to unveil hidden details not visible to naked eye. In particular, the composite Red(As-K)-Green(Fe-K map), in Figure 91, exhibits the presence of some modifications to the original drawing compared to the final composition (Figure 75). Initially, the artist painted the lotus flower, kept by the man on the left, as a long-stemmed flower, later it was covered and made uniform with the background (1). In

addition, the artist introduced on the table a third food, visible in the calcium map, but initially not present in the preparatory drawing, that isolates the figures of the composition from the background layer (2). Finally, the Kha arm that holds the flower was painted initially in a different position, and after modified (3).

Further, MA-XRF analysis provided important information by revealing the vertical inscription of hieroglyphics on the painted surface of the coffer S.8440, of which only a few traces remain visible to naked eye.

It is presumable that the black inscription was written by using carbon-based pigments, of which the organic nature does not allow to identify them by XRF. Nevertheless, the hidden text has been made readable by selection of the region-of-interest (ROI) corresponding to the Compton peak of the XRF spectrum that facilitates the visualization of the organic pigments. The inscription appears visible in the copper map; how to indicate that probably Egyptian blue was also used in the decoration. Figure 92 shows the copper image and the map obtained by the Compton scattering peak selection.
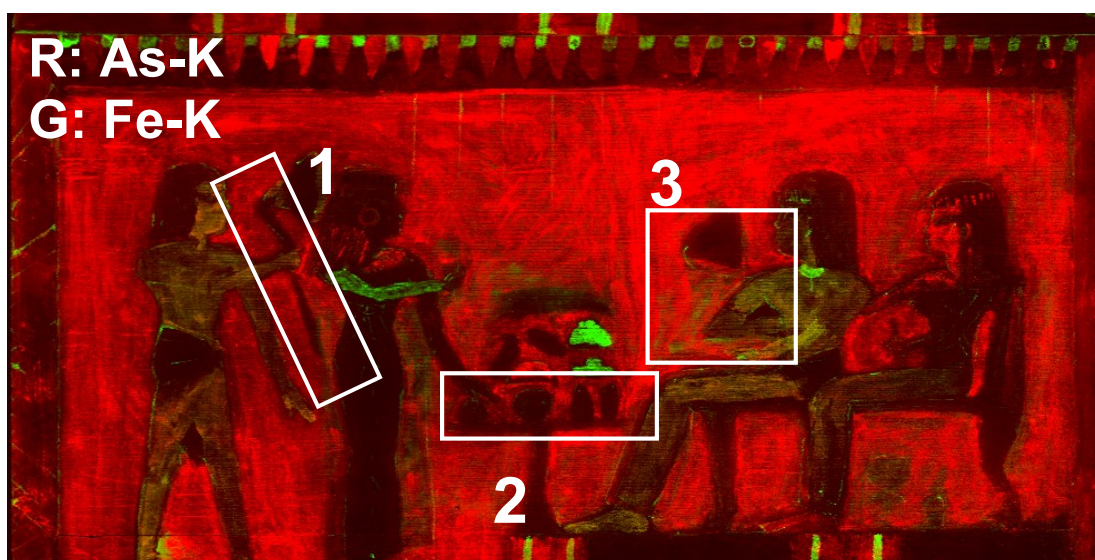
Figure 91: modifications to the original drawing visible in the Red: As-K – Green: Fe-K composite image.
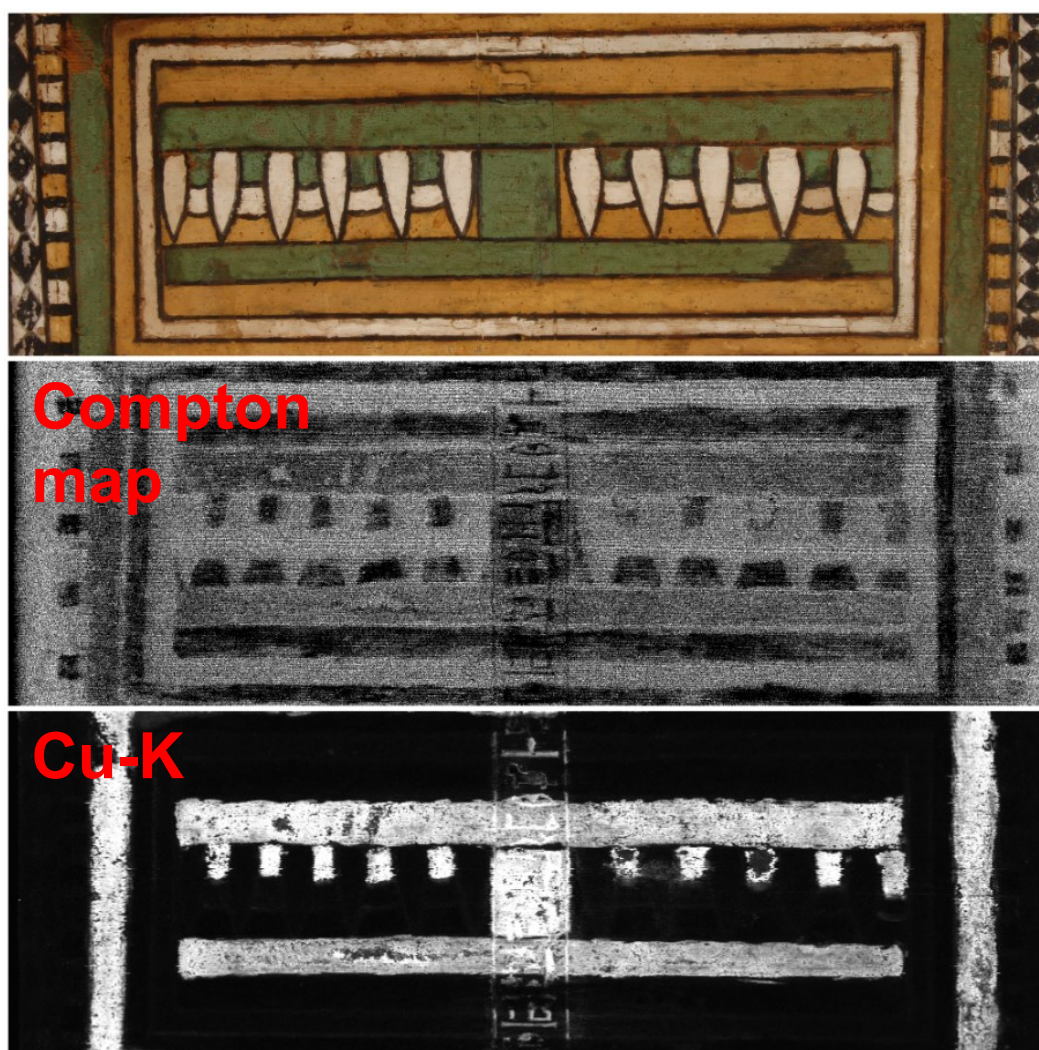
Figure 92: hieroglyphic inscription visible in the ROI-Compton scattering peak and Cu-K maps.

4.5. Illuminated Manuscripts

The third typology of artwork studied within the present PhD project concerns the study of illuminated manuscripts belonging to the Fitzwilliam Museum collection (Department of Manuscripts and Printed Books, Cambridge, UK) [295-297, 67]. Illuminated manuscripts are hand-written books with painted decoration that generally includes precious metals such as gold or silver. They were produced between the 13th and 15th centuries, in the monasteries. Contemporaneity, wealthy patrons also wanted these illustrative works for personal libraries and encouraged the formation of private workshops that flourished in French and Italian cities. Their decline coincided with the ability to produce printed text.

In particular, MA-XRF analysis was carried out on the illuminated initials of the Choir Books, a sumptuous liturgical manuscripts, considered among the finest art works created in Florence between 1370 and 1506 [298]. They were written in the scriptorium of the Camaldolese monastery of Santa Maria degli Angeli (Florence) by successive generations of artists to be destined to the religious houses of Tuscany and Veneto as well as to the own community to be read by the monks during the religious celebrations.

During the Napoleonic invasion of Italy (1797-1809), the volumes were mutilated, and some parts of the books separated from the original volumes, that now are found at the Biblioteca Laurenziana in Florence. Instead, the illuminated initials have been sold on the art market, and they are now dispersed among the public and private collections around the world.

In this section it will be presented the MA-XRF analyses performed on one of the four initials: the parchment Marlay cuttings It. 13A "Presentation in the Temple", that graced the pages of the earliest volumes. The parchment is shown in Figure 93.

The illuminated fragment exhibits the historiated initial "S" that introduces the Mass for the feast of the Purification of the Virgin (which falls on February 2) in *Corale* 2, the remaining part of the book is today conserved at the Biblioteca Laurenziana in Florence.

The parchment is one of the earliest works created by Don Silvestro dei Gherarducci, whose art was among the most recognized of that time and his illuminations are distinguished by the materials preciousness [299]. The artwork was executed between 1370 and 1375 at the Santa Maria degli Angeli monastery, where the artist led the scriptorium until his death and during which he handed down the art of miniature to the next generation of artists.

After the volume splitting, the parchment was belonged to Sir Samuel Meyrick (1783-1848) and later to Charles Brinsley Marlay, who bequeathed it to the Fitzwilliam Museum in 1912. The painted composition is one of the typical medieval and Renaissance composition, it depicts the purification of the Virgin, indicated by the white dove in Joseph's hands, and the circumcision of Christ. In the painted scene, the infant Christ is entrusted to Simeon and Anna from Joseph and Mary, and the priest behind keeps a knife in hand for the circumcision execution. The image reveals the style of the Sienese art of the 1300s particularly evident in the details of the tooled gold haloes, each painted with a different pattern (detail in Figure 93 (1-2)).

Figure 93: (top) illuminated manuscript Marlay cuttings It. 13A "Presentation in the Temple (300 x 270 mm^2, 1370-1375) painted by Don Silvestro dei Gherarducci (Florence, Italy). The manuscript belongs to the Department of Manuscripts and Printed Books of The Fitzwilliam Museum (Cambridge, UK); (bottom) detail of the tooled gold halos of Simeon (1) and the infant Christ (2).

4.6. MA-XRF analysis of miniatures

MA-XRF analysis of illuminated manuscripts provided valuable information concerning the artist's manufacturing technique and its connections with other artist's workshops through the re-construction of its pigments palette. The research activity has been carried out in collaboration with manuscripts scholars and conservators of the Fitzwilliam Museum.

Given the intrinsically high sensitivity of the artefacts to changes in environmental conditions, that can cause physical damage and accelerate aging or degradation, MA-XRF scanner was transported in situ and measurements have taken five days in total for the analysis of N.7 illuminated fragments.

In particular, the fragment (300 x 270 mm^2), of which results are reported in this section has been analyzed in a unique scan of a duration of 3 hours, positioning the cardboard support on which is glued the parchment, at 1.5 cm from the measurement head. At this distance, a beam size of 500 µm is obtained on the sample surface.

Continuous scan was performed at 10 mm/sec scanning speed long the horizontal (X axis) direction and by selecting a step size of 500 µm long the vertical direction (Y axis). Elemental images have been elaborated in real-time by using the in-house programmed software (see Section 3.10, Chapter 3) and a pixel size of 500 µm was selected corresponding to a dwell time of 50 ms per pixel. The measurements were performed at 35 kV and 300 µA. During the scan, the laser system was operated for monitoring the safety distance of the spectrometer from the parchment (0.8 cm) and the flat surface of the sample has not required the real-time correction of the focal distance. Figure 94 shows the MA-XRF scan in measuring. Analytical results will be presented and discussed in the next section.

Figure 94: MA-XRF scanner installed at the Fitzwilliam museum

4.7. The pigments palette of the illuminators

The characterization of pigment materials used by illuminators is a valuable resource for contextualizing the lack information lost when the illuminations were separated from their parent volume. Further, single fragments have been often pasted onto a support (paper, cardboard or wood), losing the information present on the reverse side. In several cases, the hidden information can aid significantly the collocation of the fragments within the parent manuscript or even provide their original position within the book.

The sum spectrum and the spectrum of maximum pixel, in Figure 95, evidences the main elements composing the artist's palette. In particular, Sulphur (S), silicon (Si), potassium (K), calcium (Ca), iron (Fe), copper (Cu), zinc (Zn), tin (Sn), gold (Au), mercury (Hg), and (Pb) are the main components of pigments used. Further, traces of manganese (Mn) and titanium (Ti) have been revealed, they are correlated to ochres (Fe-based pigments), and also strontium (Sr) associated to the pigments containing calcium. Their distribution in the painting will be presented below through the elemental images.
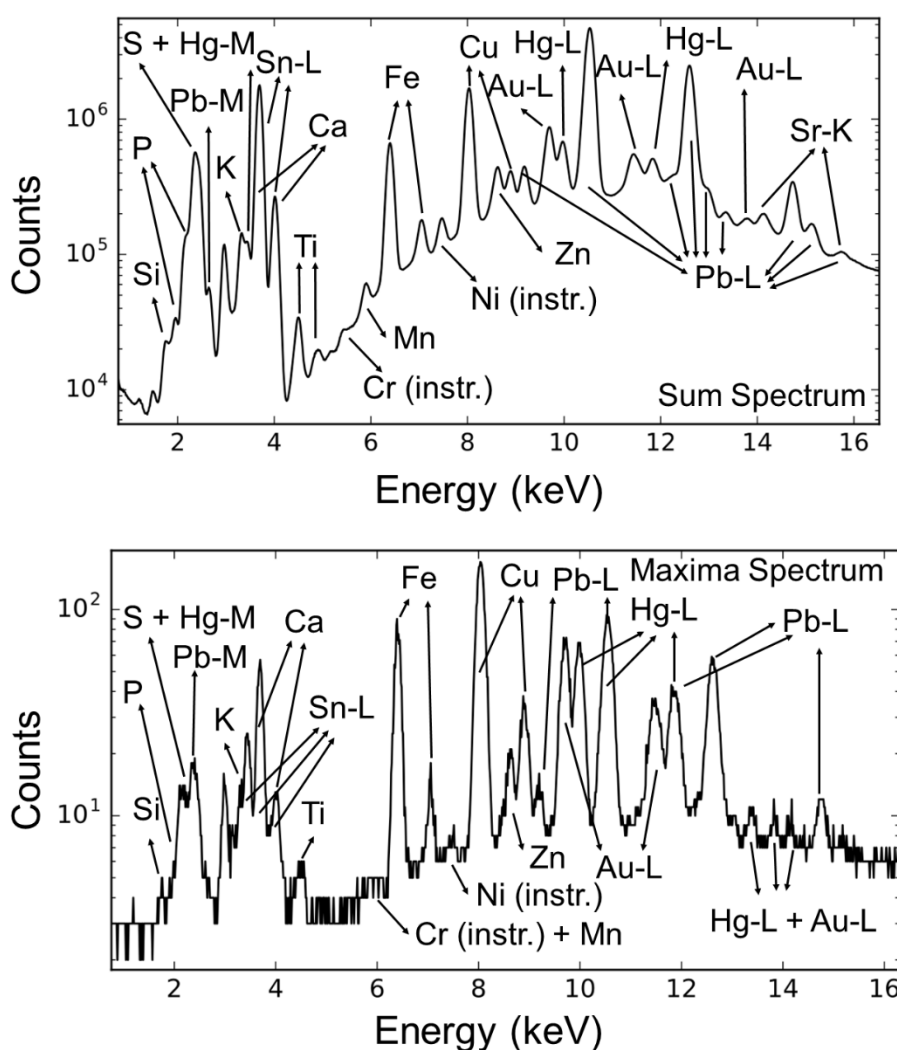
Figure 95: sum spectrum and spectrum of maximum pixel obtained by the MA-XRF analysis of the entire surface of the illuminated manuscript Marlay cuttings It. 13A.

4.7.1 Parchment preparation and white pigments

Calcium-based pigments appear homogenously distributed over the entire pictorial layer, as it can be observed in Figure 96. This makes deduce that the preparatory layer of the parchment has been treated by employing white compounds containing calcium, in the form of gypsum ($CaSO_4 \cdot 2H_2O$), or more likely calcium carbonate ($CaCO_3$), largely diffused in the art of illumination [300].

Further, the correlated presence of strontium (Sr-K) with the calcium-based pigments could indicate the presence of celestite ($SrSO_4$) or strontianite ($SrCO_3$) as impurities of the calcium-containing minerals [301]. Their correlation is visible in the magenta areas of the composite image (Red: Ca-K + Blue: Sr-K) in Figure 96.

In additional, lead-based pigments, commonly in the form of lead carbonates cerussite ($PbCO_3$) and hydrocerussite ($2PbCO_3 \cdot Pb(OH)_2$) [234], have been chosen for drawing white decorations, as it can be seen in Figure 97. Lead white characterizes the temple drawing, the skin tones of the characters, the dove (1), the bed sheet in the Mary's hands (2), the priest's headgear and the decorative motif of the floor.

However, some white painted details are characterized by the alone presence of calcium or used in mixture with a low amount of lead as for example the paper roll in the hands of Saint Anna (3). The composite image Red: Ca-K - Blue: Pb-L in Figure 97 shows the correlation of the two pigments in the magenta and violet areas, as well as in red the free-lead white areas as in the pictorial details (3) and (4) showed in Figure 98.

Finally, in Figure 99 are reported the normalized spectra related to two white areas (area 1 and area 2) painted by using respectively Ca- and Pb-based pigments. In the spectrum of the area 2, the presence of sulphur correlated to the calcium can make supposing that the ground is composed by gypsum ($CaSO_4 \cdot 2H_2O$). Differently from the areas characterized by lead white layers applied on the Ca-based ground, in this area the sulphur discrimination (S-Kα at 2.31 keV) is not affected by the overlap with the low energy line of lead (Pb-Mα at 2.34 keV).

Figure 96: Ca-K image and composite image : Red: Ca-K – Blue: Sr-K (right).

Figure 97: Ca-K image and composite image: Red: Ca-K – Blue: Sr-K.

Figure 98: visible images of areas painted by Ca- and Pb-based pigments.
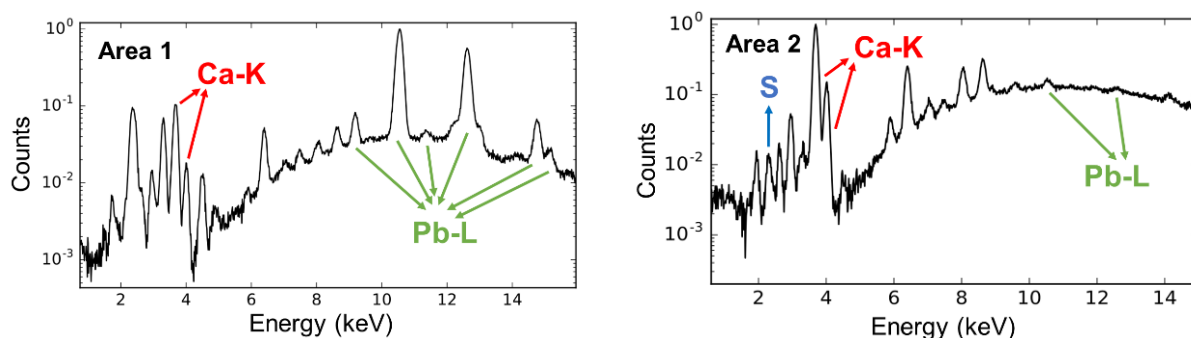
Figure 99: normalized spectra related to the area 1 and area 2 in the painting (Figure 97).

4.7.2 Red pigments and *hidden text*

The brilliant red tones of the Mary's dress (1), the decoration in the upper part of the temple (2) and of the floor (1) are visible in the mercury distribution image showed in Figure 100. Its occurrence is associated to the vermillion (HgS), or its mineral equivalent cinnabar [302]. Further, a writing text on horizontal lines, not present in the painted composition, has been also identified (3). The writing belongs to the pictorial composition painted on the reverse side of the parchment glued to the cardboard support and therefore never read before.

It is a liturgical inscription in Latin written according the rounded Italian Gothic style that flipped left-to-right reveals the following fragmentary text: "*In purifi[catione] b[ea]tissime virgi[nis] Marie. cum can[delae] ceperint dari. In[tr]at cantor*", visible in Figure 100-(3).

The hidden text is also visible in the zinc distribution (Zn-K). Its presence is related to the impurity of the iron gall ink that often can includes variable amounts of zinc and copper [293]. It is a black ink predominantly used from the 9[th] century until it was replaced by synthetic inks in the late 19th century and commonly used for the writings in medieval manuscripts. The zinc map has allowed to integrate the lacking parts of the text not visible in the mercury map. The correlation between the two elements, Hg-L and Zn-K, is showed in Figure 100.
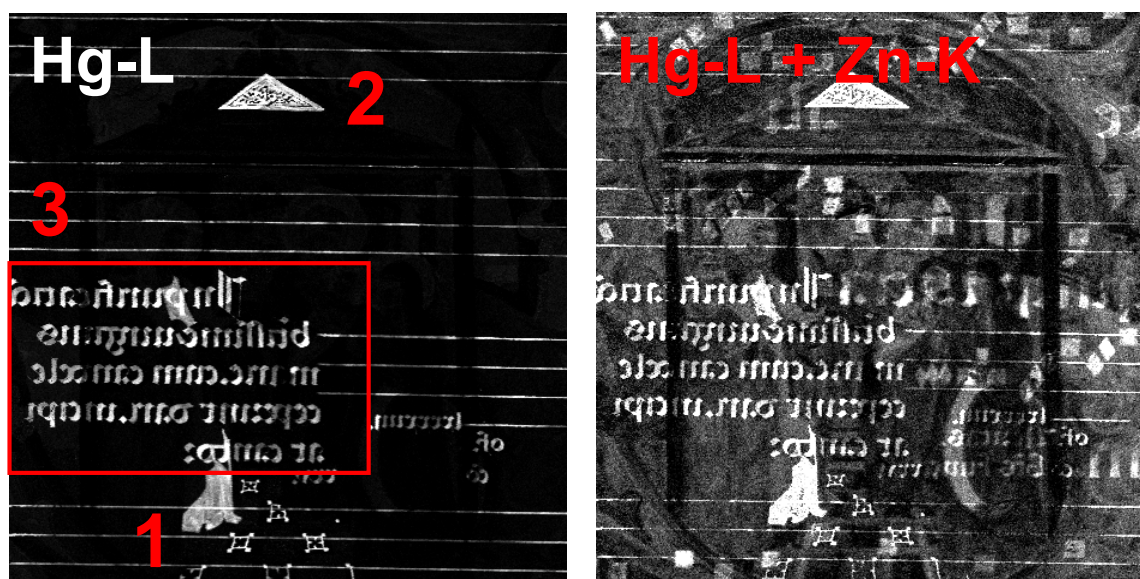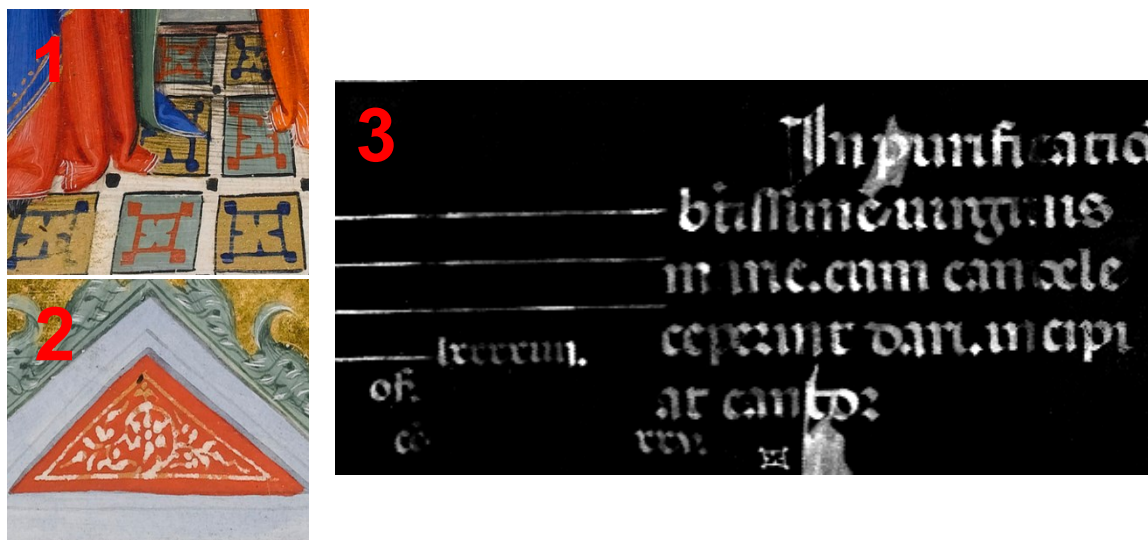
Figure 100: (top) Hg-L image and composite image Hg-L + Zn-K; (bottom) pictorial details characterized by the mercury presence (1-2) and the flipped left-to-right inscription visible in the Hg-L map (3).

4.7.3 Yellow, Orange and Brown Pigments

The presence of tin (Sn-L) in the yellow areas compatible with the 14th century pigments, has to be correlated to the Pb presence in the form of lead-tin yellow pigments [233]. Both its chemical form: lead-tin oxide (type I - Pb_2SnO_4) and lead-tin-silicon oxide (type II - Pb (Sn, Si) O3) were used between 13th and 18th centuries, and most common from 15th to 17th centuries. In particular, the second tin-lead type was found in a Bolognese manuscript, dated back the first half of the 15th century. In the spectrum, the escape peak of the Sn-Lα (1,704 keV) in overlap with Si-Kα line (1.739 keV) does not allow a clear discrimination between the two types of compound (type I or II). In the painting, tin-lead yellow was used for decorating the priest's dress (1), the floral decoration around the large letter "S" (2), and the chess motif on the floor (3) showed in Sn-L map in Figure 101. The tin-lead correlation is also showed in the spectra regarding the three selected areas (1-3).

In particular, in the area 1 spectrum (the priest's dress) the higher Fe-K intensity reveals that the yellow pigment was mixed with ochres for giving the desired chromatic effect. This is also visible in the magenta area in detailed Figure 101-(a) obtained by the correlation of Red: Fe-K + Blue: Sn-L.
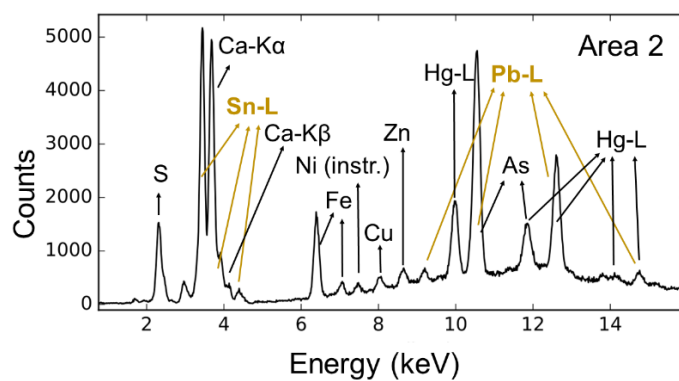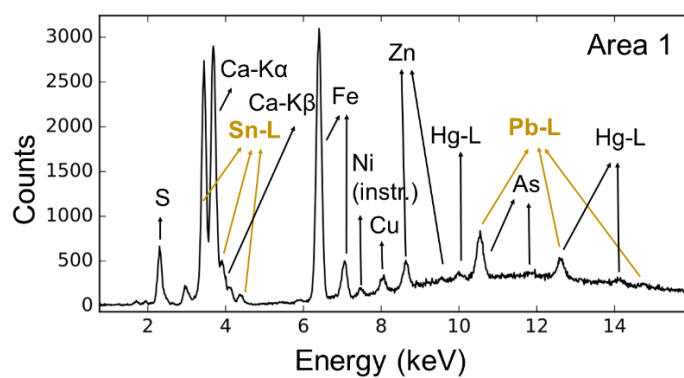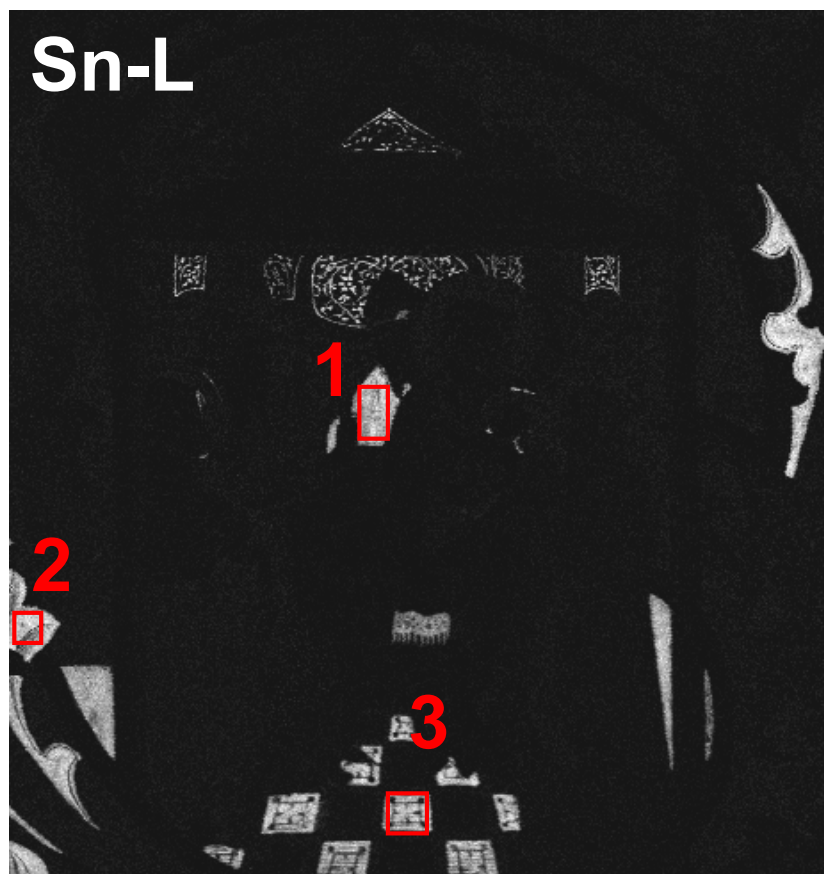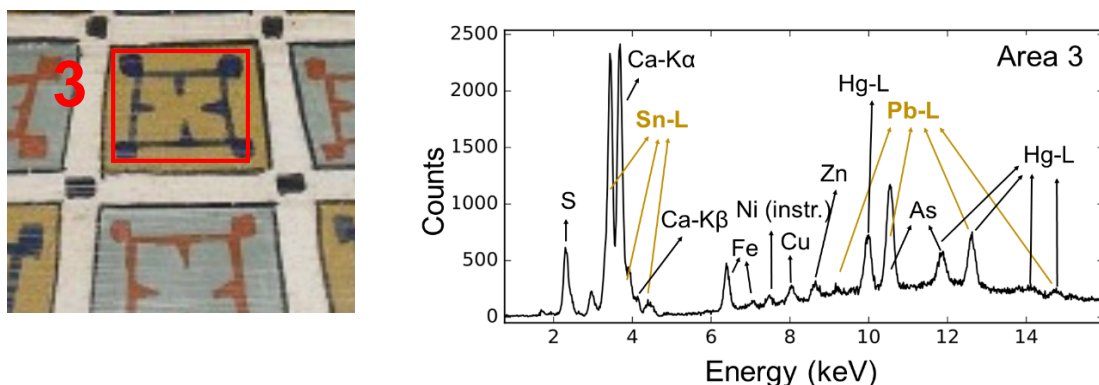
Figure 101: (top) Sn-L image and detailed composite image (Red: Fe-K – Blue: Sn-L) related to area 1, (bottom) cumulative spectra related to the area 1 (20 × 25 pxl), area 2 (15 × 15 pxl), and area 3 (20 × 15 pxl) of the painting.

Beyond the tin-lead pigments, in other yellow shiny details has been found the presence of tin not correlated to Pb. This second typology of yellow can be identified with a metallic pigment composed of stannic sulfide (SnS_2) named mosaic gold [293]. It was used as an inexpensive gold-like pigment and gilding in manuscripts as early as the 13th century and was replaced by bronze powders in the middle of the 19th century. Usually, the pigment preparation method included small quantities of mercury in the amalgam. In the parchment, probably mosaic gold has been used for decorating the upper part of the temple, showed in detailed Figure 102-(1). The related spectrum of the area 1 selected on the red decoration (Figure 102) evidences the co-presence of tin and sulphur that could be compatible with the mosaic gold presence, while lead is not detected. However, it is not possible to ascertain the nature of the pigment through the presence of sulfur (S-Kα line at 2.31 keV) due to the overlap with the low energy line of mercury (Hg-Mα at 2.19 keV). In addition, Hg is related to the vermillion layer on which the gold mosaic decorations have been painted (see paragraph 4.7.2), therefore its presence connected to yellow pigment preparation is not indicative for its identification. Presumable, the mosaic gold pigment was also used for the tiny decorations on the light-blue background behind the priest figure (2). However, as in the previous case, the co-presence of tin and lead does not allow to discriminate between the two typology of yellows due to the overlap between the Pb-Mα line (2.34 keV) and S-Kα line (2.31 keV).
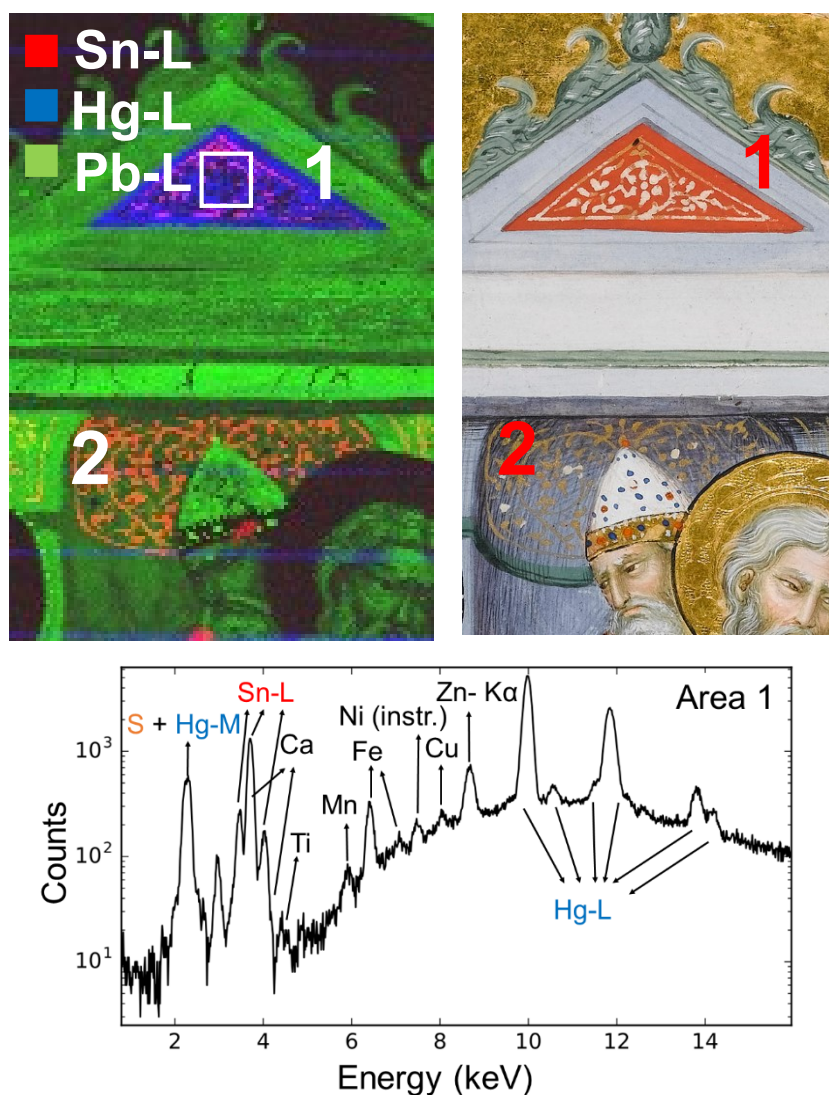
Figure 102: RGB: Sn-L – Hg-L – Pb-L composite image of a selected painted area, cumulative spectrum related to the selected area 1.

Earth pigments (ochres), i.e. iron-based pigments (iron oxide and hydroxides), characterize the details pictorial from brown to deep yellow. The artist paints the skin tones of the characters through light and shadows effects by using ochres (1- 4). In addition, iron-based pigments are used for contouring the figures, like the body of the Christ child (5) and in the floral drawing around the large letter "S" (6). Figure 103 shows the distribution of the iron-based pigments. The fineness of the decorative technique in the combined use of white lead and ochres for the details of the faces and the alternating use of tin-lead pigments and ochers in the decorative patterns that surround the central composition is highlights in the composite image (RGB: Fe-Sn-Pb) in Figure 104.

In addition, red lead (Pb_3O_4) or a few yellow lead oxides such as massicot and litharge (PbO) have been used for painting the orange colors, as the dress of Simeon (1) in Figure 104 [303, 304, 284, 293]. However, their discrimination is not possible through the only elemental analysis and additional information can obtained by complementary molecular techniques.

Figure 103: Fe-K image and pictorial details characterized by the ochres presence

Figure 104: RGB: Fe-K - Sn-L - Pb-L composite image

4.7.4 Green and Blue pigments

The intense green tones, as the Simeon's dress (1), the decorations that surround the scene (2) and the floor decorations, can be identified through the several pigments containing copper, of which their discrimination based only on the XRF technique is not possible [305]. However, it is presumed the use of natural pigments as malachite (Cu2CO3OH2), used until 16th century, and azurite (Cu3(CO3)2(OH)2), used until 18th century, or their synthetic equivalents green or blue verditer [241]. Further, copper can be associated to the green pigment verdigris, consisting of copper corrosion products, mainly acetates, used until 19th century [242], and copper resinate (Cu(C19H29COO)2), used from 15th century until 17th century [243].

The blue tones remain out of the Cu distribution, they are characterized by the presence of potassium (K-K), like the robe of Mary (3), the blue decorations around to the letter "S" (4) and the flooring decors (5). The composite image in Figure 105 shows how copper (in green) and potassium (in blue) cover the green and blue painted areas respectively. Further, the light-blue tones are obtained by a mixture of pigments containing potassium with lead white, as it is evidenced by the magenta areas in Figure 106 (Red: K-K + Blue: Pb-L).

In previous studies on 15th century Italian manuscripts the high presence of potassium correlated to the blue tones has been associated to the use of ultramarine ($Na_{8-10}Al_6Si_6O_{24}S_{2-4}$) [67]. Oltremare (or ultramarine) derives from the semi-precious gemstone lapis lazuli and it was used in its mineral form since 12th century.

Despite its chemical formula does not include the potassium, its correlation is due to the high K concentration identified directly in Afghan lapis lazuli stone samples [306], main source of ultramarine blue for over six thousand years [88].

This correlation is strengthened by the fact that the K presence in other pigments compatible with the dating of the manuscript is found in the smalt, a potassium glass containing cobalt (15th -18th century), however any presence of cobalt has been detected in the painting. Finally, the presence of potassium can be attributed to the lake pigments of organic nature.
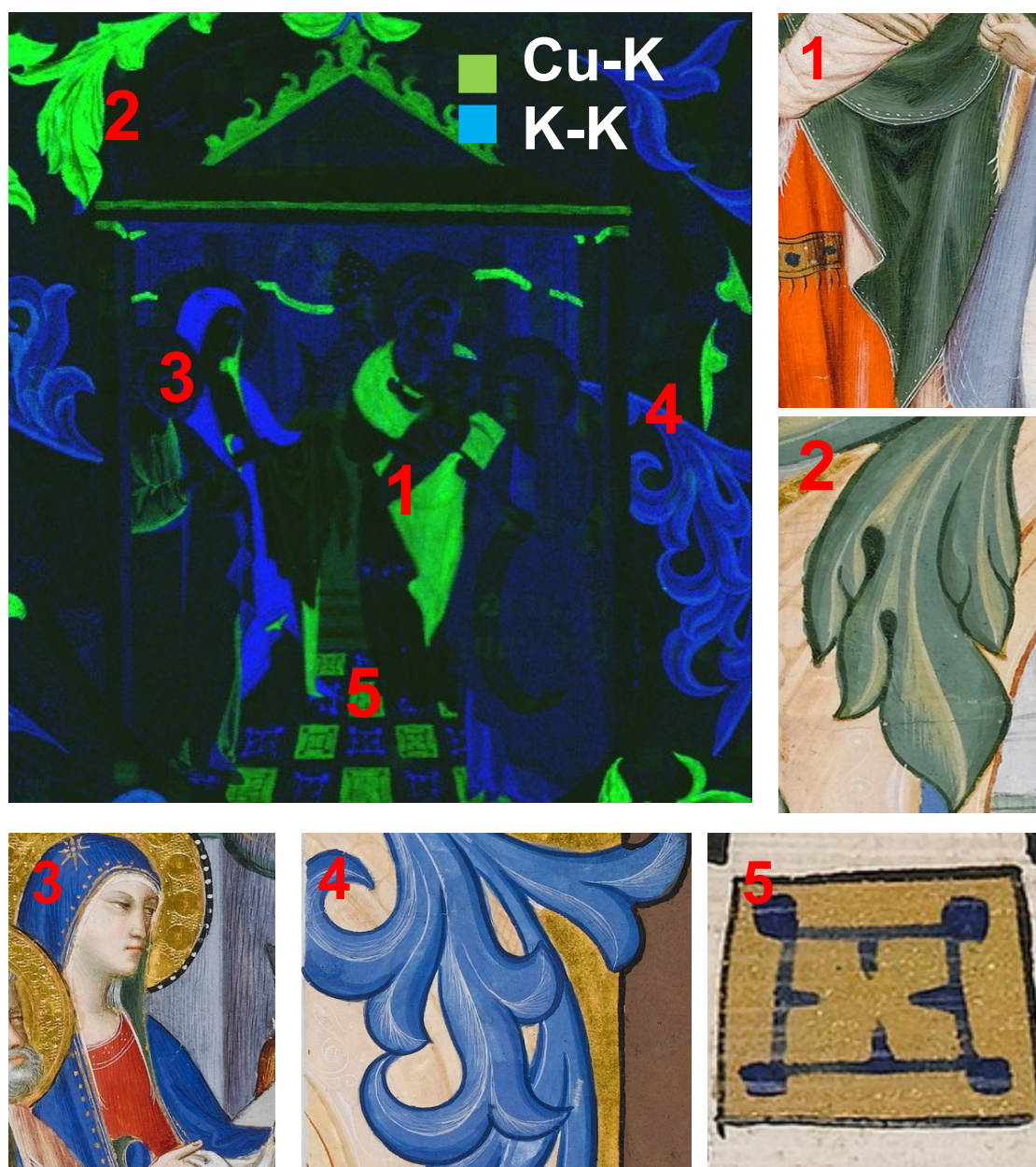
Figure 105: composite image Green: Cu-K – Blue: K-K and pictorial details characterized by copper (1-2) and potassium presence (3-5).
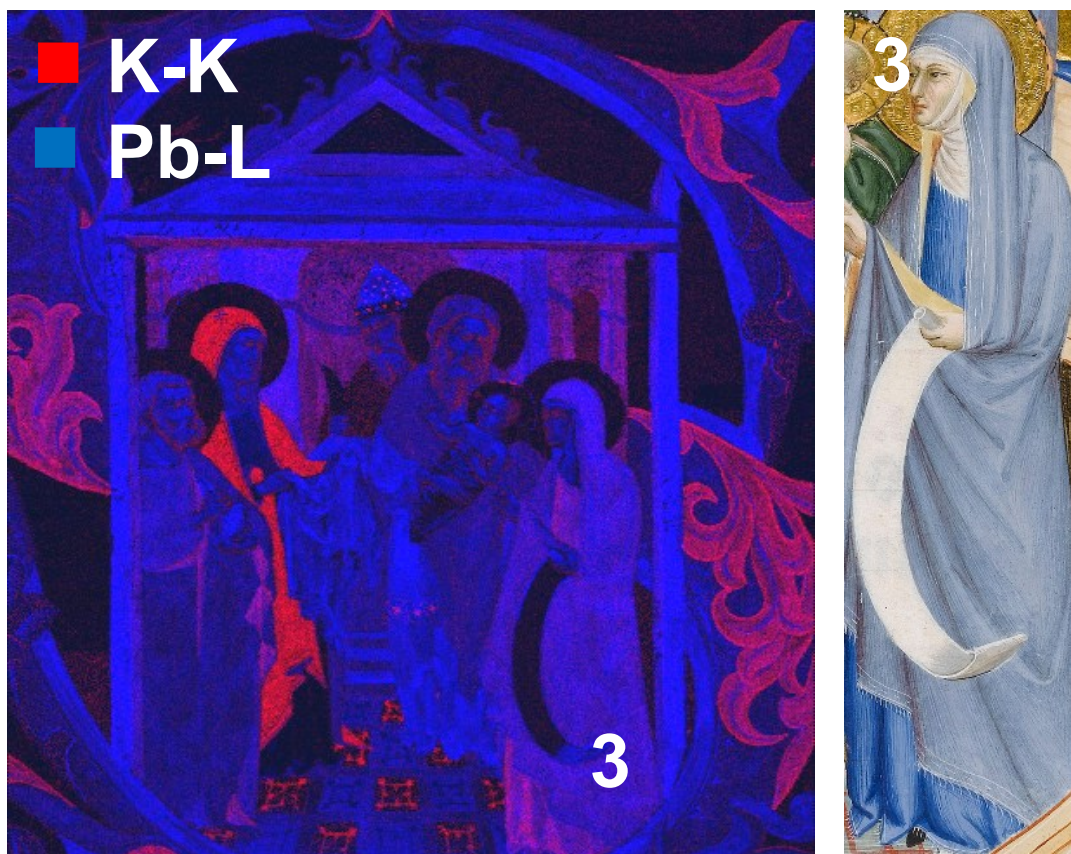
Figure 106: composite image Red: K-K – Blue: Pb-L and pictorial details characterized by potassium-lead mixture (3).

4.7.5 Gold

In the art of the illuminated manuscripts, the employment of precious materials, as gold or silver, is a hallmark of the pictorial technique used in this type of artworks [307, 308]. Figure 107 (top) shows the gold (Au-L) distribution in the parchment. In particular, gold decorations are characterized by two different painting techniques. The first consists of applying of small thin sheets of hammered gold, placed side by side over a preparatory layer, in this way the artist has decorated the background behind the temple and the halos of the Saints (1). The decorative technique is identifiable by the visible overlapping of the adjacent gold sheets and by the higher Au-L intensity recorded in the overlapped zones respect to the single layer as it is showed in the spectra in Figure 107 (bottom) related to the analysis of area 1. In additional, the tecnique includes a ground preparation containing ochres. This emerges in the magenta zones (Red: Au-L + Blue: Fe-K) in the composite Figure 107 (top).

Finally, the second technique consists of the use of finely ground gold particles held together by a binder medium used by the artist for the very fine decorations of the Mary dress (2).
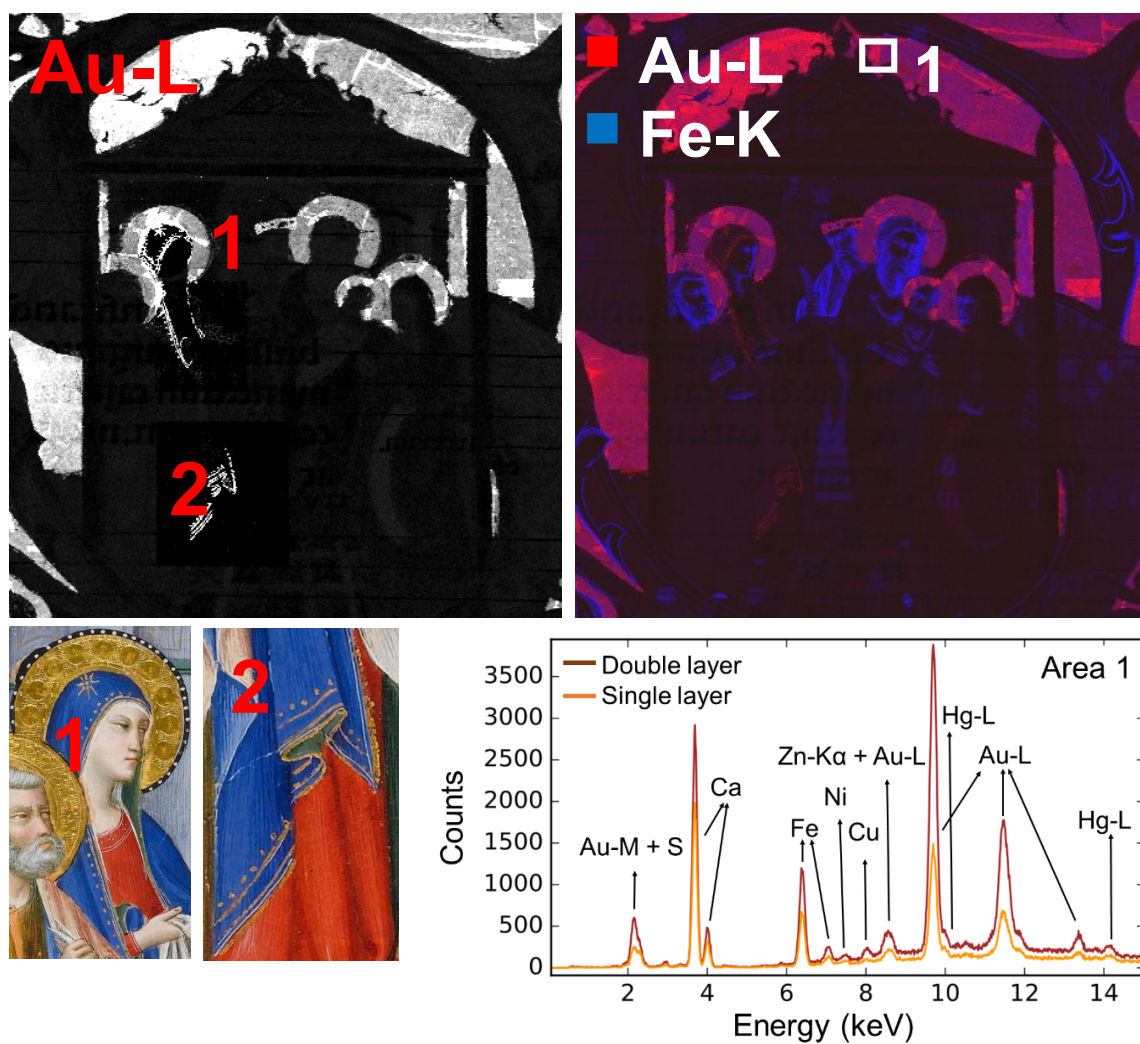
Figure 107: (top) Au-L image and composite image Red: Au-L – Blue: Fe-K, (bottom) pictorial details characterized by gold presence (1-2) and cumulative spectra comparison between a single and a double gold layer taken in rectangular selection (area 1).

APPENDIX-A

Micro XRF imaging

MA-XRF mobile scanning system developed in the present research activity, of which experimental components, spectroscopic capabilities and scanning modes have been discussed in the Chapter 3, allows to perform, in complementary way, the imaging technique operated on micrometric scale of length (micro-XRF).

The analytical capabilities of the instrument as micro-XRF scanner will be demonstrated in this appendix through the presentation of analytical results obtained on a copy of Madonna and Child with Saints Rosalia, Peter and Paul painted by Anthon van Dyck (1629, 45×35 cm^2 size, private collection), shown in Figure 108.

As explained in Section 1 in Chapter 3, the primary source of the scanner assembled on the spectrometric head consists of a microfocus X-ray tube coupled to a policapillary optics.

MA-XRF mapping takes advantage of the strong divergence of the lens for obtaining a larger beam size, in the range of few hundred microns (commonly 500 μm), making the technique suited for the analysis of large easel paintings, as described in Section 1.2 (Chapter 1)and illustrated through the analytical results in the Chapter 4.

However, the strong focusing power of the lens can be also used for illuminating the sample with a micrometric beam size in the range of tens of microns. This involves a simple adjustment of the sample position on the focus of the lens. Micro-XRF imaging is achieved with lateral resolution up to 38 μm (Section 3.5, Chapter 3) by positioning the sample at a distance of 10 mm from the lens end. The long range optical microscope (Section 3.1.3, Chapter 3) is used for positioning the sample at the polycapillary focus and the laser sensor (Section 3.1.4, Chapter 3) is used for the dynamic correction of the distance of the measurement head from the painted surface during the micrometric scan.

Micro-XRF technique is particularly indicated for investigated small details of the painted composition allowing a better knowledge of the painting technique and a more accurate pigment attribution and dating.

Elemental maps at a micrometric scale of length obtained from selected area in the upper-left part in the panel (Figure 108 (a-b)) are showed in Figure 109.

Measurements were performed at 38 kV and 400 μA with the panel positioned in the focus of the polycapillary. A pixel size of 25×25 μm^2 was elaborated by the Control Unit (CU) during the continuous scan at 1 mm/sec scanning speed corresponding to a dwell-time per pixel of 25 ms. Images of 800×800 pixels (i.e., 2×2 cm^2 area) were taken in about 4 h. The maps were processed real-time by using the in-house programmed software (Section 3.10, Chapter 3). Under these experimental parameters, the high resolution of the scanner has allowed to evidence millimetric particulars of the pictorial layers as the coarse particle size of the As and Ba component in the painting of foliage.

Micro-XRF analyses has allowed investigating more accurately the presence of anachronistic pigments in the investigated area that seems not related to a retouch or a restoration and suggests postponing the manufacturing of the panel to a later period (i.e., 19th century).

In particular, particles in the green pigment are composed of both As-K and Cu-K as evident in the yellow particles given by the correlation of Green: Cu-K and Red: As-K images in Figure 110 (a). This result could be compatible with the presence of emerald green for the pale green in the foliage. Emerald green is a 19th century pigment that collocates the dating of the panel in a later period.

In addition, barium and chrome are correlated in the green leaves of the painting, as it is showed in the yellow areas in the composite Figure 110 (b) obtained by the correlation of Cr-K (red) and Ba-L (green) images. Again, the probable use of chromates (i.e., barium chromate) suggests a pigment manufactured in 19th century.

Finally, the presence of Zn and Ti, showed in Figure 110 (c-d) and present in other areas of the painting, highlighted by MA-XRF analysis, suggests a possible later manufacturing of the painting.
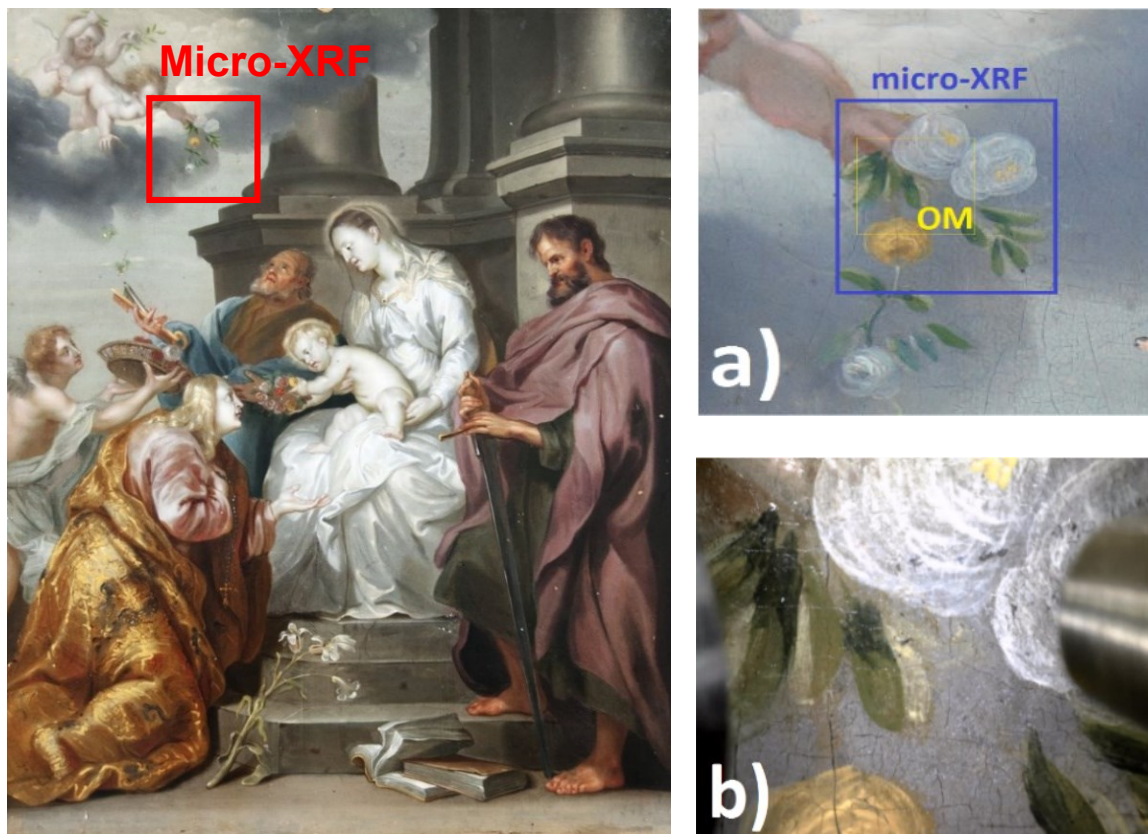
Figure 108: copy of Madonna and Child with Saints Rosalia, Peter and Paul painted by Anthon van Dyck (1629, 45×35 cm^2 size, private collection) (top), selected area investigated by micro-XRF technique (a), microscope image of the selected area (b).
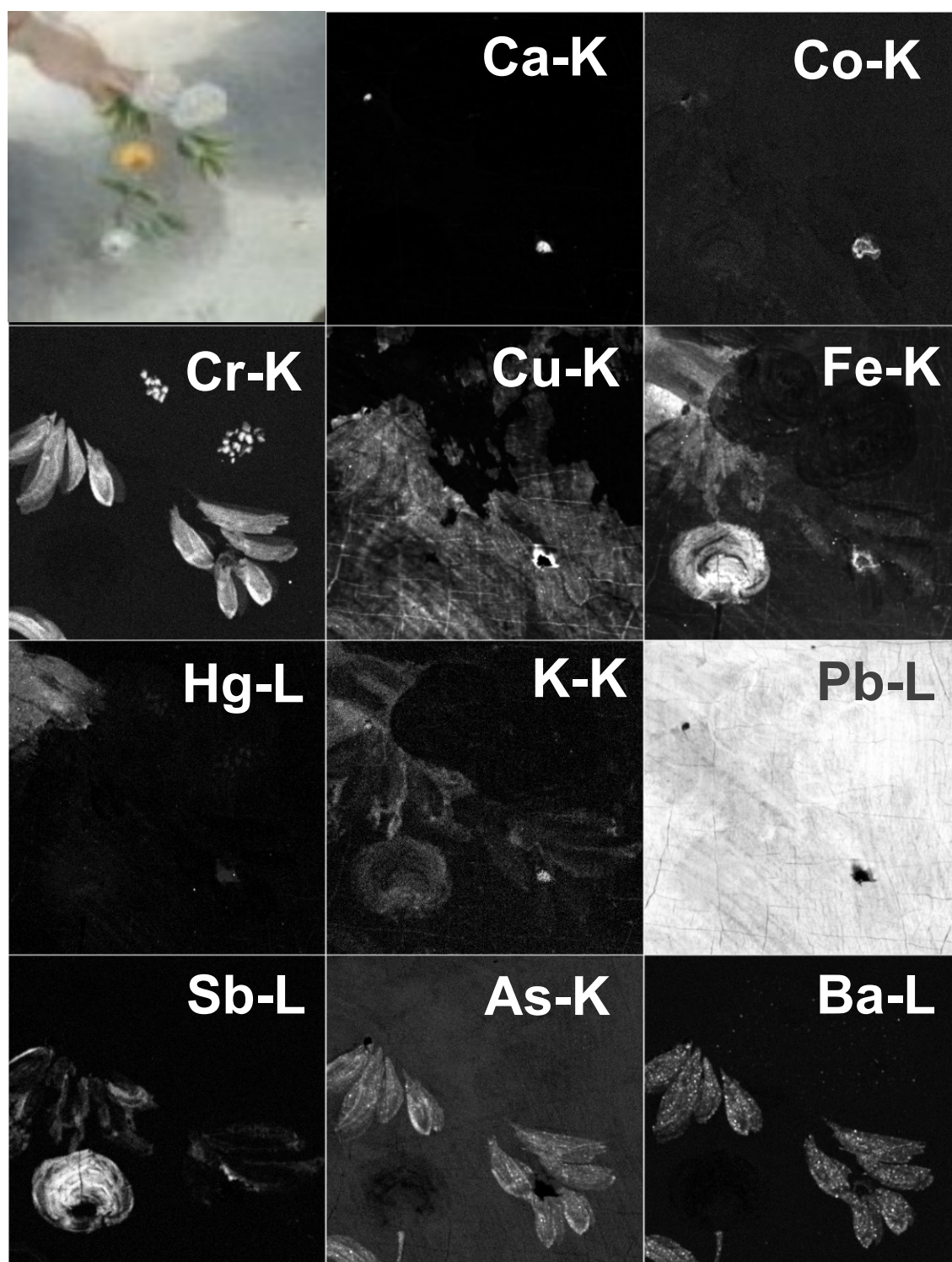
Figure 109: micro-XRF images obtained on a selected area of the painting (800 × 800 pixels, i.e., 2× 2 cm^2).
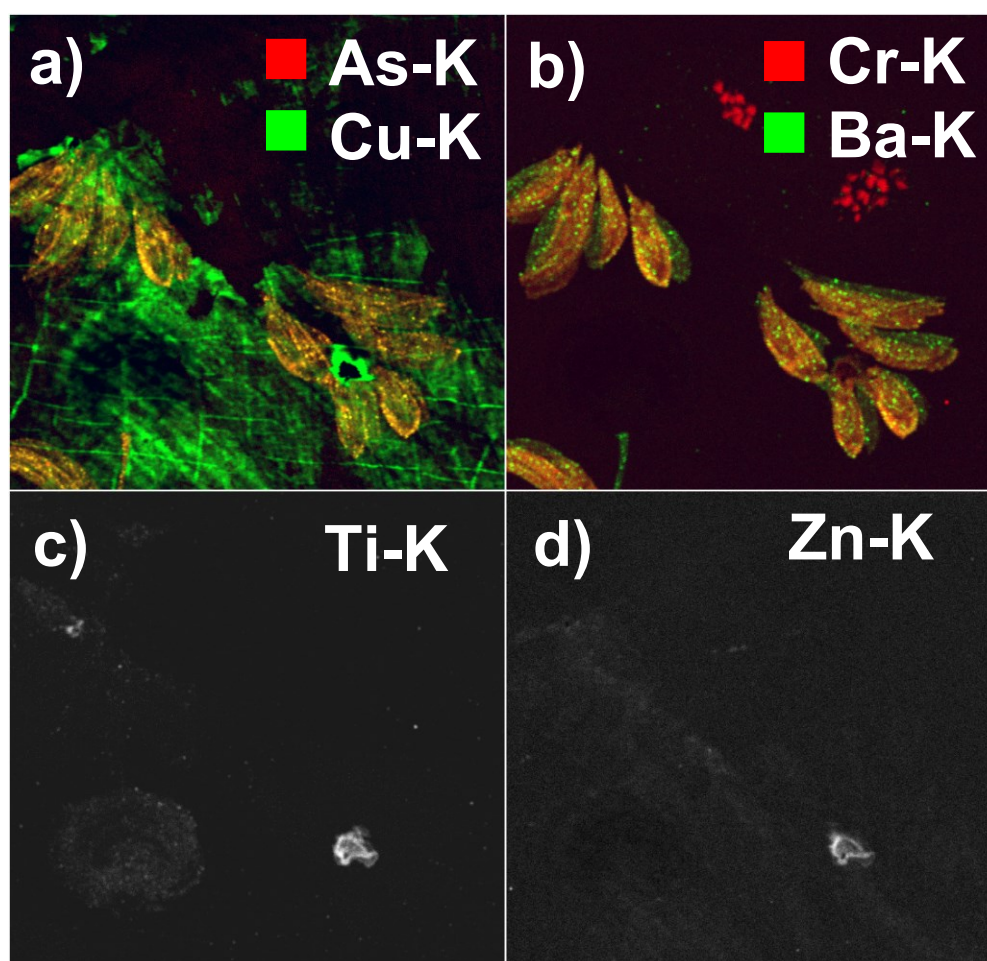
Figure 110: composite image Red: As-K – Green: Cu-K (a); composite image Red: Cr-K – Green: Ba-K (b), Ti-K and Zn-K images (c-d).

APPENDIX-B
Main cited pigments[**]

White

1) Lead White

Chemical formula: $2PbCO_3 \cdot Pb(OH)_2$
Origin: artificial
Historical period: antiquity (Greeks) – in use

Lead white (native mineral is cerusite) is a carbonate of lead prepared from metallic lead and vinegar. It was used since antiquity as early as 400 B.C. and it was the only white used in European easel paintings until the 19th century when its poisonous lead content has restricted its manufacture and sale as an artist's pigment. Lead white presents a fastest drying compared to all whites when it is used in oil. This makes it particularly valuable for painters who need a relatively fast drying time.

2) Chalk and Gypsum

Chemical formula: $CaCO_3$ (chalk); $CaSO_4-2H_2O$ (gypsum)

Origin: calcite; selenite (for gypsum)
Historical period: prehistory– continue in use

Chalk is calcium carbonate (calcite); a white pigment with limited hiding power. It is chemically stable under ordinary conditions. Chalk is known from prehistory and it is used until today.
Gypsum is a soft, transparent mineral composed of hydrated calcium sulfate.

Brown

3) Umber

Chemical formula: $Fe_2O_3 \cdot (H_2O) + MnO_2 \cdot (n\ H_2O) + Al_2O_3$
Origin: natural earth
Historical period: prehistory – in use

[**] *Sources: http://www.webexhibits.org/pigments/, http://cameo.mfa.org/wiki/Main_Page, http://colourlex.com/*

Umber is a natural mixture of iron and manganese oxides and hydroxides. Used throughout the history, its colour goes from cream to brown depending on the amount of iron and manganese compounds and it is totally stable. These pigments are known also as Sienna earths. They are permanent and they can be safely mixed with other pigments. Ochres can to vary widely in transparency: some are quite opaque, while others are valued for their use as glazes.

Green

4) Malachite

Chemical formula: 2 $CuCO_3.Cu(OH)_2$
Origin: mineral and artificial
Historical period: antiquity (Egyptians) – 16th century

Malachite is a mineral composed of basic copper carbonate. It is the oldest known green pigment., sensitive to acids and to heat.
It is found in Egyptian tomb paintings and in the European paintings its use became of importance mainly in the 15th and 16th centuries.
Malachite has often proved to be permanent in oil paintings, although it may acquire a brownish hue owing to the darkening of the oil. It is lightfast but due to the copper carbonate blackening by sulfur compounds found in polluted air, malachite may be affected by exposure to hydrogen sulfide.

5) Verdigris

Chemical formula: $Cu(C_2H_3O_2)_2-2Cu(OH)_2$
Origin: artificial
Historical period: antiquity (Greeks) – 19th century

Verdigris is a dark bluish-green pigment composed of basic copper acetate with low stability. It was used from antiquity and in particular in the Middle Ages, Renaissance and Baroque. Verdigris was the main green available until the 19th century, it was often mixed with other pigments as lead white or lead-tin yellow caused to its transparency. It is particularly reactive and unstable among all the copper pigments, often it changes into a dark brown or black.
Historically, the various types of copper corrosion products were not differentiated but rather lumped together and called aerugo or verdigris. However, these corrosion products are typically composed of copper sulfate, copper chloride, or basic copper carbonate.

6) Copper resinate

Chemical formula: $Cu(C_{19}H_{29}COO)_2$
Origin: artificial
Historical period: 15th century– 17th century

Copper resinate is a transparent green glaze containing copper salts of resin acids. Several preparation procedures indicate that it is a mixture of verdigris in Venice turpentine while others describe it as a mixture of verdigris in an oil/resin medium. In the 15th and 17th centuries the artists added copper resinate for creating a deep saturation of green colour. Often it is used in combination with azurite or layered over lead white or lead-tin yellow. Copper resinates are similar to azurite in appearance and chemistry, they can change with age by forming copper salts of fatty acids.

7) Green earth

Chemical formula: K[(Al,FeIII),(FeII,Mg)](AlSi3,Si4)O10(OH)2
Origin: artificial
Historical period: antiquity (Greeks) – in use

Green earth is a green-coloured siliceous, iron-rich clays used as pigment since ancient times. The colour of green earth can range from yellow-green to sea-green to greenish-gray. In general, green earth is translucent in oils with moderate tinting strength and poor hiding power. It is a permanent, stable pigment and compatible with all media. Earths are not affected by sunlight or by atmospheric conditions. Green earth or terre verte is sometimes imitated by mixtures of Naples yellow and Prussian blue.

Blue

8) Azurite

Chemical formula: 2 CuCO3 · Cu(OH)2
Origin: mineral and artificial
Historical period: antiquity (Egyptians), artificial (17th century) – 18th century

Azurite is a deep blue mineral composed of basic copper carbonate, naturally it is found adjacent to the green copper carbonate mineral called malachite. Its occasional use began with Egyptians, but it was uncommon until the Middle Ages when the manufacture of the ancient synthetic pigment "Egyptian blue" was forgotten. It was produced artificially from the 17th century and it was replaced by "Prussian blue", discovered in the 18th century. Azurite was the most important blue pigment in European painting throughout the Middle Ages and Renaissance. Azurite is subjected to two process of degradation into green or into black. The oxidation process causes the colour change from blue to green, in addition, it suffers of the alteration in a black pigment: the copper oxide, tenorite.

9) Egyptian Blue

Chemical formula: CaCuSi4O10
Origin: artificial
Historical period: Antiquity (Egyptians) – Antiquity (Romans)

Egyptian Blue is a synthetized pigment composed of a double silicate of calcium and copper. Egyptian blue is prepared by heating a mixture of silica, copper salts, and calcite in a sodium carbonate flux to 830 C. It was manufactured by Egyptians and used for thousands of years, it is considered to be the first synthetic pigment. Egyptian Blue was known to the Romans by the name caeruleum.

10) Smalt

Chemical formula: $SiO_2(65\%) + K_20\ (15\%) + Al_2O_3\ (5\%) + CoO\ (10\%)$
Origin: artificial
Historical period: 15th century – 18th century

Smalt is a coarsely ground blue potassium glass containing small amounts of cobalt oxide, which provides the source of the blue colour. It was diffused among the 15th and the 18th centuries. In Europe the use of smalt as an artist's pigment was widespread certainly as early as the late 16th century. Smalt was popular because of its low cost and its manufacture became a specialty of the Dutch and Flemish in the 17th century. Smalt is a stable, lightfast pigment, but it has poor covering power. In oil media, it frequently discolours to a gray or grayish brown tone through a complex interaction of pigment and medium, which involves leaching of potassium and cobalt from the particles and the formation of potassium soaps in the paint film. The process is impeded by admixture with lead white, but worsened by moisture.

Red

11) Vermilion

Chemical formula: HgS
Origin: mineral (cinnabar) and artificial (vermilion)
Historical period: antiquity (Greeks), artificial 8th century– 19th century

Vermilion is a bright red pigment composed of synthetically prepared red mercuric sulfide mineral (cinnabar) with excellent hiding power and good permanence. It was used from antiquity and produced artificially from the 8th century (vermilion). It was the main red in painting. Its use was dramatically reduced in the 20th century due to its known blackening upon reaction to hydrogen sulphides and replaced with cadmium red.

12) Red Ochre

Chemical formula: Fe2O3
Origin: mineral and artificial
Historical period: (natural) prehistoric/ (artificial) 18th century- continues in use

Red ochre is composed mainly of iron oxide or hematite. These permanent pigments have been used from prehistory and throughout history and they can be safely mixed with other

pigments. Ochres vary widely in transparency; some are quite opaque, while others are valued for their use as glazes. Throughout the Middle Ages and the Renaissance, they continued to be used by painters, as Michelangelo, Rembrandt and Antoine Watteau. From the 18th century, synthetic red iron oxide pigments were manufactured, they are called Mars Red and they were found to have all the properties, including durability and permanence, of their natural counterparts.

Yellow

13) Yellow ochre

Chemical formula: FeO (OH)
Origin: natural and artificial
Historical period: (natural) prehistoric/ (artificial) 1920s- continues in use

Yellow ochre is a natural mineral consisting of silica and clay owing its colour to an iron oxyhydroxide mineral, goethite. It is found in many shades, in hues from yellow to brown. Used throughout history, this permanent pigment can be safely mixed with other pigments. Ochres vary widely in transparency; some are quite opaque, while others are valued for their use as glazes. Synthetic yellow ochre, Mars yellow, have been produced since the early 1920s.

14) Orpiment

Chemical formula: As2S3
Origin: natural and artificial
Historical period: Antiquity (Egyptians) – 19th century

Orpiment is a soft, yellow mineral composed of arsenic trisulfide. It occurs naturally in volcanic fumaroles, hydrothermal veins, hot springs, and as a decomposition product of realgar (As4S4). Orpiment ranges in colour from a bright lemon yellow to orange. It was used as a pigment in European painting from quite early times, including in manuscript illumination and coloured sculpture, and became almost a standard material on the palette in Venice in the 16th century. Elsewhere it occurs in Dutch 17th century painting, and British and French 18th century paintings. Its use continued almost up until today, though it is moderately used due to its toxicity. Orpiment has good tinting strength but is not considered permanent as it reacts with copper pigments as well as some lead pigments to produce dark copper or lead sulfides. It can be rather light sensitive, losing its colour on prolonged exposure to light, particularly in aqueous media. Arsenic trisulfide was made synthetically in the 18th entury and sold as king's yellow.

15) Lead-tin yellow

Chemical formula: Pb_2SnO_4 (Type I) - $Pb(Sn,Si)O_3$ (Type II)
Origin: artificial
Historical period: 13th century – 18th century

Lead-tin yellow is a manufactured pigment composed of lead stannate. It is an opaque yellow with good covering power. Lead-tin yellow was used in European paintings from the beginning of the 14th century until the early years of the 18th century, although it had largely disappeared from painting at the end of the 17th century when it was replaced by Naples yellow (lead antimonate yellow). Lead-tin yellow was rediscovered and made artificially in 1941. These yellow pigments are stable and have been used as opacifiers and colorants also in glass and ceramic glazes. They are lightfast and essentially stable in all paint media. Lead-tin yellow was often used in mixtures with other pigments such as lead white, vermilion, azurite, verdigris, and indigo.

Black

16) Bone black/Ivory Black

Chemical formula: $Ca_3(PO_4)_2 + CaCO_3 + C$
Origin: animal
Historical period: Prehistory- continues in use

Bone black is blue-black in color and it contains about 10% carbon, 84% calcium phosphate and 6 % calcium carbonate. It is made from charring of bones or waste ivory and tt was used from prehistory until today. Ivory Black is therefore the least pure form of carbon black, containing a high percentage of calcium phosphate. Bone black has been identified in prehistoric paintings and found in Egyptian, Greek and Roman art. It is found throughout European medieval and Renaissance art and later in both oil and watercolour paintings until modern times. Bone black is a permanent colour for all uses on the artist's palette. It is compatible with all other pigments and can be used with good results in all media.

17) Carbon Black

Chemical formula: C
Origin: vegetable
Historical period: prehistory- continues in use

Carbon black is a fine particle carbon pigment obtained as soot from the incomplete combustion of many different types of organic materials, such as fruit pits, vine stalks, husks, bone, ivory, cork, resins, natural gas, or oil. Carbon black pigments have been used since ancient times. It is very stable and unaffected by light, acids and alkalis and it has an excellent hiding power. It is considered one of the most stable and refractory of all materials. In particular, it was largely used for the artist's sketches under the painting.

Binder

18) Alum (Potassium aluminium sulfate)

Chemical formula: $AlK(SO_4)_2.12H_2O$

Origin: metallic salt
Historical period: antiquity (Egyptians, Greeks) - continues in use

Potassium aluminium sulfate (or alum) is the reagent that forms the solid (precipitates) as hydrated alumina bound to the dye. It is a metallic salt known as the lake pigment that was used as the binder or mordant. It must be inert, colourless, chemically neutral and insoluble in the liquid medium. In the Greek and Roman periods alum, chalk, white clay, and crushed bones were often used as sources of the binder for lake pigments. In today's industry the binders used for lake pigments are barium sulfate, calcium sulfate, aluminium hydroxide and aluminium oxide (alumina). Changing the pH of the solution can change the hue and even in some cases the colour of pigments. The lake pigments were important pigments for the Greek, Roman and Renaissance artists.

Conclusions and prospective

Paintings are complex multi-layered materials that have been studied over the time with several sophisticated imaging techniques. It is well recognized that analytical result contributed efficaciously to art-history and conservation science.

Scanning MA-XRF technique provides information on pigment materials and their distribution over the painted surface in a non-destructive way, giving new insights on painting techniques used in the various artistic movements over the time. In addition, it provides information on conservation state of artworks allowing to identify appropriate conservation procedures and to identify restoration treatments occurred in the past. MA-XRF is also suitable for approaching question of authenticity of artworks through the presence of anachronistic pigments. Finally, the penetrating nature of X-rays allows visualizing sub-surface layers that can present hidden pictorial compositions, revealing what it is not visible to naked eye.

In the present PhD activity an advanced XRF scanning system for a real-time imaging of painted artworks has been developed.

The MA-XRF scanner has been developed with a modular set-up to be assembled/disassembled in a short time (30-60 min) and easily moved in museums, galleries and conservation studio for performing in-situ analyses. It consists of three linear stages with a travel range of $110 \times 70 \times 20$ cm^3 for the motion of the spectrometer in the XYZ direction respectively. To date, this is the largest area covered among the MA-XRF scanners today available. The three-axes system is based on a customized design with a wire sensor technology that offers the advantage to avoid any referencing of the axes before starting a new measurement, in this way the measurements can be interrupted and restarted (system switched on/off) from the same position. The motion of axes is entirely controlled by the Control Unit (CU) and whatever orientations (top-down and vice versa) and directions (left-right and vice versa) can be selected by the user on the basis of the sample to be investigated. Further, the CU controls the Z-axis movement, along the focal distance, via the communication with a laser triangulation sensor (750 Hz read-out rate and 4 μm linear resolution) assembled on the measurement head for monitoring in live mode the distance of the painting from the spectrometer. The distance is dynamically corrected in order to maintain the measurement head at a constant distance from the sample in the case of a non-flat sample surface. In addition, the motion of axes is immediately stopped when the measurement head reaches a sample-spectrometer safety distance preconfigured by user.

The scanning system performs scans in real-time (or in continuous mode) along one axis with a uniform speed. This is allowed by the coupling of the detection system based on a SDD detector (130 eV energy resolution at 5.9 keV) to a 100 MHz Digital X-ray Processors (DXP) that works in a time-list event mode (TLIST) with a 40 ns time resolution. The

scanning along the second axis is provided by a step mode. Also a full step-by-step mode is available if needed.

During the real-time scan, the continuous stream of data is transferred to the Control Unit (CU) with a preset time interval (usually 100 ms), however in case of data overflow occurring at the higher count rates, the CU automatically stops the scanning and dynamically adjusts the data transfer time in order to eliminate the acquisition error and restarts the measurement without any loss of data. The advantage to perform continuous scanning resulting in a reduction of the total time of 1.5 times without any lateral resolution and count rate degradation has been demonstrated by the direct comparison between continuous mode and step mode scan.

In the scanning systems, the possibility to perform scans at high speed has been often limited by the lack synchronization between the motorized stages and detector.

The present system allows ultra-fast scans with selected speed up to 100 mm/sec covering the total area in 4.2 hours with a lateral resolution of 500 μm. The high precision and synchronization between motion sensors and acquisition system is fully controlled by the custom developed and programmed Control Unit based on a deterministic Linux real-time operating system (RTOS) via embedded drivers and libraries of all sensors installed in the device. Further, CU allows to monitor the instrument operation in a real-time via a customized user-friendly interface developed in real-time LabVIEW software.

The MA-XRF device of the present work is aimed to the macroscopic analysis of large size paintings. However, the use of a polycapillary lens (1 cm focus) equipping the X-ray source, allows a dual configuration for operating the MA-XRF imaging at both the macro and micro scale of length. Micro-XRF imaging is obtained operating the scanning at the focus position; macro-XRF is performed with the sample out of the focus distance. The two imaging techniques can be combined for a better knowledge of the painting process and a more accurate pigment attribution and dating.

In particular, MA-XRF is based on the use of a broad beam of few hundred microns. The lens divergence allows obtaining a beam size of 500 μm at 15 mm from the spectrometer head. Further, micro-XRF imaging can be performed with a lateral resolution up to 35 μm at the focus. The accurate positioning of the painting from the measuring head is obtained by using a long range optical microscope with a 19 μm depth of field and about 2.5 μm lateral resolution.

To date, performances of this device in terms of lateral resolution, scanning speed and dimensions of the scanning area, makes it as one of the most (or even the most) efficient portable MA-XRF systems available in the scientific community for studying paintings.

A further distinctive feature of the instrument consisted in the development of real-time elaboration procedure of X-ray data. The real-time spectra elaboration offers the advantage to have the available images when the acquisition finish, obtaining a significant gain in terms of time, an immediate preliminary interpretation of data and also the monitoring of a correct progress of the scan.

Each pixel spectrum is processed by applying the PyMca fast-fitting plugin based on the non-linear least-squares method. Its integration in the analysis procedure differs from the

conventional real-time analysis (if present) of other devices, based on the less accurate selection of region of interest (ROI) in the spectra. The in-house programmed analysis software runs during scan and allows the (near) real-time data transferring with a maximum processing speed up to 5000 fitted spectra per second. In addition, the analysis software provides different tools for processing the images in live mode, by changing graphical settings as color-maps, contrast and brightness, resizing, etc. Arithmetic and logical operations can be also applied to the images for subtracting noise or contaminations and also eventual systematic shift correction can be operated. It allows also the RGB correlation of the maps for helping the pigments identification. Finally, the pixel size of images can be changed during the continuous scanning if images are not satisfactory in terms of lateral resolution or counts statistic.

During the present research activity, the scanner was validated by studying three painted artworks on different support (canvas, wood and paper) and different size, for which the instrument has been moved in situ.

A MA-XRF investigation of the Paston Treasure (oil on canvas, 165 x 246.5 cm^2) was carried out in collaboration with the Fitzwilliam Museum (Cambridge, UK), the Yale Centre for British Art (USA) and the Norwich Castel Museum an Art Gallery (Norwich, UK). This allowed to characterize the original materials used by the artist, highlighting the chromatic complexity of the painting technique and the meticulous research in the use of the pigments and in their mixture. Further, it was possible to identify the degradation state of some pigments as a darkening effect occurred in the vermillion and copper pigments. Also MA-XRF images have unveiled the overpainted drawing of a female figure, providing information about its original colors through the identification of the chemical nature of pigments not accessible by the radiographic imaging technique (XRR) previously performed. In particular, details of dress and combing, useful for attributing of the woman identity have been made visible by the correlation of red vermillion (Hg-L), green-blue copper-based pigments (Cu-K) and blue cobalt-based smalt (Co-K).

In a collaboration with the Egyptian Museum in Turin (Italy), MA-XRF investigation on painted wooden coffers belonging to the funeral collection of Kha and Merit (18th Dynasty) allowed the comprehension of the original pigments used in antiquity. Next to this, important information concerning the painting process was obtained through the identification of changes introduced during the creation of the work. The technique allowed also to highlight the rare use of a manganese black instead of black pigments of organic nature. The use of the two blacks can be attributed to the more practical motivation correlated to the availability of material and to a specific intent of the painter attributable to a pure aesthetic necessity and subordinated to the chromatic difference exhibited by the two different pigments.

Finally, the MA-XRF analysis on an Italian illuminated manuscript (Florence, 1370) was performed in a collaboration with Fitzwilliam Museum, providing valuable information concerning the artist's manufacturing technique and its connections with other artist's workshops through the re-construction of its pigments palette. The MA-XRF results covered the gap of information on the artwork due to the separation of the miniature from the parent volume. Further, MA-XRF analysis allowed to unveil the hidden liturgical inscription

present on the reverse side of the illuminated parchment glued to the cardboard support and therefore never read before, aiding significantly the collocation of the fragment within the parent manuscript.

In conclusion, despite the development of the present mobile XRF scanner has to be considered mature and its spectroscopic capabilities and instrumental performances have been largely validated by the analytical results obtained during the present research activity and in several other case-studies, some improvements and further technological developments have been already taken in consideration. The first forward step concerns the development of the acquisition system based on a multi-detectors station, in order to increase the counting statistics with a consequential improving of the lateral resolution in term of maps contrast and a better visualization of low-abundance elements also when ultra-fast scans are performed. In a first development phase, the system will be equipped with only two SDD detectors each coupled to a DXP, and the data reading, transferring and the data elaboration system will be consequently adapted to the new configuration of the instrument. The second aspect consists in the development of the integration of a confocal micro-XRF technique for in depth profiling along the stratigraphy of the painting. The confocal technique involves the use of a second lens on one of the detectors that works in combination to optic of the source and allows defining an analytical volume used to analyses the different pictorial layers. This way it will be possible an accurate knowledge of the sequence of the painted layers. The present set-up of the scanning system is already optimized for the confocal micro-XRF being equipped with a Z-axis that allows to move the spectrometer across the multilayered structure of the sample. In this way a unique device will allow for the first time to combine three analytical methods for XRF imaging applications.

References

[1] Gavrilov, D., Maev, R. G., & Almond, D. P. (2014). A review of imaging methods in analysis of works of art: Thermographic imaging method in art analysis. Canadian Journal of Physics, 92(4), 341-364.

[2] Eastaugh, N., Walsh, V., Chaplin, T., & Siddall, R. (2007). Pigment compendium: a dictionary of historical pigments. Routledge.

[3] Miliani, C., Rosi, F., Brunetti, B. G., & Sgamellotti, A. (2010). In situ noninvasive study of artworks: the MOLAB multitechnique approach. Accounts of chemical research, 43(6), 728-738.

[4] Ciliberto, E., & Spoto, G. (2000). Modern analytical methods in art and archaeology. John Wiley & Sons Canada.

[5] Artioli, G. (2010). Scientific methods and cultural heritage: an introduction to the application of materials science to archaeometry and conservation science. Oxford University Press.

[6] Leute, U. (1987). Archaeometry: an introduction to physical methods in archaeology and the history of art. VCH Verlagsgesellschaft mbH. Distribution, USA and Canada, VCH Publishers.

[7] Hein, A., Tsolakidou, A., Iliopoulos, I., Mommsen, H., i Garrigós, J. B., Montana, G., & Kilikoglou, V. (2002), Standardisation of elemental analytical techniques applied to provenance studies of archaeological ceramics: an inter laboratory calibration study. Analyst, 127(4), 542-553.

[8] Tite, M. S. (2008). Ceramic production, provenance and use—a review. Archaeometry, 50(2), 216-231.

[9] Wilson, A. L. (1978). Elemental analysis of pottery in the study of its provenance: a review. Journal of Archaeological Science, 5(3), 219-236.

[10] Barone, G., Crupi, V., Longo, F., Majolino, D., Mazzoleni, P., Spagnolo, G., ... & Aquilia, E. (2011). Potentiality of non-destructive XRF analysis for the determination of Corinthian B amphorae provenance. X-Ray Spectrometry, 40(5), 333-337.

[11] Wolff, T., Rabin, I., Mantouvalou, I., Kanngießer, B., Malzer, W., Kindzorra, E., & Hahn, O. (2012). Provenance studies on Dead Sea scrolls parchment by means of quantitative micro-XRF. Analytical and bioanalytical chemistry, 402(4), 1493-1503.

[12] Guerra, M. F., & Calligaro, T. (2003). Gold cultural heritage objects: a review of studies of provenance and manufacturing technologies. Measurement Science and Technology, 14(9), 1527.

[13] Van der Snickt, G., Dik, J., Cotte, M., Janssens, K., Jaroszewicz, J., De Nolf, W., ... & Van der Loeff, L. (2009), Characterization of a degraded cadmium yellow (CdS) pigment in an oil painting by means of synchrotron radiation based X-ray techniques. Analytical Chemistry, 81(7), 2600-2610.

[14] Casadio, F., Xie, S., Rukes, S. C., Myers, B., Gray, K. A., Warta, R., & Fiedler, I. (2011), Electron energy loss spectroscopy elucidates the elusive darkening of zinc potassium chromate in Georges Seurat's A Sunday on La Grande Jatte—1884. Analytical and bioanalytical chemistry, 399(9), 2909-2920.

[15] Monico, L., Janssens, K., Miliani, C., Van der Snickt, G., Brunetti, B. G., Guidi, M. C., ... & Cotte, M. (2013), Degradation process of lead chromate in paintings by Vincent van Gogh studied by means of spectromicroscopic methods. 4. Artificial aging of model samples of co-precipitates of lead chromate and lead sulfate. Anal. chem, 85(2), 860-867.

[16] Zanella, L., Casadio, F., Gray, K. A., Warta, R., Ma, Q., & Gaillard, J. F. (2011). The darkening of zinc yellow: XANES speciation of chromium in artist's paints after light and chemical exposures. Journal of Analytical Atomic Spectrometry, 26(5), 1090-10.

[17] Fleming, S. J. (1975). Authenticity in art.

[18] Szökefalvi-Nagy, Z., Demeter, I., Kocsonya, A., & Kovács, I. (2004). Non-destructive XRF analysis of paintings. Nuclear Instruments and Methods in Physics Research Section B: Beam Interactions with Materials and Atoms, 226(1), 53-59.

[19] Lahanier, C., Preusser, F. D., & Van Zelst, L. (1986). Study and conservation of museum objects: use of classical analytical techniques. Nuclear Instruments and Methods in Physics Research Section B: Beam Interactions with Materials and Atoms, 14(1), 1-9.

[20] Janssens, K., Vittiglio, G., Deraedt, I., Aerts, A., Vekemans, B., Vincze, L., ... & Rindby, A. (2000). Use of microscopic XRF for non-destructive analysis in art and archaeometry. X-ray Spectrometry, 29(1), 73-91.

[21] Shackley, M. S. (2011). An introduction to X-ray fluorescence (XRF) analysis in archaeology. In X-ray fluorescence spectrometry (XRF) in geoarchaeology (pp. 7-44). Springer New York.

[22] Mantler, M., & Schreiner, M. (2000). X-ray fluorescence spectrometry in art and archaeology. X-ray Spectrometry, 29(1), 3-17.

[23] Uda, M., Demortier, G., & Nakai, I. (Eds.). (2005). X-rays for Archaeology. Amsterdam, The Netherlands:: Springer.

[24] Schreiner, M., Frühmann, B., Jembrih-Simbürger, D., & Linke, R. (2004). X-rays in art and archaeology: an overview. Powder Diffraction, 19(01), 3-11.

[25] Neelmeijer, C., Brissaud, I., Calligaro, T., Demortier, G., Hautojärvi, A., Mäder, M., ... & Weber, G. (2000). Paintings— a challenge for XRF and PIXE analysis. X-ray spectrometry, 29(1), 101-110.

[26] Ricci, C., Borgia, I., Brunetti, B. G., Miliani, C., Sgamellotti, A., Seccaroni, C., & Passalacqua, P. (2004). The Perugino's palette: integration of an extended in situ XRF study by Raman spectroscopy. Journal of Raman Spectroscopy, 35(8-9), 616-621.

[27] Aliatis, I., Bersani, D., Campani, E., Casoli, A., Lottici, P. P., Mantovan, S., ... & Ospitali, F. (2009). Green pigments of the Pompeian artists' palette. Spectrochimica Acta Part A: Molecular and Biomolecular Spectroscopy, 73(3), 532-538.

[28] Miliani, C., Rosi, F., Burnstock, A., Brunetti, B. G., & Sgamellotti, A. (2007). Non-invasive in-situ investigations versus micro-sampling: a comparative study on a Renoirs painting. Applied Physics A, 89(4), 849-856.

[29] De Viguerie, L., Walter, P., Laval, E., Mottin, B., & Solé, V. A. (2010). Revealing the sfumato Technique of Leonardo da Vinci by X-Ray Fluorescence Spectroscopy. Angewandte Chemie International Edition, 49(35), 6125-6128.

[30] Romano, F. P., Pappalardo, G., Pappalardo, L., Garraffo, S., Gigli, R., & Pautasso, A. (2006), Quantitative non-destructive determination of trace elements in archaeological pottery using a portable beam stability-controlled XRF spectrometer. X-Ray Spectrometry, 35(1), 1-7.

[31] Sanderson, D. C. W., Hunter, J. R., & Warren, S. E. (1984). Energy dispersive X-ray fluorescence analysis of 1st millennium AD glass from Britain. Journal of Archaeological Science, 11(1), 53-69.

[32] Karydas, A. G., Kotzamani, D., Bernard, R., Barrandon, J. N., & Zarkadas, C. (2004), A compositional study of a museum jewellery collection (7th–1st BC) by means of a portable XRF spectrometer. Nuclear Instruments and Methods in Physics Research Section B: Beam Interactions with Materials and Atoms, 226(1), 15-28.

[33] Hall, E. T., Schweizer, F., & Toller, P. A. (1973). X-RAY FLUORESCENCE ANALYSIS OF MUSEUM OBJECTS: A NEW INSTRUMENT. Archaeometry, 15(1), 53-78.

[34] Jenkins, R. (1995). Quantitative X-ray spectrometry. CRC Press.

[35] De Viguerie, L., Sole, V. A., & Walter, P. (2009). Multilayers quantitative X-ray fluorescence analysis applied to easel paintings. Analytical and bioanalytical chemistry, 395(7), 2015-2020.

[36] Janssens, K., De Nolf, W., Van Der Snickt, G., Vincze, L., Vekemans, B., Terzano, R., & Brenker, F. E. (2010). Recent trends in quantitative aspects of microscopic X-ray fluorescence analysis. TrAC Trends in Analytical Chemistry, 29(6), 464-478.

[37] Karydas, A. G. (2007). Application of a Portable XRF Spectrometer for the Non-Invasive analysis of Museum Metal Artefacts. Annali di chimica, 97(7), 419-432.

[38] Papadopoulou, D. N., Zachariadis, G. A., Anthemidis, A. N., Tsirliganis, N. C., & Stratis, J. A. (2006). Development and optimisation of a portable micro-XRF method for in situ multi-element analysis of ancient ceramics. Talanta, 68(5), 1692-1699.

[39] Shackley, M. S. (2010). Is there reliability and validity in portable X-ray fluorescence spectrometry (PXRF). The SAA Archaeological Record, 10(5), 17-20.

[40] Potts, P. J., & West, M. (2008). Portable X-ray fluorescence spectrometry: Capabilities for in situ analysis. Royal Society of Chemistry.

[41] Zarkadas, C., & Karydas, A. G. (2004). A portable semi-micro-X-ray fluorescence spectrometer for archaeometrical studies. Spectrochimica Acta Part B: Atomic Spectroscopy, 59(10), 1611-1618.

[42] Hou, X., He, Y., & Jones, B. T. (2004). Recent advances in portable X-ray fluorescence spectrometry. Applied Spectroscopy Reviews, 39(1), 1-25.

[43] Brunetti, B. G., Matteini, M., Miliani, C., Pezzati, L., & Pinna, D. (2007). MOLAB, a mobile laboratory for in situ non-invasive studies in arts and archaeology. In Lasers in the Conservation of Artworks (pp. 453-460). Springer Berlin Heidelberg.

[44] Pages-Camagna, S., Laval, E., Vigears, D., & Duran, A. (2010). Non-destructive and in situ analysis of Egyptian wall paintings by X-ray diffraction and X-ray fluorescence portable systems. Applied Physics A, 100(3), 671-681.

[45] Križnar, A., Munoz, V., de la Paz, F., Respaldiza, M. A., & Vega, M. (2011). Portable XRF study of pigments applied in Juan Hispalense's 15th century panel painting. X-Ray Spectrometry, 40(2), 96-100.

[46] Migliori, A., Bonanni, P., Carraresi, L., Grassi, N., & Mando, P. A. (2011). A novel portable XRF spectrometer with range of detection extended to low-Z elements. X-Ray Spectrometry, 40(2), 107-112.

[47] Vittiglio, G., Janssens, K., Vekemans, B., Adams, F., & Oost, A. (1999). A compact small-beam XRF instrument for in-situ analysis of objects of historical and/or artistic value. Spectrochimica Acta Part B: Atomic Spectroscopy, 54(12), 1697-1710.

[48] Nazaroff, A. J., Prufer, K. M., & Drake, B. L. (2010). Assessing the applicability of portable X-ray fluorescence spectrometry for obsidian provenance research in the Maya lowlands. Journal of Archaeological Science, 37(4), 885-895.

[49] Trentelman, K., Bouchard, M., Ganio, M., Namowicz, C., Patterson, C. S., & Walton, M. (2010). The examination of works of art using in situ XRF line and area scans. X-Ray Spectrometry, 39(3), 159-166.

[50] Schreiner, M., Mantler, M., Weber, F., Ebner, R., & Mairinger, F. (1992), A new instrument for the energy dispersive X-ray fluorescence analysis of objects of art and archaeology. In Advances in x-ray analysis: proceedings of the annual Conference on Application of X-ray Analysis (Vol. 35, pp. 1157-1163).

[51] Mantler, M., Schreiner, M., Weber, F., Ebner, R., & Mairinger, F. (1992). An X-ray spectrometer for pixel analysis of art objects. Advances in X-ray Analysis, 35, 987-993.

[52] Alfeld, M., Van der Snickt, G., Vanmeert, F., Janssens, K., Dik, J., Appel, K., ... & Hendriks, E. (2013), Scanning XRF investigation of a Flower Still Life and its underlying composition from the collection of the Kroller-Muller Museum. Appl Phys A Mater Sci Process, 111, 165-175.

[53] Janssens, K., Alfeld, M., Van der Snickt, G., De Nolf, W., Vanmeert, F., Radepont, M., ... & Miliani, C. (2013), The use of synchrotron radiation for the characterization of artists' pigments and paintings. Annual Review of Analytical Chemistry, 6, 399-425.

[54] Alfeld, M., Siddons, D. P., Janssens, K., Dik, J., Woll, A., Kirkham, R., & van de Wetering, E. (2013). Visualizing the 17th century underpainting in Portrait of an Old Man by Rembrandt van Rijn using synchrotron-based scanning macro-XRF..

[55] Bull, D., Krekeler, A., Alfeld, M., Dik, J., & Janssens, K. (2011). An intrusive portrait by Goya. Burlingt Mag, 153, 668-673.

[56] Howard, D. L., de Jonge, M. D., Lau, D., Hay, D., Varcoe-Cocks, M., Ryan, C. G., ... & Thurrowgood, D. (2012). High-definition X-ray fluorescence elemental mapping of paintings. Analytical chemistry, 84(7), 3278-3286.

[57] Alfeld, M., Janssens, K., Appel, K., Thijsse, B., Blaas, J., & Dik, J. (2011). A portrait by Philipp Otto Runge-visualizing modifications to the painting using synchrotron-based X-ray fluorescence elemental scanning., Zeitschrift für Kunsttechnologie und Konservierung, 25, 157-163.

[58] Susini, J., Salomé, M., Fayard, B., Ortega, R., & Kaulich, B. (2002). The scanning X-ray microprobe at the ESRF" x-ray microscopy" beamline. Surface Review and Letters, 9(01), 203-211.

[59] Cotte, M., Welcomme, E., Solé, V. A., Salomé, M., Menu, M., Walter, P., & Susini, J. (2007). Synchrotron-based X-ray spectromicroscopy used for the study of an atypical micrometric pigment in 16th century paintings. Analytical chemistry, 79(18), 6988-6994.

[60] Haschke, M., Waldschläger, U., Tagle, R., & Rossek, U. (2012) Haschke, M., Waldschläger, U., Tagle, R., & Rossek, U. (2012). Rapid elemental distributions with high sensitivity by μ-XRF M. Haschke1,, U. Waldschläger1, R. Tagle1, U. Rossek1 1 Bruker Nano GmbH, Berlin, Germany. Microscopy and Microanalysis, 18(S2), 946-947.

[61] Alfeld, M., De Nolf, W., Cagno, S., Appel, K., Siddons, D. P., Kuczewski, A., ... & Sartorius, A. (2013), Revealing hidden paint layers in oil paintings by means of

scanning macro-XRF: a mock-up study based on Rembrandt's "An old man in military costume". Journal of Analytical Atomic Spectrometry, 28(1), 40-51.

[62] Alfeld, M., Janssens, K., Dik, J., de Nolf, W., & van der Snickt, G. (2011). Optimization of mobile scanning macro-XRF systems for the in situ investigation of historical paintings. Journal of Analytical Atomic Spectrometry, 26(5), 899-909.

[63] Alfeld, M., Pedroso, J. V., van Eikema Hommes, M., Van der Snickt, G., Tauber, G., Blaas, J., ... & Janssens, K. (2013), A mobile instrument for in situ scanning macro-XRF investigation of historical paintings. Journal of Analytical Atomic Spectrometry, 28(5), 760-767.

[64] Bronk, H., Röhrs, S., Bjeoumikhov, A., Langhoff, N., Schmalz, J., Wedell, R., ... & Waldschläger, U. (2001), ArtTAX–a new mobile spectrometer for energy-dispersive micro X-ray fluorescence spectrometry on art and archaeological objects. Fresenius' journal of analytical chemistry, 371(3), 307-316.

[65] Hocquet, F. P., del Castillo, H. C., Xicotencatl, A. C., Bourgeois, C., Oger, C., Marchal, A., ... & Strivay, D. (2011), Elemental 2D imaging of paintings with a mobile EDXRF system. Analytical and bioanalytical chemistry, 399(9), 3109-3116.

[66] Noble, P., Loon, A., Alfeld, M., Janssens, K., & Dik, J. (2012). Rembrandt and/or studio, Saul and David, c. 1655: revealing the curtain using cross-section analyses and X-ray fluorescence imaging. Technè, 35, 36-45.

[67] Ricciardi, P., Legrand, S., Bertolotti, G., & Janssens, K. (2016). Macro X-ray fluorescence (MA-XRF) scanning of illuminated manuscript fragments: potentialities and challenges. Microchemical Journal, 124, 785-791.

[68] Van der Snickt, G., Legrand, S., Caen, J., Vanmeert, F., Alfeld, M., & Janssens, K. (2016). Chemical imaging of stained-glass windows by means of macro X-ray fluorescence (MA-XRF) scanning. Microchemical Journal, 124, 615-622.

[69] Santos, H. C., Caliri, C., Pappalardo, L., Catalano, R., Orlando, A., Rizzo, F., & Romano, F. P. (2016). Identification of forgeries in historical enamels by combining the non-destructive scanning XRF imaging and alpha-PIXE portable techniques., Microchemical Journal, 124, 241-246.

[70] Legrand, S., Vanmeert, F., Van der Snickt, G., Alfeld, M., De Nolf, W., Dik, J., & Janssens, K. (2014), Examination of historical paintings by state-of-the-art hyperspectral imaging methods: from scanning infra-red spectroscopy to computed X-ray laminography. Heritage Science, 2(1), 1.

[71] Vandenabeele, P., Verpoort, F., & Moens, L. (2001), Non-destructive analysis of paintings using Fourier transform Raman spectroscopy with fibre optics. Journal of Raman Spectroscopy, 32(4), 263-269.

[72] Tomasini, E. P., Halac, E. B., Reinoso, M., Di Liscia, E. J., & Maier, M. S. (2012). Micro-Raman spectroscopy of carbon-based black pigments. Journal of Raman Spectroscopy, 43(11), 1671-1675.

[73] Pilc, J., & White, R. (1995). The application of FTIR-microscopy to the analysis of paint binders in easel paintings. National Gallery Technical Bulletin, 16, 73-84.

[74] Meilunas, R. J., Bentsen, J. G., & Steinberg, A. (1990). Analysis of aged paint binders by FTIR spectroscopy. Studies in conservation, 35(1), 33-51.

[75] Buti, D., Rosi, F., Brunetti, B. G., & Miliani, C. (2013). In-situ identification of copper-based green pigments on paintings and manuscripts by reflection FTIR. Analytical and bioanalytical chemistry, 405(8), 2699-2711.

[76] Fischer, C., & Kakoulli, I. (2006). Multispectral and hyperspectral imaging technologies in conservation: current research and potential applications. Studies in Conservation, 51(sup1), 3-16.

[77] Pelagotti, A., Del Mastio, A., De Rosa, A., & Piva, A. (2008). Multispectral imaging of paintings. IEEE Signal Processing Magazine, 25(4), 27-36.

[78] Cosentino, A. (2015). Panoramic, macro and micro multispectral imaging: An affordable system for mapping pigments on artworks. Journal of Conservation and Museum Studies, 13(1).

[79] Imai, F. H., Rosen, M. R., & Berns, R. S. (2001, April). Multi-spectral Imaging of a van Gogh's Self-portrait at the National Gallery of Art Washington DC. In PICS (pp. 185-189).

[80] Comelli, D., Valentini, G., Nevin, A., Farina, A., Toniolo, L., & Cubeddu, R. (2008). A portable UV-fluorescence multispectral imaging system for the analysis of painted surfaces. Review of Scientific Instruments, 79(8), 086112.

[81] De Boer, J. V. A. (1968). Infrared reflectography: a method for the examination of paintings. Applied Optics, 7(9), 1711-1714.

[82] Adam, A. J., Planken, P. C., Meloni, S., & Dik, J. (2009). TeraHertz imaging of hidden paint layers on canvas. Optics Express, 17(5), 3407-3416.

[83] Picollo, M., Fukunaga, K., & Labaune, J. (2015). Obtaining noninvasive stratigraphic details of panel paintings using terahertz time domain spectroscopy imaging system. Journal of Cultural Heritage, 16(1), 73-80.

[84] Abraham, E., Younus, A., Delagnes, J. C., & Mounaix, P. (2010). Non-invasive investigation of art paintings by terahertz imaging. Applied Physics A, 100(3), 585-590.

[85] Mittleman, D. M., Gupta, M., Neelamani, R., Baraniuk, R. G., Rudd, J. V., & Koch, M. (1999). Recent advances in terahertz imaging. Applied Physics B, 68(6), 1085-1094.

[86] Chan, W. L., Deibel, J., & Mittleman, D. M. (2007). Imaging with terahertz radiation. Reports on progress in physics, 70(8), 1325.

[87] Fukunaga, K., Ogawa, Y., Hayashi, S. I., & Hosako, I. (2007). Terahertz spectroscopy for art conservation. IEICE Electronics Express, 4(8), 258-263.

[88] Derrick, M. R., Stulik, D., & Landry, J. M. (1999). Infrared spectroscopy in conservation science. Scientific tools for conservation. The Getty Conservation Institute. Los Angeles Apendix II page 180. ISBN 0-89236-469-6.

[89] Mairinger, F. (2000). The infrared examination of paintings. Radiation in Art and Archeometry Eds. DC Creagh, DA Bradley, Elsevier, 40-55.

[90] H. Humphries-Black, Infrared testing in art conservation, Materials Evaluation 45 (1987) 426–429.

[91] Delaney, J. K., Zeibel, J. G., Thoury, M., Littleton, R., Palmer, M., Morales, K. M., ... & Hoenigswald, A. (2010), Visible and infrared imaging spectroscopy of Picasso's Harlequin Musician: mapping and identification of artist materials in situ. Applied Spectroscopy, 64(6), 584-594.

[92] De Boer, J. V. A. (1974). A note on the use of an improved infrared vidicon for reflectography of paintings. Studies in Conservation, 97-99.

[93] Attas, M., Cloutis, E., Collins, C., Goltz, D., Majzels, C., Mansfield, J. R., & Mantsch, H. H. (2003), Near-infrared spectroscopic imaging in art conservation: investigation of drawing constituents. Journal of Cultural Heritage, 4(2), 127-136.

[94] Mansfield, J. R., Attas, M., Majzels, C., Cloutis, E., Collins, C., & Mantsch, H. H. (2002). Near infrared spectroscopic reflectance imaging: a new tool in art conservation. Vibrational Spectroscopy, 28(1), 59-66.

[95] Asperen De Boer, J. V. (1969). Reflectography of paintings using an infrared vidicon television system. Studies in Conservation, 14(3), 96-118.

[96] Walmsley, E., Metzger, C., Delaney, J. K., & Fletcher, C. (1994). Improved visualization of underdrawings with solid-state detectors operating in the infrared. Studies in Conservation, 39(4), 217-231.

[97] Van der Weerd, J., Heeren, R. M., & de Boer, J. V. A. (2001). A European 640 x 486 PtSi camera for infrared reflectography. na.

[98] Walmsley, E., Metzger, C., Fletcher, C., & Delaney, J. K. (1993). Evaluation of platinum silicide cameras for use in infrared reflectography. In ICOM Committee for Conservation tenth triennial meeting,, Washington, DC, 22-27 August 1993: preprints (Vol. 1, pp. 57-62). International Council of Museums Committee for Conservation.

[99] Saunders, D., Billinge, R., Cupitt, J., Atkinson, N., & Liang, H. (2006). A new camera for high-resolution infrared imaging of works of art. Studies in Conservation, 51(4), 277-290.

[100] Consolandi, L., & Bertani, D. (2007). A prototype for high resolution infrared reflectography of paintings. Infrared physics & technology, 49(3), 239-242.

[101] Bertani, D., Cetica, M., Poggi, P., Puccioni, G., Buzzegoli, E., Kunzelman, D., & Cecchi, S. (1990). A scanning device for infrared reflectography. Studies in conservation, 35(3), 113-116.

[102] Delaney, J. K., Walmsley, E., Berrie, B. H., & Fletcher, C. F. (2005)., Multispectral imaging of paintings in the infrared to detect and map blue pigments. Proceedings of the National Academy of sciences, 120.

[103] Daffara, C., Pampaloni, E., Pezzati, L., Barucci, M., & Fontana, R. (2010). Scanning multispectral IR reflectography SMIRR: an advanced tool for art diagnostics. Accounts of chemical research, 43(6), 847-856.

[104] Daffara, C., & Fontana, R. (2011). Multispectral infrared reflectography to differentiate features in paintings. Microscopy and Microanalysis, 17(05), 691-695.

[105] Moutsatsou, A., Skapoula, D., & Doulgeridis, M. (2011), The Contribution of Transmitted Infrared Imaging to Non-Invasive Study of Canvas Paintings at the National Gallery–Alexandros Soutzos Museum, Greece. e-conservation magazine, 22, 53-61.

[106] Kushel, D. A. (1985). Applications of transmitted infrared radiation to the examination of artifacts. Studies in Conservation, 30(1), 1-10.

[107] Cornelius, F. D. (1977). Correspondence: transmitted infrared photography. Studies in conservation, 22(1), 42.

[108] Bridgman, C. F. (1964). The amazing patent on the radiography of paintings. Studies in Conservation, 9(4), 135-139.

[109] Magliano, P., & Boesmi, B. (1988). Xeroradiography for paintings on canvas and wood. Studies in conservation, 33(1), 41-47.

[110] van Heugten, S. (1995). Radiographic images of Vincent van Gogh's paintings in the collection of the Van Gogh museum. Van Gogh Museum Journal, 1995, 63-85.

[111] Padfield, J., Saunders, D., Cupitt, J., & Atkinson, R. (2002). Improvements in the acquisition and processing of X-ray images of paintings. National Gallery Technical Bulletin, 23, 62-75.

[112] Vermehren, A. (1952). Sulle possibilita stereo-strato-radiografiche di un nuovo tipo di apparecchio a raggi x in dotazione presso l'istituto centrale del restauro in roma. Bollettino dell'Istituto centrale del restauro, 1952(11-12), 121-133.

[113] Pease, M. (1946). A Note on the Radiography of Paintings. Bulletin of the Metropolitan Museum of Art, 4, 136-139.

[114] Bridgman, C. F., & Keck, S. (1961). The radiography of paintings. Medical radiography and photography, 37(3), 62-70.

[115] Bridgman, C. F., Michaels, P., & Sherwood, H. F. (1965). Radiography of a painting on copper by electron emission. Studies in Conservation, 10(1), 1-7.

[116] Johnson, D. H., Johnson, C. R., & Erdmann, R. G. (2013). Weave analysis of paintings on canvas from radiographs. Signal Processing, 93(3), 527-540.

[117] EMANDI, I., IOVEA, M., DULIU, O. G., & EMANDI, A. (2011). X-RAY RADIOGRAPHIC STUDY OF SOME PANEL PAINTING ICONS FROM THE BEGINNING OF THE XX TH CENTURY. International Journal of Conservation Science, 2(3).

[118] Van Tilborgh, L., Meedendorp, T., Hendriks, E., Johnson, D. H., Johnson Jr, C. R., & Erdmann, R. G. (2012). Weave matching and dating of van Gogh's paintings: An interdisciplinary approach. The Burlington Magazine, 154, 112-122.

[119] Liedtke, W., Johnson Jr, C. R., & Johnson, D. H. (2012). Canvas matches in Vermeer: A case study in the computer analysis of fabric supports. Metropolitan Museum Journal, 47(1), 101-108.

[120] Albertin, F., Franconieri, A., Gambaccini, M., Moro, D., Petrucci, F., & Chiozzi, S. (2009). A quasi-monochromatic X-rays source for art painting pigments investigation. Applied Physics A, 96(2), 503-510.

[121] Krug, K., Dik, J., Den Leeuw, M., Whitson, A. D., Tortora, J., Coan, P., ... & Bravin, A. (2006). Visualization of pigment distributions in paintings using synchrotron K-edge imaging. Applied Physics A, 83(2), 247-251.

[122] Schalm, O., Cabal, A., Van Espen, P., Laquière, N., & Storme, P. (2011). Improved radiographic methods for the investigation of paintings using laboratory and synchrotron X-ray sources. Journal of Analytical Atomic Spectrometry, 26(5), 1068-1077.

[123] Zemlicka, J., Jakubek, J., Kroupa, M., Hradil, D., Hradilova, J., & Mislerova, H. (2011). Analysis of painted arts by energy sensitive radiographic techniques with the Pixel Detector Timepix. Journal of Instrumentation, 6(01), C01066.

[124] Scharf, O., Ihle, S., Ordavo, I., Arkadiev, V., Bjeoumikhov, A., Bjeoumikhova, S., ... & Kuhbacher, M. (2011). Compact pnCCD-based X-ray camera with high spatial and energy resolution: a color X-ray camera. Analytical chemistry, 83(7), 2532-2538.

[125] Ordavo, I., Ihle, S., Arkadiev, V., Scharf, O., Soltau, H., Bjeoumikhov, A., ... & Hartmann, R. (2011)., A new pnCCD-based color X-ray camera for fast spatial and energy-resolved measurements. Nuclear Instruments and Methods in Physics Research Section A: Accelerators, Spectrometers, Detectors and Associated Equipment, 654(1), 250-257.

[126] Romano, F. P., Caliri, C., Cosentino, L., Gammino, S., Giuntini, L., Mascali, D., ... & Taccetti, F. (2014)., Macro and micro full field X-ray fluorescence with an X-ray

pinhole camera presenting high energy and high spatial resolution. Analytical chemistry, 86(21), 10892-10899.

[127] Cotter, M., Meyers, P., Van Zelst, L., & Sayre, E. (1973). Authentication of paintings by Ralph A. Blakelock through neutron activation autoradiography. Journal of Radioanalytical and Nuclear Chemistry, 15(1), 265-285.

[128] Ainsworth, M. W. (1982). Art and autoradiography: insights into the genesis of paintings by Rembrandt, Van Dyck, and Vermeer. Metropolitan Museum of Art.

[129] Cotter, M. J., Meyers, P., Van Zelst, L., Olin, C. H., & Sayre, E. V. (1976)., Study of the Materials and Techniques Used by Some XIX Century American Oil Painters by Means of Neutron Activation Autoradiography. In Congresso International Applicazione dei metodi nucleari nel campo delle opere d'arte (pp. 163-203).

[130] Sayre, E. V., & Lechtman, H. N. (1968). Neutron activation autoradiography of oil paintings. Studies in Conservation, 13(4), 161-185.

[131] Lechtman, H. N. (1966). Neutron activation autoradiography of oil paintings. Department of Fine Arts, New York University, 164.

[132] Barton, J. P. (1965). Radiology using neutrons. Studies in Conservation, 10(4), 135-141.

[133] Kühn, H. (1966). Trace elements in white lead and their determination by emission spectrum and neutron activation analysis. Studies in Conservation, 11(4), 163-169.

[134] Beckhoff, B., Kanngießer, B., Langhoff, N., Wedell, R., & Wolff, H. (Eds.). (2007). Handbook of practical X-ray fluorescence analysis. Springer Science & Business Media.

[135] Bertin, E. P. (2013). Introduction to X-ray spectrometric analysis. Springer Science & Business Media.

[136] Thomsen, V., Schatzlein, D., & Mercuro, D. (2005). Tutorial: Attenuation of X-Rays By Matter. Spectroscopy, 20(9), 22-25.

[137] Thomsen, V. (2007). Basic fundamental parameters in X-ray fluorescence. SPECTROSCOPY-SPRINGFIELD THEN EUGENE THEN DULUTH-, 22(5), 46.

[138] Siegbahn, M. (1925). The Spectroscopy of X-rays. Oxford University Press, H. Milford.

[139] Criss, J. W., & Birks, L. S. (1968). Calculation methods for fluorescent x-ray spectrometry. Empirical coefficients versus fundamental parameters. Analytical Chemistry, 40(7), 1080-1086.

[140] Sherman, J. (1955). The theoretical derivation of fluorescent X-ray intensities from mixtures. Spectrochimica Acta, 7, 283-306.

[141] Sherman, J. (1954, January). The correlation between fluorescent X-ray intensity and chemical composition. In Symposium on Fluorescent X-ray Spectrographic Analysis. ASTM International.

[142] Hubbell, J. H. (1969). Photon cross sections, attenuation coefficients, and energy absorption coefficients from 10 keV to 100 GeV (No. NSRDS-NBS-29). National Standard Reference Data System.

[143] Reynolds, R. C. (1967). ESTIMATION OF MASS ABSORPTION COEFFICIENTS BY COMPTON SCATTERING-IMPROVEMENTS AND EXTENSIONS OF METHOD. American Mineralogist, 52(9-10), 1493.

[144] Hubbell, J. H. (1982). Photon mass attenuation and energy-absorption coefficients. The International Journal of Applied Radiation and Isotopes, 33(11), 1269-1290.

[145] Berger, M. J., & Seltzer, S. M. (1999). XCOM Photon Cross Sections (Vol. 3). Version.

[146] http://physics.nist.gov/PhysRefData/XrayMassCoef/tab3.html.

[147] McMaster, W. H., Del Grande, N. K., Mallett, J. H., & Hubbell, J. H. (1969). COMPILATION OF X-RAY CROSS SECTIONS. SECTION III (No. UCRL--50174 (Sect. 3)). California Univ., Livermore. Lawrence Radiation Lab.

[148] Hirayama, H. (2000). Lecture note on photon interactions and cross sections. KEK, High Energy Accelerator Research Organization Ibaraki, Japan.

[149] Ebel, H., Svagera, R., Ebel, M. F., Shaltout, A., & Hubbell, J. H. (2003). Numerical description of photoelectric absorption coefficients for fundamental parameter programs. X-Ray Spectrometry, 32(6), 442-451.

[150] Moseley, H. G. (1913). XCIII. The high-frequency spectra of the elements. The London, Edinburgh, and Dublin Philosophical Magazine and Journal of Science, 26(156), 1024-1034.

[151] Jenkins, R., Manne, R., Robin, R., & Senemaud, C. (1991). IUPAC—nomenclature system for x-ray spectroscopy. X-Ray Spectrometry, 20(3), 149-155.

[152] http://old.iupac.org/reports/V/spectro/partVIII.pdf.

[153] Bambynek, W., Crasemann, B., Fink, R. W., Freund, H. U., Mark, H., Swift, C. D., ... & Rao, P. V. (1972). X-ray fluorescence yields, Auger, and Coster-Kronig transition probabilities. Reviews of Modern Physics, 44(4), 716.

[154] Shiraiwa, T., & Fujino, N. (1966). Theoretical Calculation of Fluorescent X-Ray Intensities in Fluorescent X-Ray Spectrochemical Analysis. Japanese Journal of Applied Physics, 5(10), 886.

[155] Shiraiwa T, Fujino N, Theoretical calculation of fluorescent X-ray intensities in fluorescent X-ray spectrochemical analysis. Jpn J Appl Phys 5, 886–899 (1966).

[156] Fink, R. W., Jopson, R. C., Mark, H., & Swift, C. D. (1966). Atomic fluorescence yields. Reviews of Modern Physics, 38(3), 513.

[157] Krause, M. O. (1979). Atomic radiative and radiationless yields for K and L shells. Journal of physical and chemical reference data, 8(2), 307-327.

[158] Firestone, R. B., & Shirley, V. S. (1998). Table of isotopes, 2 volume set. Table of Isotopes, 2 Volume Set, by Richard B. Firestone, Virginia S. Shirley (Editor), pp. 3168. ISBN 0-471-33056-6. Wiley-VCH, December 1998., 3168.

[159] http://physics.nist.gov/PhysRefData/Xcom/html/xcom1-t.html.

[160] Klein, O., & Nishina, Y. (1929). Über die Streuung von Strahlung durch freie Elektronen nach der neuen relativistischen Quantendynamik von Dirac. Zeitschrift für Physik, 52(11-12), 853-868.

[161] L. Vincze, K. Janssens, F. Adams, M. L. Rivers, and K. W. Jones. A general Monte Carlo simulation of ED-XRF spectrometers. II: Polarized monochromatic radiation, homogeneous samples. Spectrochim. Acta, Part B, 50:127 – 147, 1995.

[162] Radiation Shielding Information Center Data Library Package DLC-136/PHOTX, \Photon Interaction Cross Section Library", contributed by the National Institute of Standards and Technology.

[163] DuMond, J. W. (1933). The linear momenta of electrons in atoms and in solid bodies as revealed by X-ray scattering. Reviews of Modern Physics, 5(1), 1.

[164] Hubbell, J. H. (1989). Bibliography and current status of K, L, and higher shell fluorescene yields for computations of photon energy-absorption coefficients (No.

NISTIR-89-4144). US Dept. of Commerce, National Institute of Standards and Technology.

[165] Langhoff, N., Simionovici, A., Arkadiev, V., Knüpfer, W., Čechák, T., Leonhardt, J., & Chavanne, J. (2006). X-Ray Sources. In Handbook of Practical X-Ray Fluorescence Analysis (pp. 33-83). Springer Berlin Heidelberg.

[166] Simionovici, A., & Chavanne, J. (2007). 2.4 Synchrotron Radiation Sources. Handbook of Practical X-Ray Fluorescence Analysis, 66.

[167] Hirsch, P. B., & Kellar, J. N. (1951). An X-ray micro-beam technique: I-collimation. Proceedings of the Physical Society. Section B, 64(5), 369.

[168] Pound, R. V., & Rebka Jr, G. A. (1959). Gravitational red-shift in nuclear resonance. Physical Review Letters, 3(9), 439.

[169] Marton, L. (1966). X-ray fiber optics. Applied Physics Letters, 9(5), 194-195.

[170] Mallozzi, P. J., Epstein, H. M., Jung, R. G., Applebaum, D. C., Fairand, B. P., Gallagher, W. J., ... & Muckerheide, M. C. (1974). Laser-generated plasmas as a source of x rays for medical applications. Journal of Applied Physics, 45(4), 1891-1895.

[171] Gibson, W. M., & MacDonald, C. A. (1994, July). Polycapillary Kumakhov optics: a status report. In SPIE's 1994 International Symposium on Optics, Imaging, and Instrumentation (pp. 156-167). International Society for Optics and Photonics.

[172] Gibson, W. M., MacDonald, C. A., & Kumakhov, M. S. (1991, May). The Kumakhov Lens; a New X-Ray and Neutron Optics with Potential for Medicalapplications. In Technology Requirements for Biomedical Imaging, 1991. Proceedings (pp. 43-48). IEEE.

[173] MacDonald, C. A. (1996). Applications and measurements of polycapillary x-ray optics. Journal of X-ray Science and Technology, 6(1), 32-47.

[174] Schields, P. J., Gibson, D. M., Gibson, W. M., Gao, N., Huang, H., & Ponomarev, I. Y. (2002). Overview of polycapillary X-ray optics. Powder Diffraction, 17(02), 70-80.

[175] Bjeoumikhov, A., Langhoff, N., Wedell, R., Beloglazov, V., Lebed'ev, N., & Skibina, N. (2003). New generation of polycapillary lenses: manufacture and applications. X-Ray Spectrometry, 32(3), 172-178.

[176] Bjeoumikhov, A., Bjeoumikhova, S., & Wedell, R. (2009). New Developments and Applications of X-Ray Capillary Optics. Particle & Particle Systems Characterization, 26(3), 97-106.

[177] MacDonald, C. A., & Gibson, W. M. (2003). Applications and advances in polycapillary optics. X-Ray Spectrometry, 32(3), 258-268.

[178] Buzanich, G., Wobrauschek, P., Streli, C., Markowicz, A., Wegrzynek, D., Chinea-Cano, E., & Bamford, S. (2007)., A portable micro-X-ray fluorescence spectrometer with polycapillary optics and vacuum chamber for archaeometric and other applications. Spectrochimica Acta Part B: Atomic Spectroscopy, 62(11), 1252-1256..

[179] Hofmann, F. A., Gao, N., Owens, S. M., Gibson, W. M., MacDonald, C. A., & Lee, S. M. (1997). Polycapillary Optics for in Situ Diagnostics. In MRS Proceedings (Vol. 502, p. 133). Cambridge University Press.

[180] Erko, A., Schäfers, F., Firsov, A., Peatman, W. B., Eberhardt, W., & Signorato, R. (2004). The BESSY X-ray microfocus beamline project. Spectrochimica Acta Part B: Atomic Spectroscopy, 59(10), 1543-1548.

[181] Janssens, K., Proost, K., & Falkenberg, G. (2004). Confocal microscopic X-ray fluorescence at the HASYLAB microfocus beamline: characteristics and possibilities. Spectrochimica Acta Part B: Atomic Spectroscopy, 59(10), 1637-1645.

[182] Proost, K., Vincze, L., Janssens, K., Gao, N., Bulska, E., Schreiner, M., & Falkenberg, G. (2003). Characterization of a polycapillary lens for use in micro-XANES experiments. X-Ray Spectrometry, 32(3), 215-222.

[183] Silversmit, G., Vekemans, B., Nikitenko, S., Tirez, K., Bras, W., Brenker, F. E., & Vincze, L. (2009). Polycapillary based μ-XAS and confocal μ-XANES at a bending magnet source of the ESRF, In Journal of Physics: conference series (Vol. 190, No. 1, p. 012036). IOP Publishing.

[184] Guilherme, A., Buzanich, G., & Carvalho, M. L. (2012). Focusing systems for the generation of X-ray micro beam: An overview. Spectrochimica Acta Part B: Atomic Spectroscopy, 77, 1-8.

[185] Gao, N., Ponomarev, I. Y., Xiao, Q. F., Gibson, W. M., & Carpenter, D. A. (1997). Enhancement of microbeam x-ray fluorescence analysis using monolithic polycapillary focusing optics. Applied physics letters, 71(23), 3441-3443.

[186] http://www.ifg-adlershof.de/index.php?id=15.

[187] MacDonald, C. A. (2011). Focusing polycapillary optics and their applications. X-Ray Optics and Instrumentation, 2010.

[188] Adams, F., Janssens, K., & Snigirev, A. (1998). Microscopic X-ray fluorescence analysis and related methods with laboratory and synchrotron radiation sources. Journal of Analytical Atomic Spectrometry, 13(5), 319-331.

[189] Wu, X., & Liu, H. (2003). A general theoretical formalism for X-ray phase contrast imaging. Journal of X-ray Science and Technology, 11(1), 33-42.

[190] Carpenter, D. A. (1989). Improved laboratory X-ray source for microfluorescence analysis. X-Ray Spectrometry, 18(6), 253-257.

[191] Rhodes, J. R. (1966). Radioisotope X-ray spectrometry. A review. Analyst, 91(1088), 683-699.

[192] LaBrecque, J. J., Vaz, J. E., Cruxent, J. M., & Rosales, P. A. (1998)., A simple radioisotope X-ray fluorescence method for provenance studies of archaeological ceramics employing principal component analysis. Spectrochimica Acta Part B: Atomic Spectroscopy, 53(1), 95-100.

[193] Florkowski, T., & Stos, Z. (1975). NON-DESTRUCTIVE RADIOISOTOPE X-RAY FLUORESCENCE ANALYSIS OF OLD SILVER COINS. Archaeometry, 17(2), 165-175.

[194] Potts, P. J., Ellis, A. T., Kregsamer, P., Streli, C., Vanhoof, C., West, M., & Wobrauschek, P. (2005). Atomic spectrometry update. X-ray fluorescence spectrometry. Journal of analytical atomic spectrometry, 20(10), 1124-1154.

[195] Pérez, C. A., Radtke, M., Sánchez, H. J., Tolentino, H., Neuenshwander, R. T., Barg, W., ... & Rohwedder, J. J. (1999). Synchrotron radiation X-ray fluorescence at the LNLS: beamline instrumentation and experiments. X-Ray Spectrometry, 28(5), 320-326.

[196] Jones, K. W., Gordon, B. M., Hanson, A. L., Kwiatek, W. M., & Pounds, J. G. (1988). X-ray fluorescence with synchrotron radiation. Ultramicroscopy, 24(2-3), 313-328.

[197] Winick, H., & Doniach, S. (2012). Synchrotron radiation research. Springer Science & Business Media.

[198] Gilfrich, J. V., Skelton, E. F., Qadri, S. B., Kirkland, J. P., & Nagel, D. J. (1983). Synchrotron radiation X-ray fluorescence analysis. Analytical Chemistry, 55(2), 187-190.

[199] Codling, K., Gudat, W., Koch, E. E., Kotani, A., Lynch, D. W., Rowe, E. M., ... & Toyozawa, Y. (2013). Synchrotron radiation: techniques and applications (Vol. 10). C. Kunz (Ed.). Springer Science & Business Media.

[200] http://pocketdentistry.com/1-physics/.

[201] Ebel, H. (1999). X-ray tube spectra. X-Ray Spectrometry, 28(4), 255-266.

[202] Van Espen, P. (1994). Analysis of X-ray spectra by iterative least squares (AXIL): New developments. X-Ray Spectrometry, 23(6), 278-285.

[203] Bertin, E. P. (1975). Principles and Practice of X-Ray Spectrometric Analysis. 2nd edn Plenum Press. New York, London, 1079.

[204] Van Grieken, R., & Markowicz, A. (Eds.). (2001). Handbook of X-ray Spectrometry. CRC Press.

[205] Knoll, G. F. (2010). Radiation detection and measurement. John Wiley & Sons.

[206] Gruner, S. M., Eikenberry, E. F., & Tate, M. W. (2006). Comparison of X-ray detectors. In International Tables for Crystallography Volume F: Crystallography of biological macromolecules (pp. 143-147). Springer Netherlands.

[207] Bertolini, G., & Coche, A. (1968). SEMICONDUCTOR DETECTORS.

[208] Jaklevic, J. M., & Goulding, F. S. (1971). Detection of low energy X rays with Si (Li) detectors. IEEE Transactions on Nuclear Science, 18(1), 187-191.

[209] https://amptek.com/pdf/ansdd3.pdf.

[210] http://www.azom.com/article.aspx?ArticleID=11973.

[211] Alur, R., Arzen, K. E., Baillieul, J., & Henzinger, T. A. (2007). Handbook of networked and embedded control systems. D. Hristu-Varsakelis, & W. S. Levine (Eds.). Springer Science & Business Media.

[212] Jochum, K. P., Weis, U., Stoll, B., Kuzmin, D., Yang, Q., Raczek, I., ... & Günther, D. (2011), Determination of reference values for NIST SRM 610–617 glasses following ISO guidelines. Geostandards and Geoanalytical Research, 35(4), 397-429.

[213] Gao, N., & Ponomarev, I. Y. (2003). Polycapillary x-ray optics: manufacturing status, characterization and the future of the technology. X-Ray Spectrometry, 32(3), 186-194.

[214] Unser, M. (2000). Sampling-50 years after Shannon. Proceedings of the IEEE, 88(4), 569-587.

[215] Newport. Usaf-1951 test targets (www.newport.com).

[216] Lasch, P., & Naumann, D. (2006). Spatial resolution in infrared microspectroscopic imaging of tissues. Biochimica et Biophysica Acta (BBA)-Biomembranes, 1758(7), 814-829.

[217] Riederer, J., Schweppe, H., Winter, J., Feller, R. L., Johnston-Feller, R. M., Berrie, B. H., ... & Laver, M. (1997), Artists' pigments: a handbook of their history and characteristics, v. 3. E. W. Fitzhugh (Ed.). Washington, DC; National Gallery of Art; New York; Oxford; Dist. by Oxford University Press.

[218] Solé, V. A., Papillon, E., Cotte, M., Walter, P., & Susini, J. (2007). A multiplatform code for the analysis of energy-dispersive X-ray fluorescence spectra. Spectrochimica Acta Part B: Atomic Spectroscopy, 62(1), 63-68..

[219] Scofield, J. H. (1973). Theoretical Photoionization Cross Sections From 1 To 1500 Kev (No. Ucrl--51326). California Univ., Livermore. Lawrence Livermore Lab.

[220] Brunetti, A., Del Rio, M. S., Golosio, B., Simionovici, A., & Somogyi, A. (2004). A library for X-ray–matter interaction cross sections for X-ray fluorescence applications. Spectrochimica Acta Part B: Atomic Spectroscopy, 59(10), 1725-1731.

[221] Kissel, L. (2000). RTAB: the Rayleigh scattering database. Radiation Physics and Chemistry, 59(2), 185-200.

[222] Chen, M. H., Crasemann, B., & Mark, H. (1979). Relativistic radiationless transition probabilities for atomic K-and L-shells. Atomic Data and Nuclear Data Tables, 24(1), 13-37.

[223] Van Espen, P., Nullens, H., & Adams, F. (1977). A method for the accurate description of the full-energy peaks in non-linear least-squares analysis of X-ray spectra. Nuclear Instruments and Methods, 145(3), 579-582.

[224] Lépy, M. C. (2004). Presentation of the COLEGRAM software. Note Technique LHNB/04/26.

[225] Levenberg, K. (1944). A method for the solution of certain non-linear problems in least squares. Quarterly of applied mathematics, 2(2), 164-168.

[226] Marquardt, D. W. (1963). An algorithm for least-squares estimation of nonlinear parameters. Journal of the society for Industrial and Applied Mathematics, 11(2), 431-441.

[227] Press, W. H., Teukolsky, S. A., Vetterling, W. T., & Flannery, B. P. (1996). Numerical recipes in C (Vol. 2). Cambridge: Cambridge university press.

[228] Vekemans, B., Janssens, K., Vincze, L., Adams, F., & Van Espen, P. (1995). Comparison of several background compensation methods useful for evaluation of energy-dispersive X-ray fluorescence spectra. Spectrochimica Acta Part B: Atomic Spectroscopy, 50(2).

[229] Alfeld, M., & Janssens, K. (2015). Strategies for processing mega-pixel X-ray fluorescence hyperspectral data: a case study on a version of Caravaggio's painting Supper at Emmaus. Journal of analytical atomic spectrometry, 30(3), 777-789.

[230] Ryan, C. G., Clayton, E., Griffin, W. L., Sie, S. H., & Cousens, D. R. (1988). SNIP, a statistics-sensitive background treatment for the quantitative analysis of PIXE spectra in geoscience applications, Nuclear Instruments and Methods in Physics Research Section B: Beam Interactions with Materials and Atoms, 34(3), 396-402.

[231] Anitha, A., Brasoveanu, A., Duarte, M., Hughes, S., Daubechies, I., Dik, J., ... & Alfeld, M. (2013). Restoration of X-ray fluorescence images of hidden paintings. Signal Processing, 93(3), 592-604.

[232] Beal, M. R. S. (1984). A study of Richard Symonds: his Italian notebooks and their redevance to seventeenth-century painting techniques. Garland.

[233] Kühn, H. (1967). Bleiweiss und seine Verwendung in der Malerei: I. Farbe und Lack, 73(2), 99-105.

[234] Sabin, A. H. (1920). White-lead: its use in paint. John Wiley & Sons, Incorporated.

[235] Wallert, A., Hermens, E., & Peek, M. (1995). Historical Painting Techniques, Materials, and Studio Practice: Preprints of a Symposium, University of Leiden, the Netherlands, 26–29 June 1995. Getty Publications.

[236] Brachert, F., & Brachert, T. (1980). Zinnober. Maltechnik restauro, 86(3), 145-158.

[237] Loon, A. V. (2008). Color changes and chemical reactivity in seventeenth-century oil paintings.

[238] Cotte, M., Susini, J., Metrich, N., Moscato, A., Gratziu, C., Bertagnini, A., & Pagano, M. (2006). Blackening of Pompeian cinnabar paintings: X-ray microspectroscopy analysis. Analytical chemistry, 78(21), 7484-7492.

[239] Keune, K., & Boon, J. J. (2005). Analytical imaging studies clarifying the process of the darkening of vermilion in paintings. Analytical chemistry, 77(15), 4742-4750.

[240] Spring, M., & Grout, R. (2002). The blackening of vermilion: an analytical study of the process in paintings. National Gallery Technical Bulletin, 23, 50-61.

[241] Gettens, R. J., & Fitzhugh, E. W. (1974). Malachite and green verditer. Studies in Conservation, 19(1), 2-23.

[242] Kühn, H. (1964). Grünspan und seine Verwendung in der Malerei. Farbe u. Lack, 70, 703-711.

[243] Franquelo, M. L., Duran, A., Herrera, L. K., de Haro, M. J., & Perez-Rodriguez, J. L. (2009). Comparison between micro-Raman and micro-FTIR spectroscopy techniques for the characterization of pigments from Southern Spain Cultural Heritage, Journal of Molecular structure, 924, 404-412.

[244] Gunn, M., Chottard, G., Rivière, E., Girerd, J. J., & Chottard, J. C. (2013). Chemical reactions between copper pigments and oleoresinous media. Studies in conservation.

[245] Pavlopoulou, L. C., & Watkinson, D. (2006). The degradation of oil painted copper surfaces. Studies in Conservation, 51(sup1), 55-65.

[246] Mattei, E., De Vivo, G., De Santis, A., Gaetani, C., Pelosi, C., & Santamaria, U. (2008). Raman spectroscopic analysis of azurite blackening. Journal of Raman Spectroscopy, 39(2), 302-306.

[247] Fuller, C. (1988). Natural Colored Iron Oxide Pigments. Pigment Handbook, 2, 281-286.

[248] Thomas, A. W. (1980). Colors from the Earth. Van Nostrand Reinhold Company.

[249] Kühn, H. (1993). Lead-tin yellow. In Artists' pigments: a handbook of their history and characteristics. Volume 2 (pp. 83-112). National Gallery of Art, Washington, DC, United States.

[250] Wallert, A. (1984). Orpiment and realgar. Maltechnik restauro, (4), 45-57.

[251] Rötter, C. (2003). Auripigment: genauere Betrachtung eines historischen Farbmittels. Restauro: Zeitschrift für Kunsttechniken, Restaurierung und Museumsfragen, 109(6), 408-413.

[252] Mühlethaler, B., & Thissen, J. Smalt','Artists' Pigments', Vol. 2, 1993 (pp. 113-30). cited in note 47.

[253] Binger, H. (1996). Das blaupigment smalte. Restauro, 1, 36-39.

[254] Riederer, J. (1968). Die smalte. Deutsche Farbenzeitschrift, 22(9), 386-395.

[255] Stege, H. (2004). Out of the blue? Considerations on the early use of smalt as blue pigment in European easel painting. Zeitschrift für Kunsttechnologie und Konservierung: ZKK, 18(1), 121-142.

[256] Sparavigna, A. C. (2011). The architect Kha's protractor. ARCHAEOGATE, July, 28.

[257] Porter, B., & Moss, R. L. B. (1972). Topographical bibliography of ancient Egyptian hieroglyphic texts, reliefs, and paintings (Vol. 2). Clarendon Press.

[258] Schiaparelli, E. (2007). La tomba intatta dell'architetto Kha nella necropoli di Tebe. AdArte.

[259] Meskell, L. (1998). Intimate archaeologies: the case of Kha and Merit. World archaeology, 29(3), 363-379.

[260] Robins, G. (2008). The art of ancient Egypt. Harvard University Press.

[261] Ellis, E. L. (1965). Inorganic elements in wood.

[262] Scott, D. A. (2016). A review of ancient Egyptian pigments and cosmetics. Studies in Conservation, 61(4), 185-202.

[263] Chu, V., Regev, L., Weiner, S., & Boaretto, E. (2008). Differentiating between anthropogenic calcite in plaster, ash and natural calcite using infrared spectroscopy: implications in archaeology. Journal of Archaeological Science, 35(4), 905-911.

[264] Lucas, A., & Harris, J. R. (1962). Ancient Egyptian Materials and Industries: Edward Arnold. London, UK, 523.

[265] Blom-Böer, I. (1994). Zusammensetzung altägyptischer Farbpigmente und ihre Herkunftslagerstätten in Zeit und Raum. Oudheidkundige mededeelingen van het Rijksmuseum van Oudheden te Leiden, 74, 55-107.

[266] Green, L. R. (1995), In Conservation in ancient Egyptian collections: papers given at the conference organised by the UKIC, Archaeology Section, and International Academic Projects, held in London, 20-21 July 1995 (pp. 85-91). Archetype Publications, Ltd.

[267] Barbieri, M., Calderoni, G., Cortesi, C., & Fornaseri, M. (1974). Huntite, a mineral used in antiquity. Archaeometry, 16(2), 211-220.

[268] Moussa, A. M. A., Kantiranis, N., Voudouris, K. S., Stratis, J. A., Ali, M. F., & Christaras, V. (2009). The impact of soluble salts on the deterioration of pharaonic and Coptic wall paintings.

[269] Heywood, A. (2001). The use of huntite as a white pigment in ancient Egypt. In Colour and painting in ancient Egypt (pp. 5-9). British Museum Press.

[270] Riederer, J. (1974). Recently identified Egyptian pigments. Archaeometry, 16(1), 102-109.

[271] Uda, M., Tsunokami, T., Murai, R., Maeda, K., Harigai, I., Nakayama, Y., ... & Sasa, Y. (1993). Quantitative analysis of ancient Egyptian pigments by external PIXE, Nuclear Instruments and Methods in Physics Research Section B: Beam Interactions with Materials and Atoms, 75(1), 476-479..

[272] Franceschi, E., & Locardi, F. (2014). Strontium, a new marker of the origin of gypsum in cultural heritage?. Journal of Cultural Heritage, 15(5), 522-527.

[273] Nagashima, S., Kato, M., Kotani, T., Morito, K., Miyazawa, M., Kondo, J., ... & Uda, M. (1996). Application of the external PIXE analysis to ancient Egyptian objects, Nuclear Instruments and Methods in Physics Research Section B: Beam Interactions with Materials and Atoms, 109, 658-661.

[274] Riederer, J. (1997). Egyptian blue. Artists' pigments: a handbook of their history and characteristics, 3, 23-46.

[275] Chiavari, G., Fabbri, D., Galletti, G. C., & Mazzeo, R. (1995). Use of analytical pyrolysis to characterize Egyptian painting layers. Chromatographia, 40(9-10), 594-600.

[276] Lee, L., & Quirke, S. (2000). 4. Painting materials. Ancient Egyptian materials and technology, 104.

[277] J.Riederer, "Egyptian Blue", Artists Pigments, Volume 3, E. West FitzHugh (ed.), Oxford University Press: Oxford, 1997.

[278] Tite, M. S., Bimson, M., & Cowell, M. R. (1987). The technology of Eygptian blue. In Early vitreous materials (pp. 19-47). British Museum.

[279] Tite, M. S., Bimson, M., & Cowell, M. R. (1984). Technological examination of Egyptian blue. Advances in chemistry series, 205, 215-242.

[280] Jaksch, H., Seipel, W., Weiner, K. L., & El Goresy, A. (1983). Egyptian blue—cuprorivaite a window to ancient Egyptian technology. Naturwissenschaften, 70(11), 525-535.

[281] Colinart, S. (2003). The Egyptian green pigment: its manufacturing process and links to Egyptian blue. Archaeometry, 45(4), 637-658.

[282] Spurrell, F. C. J. (1895). Notes on Egyptian colours. Archaeological Journal, 52(1), 222-239.

[283] Evans, D., Hamburg, D. A., & Mickelson, M. P. (1980, April). A papyrus treatment: bringing the Book of the Dead to life. In Art Conservation Training Programs Conference (pp. 109-126). University of Delaware.

[284] FitzHugh, E. W. (1997). Orpiment and realgar. Artists' pigments: a handbook of their history and characteristics, 3, 47-79.

[285] Estaugh, N., Walsh, V., Chaplin, T., & Siddall, R. (2004). The Pigment Compendium: Optical Microscopy of Historical Pigments.

[286] Colinart, S. (2001). Analysis of iconographic yellow colour in ancient Egyptian painting. In Colour and painting in ancient Egypt (pp. 1-4). British Museum Press.

[287] Trentelman, K., Stodulski, L., & Pavlosky, M. (1996). Characterization of pararealgar and other light-induced transformation products from realgar by Raman microspectroscopy. Analytical Chemistry, 68(10), 1755-1761.

[288] Burgio, L., & Clark, R. J. (2000). Comparative pigment analysis of six modern Egyptian papyri and an authentic one of the 13th century BC by Raman microscopy and other techniques. Journal of Raman Spectroscopy, 31(5), 395-401.

[289] Daniels, V., & Leach, B. (2004). The occurrence and alteration of realgar on Ancient Egyptian papyri. Studies in Conservation, 49(2), 73-84.

[290] Green, L. (2001). Colour transformations of ancient Egyptian pigments. In Colour and painting in ancient Egypt (pp. 43-48). British Museum Press.

[291] Middleton, A., & Humphrey, S. (2001). Pigments on some Middle Kingdom coffins. In Colour and painting in ancient Egypt (pp. 10-16). British Museum Press.

[292] Winter, J., & FitzHugh, E. W. (2007). Pigments based on carbon. Artists' pigments, 4, 1-37.

[293] Gettens, R. J., & Stout, G. L. (1966). Painting materials: a short encyclopaedia. Courier Corporation.

[294] Middleton, A. (1999). Polychromy of some fragments of painted relief from El-Bersheh. Studies in Egyptian antiquities; a tribute to TGH James: British Museum Occasional Paper, 123, 37-44.

[295] Delaney, J. K., Ricciardi, P., Glinsman, L. D., Facini, M., Thoury, M., Palmer, M., & Rie, E. R. D. L. (2014), Use of imaging spectroscopy, fiber optic reflectance spectroscopy, and X-ray fluorescence to map and identify pigments in illuminated manuscripts. Studies in Conservation, 59(2), 91-101.

[296] Aceto, M., Agostino, A., Fenoglio, G., Idone, A., Gulmini, M., Picollo, M., ... & Delaney, J. K. (2014), Characterisation of colourants on illuminated manuscripts by portable fibre optic UV-visible-NIR reflectance spectrophotometry. Analytical Methods, 6(5), 1488-1500.

[297] Ricciardi, P., Delaney, J. K., Facini, M., & Glinsman, L. (2013), Use of imaging spectroscopy and in situ analytical methods for the characterization of the materials and techniques of 15th century illuminated manuscripts. Journal of the American Institute for Conservation, 52(1), 13-29.

[298] Kren, T., & Barstow, K. (2005). Italian illuminated manuscripts in the J. Paul Getty Museum. Getty Publications.

[299] Wormald, F., & Giles, P. M. (1952). A Handlist of the Additional Manuscripts in the Fitzwilliam Museum. Transactions of the Cambridge Bibliographical Society, 1(4), 297-309.

[300] Gettens, R. J., FitzHugh, E. W., & Feller, R. L. (1993). Calcium carbonate whites. In Artists' pigments: a handbook of their history and characteristics. Volume 2 (pp. 203-226). National Gallery of Art, Washington, DC, United States.

[301] Brady, G. S., & Clauser, H. R. Materials Handbook, ; 1986.

[302] Gettens, R. J., Feller, R. L., & Chase, W. T. (1972). Vermilion and cinnabar. Studies in Conservation, 17(2), 45-69.

[303] Kühn, H. (1969). Die pigmente in den Gemalden der Shack-Galerie, Bayerisce Staaatsgemalde-sammlungen.

[304] Patton, T. C. (1973). Pigment handbook.(Vols 1-3).

[305] Ricciardi, P., Pallipurath, A., & Rose, K. (2013). 'It's not easy being green': a spectroscopic study of green pigments used in illuminated manuscripts. Analytical Methods, 5(16), 3819-3824.

[306] Re, A., Giudice, A. L., Angelici, D., Calusi, S., Giuntini, L., Massi, M., & Pratesi, G. (2011). Lapis lazuli provenance study by means of micro-PIXE, Nuclear Instruments and Methods in Physics Research Section B: Beam Interactions with Materials and Atoms, 269(20), 2373-2377.

[307] ARS., Hamilton, G. H., & Thompson, D. V. (1933). An Anonymous Fourteenth-Century Treatise: De Arte Illuminandi. The Technique of Manuscript Illumination, The Technique of Manuscript Illumination. Translated from the Latin of the Naples Ms. XII. E. 27 by Daniel Varney Thompson... and George Heard Hamilton. Yale University Press.

[308] Trentelman, K., Patterson, C. S., Trentelman, N. T. K., & Turner, N. (2012). XRF analysis of manuscript illuminations1 XRF analysis of manuscript illuminations1. Handheld XRF for Art and Archaeology, 3, 159.